



Cavity-photon controlled electron transport through quantum dots and waveguide systems

Nzar Rauf Abdullah



Faculty of Physical Sciences
University of Iceland
2015

CAVITY-PHOTON CONTROLLED ELECTRON TRANSPORT THROUGH QUANTUM DOTS AND WAVEGUIDE SYSTEMS

Nzar Rauf Abdullah

180 ECTS thesis submitted in partial fulfillment of a
Doctor Philosophiae degree in Physics

Advisor

Prof. Viðar Guðmundsson

Ph.D. committee

Prof. Andrei Manolescu

Prof. Chi-Shung Tang

Opponents

Prof. Michael Thorwart

Editor-in-Chief New Journal of Physics

Institute for theoretical physics, University of Hamburg

Prof. Einar Örn Sveinbjörnsson

Science Institute, University of Iceland

Faculty of Physical Sciences

School of Engineering and Natural Sciences

University of Iceland

Reykjavik, May 2015

Cavity-photon controlled electron transport through quantum dots and waveguide systems

Dissertation submitted in partial fulfillment of a Ph.D. degree in Physics (Theoretical Physics: Quantum Mechanics)

Copyright © 2015 Nzar Rauf Abdullah
All rights reserved

Faculty of Physical Sciences
School of Engineering and Natural Sciences
University of Iceland
Hjarðarhaga 2-6
107, Reykjavík
Iceland

Telephone: 525 4708

Bibliographic information:

Nzar Rauf Abdullah, 2015, Cavity-photon controlled electron transport through quantum dots and waveguide systems, Ph.D. thesis, Faculty of Physical Sciences, University of Iceland.

ISBN 978-9935-9214-9-9

Printing: Háskólaprent, Fálkagata 2, 107 Reykjavík
Reykjavík, Iceland, May 2015

Abstract

In this thesis, I model quantum mechanical systems and investigate their quantum properties based on mathematical formulations of quantum mechanics. Modeling of quantum systems such as qubits in quantum information processing is studied. Transport of correlated electrons through a quantized electronic system such as single or double quantum dots embedded in a quantum wire, and double quantum waveguide is investigated using a non-Markovian quantum master equation formalism. The quantized electronic system is weakly connected to external leads and strongly coupled to a single photon mode in a cavity. The total system, the central electronic system and the leads, is in an external homogeneous magnetic field perpendicular to the plane of the electron motion in the system. The photons in the cavity are linearly polarized either parallel (x -polarization) or perpendicular (y -polarization) to the direction of electron propagation in the central system. The full electron-electron and electron-photon interactions are taken into account using an “exact diagonalization” technique in a truncated many-body space.

I observe that a cavity-photon can enhance the electron transport in the single or double quantum dot system. In the absence of the cavity, a peak (main peak) in the net charge current is found due to an electron tunneling almost elastically from the leads to the central system. In the presence of an x -polarized photon field, a side peak to the main peak is observed. The side peak indicates inelastic electron tunneling from the leads to the central system in which the electrons absorb photons in the cavity. The side peak current is very weak in the y -polarized photon field. This is caused by the anisotropy of the central system. Furthermore, I notice that the mechanism of electron transport from the leads to the central system in the main peak is different from what happens for the side peak and depends on the photon number initially in the cavity.

In addition, I use cavity-photons to implement a quantum logic gate in a double waveguide system which consists of control- and target-waveguide. The two waveguides are coupled via a coupling element the so called coupling window. The coupling window (CW) relies on interference of quantum waves causing electron switching between the waveguides.

In the case of the waveguide system without the photon cavity, oscillation in the net charge current is found by tuning the length of the CW indicating inter-waveguide backward and forward scattering. A current peak for a crossover energy displaying ‘resonant’ energy levels between the waveguides and a current dip for split energy levels are observed. In the non-interacting waveguide system, electron charge from input control-waveguide splits ‘equally’ between the output of the control- and target-waveguide at the current peak. The charge splitting feature indicates a

quantum logic gate action called square-root-of-Not-operation ($\sqrt{\text{NOT}}$ -operation). Including electron-electron interaction in the waveguide system, the net charge current is suppressed because the Coulomb interaction raises the two-electron states in the energy spectrum leading to vanishing participation the two-electron states in the electron transport.

In the presence of an x -polarized photon field, I observe suppression in the net charge current in both current peak and the current dip. This is due to contribution of the photon replica states to the electron transport leading to inter-waveguide backward scattering. We find that I can influence the logic-gate action of the system by selecting the initial status of the photon field (number of photons and polarization) and the size of the coupling window.

Útdráttur

Í þessari ritgerð er lýst flutningi víxlverkandi rafeinda um tvívítt rafeindakerfi af takmarkaðri stærð. Um er að ræða staka skammtapunkta eða pör þeirra sem komið er fyrir í stuttum skammtavír. Einnig verður fjallað um kerfi skammtabylgjuleiðara. Rafeindakerfið er veiktengt ytri leiðslum, en sterklega tengt einum ljóseindahætti í rafsegulholi. Rafeindakerfið og leiðslurnar eru í ytra einsleitu þverstæðu segulsviði. Ljóseindasviðið er skautað samsíða (x -stefna) flutningsstefnunni eða þvert á hana (y -stefna). Innbyrðis víxlverkun rafeindanna og víxlverkun þeirra við ljóseindasviðið er reiknuð nákvæmlega í stýfðu fjöleinda Fock-rúmi.

Við sjáum að holljóseind getur aukið leiðni rafeinda um skammtapunktakerfið. Án ljóseindaholsins finnast smughermur milli leiðslanna og rafeindakerfisins sem leiða til topps í strauminum í gegnum kerfið. Þegar rafeindakerfið er í ljóseindaholi finnast hliðartoppar við aðaltoppana. Hliðartopparnir eru vegna ófjaðrandi flutnings rafeinda um kerfið þar sem ljóseindir koma við sögu. Fyrir y -skautun eru hliðartoppar mjög veikir. Skautunarmunurinn er vegna þess hve kerfið er fjarri að vera einsleitt. Mikill munur er á smásæju ferlunum sem liggja að baki aðal- og hliðartoppunum og upphaflegur ljóseindafjöldi breytir miklu þar um.

Við sýnum einnig að hægt er að nýta holljóseindir til þess að stýra rökaðgerðum rafeindanna í kerfi tveggja bylgjuleiðara. Þeir eru tengdir saman um svo kallaðan tengiglugga milli þeirra. Tengiglugginn verkar vegna bylgjuvígla rafeindanna í leiðurunum.

Án ljóseindaholsins finnast sveiflur í rafeindastraumnum í leiðurunum sem breyta má með lengd tengigluggans. Rafeindir geta skipt um leiðara (akrein) og haldið áfram eða snúið til baka. Straumtoppur frá öðrum leiðaranum til hins finnst þegar orkustig þeirra lenda í hermu, en straumdæld þegar orkustigin leyfa ekki samtalið leiðaranna. Án innbyrðisvíxlverkunar rafeindanna er jafnlíklegt að þær skipti um leiðara eða haldi beint áfram í straumtoppi. Straumurinn getur því hermt eftir svo kallaðri kvaðratrót af EKKI-aðgerð. Með innbyrðisvíxlverkun þeirra er líkleggra að rafeindirnar haldi beint áfram vegna þess að tveggja rafeindaástöndin sem eru nauðsynleg til leiðaraskiptanna liggja hærra í orkurófinu.

Fyrir víxlverkandi rafeindakerfið í rafsegulholi með x -skautað ljóseindasvið sést að bæði straumtoppurinn og dældin fletjast út. Það er vegna þess að ljóseindasviðið virðist hvetja rafeindirnar til þess að snúa við. Enn fremur komust við að því að við getum valið rökaðgerð kerfisins með því að still fjölda ljóseinda og skautun þeirra í upphafi.

List of publications

Publications included in this thesis

- I **Electron transport through a quantum dot assisted by cavity photons.**
Nzar R. Abdullah, C.-S. Tang, A. Manolescu, and V. Gudmundsson.
Journal of Physics: Condensed Matter **25**, 465302 (2013).
- II **Delocalization of electrons by cavity photons in transport through a quantum dot molecule.**
Nzar R. Abdullah, C.-S. Tang, A. Manolescu, and V. Gudmundsson.
Physica E: Low-dimensional Systems and Nanostructures **64**, 254 (2014).
- III **Cavity-photon-switched coherent transient transport in a double quantum waveguide.**
Nzar R. Abdullah, C.-S. Tang, A. Manolescu, and V. Gudmundsson.
Journal of Applied Physics **116**, 233104 (2014).
- IV **Coherent transient transport of interacting electrons through a quantum waveguide switch.**
Nzar R. Abdullah, C.-S. Tang, A. Manolescu, and V. Gudmundsson.
Journal of Physics: Condensed Matter **27**, 015301 (2015).

Publications not included in this thesis

- V **Coupled collective and Rabi oscillations triggered by electron transport through a photon cavity.**
V. Gudmundsson, A. Sitek, P. Lin, N. R. Abdullah, C-S Tang, and A. Manolescu.
Submitted for publication, arXiv:1502.06242 (2015).

Acknowledgments

I would like to express my special and deep thanks to my supervisor Professor Viðar Guðmundsson who gave me a golden opportunity to do this wonderful project on the topic of modeling of quantum mechanical systems and quantum mechanical transport, which helped me in research giving insight into so many new things. I am also grateful for his fruitful discussions, honest answers, and patience. He has shown me how to use time efficiently and usefully to get expected goals. I am really thankful to him.

I thank Chi-Shung Tang for his aspiring guidance, and his comments on my results and papers for the sake of improvement, Andrei Manolescu for his guidance and constructive criticism on my papers, and Thorsten Arnold for his help in some technical programming.

I am using this opportunity to thank everyone in Science institute - Physics department specially Pei-yi Lin, Tómas Örn Rosdahl, Anna Sitek, and Seyedmohammad Shayestehaminzadeh, Bing Cui, Rabia Yasmin, and all members in Hannes group in Chemistry department, specially Avan Anwar, Younes Abghoui, and Javed Hussain. Their friendship is so great to me.

I would also like to thank Arann Taha and Dr. Aram Namiq for providing me with all the necessary facilities at the beginning of my study. I place on record, my sincere thank to my colleagues at the University of Sulaimani especially Dr. Adil, Dr. Omed, Dr. Aras, Mr. Hossien, and Dr. Hawri, thank you for the continuous encouragement.

I express my warm thanks to Aysun, Gerlinde, Dara, Bnar, Salah, Sausan, Yousf, Aras, Kawa, Mustafa for sharing wonderful time together in Iceland. I would especially like to thank my friends, Surkew, Harem, Hiwa, Rebwar, Rebin, Zanst, Jamawar, Rzgar, Mzhda for the unforgotten times we spend together.

Finally, a special thanks to my family. Words cannot express how grateful I am to my parents, sisters, and brothers-in-law for all kinds of supports and all of the sacrifices that you've made on my behalf. I know my life will not be easy and enjoyable without them.

Financial support is acknowledged from the Icelandic Research and Instruments

Funds, and Eimskip Fund of the University of Iceland. The calculations were carried out on the Nordic high Performance computer (Gardar). I acknowledge workshop invitations from the Norden Network NANOCONTROL.

Contents

List of Figures	xv
1. Introduction	1
1.1. Photon-assisted electron transport	2
1.2. Implementation of quantum logic gate in qubit systems	3
2. Theoretical basis	5
2.1. Single-electron states	5
2.1.1. Closed system	5
2.1.2. Electron reservoirs	8
2.1.3. Contact area	10
2.2. Fock-space and many-electron calculations	12
2.2.1. Central system with Coulomb interaction	13
2.2.2. The leads and Coupling Hamiltonian	15
2.3. Cavity photons and the many-body Hamiltonian	17
3. Non-Markovian approach to a generalized quantum master equation	23
3.1. Liouville-von Neumann equation	23
3.2. Nakajima-Zwanzig Formalism	24
4. Physical observables	29
4.1. Electron and photon number operator	29
4.2. Charge density	30
4.3. Charge current density	30
4.4. Net charge current	31
5. Results and Conclusions	33
5.1. Cavity-photon-assisted electron transport	34
5.1.1. Single quantum dot system	34
5.1.2. Double quantum dot system	38
5.2. Quantum Logic gate actions in a qubit system	40
5.3. Conclusions	51
A. Matrix elements of the single-electron Hamiltonian	53
A.1. Closed system	53
A.1.1. Matrix elements of \mathbf{p} and \mathbf{A}_{ext} terms	53

Contents

A.1.2. Matrix elements of a Gaussian potential	55
A.1.3. Matrix elements of V_{pg} and h_Z terms	57
A.2. Matrix elements of the lead Hamiltonian in the SE basis	58
B. Many-Body Hamiltonian	61
B.1. Electron-photon coupling function	61
B.2. \mathbf{A}^2 - term	62
C. Charge current density	65
D. Quantum Master equation	69
D.1. Properties of Projection operator	69
D.2. Derivation of Eq. (3.24)	70
Bibliography	73

List of Figures

2.1. Eigenvalues of the central system	7
2.2. Energy spectrum of the leads	10
2.3. Many-electron energy spectrum of the central system	15
2.4. Schematic of an electron system coupled to a photon cavity	17
5.1. Quantum dot system	35
5.2. Energy spectrum of the leads and the QD system	35
5.3. The net charge current of the QD system without the photon cavity .	36
5.4. MB energy spectrum of the QD system coupled to the photon cavity	37
5.5. The net charge current of the QD system coupled to the photon cavity	37
5.6. Electron charge density of DQD in the absence of a photon cavity . .	39
5.7. Electron charge density of DQD in the presence of photon cavity . . .	39
5.8. Schematic representation of a double waveguide	40
5.9. The net charge current of the DQW without a photon cavity	42
5.10. The ME energy spectrum of the DQW system	43
5.11. Charge current density in the DQW without photon cavity	44
5.12. The net charge current of DQW with photon cavity	45
5.13. MB-energy spectrum of the DQW	46

LIST OF FIGURES

5.14. The charge current density of the DQW coupled to photon cavity . .	47
5.15. The charge current density at $N_{\text{ph}} = 2$, and $\hbar\omega_{\text{ph}} = 0.6$ meV	48
5.16. The charge current density at $N_{\text{ph}} = 1$, and $\hbar\omega_{\text{ph}} = 0.9$ meV	49
5.17. The charge current density at $N_{\text{ph}} = 2$, and $\hbar\omega_{\text{ph}} = 0.6$ meV, y - polarization	50

1. Introduction

Theoretical development of quantum mechanical systems is an initiation point for new technological devices. Particularly, modeling of quantum mechanical systems and investigation quantum transport are essential in the field of quantum information processing [1] and opto-electronic systems in the nanoscale range [2, 3]. Different geometrical structures can be realized in a two-dimensional electron gas (2DEG) such as quantum dots [4], double dots [5], rings [6], quantum point contacts [7] and double quantum wires [8]. Investigation of quantum properties of nanostructures is also motivated by the scientific interest in transport characteristics such as electrical [9], spin [10], thermal [11] transport, that are conveniently studied because of the large Fermi wavelength and mean free path in the 2DEG at low temperature.

A quantized electronic system in a nanoscale range can be coupled to electron reservoirs to form an open quantum system. In theory of open quantum systems, environments are assumed to be bosonic or fermionic. In the electronic circuit, a quantized system is usually connected to fermionic reservoirs which act as electron sources. Therefore, electrons and information exchange between the subsystems is enabled. A number of approaches have been employed to investigate exchange of electrons or electron transport in an open system, such as Wigner-function formalism [12], Landauer formalism [13, 14], Green-Keldysh approach [15], Lippmann-Schwinger equation [8], and master equation approach [16]. To study time-dependent transport in many-electron open systems, the master equation describing time evolution of the probability of a given physical system is broadly used. The Jarzynski equation was derived using a master equation formalism to study fluctuation theorems [17], and dissipative quantum dynamics [18]. Interaction effects can be investigated with the master equation, the current noise spectrum [19], statistics of electron transfers through a coupled system [20], and the evolution of the charge in the presence of Nyquist or Schottky noise [21].

The quantum master equations are commonly classified as Markovian [22–24] or non-Markovian [25–29]. It has been reported that the Markovian limit neglects coherent oscillations in the transient regime, and that the rate at which the steady state is reached does not agree with the non-Markovian model [30]. The Markov approximation shows significantly longer time to reach a steady state when the tunneling anisotropy is high, thus confirming its applicability only in the long-time limit. To investigate the transient transport, a non-Markovian density-matrix formalism

1. Introduction

should be explicitly considered [31].

In addition to the electron transport in open systems, the interaction of electrons in nanoscale system with a photon radiation field has opened a new area of research with the aim to construct optoelectronic devices. In this case one needs to seek for optical properties of a quantum system [32]. An interesting study of electronic system coupled to a photon radiation is photon-assisted transport (PAT), which is highlighted by many scientific research groups [33, 34]. In the PAT the photon radiation is used to enhance electron transport in a quantum structure. The photon radiation can also be used for switching electrons between coupled systems such as double quantum dot and double quantum waveguides. The electron-switching process has been achieved implementing a quantum logic gate action in quantum bits [35]. In the following the PAT phenomenon in quantum dots and the implementation of quantum logic gate in qubit systems shall be described using a non-Markovian master equation formalism.

1.1. Photon-assisted electron transport

A crucial development in experimental and theoretical physics is the capability for studying dynamical processes in open systems. The electron transport through a quantized electronic structure connected to the electron reservoirs can be controlled by a plunger-gate voltage. The plunger-gate voltage can shift the energy levels of a system with respect to other connected subsystems bringing energy levels into resonance. The electrons perform elastic transport between the quantized systems. The elastic electron transport phenomena in the composed electronic system have received attention in recent years due to their potential application in various fields, such as for implementation of quantum computing [36], nanoelectromechanical systems [37], photo-detectors [38].

An opto-electronic device provides a different platform of electron transport, namely photon-assisted transport [39]. In the presence of an external photon radiation electron transport is drawing interest because the electron-photon interaction plays an essential role to enhance the electron transport characteristics [40–43]. In the PAT, the energy levels of an electronic system have to match the photon frequency of a radiation source for the electron motion to be influenced. For that purpose, an electrostatic potential produced by a plunger-gate is applied to the electronic system to shift its energy levels in and out of resonance. The plunger-gate is widely used to control charge current [44–46], thermal current [47], photo-current [48–50] and spin-dependent current [51] for various quantized systems coupled to photon radiation [52–56]. A convenient structure for investigating PAT is a quantum dot (QD) or a double quantum dot (DQD) because of their discrete energy levels and

potential for application in information storage in a quantum state [57], quantum-bits for quantum computing [58, 59], and quantum information processing in two-state system [60]. Recent experimental work has studied PAT using the two lowest energy states contributing to electron tunneling: A ground state resonance, and a photon-induced excited state resonance. The study shows multiphoton absorption processes up to the fourth-order participating in the electron tunneling [61].

In the above mentioned examples the photon-assisted transport was induced by a classical electromagnetic field. It is also interesting to investigate electron transport through a QD or DQD system influenced by a quantized photon field because in the quantized field a single photon can be used to obtain a PAT process. In fact there are potential efforts for implementing fully optoelectronic device by providing single photon sources. An example of that is a DQD coupled to a photon field in which the resonant current and resonant tunneling between two QDs assisted by a single photon are calculated [57, 62]. However, modeling of transient electronic transport through QD system in a photon cavity is still in its infancy. In this thesis, the full quantum description of PAT is considered in which both the electronic and the photon sources are assumed to be quantized. Furthermore, it is shown how a single photon mode polarized parallel or perpendicular to the direction of the electron transport through the system influences the electron motion through it.

1.2. Implementation of quantum logic gate in qubit systems

An electronic waveguide can be used to implement a quantum logic gate in a quantum information processing [63]. A quantum wire can be considered as a waveguide in which the electron wave is transported in quantized modes without losing phase coherence. The essential idea is to use parallel quantum waveguides with a coupling-window placed between them. Tuning the window-coupling allows an electron wave interference between the waveguides. Therefore, the electrons can switch from one waveguide to the other through a coupling element [64]. There are some other suggestions to construct qubit system such as double quantum dots [65], double waveguides with double coupling windows [66], and superconducting elements [67]. In this thesis, we only focus on double waveguides with a single coupling window to implement quantum logic gates.

The electron motion characteristics in the double waveguide system determines possible quantum logic operations; in particular, a square-root-of-NOT-operation ($\sqrt{\text{NOT}}$ -operation) is performed if the electron charge splits equally between the waveguides [68], a NOT-operation is realized if the electron wavefunction switches

1. Introduction

from the first waveguide to the second waveguide [69], and the charge might switch from the first waveguide to the second one and then re-enter the first. The presence of the magnetic field corresponds to the input of the control bit in the controlled NOT function [70].

It is possible to control the fraction (probability) of the electron wave transferred from one waveguide to the other. There are several techniques that have been suggested to switch electron charge providing the qubit operation as is presented in the following. Electron switching by an electrostatic potential, in this technique the coupling window is formed by a saddle potential that washes out fluctuation resonance peaks, but reduces the efficiency of the gate-operation to below 100% [35]. Another method for increasing inter-waveguide transport in a Coulomb blockade regime is to use a single quantum dot that is embedded close to the coupling window [71], the quantum dot increases the coupling between the waveguides. Magnetic switching can be seen as a different technique to transfer an electron wave between two asymmetric waveguides. Ferry considered an external magnetic field that is applied to a double waveguide where the magnetic field is used as an external ‘force’ to switch electron motion between the waveguides [72]. Another suggestion is to vary the length of the coupling window between the waveguides implementing different quantum logic gates and increasing the efficiency of the device [73]. Acoustic waves have been considered for electron switching [74].

In this thesis, we model a double quantum waveguide (DQW) system weakly connected to the leads and strongly coupled to a photon cavity. The double waveguides are coupled through a coupling window to facilitate inter-waveguide transport. The importance of the electron-electron interaction on the quantum logic gates is presented. In addition, the role of photon energy, photon number, and photon polarization in the cavity on the electron transport and implementation of the quantum logic gate is demonstrated. This cavity-photon-switched electron transport can be seen as a new technique in quantum information processing and quantum computer.

This thesis is organized as follows. The theoretical basis and the Hamiltonian of the total system are described in Chapter 2. In Chapter 3 the non-Markovian generalized master equation formalism is provided. We describe some physical observables that we calculate in Chapter 4. Finally, Chapter 5 shows the main result of this thesis.

2. Theoretical basis

In nanoscale systems, wave-behavior of a particle becomes important because the dimensions of the system are comparable to the wavelength of the particle. In this case, the Schrödinger equation is the equation of motion for the wavefunction Ψ of the particle [75]

$$\hat{H} |\Psi, t\rangle = i\hbar \frac{\partial}{\partial t} |\Psi, t\rangle, \quad (2.1)$$

with \hat{H} being the Hamiltonian of the system which can either depend on, or be independent of time. In this Thesis, the time-independent Schrödinger equation is used to explore the static properties of a closed system but the time-dependent one is needed when the closed system is opened by weakly coupling it to the environment or electron reservoirs.

2.1. Single-electron states

In this section, the Hamiltonian of the system in a single electron state (SES) basis is presented. The system consists of a finite quantized electronic system connected to electron reservoirs and coupled to a photon cavity. The Hamiltonian of the system, closed electronic system, electron reservoirs, and the photon cavity, shall be described in the following. Later we resort to a many-body description since the number of electrons can vary.

2.1.1. Closed system

A quantized system is a “closed system” if it does not interact with its environment or couple to external electron reservoirs. For instance, a 2DEG can be seen as a closed system before applying to it a bias voltage [76]. The physical properties of 2DEG have been investigated theoretically [77] and experimentally [78]. The time-independent Schrödinger equation for the Hamiltonian of the central system, as considered in this thesis, reduces to the energy eigenvalue problem

$$\hat{H}_{\text{SE}} |\Psi\rangle = E_{\text{SE}} |\Psi\rangle, \quad (2.2)$$

2. Theoretical basis

where E_{SE} is the single-electron (SE) energy, \hat{H}_{SE} is the time-independent Hamiltonian of the system, and $|\Psi\rangle$ is an eigenstate. The electronic system is a two-dimensional finite system that is hard-wall confined at $x = \pm L_x/2$ in the x -direction, and parabolically confinement in the y -direction, where L_x is the length of the system. The system is put into an external perpendicular magnetic field $\mathbf{B} = B\hat{z}$ defining a magnetic length $l = (h/eB)^{1/2} = 25.67[B(\text{T})]^{-1/2}$ nm. The single-electron Hamiltonian of the system is

$$\hat{H}_{\text{SE}} = \frac{1}{2m^*}(\mathbf{p} + \frac{e}{c}\mathbf{A}_{\text{ext}})^2 + \frac{1}{2}m^*\Omega_0^2 y^2 + V_G + eV_{\text{pg}} + h_Z. \quad (2.3)$$

Herein, m^* is the effective mass of the electron, \mathbf{p} indicates the canonical momentum operator, $\mathbf{A}_{\text{ext}} = -By\hat{\mathbf{x}}$ is the vector potential of the external magnetic field defined in the Landau gauge with the cyclotron frequency $\omega_c = eB/m^*$. The effective confinement frequency is thus $\Omega_w^2 = \omega_c^2 + \Omega_0^2$, where Ω_0 is the transverse electron confinement frequency. In addition, V_G stands for the potential that forms the geometry of the central system, V_{pg} is the plunger-gate voltage, and h_Z the Zeeman energy $\pm \frac{1}{2}g^*\mu_B B$ indicating the interaction between spin and the external magnetic field where μ_B is the Bohr magneton and g^* is the effective Lande g-factor for the material. Including the vector potential of the external magnetic field and performing the square of the first term, the Hamiltonian presented in Eq. (2.3) can be reformulated as

$$\hat{H}_{\text{SE}} = -\frac{\hbar^2}{2m^*}\nabla_x^2 + \left[-\frac{\hbar^2}{2m^*}\nabla_y^2 + \frac{1}{2}m^*\Omega_w^2 y^2\right] + i\hbar\omega_c y\nabla_x + V_G + eV_{\text{pg}} + h_Z. \quad (2.4)$$

Where $\nabla_x = \partial/\partial x$ and $\nabla_y = \partial/\partial y$. The Schrödinger equation can not be solved analytically using the Hamiltonian shown in Eq. (2.4). So, a numerical diagonalization is employed to calculate the eigenvalues and eigenfunctions using basis functions. We know that the problem with the first two terms of the Hamiltonian in Eq. (2.4) is separable. The first term is the Hamiltonian for an infinite square well and the second term is the Hamiltonian for a harmonic oscillator. In this case, the boundary conditions for the states confined by the walls is $\Psi(-L_x/2, y) = \Psi(L_x/2, y) = 0$ and by the parabolic confinement it is $\Psi(x, y \rightarrow \pm\infty) \rightarrow 0$ where the superscript 0 indicates the basis eigenfunction for only the first two terms of the Hamiltonian. Then one can get the eigenfunctions for the hard-wall confinement in the x -direction [79, 80]

$$\langle x|\psi_n\rangle = \psi_n(x) = \begin{cases} \sqrt{\frac{2}{L_x}} \cos\left(\frac{n\pi x}{L_x}\right) & \text{if } n = 1, 3, 5, \dots \\ \sqrt{\frac{2}{L_x}} \sin\left(\frac{n\pi x}{L_x}\right) & \text{if } n = 2, 4, 6, \dots \end{cases} \quad (2.5)$$

and the harmonic oscillator in the y -direction

$$\langle y|\psi_m\rangle = \psi_m(y) = \frac{\exp\left(-\frac{y^2}{2a_w^2}\right)}{\sqrt{2^m\sqrt{\pi}m!a_w}} H_m\left(\frac{y}{a_w}\right), \quad (2.6)$$

with H_m being the Hermite polynomials and $a_w = \sqrt{\hbar/m^*\Omega_w}$. The eigenfunctions of the first two terms of the Hamiltonian are thus the product of the two above eigenfunctions $\Psi_{n,m}(x, y) = \psi_n(x) \psi_m(y)$.

The eigenfunction in Eq. (2.5) and Eq. (2.6) are used to form a basis for the eigenstates for the total Hamiltonian written in Eq. (2.4)

$$|n', m'\rangle = \sum_{n,m} C_{n',n}^{m',m} |n, m\rangle \quad (2.7)$$

where $C_{n',n}^{m',m}$ are complex valued coefficients.

The Hamiltonian of the system presented in Eq. (2.4) is diagonalized using the basis Eq. (2.7) to find the single-electron energy spectrum E_{SE} and the corresponding states. The details of the derivation of the matrix elements can be found in appendix A.

The energy spectrum of the central system as a function of the single-electron dummy-index quantum number $i = (n, m)$ is plotted in Fig. 2.1 for plunger-gate voltage $V_{\text{pg}} = 0.1$ meV (red diamonds) and 0.4 mV (green triangles). The central system is a quantum dot embedded in the quantum wire. The energy values for

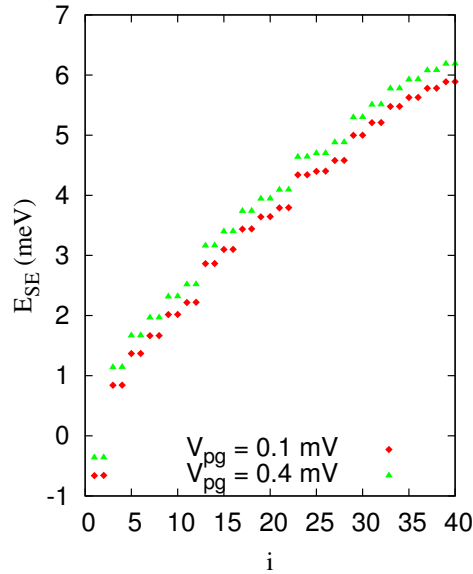


Figure 2.1: (Color online) Eigenvalues of the central system (cross dots) versus the SES quantum number $i = (n, m)$ for plunger-gate voltage $V_{\text{pg}} = 0.1$ meV (red diamonds) and 0.4 mV (green triangles). The magnetic field $B = 0.1$ T, $\hbar\Omega_0 = 2.0$ mV.

$V_{\text{pg}} = 0.4$ meV are higher than that for the case of $V_{\text{pg}} = 0.1$ meV because the

2. Theoretical basis

positive plunger gate voltage raises the energy spectrum. A Gaussian potential is used to form the embedded quantum dot in which the parameters of V_G potential Eq. (2.3) and Eq. (A.12) are $V_0 = -3.3$ meV and $\beta_x = \beta_y = 3.0 \times 10^{-3}$ nm $^{-1}$.

2.1.2. Electron reservoirs

The closed system described in the previous section is assumed to be connected to two electron reservoirs or leads with which they exchange electrons. The leads are considered to be two-dimensional semi-infinite quantum wires. They are parabolically confined in the y direction. The leads are exposed to an external magnetic field in the z -direction. The Hamiltonian of the leads is

$$\hat{H}_{\text{SE}}^l = \frac{1}{2m^*}(\mathbf{p} + \frac{e}{c}\mathbf{A}_{\text{ext}})^2 + \frac{1}{2}m^*\Omega_l^2 y^2, \quad (2.8)$$

where l refers to the left (L) or right (R) lead, \mathbf{p} is the momentum operator of an electron, and $\mathbf{A}_{\text{ext}} = -By\hat{x}$ is the vector potential of the external magnetic field in the Landau gauge. The second term of the Hamiltonian describes the parabolic confinement in the y -direction in the leads with transverse confinement frequency Ω_l . Eq. (2.8) is thus modified to

$$\hat{H}_{\text{SE}}^l = -\frac{\hbar^2}{2m^*}\nabla_x^2 + \left[-\frac{\hbar^2}{2m^*}\nabla_y^2 + \frac{1}{2}m^*(\Omega_w^l)^2 y^2 \right] + i\hbar\omega_c y \nabla_x, \quad (2.9)$$

with $\Omega_w^l = \sqrt{\Omega_l^2 + \omega_c^2}$ being the effective confinement frequency of an electron in the leads in the y -direction.

The Hamiltonian of the leads is time-independent, therefore, the corresponding Schrödinger equation is reduced to energy eigenvalue problem

$$\hat{H}_{\text{SE}}^l |\Phi^l\rangle = E_{\text{SE}}^l |\Phi^l\rangle, \quad (2.10)$$

herein, $|\Phi^l\rangle$ is an eigenstate of the l lead. Again Eq. (2.10) can not be solved analytically because of the last term of the Hamiltonian shown in Eq. (2.9), so we use diagonalization technique to calculate the matrix elements of the Hamiltonian. The eigenfunctions of the first two terms of the Hamiltonian, the hard-wall and the harmonic oscillator, can be used to form a basis, $\Phi_{m,q}^l(x, y) = \phi_m^l(x) \phi_q^l(y)$. The boundary conditions for a semi-infinite quantum wire are

$$\Phi_{m,q}^L\left(\frac{-L_x}{2}, y\right) = \Phi_{m,q}^R\left(\frac{L_x}{2}, y\right) = 0, \quad (2.11)$$

and

$$\Phi_{m,q}^L(x, y \rightarrow 0) = \Phi_{m,q}^R(x, y \rightarrow 0) = 0, \quad (2.12)$$

with q being the wave number describing the electron motion in the x -direction and m a quantum number of the discrete subband energy levels in the y -direction. One can directly get

$$\langle x | \phi_q^l \rangle = \phi_q^l(x) = \begin{cases} \sqrt{\frac{2}{\pi}} \sin \left(q \left(x + \frac{L_x}{2} \right) \right) & \text{if } l = \text{L}, \\ \sqrt{\frac{2}{\pi}} \sin \left(q \left(x - \frac{L_x}{2} \right) \right) & \text{if } l = \text{R}, \end{cases} \quad (2.13)$$

and

$$\langle y | \phi_m^l \rangle = \phi_m^l(y) = \psi_m(y), \quad (2.14)$$

where $\psi_m(y)$ is given by Eq. (2.6). The eigenvalues are

$$\varepsilon_m^l(q) = \hbar \Omega_w^l \left(m + 0.5 + \frac{q^2 a_l^2}{2} \right), \quad (2.15)$$

with $a_l = \sqrt{\hbar/m^* \Omega_w^l}$ being the effective magnetic length in the leads.

The basis eigenfunctions are employed to form new eigenfunctions for all the terms of the Hamiltonian presented in Eq. (2.9)

$$\begin{aligned} |m', q'\rangle &= \sum_m \int dq C_{m',m}(q', q) \phi_q^l(x) \phi_m^l(y) \\ &= \sum_m \int dq C_{m',m}(q', q) |m, q\rangle, \end{aligned} \quad (2.16)$$

where $C_{m',m}$ are complex expansion coefficients.

One can substitute the Hamiltonian presented in Eq. (2.9), and the new eigenfunctions, Eq. (2.16), into the Schrödinger equation, Eq. (2.10), to form an integral equation in with the matrix elements of the Hamiltonian of the leads

$$E_{\text{SE}}^l(m', q') C_{m',m''}(q', q'') = \sum_m \int dq \langle m'', q'' | \hat{H}_{\text{SE}}^l | m, q \rangle C_{m',m}(q', q). \quad (2.17)$$

Herein, $\langle m'', q'' | \hat{H}_{\text{SE}}^l | m, q \rangle$ are the matrix elements of the Hamiltonian and $E_{\text{SE}}^l(m', q')$ are the eigenvalues of the l lead. Further derivations of the Eq. (2.17) is presented in appendix A.2.

The energy spectrum for the leads (E_{SE}^l) as a function of the ‘wave number’ $\mathbf{q} = (m, q)$ scaled by a_w^{-1} is shown in Fig. 2.2. The lowest four energy subband are seen in the spectra.

2. Theoretical basis

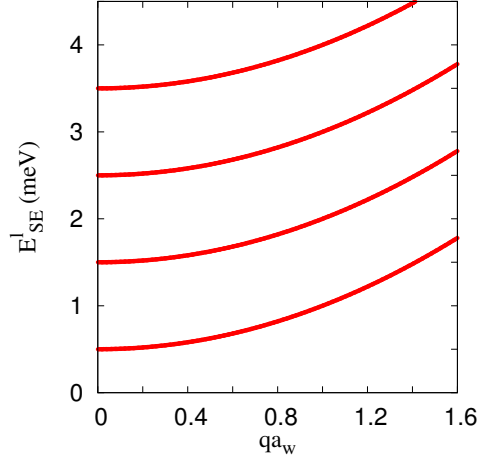


Figure 2.2: (Color online) Energy spectrum of the leads (solid red) versus the wave number $\mathbf{q} = (q, m)$. The magnetic field $B = 0.1$ T, $\hbar\Omega_l = 1.0$ meV.

2.1.3. Contact area

The central system and the leads are connected via a region which is the so called coupling region or transfer region. The transfer region is described by a time-dependent Hamiltonian

$$H_{\text{SE,T}}^l(t) = \sum_m \int dq \chi^l(t) \left[T_{mq,nm}^l |\Psi_{n,m}\rangle \langle \Phi_{m,q}^l| + (T_{mq,nm}^l)^* |\Phi_{m,q}^l\rangle \langle \Psi_{n,m}| \right], \quad (2.18)$$

where $\chi^l(t)$ is a function describing the switching-on

$$\chi^l(t) = \theta(t - t_0) \left[1 - \frac{2}{e^{\gamma(t-t_0)} + 1} \right], \quad (2.19)$$

with γ being the switching rate of the coupling, t_0 the initial time of the coupling between the central system and the leads. We assume the switching function of the left and the right leads are equal $\chi^L(t) = \chi^R(t)$ for $t > t_0$. The coupling between eigenstates of the central system $\Psi_{n,m}$ and the leads $\Phi_{m,q}^l$ is described by the transfer or coupling tensor

$$T_{nm,mq}^l = \int d\mathbf{r} d\mathbf{r}' \Phi_{m,q}^l(\mathbf{r}')^* g_{nm,mq}^l(\mathbf{r}, \mathbf{r}') \Psi_{n,m}(\mathbf{r}). \quad (2.20)$$

The function $g_{nm,mq}^l$ is a nonlocal ‘overlap’ facilitating the electron motion between the single-electron states of the central system $|n, m\rangle$ and the leads $|m, q\rangle$. The nonlocal overlap function $g_{nm,mq}^l$ is given by

$$\begin{aligned} g_{nm,mq}^l(\mathbf{r}, \mathbf{r}') &= g_0^l \exp \left[-\delta_x^l (x - x')^2 - \delta_y^l (y - y')^2 \right] \\ &\times \exp \left(-|E_{n,m} - \epsilon_m^l(q)| / \Delta_E \right). \end{aligned} \quad (2.21)$$

Herein, g_0^l is the strength of the coupling, δ_x^l and δ_y^l are constants that control the extent of the overlap in the x - and y -direction, respectively, and Δ_E is a constant determining an electron ‘affinity’.

2.2. Fock-space and many-electron calculations

The states of the single-electron systems are represented by $|\Psi\rangle$ lie in a Hilbert space. In the presence of more than one electron in the system we need different states. In this case, the states of the system can be represented in a Fock space in which the state basis in the occupation number representation is denoted as [81]

$$|\mu\rangle = |n_1^\mu, n_2^\mu, \dots, n_k^\mu, \dots, n_\infty^\mu\rangle, \quad (2.22)$$

where n^μ is either 0 in the case of an empty state or 1 for an occupied state in a fermionic system. The many-electron (ME) system is formulated in terms of the so-called second quantization representation in which the fundamental creation and annihilation operators are used to form the Hamiltonian of the system. The properties of Fermi creation and annihilation operators are shown in the following [82]. The way a creation operator acts is

$$d_k^\dagger |n_1^\mu, n_2^\mu, \dots, n_k^\mu, \dots, n_{N_{\text{SES}}}^\mu\rangle = \begin{cases} 0 & \text{if } n_k^\mu = 1, \\ (-1)^{\gamma_k} |n_1^\mu, n_2^\mu, \dots, 1, \dots, n_{N_{\text{SES}}}^\mu\rangle & \text{if } n_k^\mu = 0, \end{cases} \quad (2.23)$$

and for the annihilation operator

$$d_k |n_1^\mu, n_2^\mu, \dots, n_k^\mu, \dots, n_{N_{\text{SES}}}^\mu\rangle = \begin{cases} (-1)^{\gamma_k} |n_1^\mu, n_2^\mu, \dots, 0, \dots, n_{N_{\text{SES}}}^\mu\rangle & \text{if } n_k^\mu = 1, \\ 0 & \text{if } n_k^\mu = 0, \end{cases} \quad (2.24)$$

with $\gamma_k = \sum_{i=1}^{k-1} n_i^\mu$. The Fock space in Eq. (2.23) and Eq. (2.24) is truncated by replacing ∞ by a chosen positive integer N_{SES} . This indicates that a finite number of single-electron states is used to construct the Fock space in the calculations.

The creation and the annihilation operator can be used to define the electron number operator as $\hat{N}_k = d_k^\dagger d_k$. The number operator acts on a state and gives

$$d_k^\dagger d_k |n_1^\mu, n_2^\mu, \dots, n_k^\mu, \dots, n_{N_{\text{SES}}}^\mu\rangle = n_k^\mu |n_1^\mu, n_2^\mu, \dots, n_k^\mu, \dots, n_{N_{\text{SES}}}^\mu\rangle, \quad (2.25)$$

where n_k^μ is the number of electrons in the state k .

An operator ($\hat{\mathbf{O}}$) can be represented in terms of creation and annihilation operators in second quantization using its first quantized form \hat{O}

$$\hat{\mathbf{O}} = \sum_{i', i} \langle \Psi_{i'} | \hat{O} | \Psi_i \rangle d_{i'}^\dagger d_i \quad (2.26)$$

where $|\Psi\rangle_i$ is an eigenstate of the system.

In the following we shall construct the interacting many-electron Hamiltonian in a Fock space.

2.2.1. Central system with Coulomb interaction

In this section we use the second quantization to represent the Hamiltonian of the central system. Using Eq. (2.26) the Hamiltonian in Eq. (2.4) can be written as

$$\hat{H}_e^0 = \sum_{i,i'} \langle \Psi_{i'} | \hat{H}_{SE} | \Psi_i \rangle d_{i'}^\dagger d_i, \quad (2.27)$$

where $i(i')$ is a bijection of quantum numbers of n and m (n' and m'), introduced in section 2.1, respectively. Performing the matrix elements, we obtain

$$\hat{H}_e^0 = \sum_i E_{SE,i} d_i^\dagger d_i, \quad (2.28)$$

where E_{SE} is a single-electron energy.

We include the electron-electron Coulomb interaction in the central system. The electron-electron interaction H_{ee} is a two-electron operator

$$\hat{H}_{ee} = \frac{1}{2} \sum_{i',j',i,j} \langle \Psi_{i'} \Psi_{j'} | V | \Psi_i \Psi_j \rangle d_{i'}^\dagger d_{j'}^\dagger d_j d_i, \quad (2.29)$$

with the two-electron matrix elements in a double integral form

$$\langle \Psi_{i'} \Psi_{j'} | V | \Psi_i \Psi_j \rangle = \int d\mathbf{r} \Psi_{i'}(\mathbf{r})^* \mathcal{I}_{j'i}(\mathbf{r}) \Psi_j(\mathbf{r}), \quad (2.30)$$

where $\Psi(\mathbf{r})$ is a single-electron wavefunction of the central system, and $\mathcal{I}_{j'i}(\mathbf{r})$ is an integral with respect to \mathbf{r}'

$$\begin{aligned} \mathcal{I}_{j'i}(\mathbf{r}) &= \int d\mathbf{r}' \Psi_{j'}(\mathbf{r}')^* V(\mathbf{r} - \mathbf{r}') \Psi_i(\mathbf{r}') \\ &= \int d\mathbf{r}' [\Psi_{j'}(\mathbf{r}')^* - \Psi_{j'}(\mathbf{r})^*] V(\mathbf{r} - \mathbf{r}') [\Psi_i(\mathbf{r}') - \Psi_i(\mathbf{r})] \\ &\quad + \int d\mathbf{r}' V(\mathbf{r} - \mathbf{r}') [\Psi_{j'}(\mathbf{r}')^* \Psi_i(\mathbf{r}) + \Psi_{j'}(\mathbf{r}) \Psi_i(\mathbf{r}')] \\ &\quad - \int d\mathbf{r}' \Psi_{j'}(\mathbf{r}') \Psi_i(\mathbf{r}) V(\mathbf{r} - \mathbf{r}'), \end{aligned} \quad (2.31)$$

with the electron-electron Coulomb potential

$$V(\mathbf{r} - \mathbf{r}') = \frac{e^2}{2\kappa} \frac{1}{\sqrt{|\mathbf{r} - \mathbf{r}'|^2 + \eta^2}}. \quad (2.32)$$

Herein, $\kappa = 2\pi\epsilon_0\epsilon_r$, ϵ_r is the relative dielectric constant of the material, and η is an infinitesimal positive convergence parameter. The constant appearing Eq. (2.32)

2. Theoretical basis

can be scaled in the energy and length scale, $e^2/2\kappa = \hbar\Omega_w(a_w/a_0^*)$, where a_0^* is the effective Bohr radius. The second and third terms of Eq. (2.31) vanish identically [83–85], resulting in

$$\mathcal{I}_{j'i}(\mathbf{r}) = \int d\mathbf{r}' [\Psi_{j'}(\mathbf{r}')^* - \Psi_{j'}(\mathbf{r})^*] V(\mathbf{r} - \mathbf{r}') [\Psi_i(\mathbf{r}') - \Psi_i(\mathbf{r})]. \quad (2.33)$$

Adding Eq. (2.28) and Eq. (2.29) gives the ME Hamiltonian of the central system

$$\hat{H}_{\text{ME}} = \hat{H}_{\text{e}}^0 + \hat{H}_{\text{ee}} = \sum_i E_{\text{SE},i} d_i^\dagger d_i + \frac{1}{2} \sum_{i',j',i,j} V_{i',j',i,j} d_i^\dagger d_{j'}^\dagger d_j d_i. \quad (2.34)$$

There are several techniques to approximate the Coulomb interaction shown in Eq. (2.34), such as the Hartree approximation [86–88], Hartree-Fock [89–92], and Exact-diagonalization method [93–95]. In this work, the properties of the Coulomb interacting ME Hamiltonian of the isolated central system are derived with the *exact diagonalization* method [93]. One can calculate the matrix representation of \hat{H}_{ME} in a many-electron basis $\{|\mu\rangle\}$ using

$$\langle\mu'|\hat{H}_{\text{ME}}|\mu\rangle = \sum_i E_{\text{SE},i} \langle\mu'|d_i^\dagger d_i|\mu\rangle + \frac{1}{2} \sum_{i',j',i,j} V_{i',j',i,j} \langle\mu'|d_i^\dagger d_{j'}^\dagger d_j d_i|\mu\rangle. \quad (2.35)$$

The Hamiltonian matrix is diagonalized in a truncated Fock-space. Consequently, the eigenvalues $E_{\text{ME},\mu}^0$ and a unitary transformation \mathcal{V} are obtained. Then the unitary transformation is used to construct the interacting many-electron states (MESs)

$$|\nu\rangle = \sum_{\mu=1}^{N_{\text{mes}}} \mathcal{V}_{\nu\mu} |\mu\rangle. \quad (2.36)$$

Herein, N_{mes} is the number of many-electron states which is $\binom{N_{\text{SES}}}{N_e}$ with N_e being the number of electrons, and the parenthesis bracket $|\nu\rangle$ denotes the interacting many-electron state basis while $|\mu\rangle$ is the non-interacting many-electron state basis. The matrix elements in the second term of Eq. (2.35) can be calculated using Eq. (2.23) and Eq. (2.24) [81].

The many-electron energy spectrum versus the many electron state μ is presented in Fig. 2.3 for non-interacting (0) (blue triangles), and interacting (I) system (red diamonds). The central system is assumed to be a quantum dot embedded in a quantum wire with the parameters of Fig. 2.1. It can be clearly seen that the electron-electron Coulomb repulsion increases the energy value of two-electron states for $\mu \geq 14$. The enhancement of the energy influences the electron transport. The effects of Coulomb interaction on the electron motion in the system will be discussed in the result section later.

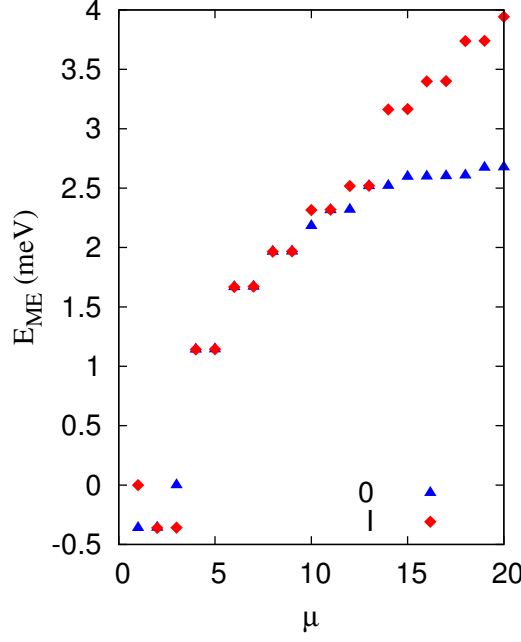


Figure 2.3: (Color online) Many-electron energy spectrum of the central system (cross dots) versus the many-electron state μ for non-interacting (0) (blue triangles) and interacting (I) of the system (red diamonds) is plotted. The central system is assumed to be a quantum dot embedded in a quantum wire. The plunger-gate voltage is $V_{pg} = 0.4$ mV and same parameters as in Fig. 2.1 are used here.

2.2.2. The leads and Coupling Hamiltonian

In this section, we define the Hamiltonian of the leads and the coupling region in second quantization form. We assume the Fermi creation and annihilation operators in the leads are c^\dagger and c , respectively. The Hamiltonian of the leads is thus introduced as

$$\hat{H}_{SE}^l = \sum_{l=L,R} \sum_m \int dq \langle \Phi_{m',q'}^l | H_{SE}^l | \Phi_{m,q}^l \rangle c_{m',q'}^l{}^\dagger c_{m,q}^l. \quad (2.37)$$

Using the matrix elements $\langle \Phi_{m',q'}^l | H_{SE}^l | \Phi_{m,q}^l \rangle$ calculated in Eq. (2.17) we get the Hamiltonian of the leads in the form

$$\hat{H}_{SE}^l = \sum_{l=L,R} \sum_m \int dq E_{SE}^l(m, q) c_{m,q}^l{}^\dagger c_{m,q}^l. \quad (2.38)$$

The electron-electron Coulomb repulsion is neglected in the leads.

The central system and the leads are connected via a coupling area which allows electron tunneling between the systems. The electron motion between the central

2. Theoretical basis

system and the leads is described by the transfer Hamiltonian presented Eq. (2.18). Using the quantum number \mathbf{q} which refers to the wave number q and the sub-band quantum number m of the leads, one can express the time dependent transfer Hamiltonian in the second quantization

$$\hat{H}_{\text{SE,T}}^l(t) = \sum_{l=\text{L,R}} \chi^l(t) \sum_i \int d\mathbf{q} \left[c_{\mathbf{q}}^{l\dagger} T_{\mathbf{q}i}^l d_i + d_i^\dagger (T_{i\mathbf{q}}^l)^* c_{\mathbf{q}}^l \right]. \quad (2.39)$$

The quantum number i represents n and m , the quantum numbers in the central system. Here, the electrons are allowed to tunnel from the central system to the leads as stated in the first part of the Hamiltonian in Eq. (2.39), or an electron tunnels from a lead to the central system as is described by the second part.

To introduce Eq. (2.39) in a MES basis, we use the completeness of MESs

$$\sum_{\mu} |\mu\rangle \langle \mu'| = \mathbf{1} \quad (2.40)$$

to convert $H_{\text{SE,T}}^l(t)$ from a SES to a MES basis. Then the transfer Hamiltonian in the MES basis can be written as

$$H_{\text{ME,T}}^l(t) = \chi^l(t) \int d\mathbf{q} \left(\mathcal{T}^l(\mathbf{q}) c_{\mathbf{q}}^l + c_{\mathbf{q}}^{l\dagger} (\mathcal{T}^l(\mathbf{q}))^\dagger \right), \quad (2.41)$$

with $\mathcal{T}^l(\mathbf{q})$ being the many-electron coupling matrix in the non-interacting electron basis

$$\mathcal{T}^l(\mathbf{q}) = \sum_{\mu',\nu} \mathcal{T}_{\mu',\nu}^l(\mathbf{q}) |\nu\rangle \langle \mu'|, \quad (2.42)$$

where $\mathcal{T}_{\mu\nu}^l(\mathbf{q})$ is defined in terms of the single-electron coupling matrix $T_{n\mathbf{q}}^l$ as $\mathcal{T}_{\mu\nu}^l(\mathbf{q}) = \sum_n \sum_{\mu,\nu'} T_{n\mathbf{q}}^l |\mu\rangle d_n^\dagger \langle \nu'|$.

2.3. Cavity photons and the many-body Hamiltonian

In this section, we consider the central electronic system coupled to a cavity electromagnetic field with a single photon mode. The photons in the cavity are quantized and polarized in either parallel or perpendicular to the electron motion in the central system. We assume the cavity photon field is in a large but finite rectangular cavity with boundaries at $-a_c/2 < x, y < a_c/2$ and $-d_c < z < d_c$. Figure 2.4 shows a schematic representation of the electronic central system (dark blue) coupled to the photon cavity (light blue) in an external magnetic field B .

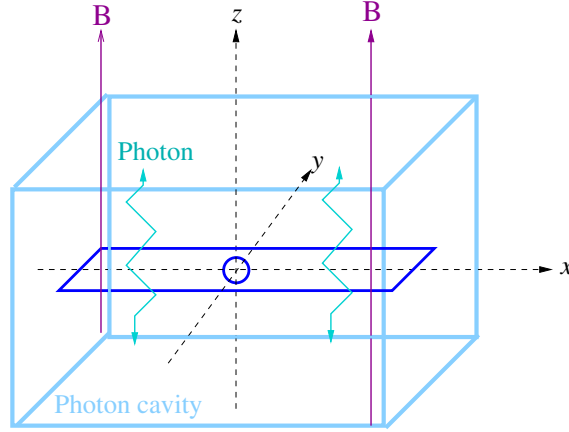


Figure 2.4: (Color online) Schematic of an electron system (dark blue) coupled to a photon cavity (light blue) in an external magnetic field B .

The photon cavity couples the electronic system via the vector potential. The vector potential of the quantized electromagnetic field is [96]

$$\mathbf{A}_{\text{ph}} = A_{\text{ph}} \times \begin{pmatrix} \hat{\mathbf{e}}_x \\ \hat{\mathbf{e}}_y \end{pmatrix} (a + a^\dagger) \begin{pmatrix} \cos(\frac{2\pi x}{a_c}) \\ \cos(\frac{2\pi y}{a_c}) \end{pmatrix} \cos\left(\frac{2\pi z}{d_c}\right), \quad (2.43)$$

in the Coulomb gauge where A_{ph} is the amplitude of the vector potential, a^\dagger (a) are Bosonic creation and annihilation operator respectively, and $\hat{\mathbf{e}}_{x,y}$ are the Cartesian unit vectors. We assume that the vector potential does not change considerably over the size of the electronic system. We consider the electron-photon coupling strength to be $g_{\text{ph}} = eA_{\text{ph}}\Omega_w a_w$, so one can write the vector potential as

$$\mathbf{A}_{\text{ph}} = \frac{g_{\text{ph}}}{e\Omega_w a_w} \times \hat{\mathbf{e}} (a + a^\dagger), \quad (2.44)$$

where $\hat{\mathbf{e}} = (\hat{e}_x, \hat{e}_y)$. The Many-Body (MB) Hamiltonian of the central system coupled

2. Theoretical basis

to the cavity photon including the vector potential of the photon field is

$$\begin{aligned} \hat{H}_{\text{MB}} = \sum_{ij} \langle \Psi_i | \left(\frac{1}{2m^*} \left[\mathbf{p} + \frac{e}{c} \mathbf{A}_{\text{ext}} + \frac{e}{c} \mathbf{A}_{\text{ph}} \right]^2 + \frac{1}{2} m^* \Omega_0^2 y^2 + V_G + eV_{\text{pg}} + h_Z \right) | \Psi_j \rangle d_i^\dagger d_j \\ + \hat{H}_{\text{ee}} + \hat{H}_{\text{ph}}. \end{aligned} \quad (2.45)$$

Two terms in the MB Hamiltonian describing the cavity photons are \mathbf{A}_{ph} and \hat{H}_{ph} , where

$$\hat{H}_{\text{ph}} = \hbar \omega_{\text{ph}} a^\dagger a \quad (2.46)$$

is the free Hamiltonian of a single-photon mode with the energy $\hbar \omega_{\text{ph}}$. In the first part of the Hamiltonian shown in Eq. (2.45)

$$\hat{H}_{\text{e-ph}} = \sum_{ij} \langle \Psi_i | \frac{1}{2m^*} \left[\mathbf{p} + \frac{e}{c} \mathbf{A}_{\text{ext}} + \frac{e}{c} \mathbf{A}_{\text{ph}} \right]^2 | \Psi_j \rangle d_i^\dagger d_j \quad (2.47)$$

We write $\boldsymbol{\pi}_e := \mathbf{p} + \frac{e}{c} \mathbf{A}_{\text{ext}}$ and obtain

$$\begin{aligned} \hat{H}_{\text{e-ph}} = \sum_{i,j} \langle \Psi_i | \frac{\boldsymbol{\pi}_e^2}{2m^*} | \Psi_j \rangle d_i^\dagger d_j + \sum_{i,j} \langle \Psi_i | \frac{e}{2m^*} (\boldsymbol{\pi}_e \cdot \mathbf{A}_{\text{ph}} + \mathbf{A}_{\text{ph}} \cdot \boldsymbol{\pi}_e) | \Psi_j \rangle d_i^\dagger d_j \\ + \sum_{i,j} \frac{e^2}{2m^*} \langle \Psi_i | \mathbf{A}_{\text{ph}}^2 | \Psi_j \rangle d_i^\dagger d_j, \end{aligned} \quad (2.48)$$

We previously obtained the first term of the Hamiltonian in Eq. (2.28). The second and the third term of the Hamiltonian in Eq. (2.48) represent the paramagnetic and diamagnetic electron-photon interactions, respectively. Below, we shall further describe both the paramagnetic and the diamagnetic terms of the Hamiltonian.

Paramagnetic term

The photon cavity partially influences the electron motion through the paramagnetic term of the Hamiltonian. In the Coulomb gauge $\nabla \cdot \mathbf{A}_{\text{ph}} = 0$, so

$$\boldsymbol{\pi}_e \cdot \mathbf{A}_{\text{ph}} = \mathbf{A}_{\text{ph}} \cdot \boldsymbol{\pi}_e. \quad (2.49)$$

Using Eq. (2.49), the paramagnetic term of the Hamiltonian presented in Eq. (2.48) is modified to

$$\hat{H}_{\text{P}} = \sum_{i,j} \langle \Psi_i | \frac{e}{m^*} \mathbf{A}_{\text{ph}} \cdot \boldsymbol{\pi}_e | \Psi_j \rangle d_i^\dagger d_j. \quad (2.50)$$

Substituting the photon vector potential shown in Eq. (2.44) into the Eq. (2.50) we get

$$\hat{H}_{\text{P}} = (a + a^\dagger) \sum_{i,j} g_{i,j} \times d_i^\dagger d_j \quad (2.51)$$

2.3. Cavity photons and the many-body Hamiltonian

where $g_{i,j}$ is the dipole coupling between the electron system and the photon cavity mode defined as

$$g_{i,j} = \frac{a_w g_{\text{ph}}}{\hbar} \int dr \Psi_i^*(r) (\hat{\mathbf{e}} \cdot \boldsymbol{\pi}) \Psi_j(r) \quad (2.52)$$

with g_{ph} being the electron-photon coupling strength.

Diamagnetic term

The diamagnetic interaction is the third term of the Hamiltonian Eq. (2.48)

$$\hat{H}_{\text{D}} = \frac{e^2}{2m^*} \mathbf{A}_{\text{EM}}^2 \sum_{i,j} \langle \Psi_i | \Psi_j \rangle d_i^\dagger d_j. \quad (2.53)$$

Using the completeness relation $\sum_i \langle \Psi_i | \Psi_i \rangle = 1$ and defining the electron number operator $N_e = \sum_i d_i^\dagger d_i$, one can get

$$\hat{H}_{\text{D}} = \frac{g_{\text{ph}}^2}{\hbar \Omega_w} N_e \times \left((a^\dagger a + \frac{1}{2}) + \frac{1}{2} (a^\dagger a^\dagger + aa) \right). \quad (2.54)$$

Substituting Eq. (2.28), Eq. (2.51), and Eq. (2.54) into Eq. (2.48) modifies the Hamiltonian describing electron-photon coupling into

$$\begin{aligned} \hat{H}_{\text{e-ph}} = & \sum_i E_{\text{SE},i} d_i^\dagger d_i + \sum_{i,j} g_{i,j} (a + a^\dagger) d_i^\dagger d_j \\ & + \frac{\varepsilon_{\text{ph}}^2}{\hbar \Omega_w} N_e \times \left((a^\dagger a + \frac{1}{2}) + \frac{1}{2} (a^\dagger a^\dagger + aa) \right). \end{aligned} \quad (2.55)$$

The MB Hamiltonian presented in Eq. (2.45) for the central electron-photon system thus becomes

$$\begin{aligned} \hat{H}_{\text{MB}} = & \sum_i E_{\text{SE},i} d_i^\dagger d_i + \sum_{i,j} g_{i,j} (a + a^\dagger) d_i^\dagger d_j + \frac{\varepsilon_{\text{ph}}^2}{\hbar \Omega_w} N_e \times \left((a^\dagger a + \frac{1}{2}) + \frac{1}{2} (a^\dagger a^\dagger + aa) \right) \\ & + \hat{H}_{\text{ee}} + \hbar \omega_{\text{ph}} a^\dagger a. \end{aligned} \quad (2.56)$$

Computational Implementation

We need to construct a MB basis from the many-electron basis of the interacting electrons $\{|\mu\rangle\}$ and the photon number basis $\{|M\rangle\}$. A straight forward MB basis is the tensor product of the many-electron and the photon bases

$$\{|\check{\mu}\rangle\} \equiv \{|\mu\rangle \otimes |M\rangle\}. \quad (2.57)$$

2. Theoretical basis

where $|\mu\rangle$ are the eigenstates of the central electronic system and $|M\rangle$ are the eigenstates of the single cavity photon mode.

Using the MB basis Eq. (2.57) and the the MB Hamiltonian Eq. (2.56), the matrix elements of the MB Hamiltonian including the photon field and electron-photon interaction are

$$\begin{aligned} \langle \check{\mu}' | \hat{H}_{\text{MB}} | \check{\mu} \rangle &= \sum_i E_{\text{SE},i} \langle \check{\mu}' | d_i^\dagger d_i | \check{\mu} \rangle + \sum_{i,j} \langle \check{\mu}' | g_{i,j} (a + a^\dagger) d_i^\dagger d_j | \check{\mu} \rangle \\ &+ \frac{\varepsilon_{ph}^2}{\hbar \Omega_w} \sum_{i,j} \langle \check{\mu}' | N_e \times \left((a^\dagger a + \frac{1}{2}) + \frac{1}{2} (a^\dagger a^\dagger + a a) \right) | \check{\mu} \rangle \\ &+ \langle \check{\mu}' | \hat{H}_{\text{ee}} | \check{\mu} \rangle + \hbar \omega_{\text{ph}} \langle \check{\mu}' | a^\dagger a | \check{\mu} \rangle. \end{aligned} \quad (2.58)$$

The first term of the matrix elements represented in Eq. (2.58) yields

$$\sum_i E_{\text{SE},i} \langle \mu'; M' | d_i^\dagger d_i | \mu; M \rangle = \sum_i E_{\text{SE},i} N_i^e \delta_{\mu\mu'} \delta_{MM'} = E_\mu^0 \delta_{\mu\mu'} \delta_{MM'} \quad (2.59)$$

where E_μ^0 is the many-body energy of the Coulomb interacting electrons in the purely electronic state $|\mu\rangle$, and N_i^e is the electron number.

The second term of Eq. (2.58) is the matrix elements of the paramagnetic Hamiltonian that describes the electron-photon interaction. This can be evaluated as

$$\begin{aligned} \langle \check{\mu}' | \hat{H}_{\text{P}} | \check{\mu} \rangle &= \sum_{i,j} \langle \check{\mu}' | g_{i,j} (a + a^\dagger) d_i^\dagger d_j | \check{\mu} \rangle \\ &= \sum_{i,j} g_{i,j} \times (\mu' | d_i^\dagger d_j | \mu) \times \langle M' | (a + a^\dagger) | M \rangle, \end{aligned} \quad (2.60)$$

with

$$(\mu' | d_i^\dagger d_j | \mu) = \langle \mu' | \mathcal{V}^\dagger d_i^\dagger d_j \mathcal{V} | \mu \rangle, \quad (2.61)$$

and

$$\langle M' | (a + a^\dagger) | M \rangle = \left(\sqrt{N_{\text{ph}}} \delta_{M', M-1} + \sqrt{N_{\text{ph}} + 1} \delta_{M', M+1} \right). \quad (2.62)$$

\mathcal{V} is the unitary transformation which is obtained from the exact diagonalization of the ME Hamiltonian.

2.3. Cavity photons and the many-body Hamiltonian

The matrix elements of the diamagnetic term Eq. (2.58) are

$$\begin{aligned}
\langle \check{\mu}' | \hat{H}_D | \check{\mu} \rangle &= \frac{\varepsilon_{ph}^2}{\hbar \Omega_w} \langle \check{\mu}' | N_e \times \left((a^\dagger a + \frac{1}{2}) + \frac{1}{2}(a^\dagger a^\dagger + aa) \right) | \check{\mu} \rangle \\
&= \frac{\varepsilon_{ph}^2}{\hbar \Omega_w} \times (\mu' | N^e | \mu) \times \langle M' | \left((a^\dagger a + \frac{1}{2}) + \frac{1}{2}(a^\dagger a^\dagger + aa) \right) | M \rangle \\
&= \frac{\varepsilon_{ph}^2}{\hbar \Omega_w} N_\mu^e \delta_{\mu'\mu} \left(\sqrt{N_{ph} + \frac{1}{2}} \times \delta_{M',M} + \frac{1}{2} \sqrt{N_{ph}(N_{ph} - 1)} \times \delta_{M',M-2} \right. \\
&\quad \left. + \frac{1}{2} \sqrt{(N_{ph} + 1)(N_{ph} + 2)} \times \delta_{M',M+2} \right).
\end{aligned} \tag{2.63}$$

where N_{ph} is the photon number.

The last term of Eq. (2.58) indicates the matrix elements of the free photon Hamiltonian

$$\hbar \omega_{ph} \langle M' | a^\dagger a | M \rangle \delta_{\mu'\mu} = N_{ph} \hbar \omega_{ph} \delta_{\mu'\mu} \delta_{M'M}. \tag{2.64}$$

Herein, N_{ph} is the photon number operator and $\hbar \omega_{ph}$ is the single photon energy.

Finally, we diagonalize the total MB Hamiltonian obtaining the many-body energies $\check{E}_{\check{\nu}}$ and the corresponding eigenstates $|\check{\nu}\rangle$ which are related to $|\check{\mu}\rangle$ by a unitary transformation

$$|\check{\nu}\rangle = \sum_{\check{\mu}} \mathcal{W}_{\check{\nu}\check{\mu}} |\check{\mu}\rangle. \tag{2.65}$$

with \mathcal{W} the unitary transformation.

3. Non-Markovian approach to a generalized quantum master equation

Electrons in an active area of a nanoscale system connected to electron reservoirs constitute a many-body open quantum system. There are several formalisms used to describe electron motion in an open system, such as Markovian and non-Markovian master equations in which a density matrix is used to describe the state of the system. In the following, we shall focus on a non-Markovian master equation approach to model the transport of electrons through an electronic quantum system coupled to a photon cavity.

3.1. Liouville-von Neumann equation

Electron motion in a closed system satisfies Liouville-von Neumann equation which describes how a density operator evolves in time where the density operator is defined as a superposition of pure states [97, 98]

$$\hat{\rho}_S = \sum_i p_i |\Psi_i\rangle \langle \Psi_i|, \quad (3.1)$$

with p_i being the weight of the probability of the i state. The density matrix for a close system evolves unitarily in time

$$\hat{\rho}_S(t) = \sum_i p_i U_t |\Psi_i\rangle \langle \Psi_i| U_t^\dagger = U_t \hat{\rho}_S U_t^\dagger, \quad (3.2)$$

where $U_t = e^{-it\hat{H}_S/\hbar}$ is the time evolution operator and \hat{H}_S is Hamiltonian of the system. Consequently, the Liouville-von Neumann equation in the Schrödinger picture is

$$\frac{\partial}{\partial t} \hat{\rho}_S(t) = -\frac{i}{\hbar} [\hat{H}_S, \hat{\rho}_S(t)]. \quad (3.3)$$

Herein, the Hamiltonian of the system \hat{H}_S is assumed to be time-independent.

3.2. Nakajima-Zwanzig Formalism

We consider the system interacting with its environment, exchanging electrons. So, we need to modify the density operator mentioned in Eq. (3.3). There are several methods for defining the density operator and its time evolution for a composite system, we introduce the Nakajima-Zwanzig approach [99, 100]. This method provides a systematic theoretical approach to non-Markovian and Markovian dynamics. The Liouville-von Neumann equation in this approach is written as

$$\frac{\partial}{\partial t}\hat{\rho}(t) \equiv \frac{1}{\hbar}\mathcal{L}(t)\hat{\rho}(t), \quad (3.4)$$

where \mathcal{L} is the Liouville operator satisfying $\mathcal{L}(t)\hat{\rho}(t) \equiv -i[\hat{H}(t), \hat{\rho}(t)]$, and $\hat{\rho}(t)$ is the total density operator of the composite system.

Before the coupling of the central system to the leads, the initial density matrix of the system is assumed uncorrelated

$$\hat{\rho}(t_0) = \hat{\rho}_S(t_0) \otimes \hat{\rho}_l(t_0), \quad (3.5)$$

where $\hat{\rho}_l$ is the density operator of the leads

$$\rho_l = \frac{e^{-\beta(H_l - \mu_l N_l)}}{\text{Tr}_l\{e^{-\beta(H_l - \mu_l N_l)}\}}. \quad (3.6)$$

Herein, $\beta = 1/(k_B T)$ where k_B is the Boltzmann constant and T is the temperature of the leads, N_l is the number of electrons in lead l , and μ_l is the chemical potential in lead l . In addition, the Liouville operator \mathcal{L} before the coupling is

$$\mathcal{L}(t) = \mathcal{L}_S + \mathcal{L}_l + \mathcal{L}_T(t) \quad (3.7)$$

where S, l and T stand for the sample (central system), lead and transfer region, respectively.

In the Nakajima-Zwanzig approach the density matrix of the leads generates a projection operator \mathcal{P} and a complementary projection operator $\mathcal{Q} = 1 - \mathcal{P}$. The projection operator is

$$\mathcal{P} = \text{Tr}_l \otimes \hat{\rho}_l. \quad (3.8)$$

The projection operator acts on the operators of the state space of the total system in which $\mathcal{P}\hat{\rho}(t)$ gives the relevant part of the total density matrix and $\mathcal{Q}\hat{\rho}(t)$ projects out the irrelevant part. One can write the total density matrix in terms of the projection and complementary projection operators in the following form

$$\hat{\rho}(t) = \mathcal{P}\hat{\rho}(t) + \mathcal{Q}\hat{\rho}(t). \quad (3.9)$$

We substitute Eq. (3.9) into Eq. (3.4) and multiply the first equation by projection the operator \mathcal{P} and the second one by the complementary operator \mathcal{Q} to get two coupled equations of motion for the projection and the complementary operator

$$\hbar \frac{\partial}{\partial t} \mathcal{P} \hat{\rho}(t) = \mathcal{P} \mathcal{L}(t) \mathcal{P} \hat{\rho}(t) + \mathcal{P} \mathcal{L}(t) \mathcal{Q} \hat{\rho}(t), \quad (3.10)$$

$$\hbar \frac{\partial}{\partial t} \mathcal{Q} \hat{\rho}(t) = \mathcal{Q} \mathcal{L}(t) \mathcal{P} \hat{\rho}(t) + \mathcal{Q} \mathcal{L}(t) \mathcal{Q} \hat{\rho}(t). \quad (3.11)$$

We assume the central system is weakly connected to the leads. In addition, the properties of the projection operator presented in appendix D.1 are used to modify the Eq. (3.10) and Eq. (3.11) to

$$\hbar \frac{\partial}{\partial t} \mathcal{P} \hat{\rho}(t) = \mathcal{L}_S \mathcal{P} \hat{\rho}(t) + \mathcal{P} \mathcal{L}_T(t) \mathcal{Q} \hat{\rho}(t), \quad (3.12)$$

$$\hbar \frac{\partial}{\partial t} \mathcal{Q} \hat{\rho}(t) = \mathcal{L}_T(t) \mathcal{P} \hat{\rho}(t) + \mathcal{L}_0 \mathcal{Q} \hat{\rho}(t), \quad (3.13)$$

where $\mathcal{L}_0 = \mathcal{L}_S + \mathcal{L}_l$.

Including the weak coupling condition $\mathcal{Q} \hat{\rho}(0) = 0$, the solution of Eq. (3.13) for $\mathcal{Q} \hat{\rho}(t)$ is [97, 101]

$$\mathcal{Q} \hat{\rho}(t) = \frac{1}{\hbar} \int_{t_0}^t dt' \hat{U}_0(t-t') \mathcal{L}_T \mathcal{P} \hat{\rho}(t') \hat{U}_0^\dagger(t-t'). \quad (3.14)$$

Herein, the evolution operator is $\hat{U}_0(t-t') = e^{-\frac{i}{\hbar} \hat{H}_0(t-t')}$ with $\hat{H}_0 = \hat{H}_S + \hat{H}_l$ where \hat{H}_S is the Hamiltonian of the central system and \hat{H}_l is the Hamiltonian of the leads. Substituting Eq. (3.14) into Eq. (3.12) we obtain the Nakajima-Zwanzig equation

$$\frac{\partial}{\partial t} \mathcal{P} \hat{\rho}(t) = \frac{1}{\hbar} \mathcal{L}_S \mathcal{P} \hat{\rho}(t) + \frac{1}{\hbar^2} \mathcal{P} \mathcal{L}_T \left\{ \int_{t_0}^t dt' \hat{U}_0(t-t') \mathcal{L}_T \mathcal{P} \hat{\rho}(t') \hat{U}_0^\dagger(t-t') \right\}, \quad (3.15)$$

where we have kept terms in the system lead coupling up to second order in the integral kernel. Due to the structure of the integro-differential equation specific terms of all higher order are present in the solution.

Now, we are interested in the relevant part of the density operator $\hat{\rho}(t)$. Taking the trace over the Fock space of the leads of the full density operator, the reduced density operator (RDO) is obtained

$$\hat{\rho}_S(t) = \text{Tr}_l(\mathcal{P} \hat{\rho}(t)). \quad (3.16)$$

The density operator $\hat{\rho}_S(t)$ in Eq. (3.16) describes the evolution in the central system under the influence of the leads. Using $\text{Tr}_l \rho_l = 1$, $\mathcal{P} = \hat{\rho}_l \text{Tr}_l$ and Eq. (3.16) in Eq. (3.15), the equation of motion for the reduced density operator can be written as

$$\dot{\hat{\rho}}_S(t) = \frac{1}{\hbar} \mathcal{L}_S \hat{\rho}_S(t) + \frac{1}{\hbar^2} \text{Tr}_l \left\{ \mathcal{L}_T \int_{t_0}^t dt' \hat{U}_0(t-t') \mathcal{L}_T \hat{\rho}_l \hat{\rho}_S(t') \hat{U}_0^\dagger(t-t') \right\}. \quad (3.17)$$

3. Non-Markovian approach to a generalized quantum master equation

Using the definition of a Liouvillian super operator for the transfer Hamiltonian

$$\mathcal{L}_T \hat{\rho}_l \hat{\rho}(t') = -i [\hat{H}_T^l(t'), \hat{\rho}_l \hat{\rho}(t')] \quad (3.18)$$

we modify the equation of motion Eq. (3.17) for the reduced density operator

$$\begin{aligned} \dot{\hat{\rho}}_S(t) = & -\frac{i}{\hbar} [\hat{H}_S, \hat{\rho}_S(t)] \\ & - \frac{1}{\hbar^2} \text{Tr}_l \left\{ \left[\hat{H}_T^l(t), \int_{t_0}^t dt' \hat{U}_0(t-t') [\hat{H}_T^l(t'), \hat{\rho}_l \hat{\rho}_S(t')] \hat{U}_0^\dagger(t-t') \right] \right\}. \end{aligned} \quad (3.19)$$

To end the derivation of the Nakajima-Zwanzig equation, we compactify the notation [102]

$$\dot{\hat{\rho}}_S(t) = -\frac{i}{\hbar} [\hat{H}_S, \hat{\rho}_S(t)] + \int_{t_0}^t dt' \mathcal{K}(t, t') \hat{\rho}_S(t'), \quad (3.20)$$

where $\mathcal{K}(t, t')$ is the kernel [102] in the integro-differential equation of motion for the RDO.

$$\mathcal{K}(t, t') \hat{\rho}_S(t') = -\frac{1}{\hbar^2} \text{Tr}_l \left\{ \left[\hat{H}_T^l(t), \hat{U}_0(t-t') [\hat{H}_T^l(t'), \hat{\rho}_l \hat{\rho}_S(t')] \hat{U}_0^\dagger(t-t') \right] \right\}. \quad (3.21)$$

We rewrite the general master equation from the Nakajima-Zwanzig equation explicitly performing the commutation relation in the integration kernel term and taking the trace with respect to the states of the leads, then

$$\begin{aligned} \int_{t_0}^t dt' \mathcal{K}(t, t') \hat{\rho}_S(t') = & -\frac{1}{\hbar^2} \text{Tr}_l \int_{t_0}^t dt' \\ & \times \left(\hat{H}_T^l(t) \hat{U}_0(t-t') \hat{H}_T^l(t') \hat{U}_0^\dagger(t-t') \hat{U}_0(t-t') \hat{\rho}_S(t') \hat{U}_0^\dagger(t-t') \hat{\rho}_l \right. \\ & - \hat{H}_T^l(t) \hat{U}_0(t-t') \hat{\rho}_S(t') \hat{U}_0^\dagger(t-t') \hat{\rho}_l \hat{U}_0(t-t') \hat{H}_T^l(t') \hat{U}_0^\dagger(t-t') \\ & - \hat{U}_0(t-t') \hat{H}_T^l(t') \hat{U}_0^\dagger(t-t') \hat{U}_0(t-t') \hat{\rho}_S(t') \hat{U}_0^\dagger(t-t') \hat{\rho}_l \hat{H}_T^l(t) \\ & \left. + \hat{U}_0(t-t') \hat{\rho}_S(t') \hat{U}_0^\dagger(t-t') \hat{\rho}_l \hat{U}_0(t-t') \hat{H}_T^l(t') \hat{U}_0^\dagger(t-t') \hat{H}_T^l(t) \right). \end{aligned} \quad (3.22)$$

The transfer Hamiltonian shown in Eq. (2.41) is put in Eq. (3.22). For the sake of consistency, we use the notation $\hat{H}_T^l(t)$ instead of $\hat{H}_{\text{ME},T}(t)$, and use Eq. (2.41) in the form

$$\hat{H}_T^l(t) = \chi^l(t) \int d\mathbf{q} \left(\mathcal{T}^l(\mathbf{q}) c_{\mathbf{q}}^l + c_{\mathbf{q}}^{l\dagger} (\mathcal{T}^l(\mathbf{q}))^\dagger \right), \quad (3.23)$$

to explicitly write the integral of the kernel as

$$\begin{aligned}
\int_{t_0}^t dt' \mathcal{K}(t, t') \rho_S(t') = & -\frac{\chi^l(t)}{\hbar^2} \int_{t_0}^t dt' \chi^l(t') \int d\mathbf{q} \\
& \times \left[\left\{ \mathcal{T}^l(\mathbf{q}') \hat{U}_S(t-t') \left((\mathcal{T}^l(\mathbf{q}'))^\dagger \rho_S(t') [1 - f(E_{SE}^l(\mathbf{q}))] \right. \right. \right. \\
& - \rho_S(t') (\mathcal{T}^l(\mathbf{q}'))^\dagger f(E_{SE}^l(\mathbf{q})) \Big) \times \hat{U}_S^\dagger(t-t') e^{(-i(t-t')E_{SE}^l(\mathbf{q}))} \Big\} \\
& - \left\{ \hat{U}_S(t-t') \left((\mathcal{T}^l(\mathbf{q}'))^\dagger \rho_S(t') [1 - f(E_{SE}^l(\mathbf{q}))] \right. \right. \\
& - \rho_S(t') (\mathcal{T}^l(\mathbf{q}'))^\dagger f(E_{SE}^l(\mathbf{q})) \Big) \hat{U}_S^\dagger(t-t') \times \mathcal{T}^l(\mathbf{q}) e^{(-i(t-t')E_{SE}^l(\mathbf{q}))} \Big\} \\
& + \left\{ \hat{U}_S(t-t') \left(\rho_S(t') \mathcal{T}^l(\mathbf{q}) [1 - f(E_{SE}^l(\mathbf{q}))] \right. \right. \\
& - \mathcal{T}^l(\mathbf{q}) \rho_S(t') f(E_{SE}^l(\mathbf{q})) \Big) \hat{U}_S^\dagger(t-t') \times (\mathcal{T}^l(\mathbf{q}))^\dagger e^{(i(t-t')E_{SE}^l(\mathbf{q}))} \Big\} \\
& - \left\{ (\mathcal{T}^l(\mathbf{q}))^\dagger \hat{U}_S(t-t') \left(\rho_S(t') \mathcal{T}^l(\mathbf{q}) [1 - f(E_{SE}^l(\mathbf{q}))] \right. \right. \\
& - \mathcal{T}^l(\mathbf{q}) \rho_S(t') f(E_{SE}^l(\mathbf{q})) \Big) \times \hat{U}_S^\dagger(t-t') e^{(i(t-t')E_{SE}^l(\mathbf{q}))} \Big\} \Big], \quad (3.24)
\end{aligned}$$

where $f(E_{SE}^l(\mathbf{q}))$ is the Fermi function of lead l . Further details are provided in appendix D.2 on how we obtain Eq. (3.24) from Eq. (3.22). In addition, $\hat{U}_S(t-t')$ is the evolution operator of the central system

$$\hat{U}_S(t-t') = e^{-\frac{i}{\hbar} \hat{H}_S(t-t')} = e^{-\frac{i}{\hbar} \hat{H}_S t} \times e^{\frac{i}{\hbar} \hat{H}_S t'}. \quad (3.25)$$

We now introduce

$$\begin{aligned}
\Omega^l(\mathbf{q}) := & e^{-\frac{i}{\hbar} \hat{H}_S t} \int_{t_0}^t dt' \chi^l(t') \times e^{\frac{i}{\hbar} \hat{H}_S t'} \left((\mathcal{T}^l(\mathbf{q}'))^\dagger \rho_S(t') [1 - f(E_{SE}^l(\mathbf{q}))] \right. \\
& - \rho_S(t') (\mathcal{T}^l(\mathbf{q}'))^\dagger f(E_{SE}^l(\mathbf{q})) \Big) e^{-\frac{i}{\hbar} \hat{H}_S t'} \times e^{\frac{i}{\hbar} \hat{H}_S t} e^{(-i(t-t')E_{SE}^l(\mathbf{q}))}, \quad (3.26)
\end{aligned}$$

to rewrite Eq. (3.24) into

$$\begin{aligned}
\int_{t_0}^t dt' \mathcal{K}(t, t') \rho_S(t') = & -\frac{\chi^l(t)}{\hbar^2} \int d\mathbf{q} \times \left\{ \left(\mathcal{T}^l(\mathbf{q}) \Omega^l(\mathbf{q}) - \Omega^l(\mathbf{q}) \mathcal{T}^l(\mathbf{q}) \right) \right. \\
& + \left. \left((\Omega^l(\mathbf{q}))^\dagger (\mathcal{T}^l(\mathbf{q}))^\dagger - (\Omega^l(\mathbf{q}))^\dagger (\mathcal{T}^l(\mathbf{q}))^\dagger \right) \right\}. \quad (3.27)
\end{aligned}$$

Using the commutation relation between $\mathcal{T}^l(\mathbf{q})$ and $\Omega^l(\mathbf{q})$

$$[\mathcal{T}^l(\mathbf{q}), \Omega^l(\mathbf{q})] = \mathcal{T}^l(\mathbf{q}) \Omega^l(\mathbf{q}) - \Omega^l(\mathbf{q}) \mathcal{T}^l(\mathbf{q}) \quad (3.28)$$

3. Non-Markovian approach to a generalized quantum master equation

the integration kernel of Eq. (3.27) becomes

$$\int_{t_0}^t dt' \mathcal{K}(t, t') \check{\rho}_S(t') = -\frac{\chi^l(t)}{\hbar^2} \int d\mathbf{q} \times \left(\left[\mathcal{T}^l(\mathbf{q}), \Omega^l(\mathbf{q}) \right] + \left[\mathcal{T}^l(\mathbf{q}), \Omega^l(\mathbf{q}) \right]^\dagger \right). \quad (3.29)$$

In an analogous way, the equation of motion for the reduced density operator by substituting Eq. (3.29) into Eq. (3.20) becomes

$$\dot{\rho}_S(t) = -\frac{i}{\hbar} \left[\hat{H}_S, \rho_S(t) \right] - \frac{1}{\hbar^2} \sum_{l=L,R} \chi^l(t) \int d\mathbf{q} \left(\left[\mathcal{T}^l(\mathbf{q}), \Omega^l(\mathbf{q}) \right] + \left[\mathcal{T}^l(\mathbf{q}), \Omega^l(\mathbf{q}) \right]^\dagger \right). \quad (3.30)$$

The Eq. (3.30) is the non-Markovian quantum master equation of the reduced density operator. It is here in a form that is directly appropriate for numerical calculations.

4. Calculation of Physical observables

The properties of the system can be determined by mean values of physical operators. In this section, we construct physical observables, or “measurables”. The expectation or mean value of a physical operator (\hat{O}) can be written as

$$\langle \hat{O} \rangle = \text{Tr}(\hat{\rho} \hat{O}), \quad (4.1)$$

where $\hat{\rho}$ is the total density matrix of the system. We are interested in a calculation of the mean value of the observables of the central system. The reduced density matrix

$$\hat{\rho}_S = \text{Tr}_l(\hat{\rho}) \quad (4.2)$$

can be used to rewrite the expectation value as

$$\langle \hat{O} \rangle = \text{Tr}_S(\hat{\rho}_S \hat{O}). \quad (4.3)$$

In the following we shall show how some physical observables of interest will be calculated for our system.

4.1. Electron and photon number operator

We introduce the electron and the photon number operators and their expectation values to get insight into the nature of the MB states of the central system.

Electron number operator

The electron number operator counts the number of electrons in the system. The number operator is defined as $\hat{N}_e = \sum_i d_i^\dagger d_i$, and its expectation value is

$$\langle \hat{N}_e \rangle = \text{Tr}(\hat{\rho}_S \hat{N}_e) = \sum_i \sum_{\check{\mu}} (\check{\mu} | d_i^\dagger d_i \rho_S | \check{\mu}). \quad (4.4)$$

4. Physical observables

Using the completeness relation $\sum_{\check{\mu}'} |\check{\mu}'\rangle \langle \check{\mu}'| = \mathbf{1}$ we obtain

$$\langle \hat{N}_e \rangle = \sum_i \sum_{\check{\mu}' \check{\mu}} (\check{\mu}' | d_i^\dagger d_i | \check{\mu}) \check{\rho}_{S; \check{\mu}' \check{\mu}}. \quad (4.5)$$

Photon number operator

The photon number operator is $\hat{N}_{\text{ph}} = a^\dagger a$ for a state in a single photon mode. The expectation value of the photon number is given by

$$\begin{aligned} \langle \hat{N}_{\text{ph}} \rangle &= \sum_i \sum_{\check{\mu}} (\check{\mu} | a^\dagger a \rho_S | \check{\mu}) \\ &= \sum_{\check{\mu}' \check{\mu}} (\check{\mu}' | a^\dagger a | \check{\mu}) \hat{\rho}_{S; \check{\mu}' \check{\mu}}. \end{aligned} \quad (4.6)$$

4.2. Charge density

To investigate the electron motion in the central system, we calculate the time-dependent electron charge density $\hat{Q}(\mathbf{r}, t)$, where the charge density operator is

$$\hat{Q}(\mathbf{r}) = e \sum_{i,j} \Psi_i^*(\mathbf{r}) \Psi_j(\mathbf{r}) d_i^\dagger d_j, \quad (4.7)$$

and the expectation value of the time-dependent charge density is thus

$$Q(\mathbf{r}, t) = \text{Tr} \left[\hat{Q}(\mathbf{r}) \rho_S(t) \right] = e \sum_{i,j} \Psi_i^*(\mathbf{r}) \Psi_j(\mathbf{r}) \sum_{\check{\mu}' \check{\mu}} (\check{\mu}' | d_i^\dagger d_j | \check{\mu}) \check{\rho}_{S; \check{\mu}' \check{\mu}}(t). \quad (4.8)$$

4.3. Charge current density

We are also interested in a calculation of the charge current density in the central system. The mean value of the charge current density operator is defined by

$$\mathbf{J}(\mathbf{r}, t) = \text{Tr} \left(\rho_S(t) \hat{\mathbf{J}}(\mathbf{r}) \right), \quad (4.9)$$

where the charge current density operator is

$$\begin{aligned} \hat{\mathbf{J}}(\mathbf{r}) = \sum_{ij} \left(\frac{e\hbar}{2m^*i} \left[\Psi_i^*(\mathbf{r})(\nabla\Psi_j(\mathbf{r})) - (\nabla\Psi_i^*(\mathbf{r}))\Psi_j(\mathbf{r}) \right] \right. \\ \left. + \frac{e^2}{m^*} \left[\mathbf{A}_{\text{ext}} + \mathbf{A}_{\text{ph}} \right] \Psi_i^*(\mathbf{r})\Psi_j(\mathbf{r}) \right) d_i^\dagger d_j. \end{aligned} \quad (4.10)$$

More information regarding to the charge current density is provided in appendix C.

4.4. Net charge current

Finally, we seek to investigate the characteristics of electron transport from the leads to the central system and vice versa. We define the left and right partial current describing the current from the left lead and the right lead into the central system, respectively, as

$$I_l(t) = \lambda \frac{e}{\hbar^2} \chi_l(t) \times \sum_{\check{\mu}} \int d\mathbf{q} (\check{\mu} | \{ [\mathcal{T}^l(\mathbf{q}), \Omega^l(\mathbf{q})] + [\mathcal{T}^l(\mathbf{q}), \Omega^l(\mathbf{q})]^\dagger \} | \check{\mu}), \quad (4.11)$$

where λ is a positive sign for the left current and a negative sign for the right current. The net charge current is thus expressed as

$$I_Q = I_L + I_R. \quad (4.12)$$

with I_L being the left current and I_R the right current.¹

¹ We have used Eq. (4.12) to define the net charge current for investigation of PAT phenomena. But the net charge current is defined as $I_Q = I_L - I_R$ to implement quantum logic gate in the waveguide system.

5. Results and Conclusions

In this section, we summarize our results on the characteristics of the electron transport through a quantized system made of a GaAs material with the effective mass $m^* = 0.067m_e$, and with the relative dielectric constant $\kappa = 12.4$. The system is placed in a static or vanishing perpendicular external magnetic field. The length scale associated with the magnetic field and the transverse confinement, the effective magnetic length is $a_w = (\hbar/[m^*\sqrt{(\omega_c^2 + \Omega_0^2)}])^{1/2}$, where $\omega_c = eB/m^*$ is the cyclotron frequency, and Ω_0 is the transverse confinement frequency. For convenience we give the following formula for numerical values of the effective magnetic

$$\begin{aligned} a_w &= \left(\frac{\hbar}{m^*\Omega_0} \right)^{1/2} \left(\frac{1}{1 + (eB/(m^*\Omega_0))^2} \right)^{1/4} \\ &= \frac{33.74}{\sqrt[4]{1 + 2.982[B(\text{T})]^2}} \text{ nm}. \end{aligned} \quad (5.1)$$

The external magnetic field influences the magnetic length such that increasing magnetic field leads to decreasing effective magnetic length.

In order to provide coherent electron transport in our system, the length of the central system is assumed to be $\sim 150 - 300$ nm and the temperature of the leads is $\sim 0.01 - 0.5$ K. As we know the phase coherence length L_ϕ of GaAs material is around $\sim (30 - 40) \times 10^2$ nm at low temperature $T \sim 0.1 - 2.0$ K [13]. Therefore, the coherence length is much larger than the length of the central system in our model.

The central system is connected to lead l with the chemical potential μ_l . The Fermi function of lead l before the coupling to the central system is

$$f^l(E_{\text{SE}}^l(\mathbf{q})) = \left[\exp(E_{\text{SE}}^l(\mathbf{q}) - \mu_l) + 1 \right]^{-1}, \quad (5.2)$$

where $E_{\text{SE}}^l(\mathbf{q})$ is the SE subband energy of lead l found in Eq. (2.17). The chemical potentials of the leads imply an applied potential difference or bias window $\Delta\mu = \mu_L - \mu_R = eV_{\text{bias}}$.

In addition, the parameters of the Gaussian potential that forms the structure of the central system and the photon cavity parameters are not fixed throughout this work.

These parameters will be stated later for each specific geometrical confinement of the central system.

5.1. Cavity-photon-assisted electron transport

The electron-photon interaction in the system leads to an interesting phenomenon, in electron transport, the so called photon-assisted electron transport. In this section we show how the photons in the cavity can enhance the electron transport in the electronic system where we consider a single quantum dot or serial double quantum dots system.

The magnetic field is assumed to be $B = 0.1$ T, and the transverse confinement energy of the central system and the leads is $\hbar\Omega_0 = \hbar\Omega_l = 2.0$ meV. The temperature of the leads before the coupling to the central system is $T = 0.01$ K, such that the MB energy level spacing in the central system is greater than the thermal energy of the leads, namely $\Delta E_{\text{MB}} > k_B T$, the thermal smearing effect is thus sufficiently suppressed.

In the following we shall demonstrate the main results of the single and double quantum dot systems coupled to a single photon mode of the cavity.

5.1.1. Single quantum dot system

We consider a central system consisting of a quantum dot (QD) embedded in a quantum wire. The quantum wire is a two-dimensional finite wire which is scaled by the effective magnetic length a_w , with the length $L_x = 300$ nm. In addition, we assume the potential V_G presented in Eq. (2.3) to be $V_G = V_{\text{QD}}$ where the QD potential V_{QD} shown in Fig. 5.1 is defined as

$$V_{\text{QD}}(x, y) = V_0 \exp[-\beta_0^2 (x^2 + y^2)]. \quad (5.3)$$

Herein, the strength of the potential is $V_0 = -3.3$ meV and $\beta_0 = 3.0 \times 10^{-2} \text{ nm}^{-1}$, such that the radius of the QD is $R_{\text{QD}} \approx 33.3$ nm.

The QD system is connected to the left lead with the chemical potential $\mu_L = 1.2$ meV, and to the right lead with $\mu_R = 1.1$ meV. The bias window is thus $\Delta\mu = eV_{\text{bais}} = 0.1$ meV. Figure 5.2(a) shows the energy spectrum of the leads versus wave number \mathbf{q} where the green lines are the chemical potentials of the leads. We notice that the first subband energy (red) is located in the bias window indicating the activation of the first subband in the electron transport. Figure 5.2(b) demonstrates

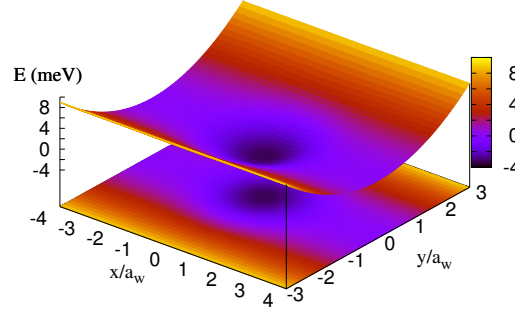


Figure 5.1: (Color online) The potential shows a QD embedded in a quantum wire with parameters $B = 0.1$ T, $a_w = 23.8$ nm, and $\hbar\Omega_0 = 2.0$ meV.

the ME energy spectrum of the QD system as a function of the plunger-gate voltage in the absence of the electron-photon interaction. The energies of one-electron states $N_e = 1$ (1ES, red dots) and two-electron states $N_e = 2$ (2ES, blue dots) vary linearly proportional to the applied plunger gate voltage V_{pg} . We find a 1ES in the bias window at $V_{pg} = 0.4$ mV labeled by a red rectangle.

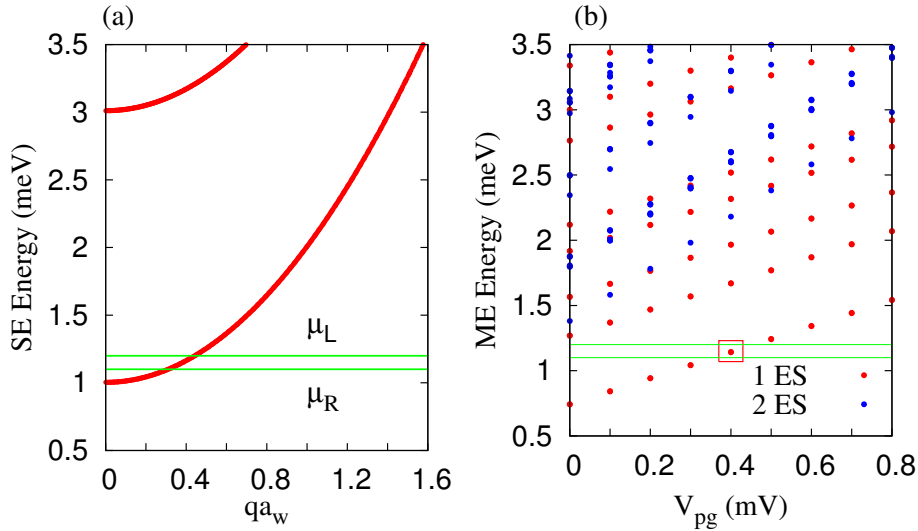


Figure 5.2: (Color online) (a) SE energy spectrum in the leads (red) is plotted versus wave number \mathbf{q} , where the chemical potentials are $\mu_L = 1.2$ meV and $\mu_R = 1.1$ meV (green). (b) ME energy spectrum in the central system as a function of the plunger gate voltage V_{pg} including SE states (1ES, red dots), and two-electron states (2ES, blue dots). The one-electron state in the bias window is almost doubly degenerate due to the small Zeeman energy.

The electrons occupying the first subband in the left lead are allowed to tunnel into the 1ES of the QD system making resonant tunneling from the left to the right lead

5. Results and Conclusions

manifesting a peak (main-peak) in charge current at $V_{\text{pg}} = 0.4$ mV as is shown in Fig. 5.3.

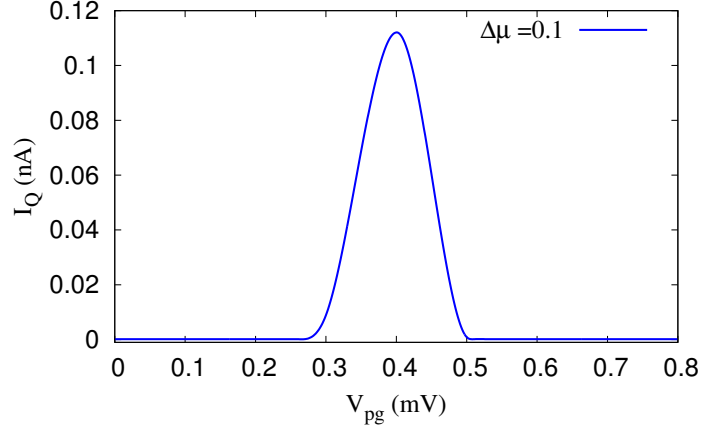


Figure 5.3: (Color online) The net charge current versus the plunger gate voltage V_{pg} plotted at time $t = 220$ ps in the absence of a photon cavity. The magnetic field is $B = 0.1$ T, and the bias window is $\Delta\mu = 0.1$ meV.

Now, we assume the QD system to be placed in a photon cavity with photon energy $\hbar\omega_{\text{ph}} = 0.3$ meV, and one photon $N_{\text{ph}} = 1$ initially in the cavity. The photons in the cavity are considered to be either parallel (x -direction) or perpendicular (y -direction) polarized to the electron transport through the QD system. The many-body (MB) energy spectrum of the QD system coupled to the photon cavity including the electron-photon interaction is shown in Fig. 5.4. In the absence of the photon cavity, only one active state around $V_{\text{pg}}^0 = 0.4$ mV gets into the bias window. But in the case of the system in the photon cavity additional active states can be found around $eV_{\text{pg}} = eV_{\text{pg}}^0 \pm \hbar\omega_{\text{ph}}$. This implies that the single photon mode induces active propagating states around $V_{\text{pg}} = 0.1$ and 0.7 mV when the photon energy is $\hbar\omega_{\text{ph}} = 0.3$ meV.

The electrons in the additional states manifest different mechanism of transport. Figure 5.5 shows the net charge current I_Q versus the plunger-gate voltage V_{pg} at time $t = 220$ ps in the presence of the x -polarized (a) and y -polarized (b) photon field with the energy $\hbar\omega_{\text{ph}} = 0.3$ meV. We test three values of the electron-photon coupling strength, $g_{\text{ph}} = 0.1$ meV (blue solid), 0.2 meV (green dashed), and 0.3 meV (red dotted). In addition to the main peak around $V_{\text{pg}}^0 = 0.4$ mV, a robust left side peak around $eV_{\text{pg}} = eV_{\text{pg}}^0 - \hbar\omega_{\text{ph}}$ is clearly observed, and a right side peak around $eV_{\text{pg}} = eV_{\text{pg}}^0 + \hbar\omega_{\text{ph}}$ can be barely recognized in the presence of the x -polarized photon field as is shown in Fig. 5.5(a). The left side peak exhibits a photon-assisted transport, i.e. a transition from the one-electron MB state in the bias window,

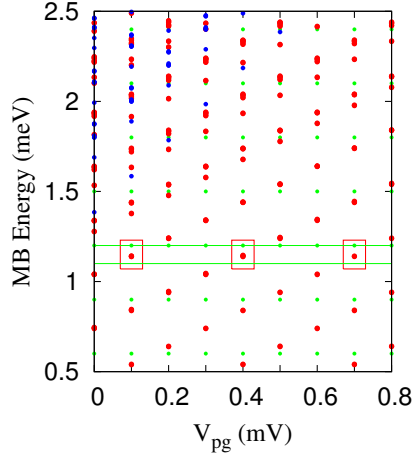


Figure 5.4: (Color online) The MB Energy spectrum as a function of the plunger gate voltage V_{pg} in the presence of a photon cavity with an x -polarized photon field, with zero-electron states ($N_e = 0$, green dots), one-electron states ($N_e = 1$, red dots), and two-electron states ($N_e = 2$, blue dots) are included. $B = 0.1$ T, $\Delta\mu = 0.1$ meV, and $\hbar\omega_{ph} = 0.3$ meV.

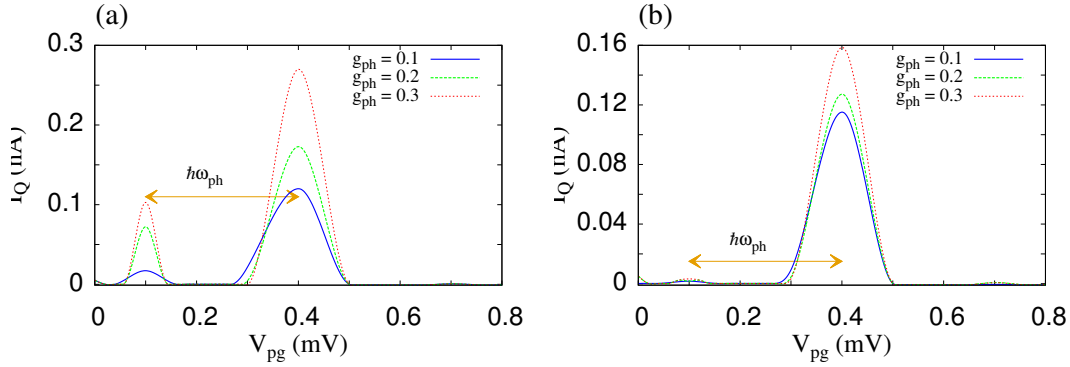


Figure 5.5: (Color online) The net charge current versus plunger gate voltage V_{pg} at time $t = 220$ ps in the presence of x -polarized (a) and y -polarized (b) of the photon field with different electron-photon coupling strength: $g_{ph} = 0.1$ meV (blue solid), $g_{ph} = 0.2$ meV (green dashed), and $g_{ph} = 0.3$ meV (red dotted). The photon energy $\hbar\omega_{ph} = 0.3$ meV. $B = 0.1$ T, and $\Delta\mu = 0.1$ meV.

absorbing a photon with energy $\hbar\omega_{ph}$, to the photon activated one-electron MB states above the bias window. Our results show that the transport of electrons with energy within the bias window can be enhanced by increasing electron-photon coupling strength. This indicates that the electrons may absorb a single-photon and, hence, the charge current manifests a photon-assisted transport.

5. Results and Conclusions

We have seen that the photon-assisted transport is much weaker in the case of a y -polarized photon mode in comparison with that of x -polarization as is presented in Fig. 5.5(b). This is caused by the anisotropy of QD system. The photon energy is much smaller than the confinement energy in the perpendicular direction (the y -direction).

5.1.2. Double quantum dot system

In addition to the single QD system, we investigate a double serial quantum dot system in order to obtain or enhance inter-dot electron tunneling via the photons in the cavity. The double dot system is a promising structure for constructing a qubit in a quantum computer.

We consider the length of the quantum wire $L_x = 165$ nm, and two serial quantum dots embedded in the wire with radii $R_{\text{QD}} \simeq 20$ nm. The DQD system is put in an external magnetic field $B = 0.1$ T. The two dots are modeled by two identical Gaussian potentials in the quantum wire defined as

$$V_{\text{DQD}}(x, y) = \sum_{i=1}^2 V_i \exp \left[-\beta_i^2 \left((x - x_i)^2 + y^2 \right) \right], \quad (5.4)$$

with strength $V_{1,2} = -2.8$ meV, $x_1 = 35$ nm, $x_2 = -35$ nm, and $\beta_{1,2} = 5.0 \times 10^{-2} \text{ nm}^{-1}$. The distance between the dots is thus $L_{\text{DQD}} = 35 \text{ nm} \simeq 1.47a_w$, and each dot is $25 \text{ nm} = 1.05a_w$ away from the nearest lead. Again the V_G presented in Eq. (2.3) is assumed to be $V_G = V_{\text{DQD}}$ in the calculations of the DQD system.

The DQD system is weakly connected to the leads and strongly coupled to a photon cavity. The chemical potential of the leads are $\mu_L = 1.4$ meV and $\mu_R = 1.3$ meV. Therefore, the bias window $\Delta\mu = 0.1$ meV. In addition, the cavity initially contains two photons $N_{\text{ph}} = 2$ with the photon energy $\hbar\omega_{\text{ph}} = 0.25$ meV.

In the absence of the photon cavity, two one-electron states are found in the bias window, namely, ground state and the first excited state. Therefore, two corresponding peaks in the net charge current are observed [103]. The electron charge density is accumulated in the dots for the ground state with a strong inter-dot tunneling as is shown in Fig. 5.6(a). Consequently, the left and the right currents increase in the system. But the electron charge density of the first-excited state presented in Fig. 5.6(b) is strongly localized in the dots without much tunneling between the dots. The tunneling between the dots is thus sufficiently suppressed as is seen in the current.

In the presence of the photon cavity, two extra side peaks are found at $eV_{\text{pg}}^{\text{GS}} = eV_{\text{pg}}^{\text{GM}} - \hbar\omega_{\text{ph}}$ and $eV_{\text{pg}}^{\text{FES}} = eV_{\text{pg}}^{\text{FEM}} - \hbar\omega_{\text{ph}}$, where GS and GM indicate ground-state

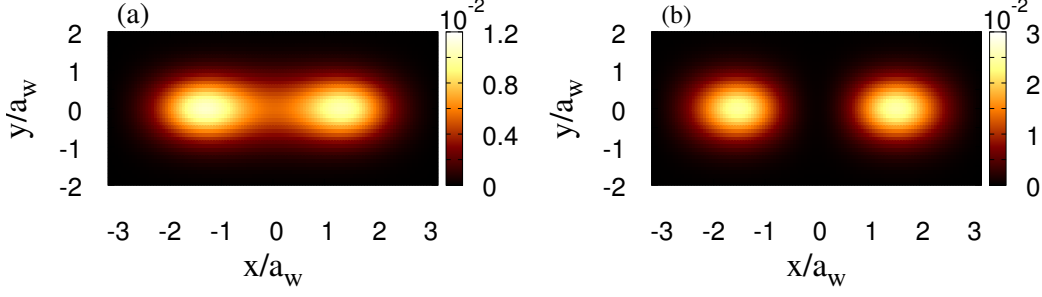


Figure 5.6: The electron charge density at $t = 220$ ps in the ground state (a), and the first-excited state (b), in the absence of a photon cavity. The magnetic field is $B = 0.1$ T, $a_w = 23.8$ nm, $L_x = 165$ nm, and $\Delta\mu = 0.1$ meV.

side-peak and ground-state main-peak, and FES and FEM stand for side-peak of the first-excited state and the main peak of the first-excited state, respectively [103]. The side peaks indicate photon-assisted electron transport from the leads to the photon activated states of the DQD system. Figure 5.7 shows the electron charge density in the first-excited state of the DQD system coupled to the cavity in the case of an x -polarized of the photon field. Comparing to the electron charge density presented in Fig. 5.6(b) the inter-dot tunneling is enhanced in the main-peak of the first-excited state. The enhancement is due to participation of the photon activated states in the electron transport.

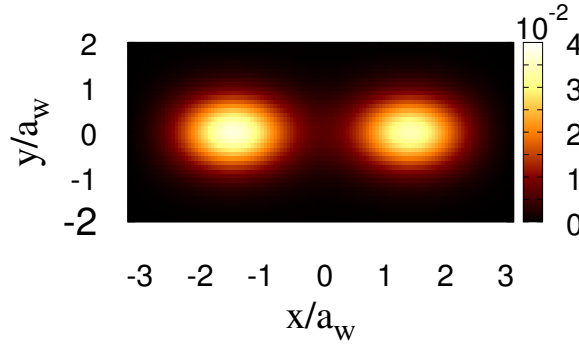


Figure 5.7: The electron charge density at $t = 220$ ps in the first-excited state in the presence of a photon cavity. Other parameters are $B = 0.1$ T, and $a_w = 23.8$ nm, $L_x = 165$ nm, $\Delta\mu = 0.1$ meV, $g_{\text{ph}} = 0.1$ meV, $\hbar\omega_{\text{ph}} = 0.25$ meV, and $N_{\text{ph}} = 2$.

5.2. Quantum Logic gate actions in a qubit system

It is known that waveguides can be used to implement quantum logic gates in a quantum computer. Many techniques have been used to investigate both classical and quantum properties of logic gates. In this section, we focus on a different technique from previous methods to control and implement logic gates in a double quantum waveguide.

We consider two laterally coupled waveguides connected to two leads as is shown in Fig. 5.8. The lower waveguide is the so called control-waveguide while the upper waveguide is the target-waveguide. The double waveguide can be defined as two parallel finite quantum wires coupled via a window to facilitate coherent electron inter-wire transport. In our model the DQW has a hard-wall confinement in the contact area to the external leads at $x = \pm L_x/2$, with $L_x = 300$ nm the length of the waveguides in the transport direction, but parabolic confinement in the y -direction. The waveguide system and the leads have the same transverse confinement energy ($\hbar\Omega_0 = \hbar\Omega_l = 1.0$ meV). In addition, the total system is exposed to a weak or a vanishing external static magnetic field in the z -direction. The temperature of the leads before the coupling to the DQW system is $T = 0.5$ K.

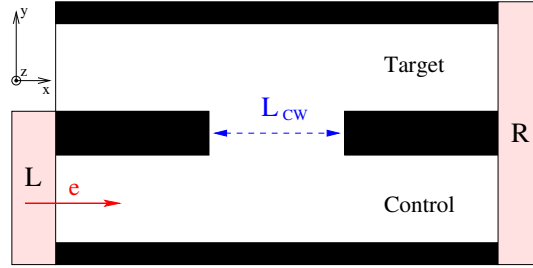


Figure 5.8: Schematic diagram of the double waveguide with a CW of length L_{CW} (blue dashed arrow). The lower waveguide is called the ‘Control’ while the upper waveguide is the ‘Target’. An electron from left side enters the control waveguide (red arrow). Asymmetric contacts are indicated by the light red rectangles marked L and R .

The potential defining the DQW system is

$$V_{DQW}(\mathbf{r}) = V_B(y) + V_{CW}(x, y), \quad (5.5)$$

with $V_B(y)$ the barrier potential between the waveguides

$$V_B(y) = V_0 \exp(-\beta_0^2 y^2). \quad (5.6)$$

Herein, $V_0 = 18.0$ meV is the strength of the barrier potential and $\beta_0 = 0.03$ nm⁻¹ a smoothness parameter. The coupling window (CW) potential is

$$V_{CW}(x, y) = -V_1 \exp(-\beta_x^2 x^2 - \beta_y^2 y^2), \quad (5.7)$$

with $V_1 = 18.0$ meV, and $\beta_y = 0.03$ nm⁻¹. β_x is a parameter that defines the CW length. Therefore, the length of the CW can be estimated as $L_{CW} = 2/\beta_x$.

The waveguide system is asymmetrically coupled to the leads by modification of the nonlocal coupling function demonstrated in Eq. (2.21) to

$$g_{nm,mq}^l(\mathbf{r}, \mathbf{r}') = g_0^l \exp \left[-\delta_x^l (x - x')^2 - \delta_y^l (y - y' - \alpha)^2 \right] \times \exp \left(-|E_{n,m} - \epsilon_m^l(q)|/\Delta_E \right). \quad (5.8)$$

where $\alpha = 4.0a_w$ is a skewing parameter that shifts the weight of the coupling to the control-waveguide. The electrons from the left lead are thus injected into the control waveguide. Below, we shall show the transport properties through the DQW system without and with the photon cavity.

The DQW without a photon cavity

We now demonstrate the electron transport properties of the DQW in the case of no coupling between the DQW and a photon cavity. In order to perform electron switching between the waveguides, we first tune the CW length between the waveguides. In Fig. 5.9 we plot the net charge current versus the CW length at $t = 200$ ps and $B = 0.0$ T in the case without (solid blue), and with (dashed red) the electron-electron Coulomb interaction. We find oscillations in the net charge current indicating charge switching between the control- and the target-waveguide. The oscillations give rise a maxima (peak) and a minima (dip) in the net charge current at $L_{CW} \simeq 40$ nm and 110 nm, respectively. Furthermore, it is clearly shown that the electron-electron interaction suppresses the net charge current. Both Zibold *et al.* and Gong *et al* reported the same oscillation characteristics in the absence of the Coulomb interaction. They explained the oscillations by energy-dependent inter-waveguide transmission in the quantum regime. They pointed out that the inter-waveguide transmission can be enhanced when the energy levels of the coupled-waveguide system to achieve a resonance conditions for a specific CW length [104, 105].

In order to explain the oscillation property in the net charge current, we present Fig. 5.10 indicating the non-interacting (a) and interacting (b) ME energy spectrum of the DQW system at $B = 0.0$ T, where the red dots are one-electron state (1ES) and the blue dots are two-electron states (2ES). The back lines denote the chemical potentials of the leads which are $\mu_L = 4.0$ meV and $\mu_R = 3.0$ meV. We observe that the 2ES are shifted up away from the bias window in the presence of the electron-electron interaction leading to blocking the 2ES. This causes non-participation of the 2ES in the electron transport. As a result, the net charge current is suppressed.

In the case of a short CW ($L_{CW} < 40$) there is a weak tunneling between the

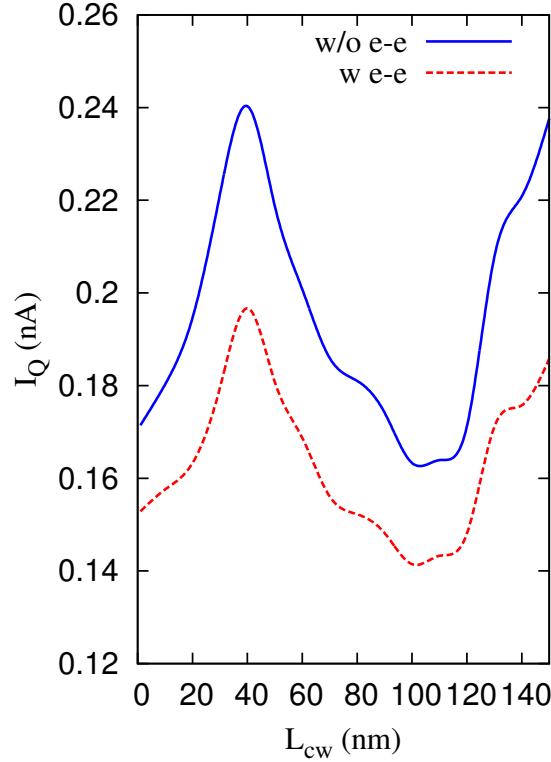


Figure 5.9: Net charge current I_Q versus CW length L_{CW} at $t = 200$ nm without (w/o) (blue solid) and with (w) (red dashed) the Coulomb interaction. The chemical potentials are $\mu_L = 4.0$ meV and $\mu_R = 3.0$ meV implying $\Delta\mu = 1.0$ meV. The magnetic field is $B = 0.0$ T.

control- and target-waveguide. In this case the coupling between the waveguides is caused by the electron tunneling and the Coulomb interaction leading to nearly degenerate states [94]. Increasing the CW length, the ME energy states are no longer degenerate and the energy spectrum decreases monotonically [104]. Furthermore, higher excited states enter the active bias window resulting in a level crossover with lower excited states. A crossover energy observed at $L_{CW} \simeq 40$ nm (left green rectangular) indicates a resonant energy between the waveguides. The contribution of the higher excited states to the electron transport increases the net charge current forming a current peak as is shown in Fig. 5.9. At this point, the inter-waveguide electron transport is enhanced leading to an increase in the net charge current. By tuning further the CW length to $L_{CW} \simeq 110$ nm (right green rectangular), the splitting of the energy levels increases. In addition, the lowest energy state of the second subband (the highest state in the green rectangle) enters the bias window leading to a strong ‘interaction’ between the waveguides. Consequently, the inter-waveguide back-scattering is enhanced.

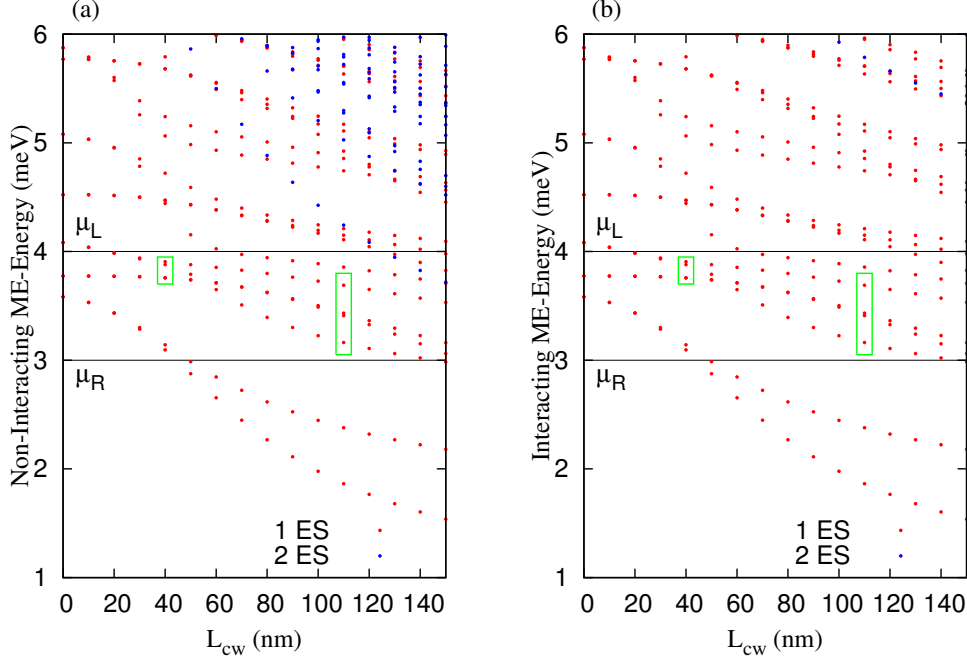


Figure 5.10: The ME energy spectrum of the DQW system versus the CW length L_{CW} without (a), and with (b) the electron-electron interaction including one-electron states (1ES, red dots) and two-electron states (2ES, blue dots) at $B = 0.0$ T. The one-electron states in the left green rectangle are close to be in resonance, but the one-electron states in the right green rectangle are not. The chemical potentials are $\mu_L = 4.0$ meV and $\mu_R = 3.0$ meV (black) implying $\Delta\mu = 1.0$ meV.

It is interesting to see the charge motion at the crossover energy. Figure 5.11 shows the charge current density for the resonant energy levels at $L_{CW} \simeq 40$ nm for both non-interacting (a) and interacting (b) DQW system at $t = 200$ ps and $B = 0.0$ T.

In Fig. 5.11(a) the charge current density coming from the input of the control-waveguide splits equally to the control and the target output. This is similar to the condition of splitting of electron transmission ratio in the DQW at a crossover energy [104]. The dynamical evolution occurring in the CW region implements a $\sqrt{\text{NOT}}$ -operation quantum logic gate [68].

In Fig. 5.11(b) the charge current density mostly transfers through the control-waveguide with a weak inter-waveguide forward scattering in the presence of the Coulomb interaction. The charge does not split in the interacting DQW system because the 2ESs do not participate in the electron transport.

In the following we connect the DQW system to a photon cavity with a single photon

5. Results and Conclusions

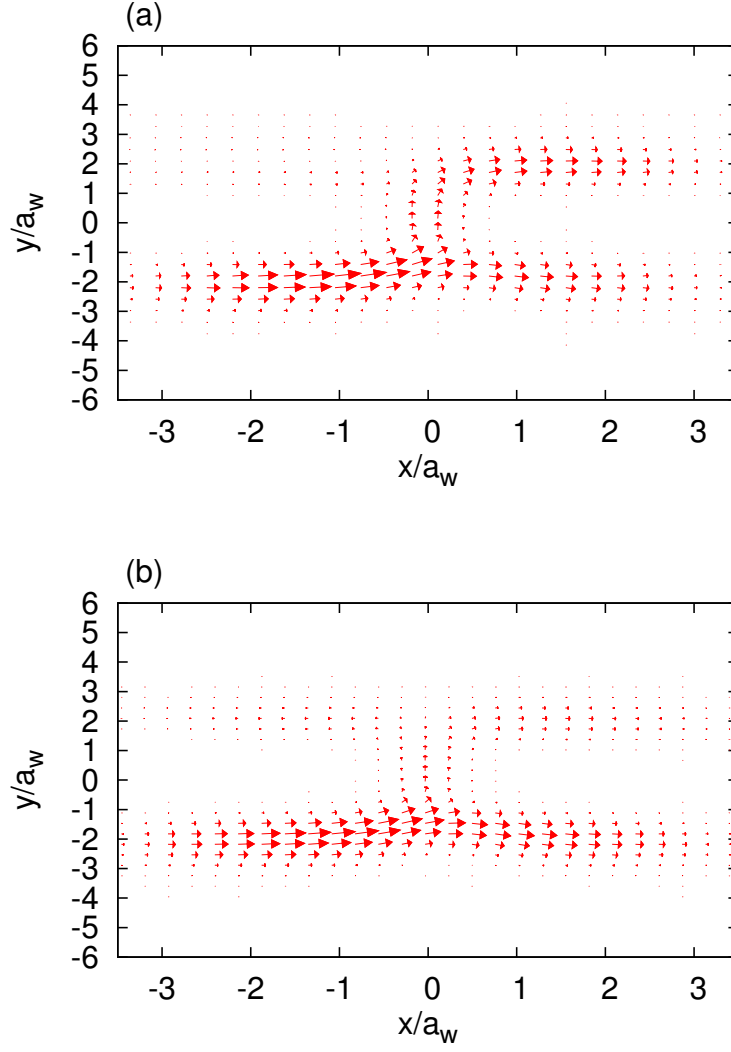


Figure 5.11: Charge current density in the DQW at $t = 200$ ps without (a), and with (b) the electron-electron interaction in the peak of the net charge current at $L_{\text{CW}} = 40$ nm shown in Fig. 5.9. The magnetic field is $B = 0.0$ T and the effective magnetic length is $a_w = 33.72$ nm.

mode.

The DQW in a photon cavity

In this section, we connect the DQW system to a photon cavity in which the photons are polarized in either the x -direction or the y -direction. The electron-photon coupling strength is fixed at $g_{\text{ph}} = 0.1$ meV, but the photon energy and the photon number in the cavity are varied to control the electron switching between the waveguides. Our goal here is to use the photon cavity to facilitate or control the implementation of a quantum logic gate in the double waveguide system.

We first compare the net charge current in the DQW without and with the photon cavity in order to understand the effects of the electron-photon interaction. Figure

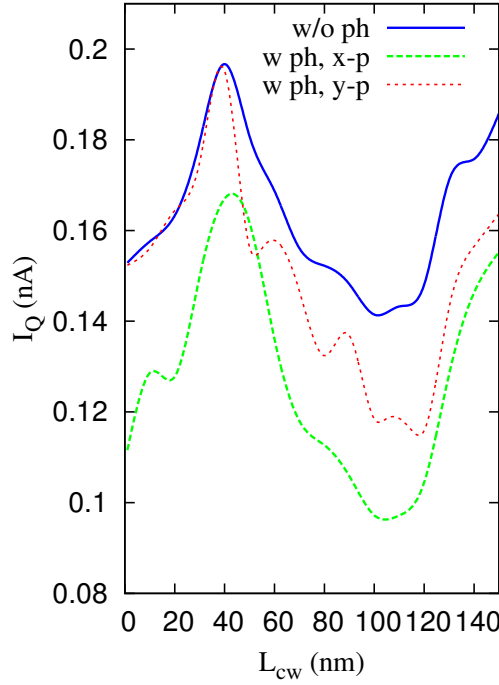


Figure 5.12: The net charge current I_Q as a function of the CW length L_{CW} without (w/o) a photon (ph) cavity (blue solid), and with a photon (w ph) cavity in the case of x -polarization (green dashed) and y -polarization (red dotted) at time $t = 200$ ps. The photon energy $\hbar\omega_{\text{ph}} = 0.3$ meV, $g_{\text{ph}} = 0.1$ meV, $B = 0.001$ T, and the chemical potentials are $\mu_L = 4.0$ meV and $\mu_R = 3.0$ meV, implying $\Delta\mu = 1.0$ meV.

5.12 shows the net charge current in the DQW without a photon cavity (blue solid) and with a photon cavity in the case of an x -polarization (green dashed) and a y -polarization (red dotted) of the photon field with energy $\hbar\omega_{\text{ph}} = 0.3$ meV and one

5. Results and Conclusions

photon initially in the cavity $N_{\text{ph}} = 1$. We previously explained the characteristics of net charge current in the DQW without the photon cavity in Fig. 5.9. It is clearly seen that the net charge current is generally reduced in the presence of a cavity initially containing one photon. The reduction is due to the participation of photon replica states in the electron transport as is shown in Fig. 5.13.

Figure 5.13 displays the MB energy spectrum of the DQW coupled to the x -polarized photon field including zero-electron states (0ES) (green dots) and 1ES (red dots) with the photon energy $\hbar\omega_{\text{ph}} = 0.3$ meV, and one photon initially in the cavity. It can be seen that the photon replica states are produced with different photon

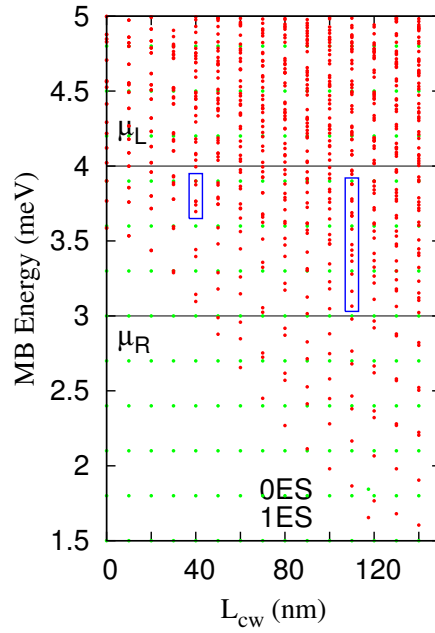


Figure 5.13: Energy spectra of the DQW system versus CW length L_{CW} with a photon cavity including zero-electron states (0ES, green dots) and one-electron states (1ES, red dots) at $B = 0.001$ T. The 1ES states in the left blue rectangle are close to the crossover region of states, but the 1ES states in the right blue rectangular are not. The left rectangle contains the most active transport states. The change in the height of the rectangle from left to right indicates the spreading of states from the resonance to the off-resonance condition. The photon energy $\hbar\omega_{\text{ph}} = 0.3$ meV with x -polarization, $g_{\text{ph}} = 0.1$ meV. The chemical potentials are $\mu_L = 4.0$ meV and $\mu_R = 3.0$ meV (black) implying $\Delta\mu = 1.0$ meV.

content in the presence of the photon cavity. The energy difference between two photon replicas is close to multiples of the photon energy in case of weak electron-photon coupling [103]. At $L_{\text{CW}} \simeq 40$ nm (left blue rectangle), the one-photon replicas of the states in the energy crossover region are found to be active in the

transport at 4.1-4.3 meV instead of the states themselves in the bias window. Since the photon energy is $\hbar\omega_{\text{ph}} = 0.3$ meV the replicas of the states in the energy crossover region still are in the first subband. Therefore, a total switching of electron charge from the control- to the target-waveguide does not happen. But, we found a weak inter-waveguide backward scattering leading to current suppression in the case of an x -polarized photon as is shown in Fig. 5.12 (green dashed line). In addition, the two-photon replicas of the ground state and first-excited state enter the energy crossover region in the bias window. The participation of the two photon state in the electron transport is weak because the cavity initially contains only one photon.

At $L_{\text{CW}} \simeq 110$ nm (right blue rectangle), the photon replicas of the ground state and the first excited state containing three and four photons appear in the split energy levels. Their contribution to the electron transport is not influential. But the most active state here is the photon replica of the lowest state of the second subband containing one photon. This photon replica is a localized state in the CW region leading to a suppression in the net charge current for both x - (green dashed) and y -polarized (red dotted) photon field at the dip as is shown in Fig. 5.12.

Figure 5.14 demonstrates the charge current density in the x -polarized (a), and the y -polarized (b) photon field at $L_{\text{CW}} \simeq 40$ nm (current peak) presented in Fig. 5.12 where the electron-photon coupling is $g_{\text{ph}} = 0.1$ meV and the photon energy is $\hbar\omega_{\text{ph}} = 0.3$ meV. In the case of an x -polarization the charge distribution indicates

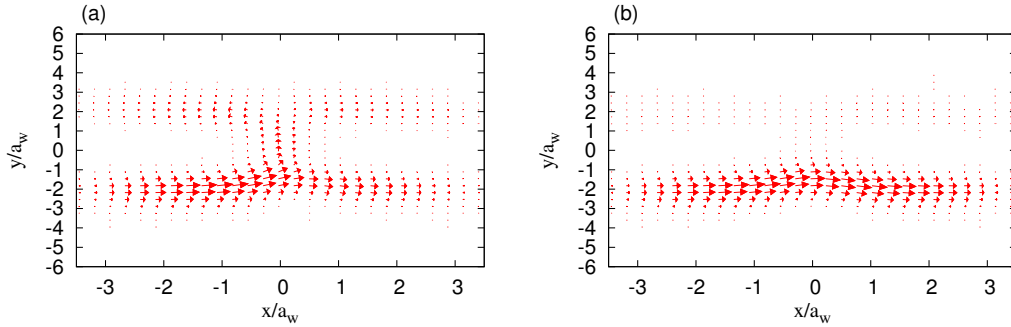


Figure 5.14: (Color online) The charge current density of the DQW coupled to a cavity with an x -polarized (a) and a y -polarized (b) photon field at $t = 200$ ps in the current peak at $L_{\text{CW}} \simeq 40$ nm shown in Fig. 5.14. The photon energy $\hbar\omega_{\text{ph}} = 0.3$ meV, $N_{\text{ph}} = 1$, and $g_{\text{ph}} = 0.1$ meV. Other parameters are $L_x = 300$ nm, $\hbar\Omega_0 = 1.0$ meV, $B = 0.001$ T, and $a_w = 33.72$ nm.

an inter-waveguide transport. Comparing to the charge current density in the absence of the photon cavity presented in Fig. 5.11(b), the inter-waveguide backward scattering is increased as is shown in Fig. 5.14(a). The inter-waveguide backward scattering may be partially related to the charge polarization in the x -direction induced by the photon field, and the activation of the one-photon replicas of the states

5. Results and Conclusions

in energy crossover regime in the transport. Consequently, the net charge current decreases in the dip.

It is interesting to see the charge current density in the current peak at $L_{\text{CW}} \simeq 40$ nm in the presence of y -polarization as is displayed in Fig. 5.14(b), where the electron transverse confinement energy and the photon energy are $\hbar\Omega_0 = 1.0$ meV, and $\hbar\omega_{\text{ph}} = 0.3$ meV, respectively. The charge transfers from the input control-waveguide to the output control-waveguide without inter-waveguide transport. This is because the photon energy is much smaller than the electron confinement energy in the waveguide system in the y -direction.

Tuning the photon number and energy

We mentioned that the photon replica states influence the electron switching between the waveguides. Now, we tune the photon number and energy in order to control the electron switching process. We first consider two photons initially in the cavity and increase the photon energy to $\hbar\omega_{\text{ph}} = 0.6$ meV with $g = 0.1$ meV and x -polarization of the photon field. In this case the electron charge at the CW length $L_{\text{CW}} \simeq 40$ nm switches from the input control-waveguide to the output target-waveguide as is shown in the Fig. 5.15. The electron switching process is caused by

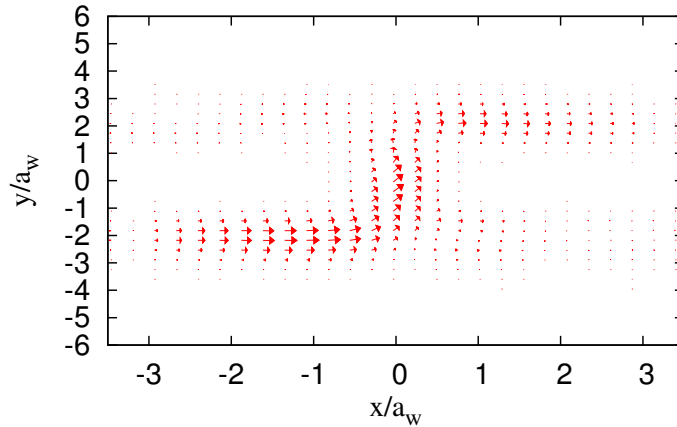


Figure 5.15: (Color online) The charge current density at $t = 200$ ps with an x -polarized photon field at $L_{\text{CW}} \simeq 40$ nm. The photon number in the cavity initially is $N_{\text{ph}} = 2$, $\hbar\omega_{\text{ph}} = 0.6$ meV, and $g_{\text{ph}} = 0.1$ meV. Other parameters are $L_x = 300$ nm, $\hbar\Omega_0 = 1.0$ meV, $B = 0.001$ T, and $a_w = 33.72$ nm.

the participation of two-photon replicas of states at the energy crossover located in the second subband. In this case the electron may absorb two photons with energy

$N_{\text{ph}} \times \hbar\omega_{\text{ph}} = 1.2$ meV and subsequently be transferred to the second subband from the first subband of the waveguide system. As a result, the charge is totally switched from the control to the target waveguide. In addition to that the one-photon replicas of the ground state and the first-excited state are seen in the energy crossover regime in the bias window. But, they contribute weakly to the electron transport. The charge motion occurring in the DQW system implements a quantum logic gate operation and a Not-operation is realized.

We mentioned that an inter-waveguide transport at the crossover energy is not found in the y -polarization because the photon energy is smaller than transverse confinement energy of electron. In order to obtain inter-waveguide transport, we need to increase either the photon energy or the photon number initially in the cavity. Figure 5.16 shows the charge current density at $L_{\text{CW}} \simeq 40$ nm where the photon energy is increased to $\hbar\omega_{\text{ph}} = 0.9$ meV but keeping one photon initially in the cavity. Comparing to the charge current density shown in Fig. 5.14(b) when the photon energy is $\hbar\omega_{\text{ph}} = 0.3$ meV, inter-waveguide transport is increased because the photon energy is close to the electron confinement energy in the waveguide system in the y -direction. An electron in the control-waveguide may obtain energy from the photon to partially occupy a state in the second subband of the two parallel waveguides and thus being transferred to the target-waveguide.

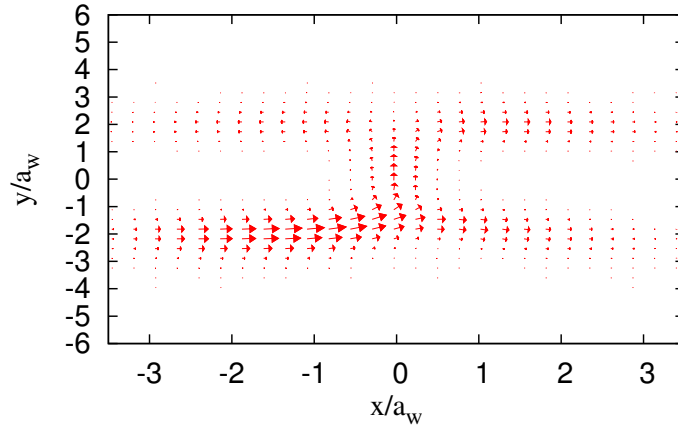


Figure 5.16: (Color online) The charge current density at $t = 200$ ps with y -polarized photon field in the current peak at $L_{\text{CW}} \simeq 40$ nm. The photon energy $\hbar\omega_{\text{ph}} = 0.9$ meV, $g_{\text{ph}} = 0.1$ meV and $N_{\text{ph}} = 1$. Other parameters are $L_x = 300$ nm, $\hbar\Omega_0 = 1.0$ meV, $B = 0.001$ T, and $a_w = 33.72$ nm.

Let us consider two photons ($N_{\text{ph}} = 2$) initially in the cavity and the photon energy is $\hbar\omega_{\text{ph}} = 0.6$ meV, which is smaller than the electron confinement energy ($\hbar\Omega_0 = 1.0$ meV). In this case, an electron coming from the left lead may absorb two

5. Results and Conclusions

photon with the total energy $N_{\text{ph}} \times \hbar\omega_{\text{ph}} \simeq 1.2$ meV and then being transferred to the target-waveguide. Consequently, the charge from the input control-waveguide totally transfers to the target-waveguide as is shown in Fig. 5.17. The charge motion occurring here implements a NOT-operation quantum logic gate action.

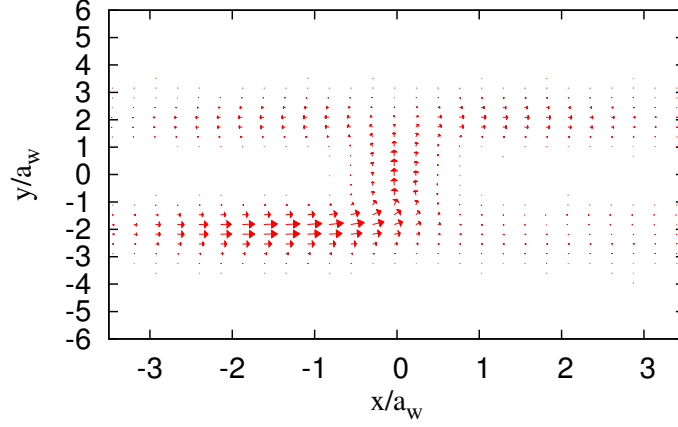


Figure 5.17: (Color online) The charge current density in the y -polarized photon field at $L_{\text{CW}} \simeq 40$ nm and $t = 200$ ps. The photon energy $\hbar\omega_{\text{ph}} = 0.6$ meV, $N_{\text{ph}} = 2$, and $g_{\text{ph}} = 0.1$ meV. Other parameters are $L_x = 300$ nm, $\hbar\Omega_0 = 1.0$ meV, $B = 0.0$ T, and $a_w = 33.72$ nm.

As a last relevant consideration, the features of the coherent electron transport in a DQW coupled to a photon cavity discussed in this thesis offer interesting and innovative new possibilities for implementing quantum logic gate in waveguide system in nanoscale range.

5.3. Conclusions

In this thesis we have investigated physical properties of quantum systems with various complicated geometrical structures. We considered a two-dimensional finite electronic system connected to electron reservoirs (leads). The chemical potentials of the leads define a bias window or potential difference driving electrons through the total system. The total system is exposed to an external static magnetic field perpendicular to the electron motion in the system. The electron-electron interaction in the central finite size system is taken into account while the Coulomb interaction in the leads is neglected. The electron transport is investigated in the system using a general master equation. In this approach, we use a non-Markovian master equation for a reduced density matrix describing the electron motion in the central system under the influence of the leads.

The central system is coupled to cavity photons of a single mode. The photons in the cavity are assumed to be polarized either parallel or perpendicular to the electron motion in the central system. The electron-photon interaction plays an essential role in the electron transport properties in such a way that the electrons absorb or emit photons in the cavity leading to enhancement or suppression the electron transport.

In addition, a plunger gate voltage is applied to the central system to move the quantized energy states up or down with respect the the bias window. Therefore, one can investigate the physical properties of each quantized energy state of the central system. Furthermore, the absorption and emission photon processes and their roles to the electron transport can be controlled or selected by the plunger gate voltage.

We have focused on two physical phenomena which are the cavity photon-assisted electron transport through a single quantum dot or double quantum dot system and implementation of quantum logic gate in waveguides or qubit systems. In the first part, we have used the cavity-photon to enhance the electron transport in a quantum dot system. In the case of a quantum dot embedded in a photon cavity, a peak in the net charge current is found by tuning the plunger-gate voltage. The current peak is due to a resonance of a one-electron state with the chemical potential of the leads. We call this current peak the main peak. In the case of a QD system coupled to an x -polarized photon mode, the main current peak is enhanced by the electron-photon coupling. The electrons may absorb a single photon manifesting a photon-assisted secondary peak which also incorporates correlation effects. In the case of a QD coupled to a y -polarized photon mode, the main current peak is contributed to by two photon-activated one-electron states and a correlation-induced two-electron state. In the y -polarization the secondary peak current is suppressed due to the anisotropy of our system.

5. Results and Conclusions

In the second part of this thesis, we have studied quantum logic gate action in a charge qubit. We have presented a model for a window coupled double quantum waveguide in an external perpendicular magnetic field. The DQW is weakly connected to two leads and strongly coupled to a photon cavity. We investigate coherent switching in the electron transport between the waveguides for the implementation of quantum logic gates.

By tuning the length of the CW, we have shown two important physical characteristics of the waveguide system: resonant energy-levels and oscillations in the net charge current. The resonant energy levels indicate coupling between the DQW and the oscillations denote the resonance conditions that are governed by the length of the CW.

In the absence of the electron-electron and electron-photon interactions, the charge current density splits equally between the waveguides at resonant energies, therefore, the net charge current reaches its maximum value and the waveguide system works as a $\sqrt{\text{NOT}}$ -operation qubit. The split charge current is facilitated by the participation of two-electron states to the electron transport. But in the presence of the electron-electron interaction the charge splitting is strongly reduced because the 2ES are lifted out of the group of active states in the transport.

We have identified the implementation of various types of quantum logic gates by varying the photon number and energy, or the photon polarization in the presence of the photon cavity in the system. Photon replicas for each MB energy state are produced in the presence of the photon cavity. The character of the active photon replicas in the electron transport depends on the photon energy, the photon number, and the photon polarization. In the presence of an x -polarized single photon mode with two photons initially in the cavity, the charge from input control-waveguide switches to the output of the target-waveguide. In this case, an electron in the control-waveguide may interact with two photons and transfer to the target-waveguide. Consequently, a Not-operation quantum logic gate is implemented. For the y -polarized photon field, the electron-switching processes only occurs if the photon energy is equal to or greater than the electron confinement energy in the DQW system in the y -direction.

In addition, we have used side QDs in the double waveguide system to enhance the electron switching process. We see that more energy-levels of the two waveguides are brought into resonance which can lead to stronger coupling between them. Effectively, the dots can increase the density of states around the resonant transport states.

A. Matrix elements of the single-electron Hamiltonian

A.1. Closed system

In section 2, we have shown the Hamiltonian of the central system. In this appendix we present the derivation of the matrix elements of the Hamiltonian shown in Eq. (2.3). The matrix elements are

$$\begin{aligned} \langle n'', m'' | H_{\text{SE}} | n, m \rangle = & \langle n'', m'' | \left(\frac{1}{2m^*} (\mathbf{p} + \frac{e}{c} \mathbf{A}_{\text{ext}})^2 \right. \\ & \left. + \frac{1}{2} m^* \Omega_0^2 y^2 + V_G + eV_{\text{pg}} + h_Z \right) | n, m \rangle. \end{aligned} \quad (\text{A.1})$$

Reorganizing Eq. (A.1) to simplify the the matrix elements we split it into four terms

$$\begin{aligned} \langle n'', m'' | H_{\text{SE}} | n, m \rangle = & \langle n'', m'' | \left(\frac{1}{2m^*} (\mathbf{p} + \frac{e}{c} \mathbf{A}_{\text{ext}})^2 + \frac{1}{2} m^* \Omega_0^2 y^2 \right) | n, m \rangle \\ & + \langle n'', m'' | V_G | n, m \rangle + \langle n'', m'' | eV_{\text{pg}} | n, m \rangle + \langle n'', m'' | h_Z | n, m \rangle. \end{aligned} \quad (\text{A.2})$$

In the following, we shall calculate each term of Eq. (A.2) separately.

A.1.1. Matrix elements of \mathbf{p} and \mathbf{A}_{ext} terms

The matrix element of the canonical momentum operator and the vector potential of the external magnetic field are calculated here. We begin with the \mathbf{p} and \mathbf{A}_{ext} terms of the Hamiltonian which are combined as

$$h_{\text{ES}} = \frac{1}{2m^*} (\mathbf{p} + \frac{e}{c} \mathbf{A}_{\text{ext}})^2 + \frac{1}{2} m^* \Omega_0^2 y^2, \quad (\text{A.3})$$

where the magnetic field is assumed to be homogenous and perpendicular to the electron motion. The vector potential described in Landau gauge is $\mathbf{A}_{\text{ext}} = (-By, 0, 0)$,

A. Matrix elements of the single-electron Hamiltonian

then the Hamiltonian is modified to

$$h_{\text{ES}} = -\frac{\hbar^2}{2m^*}\nabla_x^2 + \left[-\frac{\hbar^2}{2m^*}\nabla_y^2 + \frac{1}{2}m^*\Omega_w^2 y^2 \right] + i\hbar\omega_c y \nabla_x. \quad (\text{A.4})$$

Using the eigenfunctions of the central system in Eq. (2.5) and Eq. (2.6), the matrix elements of Eq. (A.4) can be divided into three terms:

First term is the matrix elements of the x -component of the canonical momentum operator

$$\langle n'', m'' | \left(-\frac{\hbar^2 \nabla_x^2}{2m^*} \right) | n, m \rangle = \frac{n^2 \pi^2}{2} \left(\frac{a_w^2}{L_x} \right)^2 (\hbar\Omega_w) \delta_{n'',n} \delta_{m'',m}, \quad (\text{A.5})$$

Second term is y -component of canonical momentum operator and harmonic potential

$$\langle n'', m'' | \left[-\frac{\hbar^2 \nabla_y^2}{2m^*} + \frac{1}{2}m^*\Omega_w^2 y^2 \right] | n, m \rangle = \left(m + \frac{1}{2} \right) (\hbar\Omega_w) \delta_{n'',n} \delta_{m'',m}, \quad (\text{A.6})$$

And the last term is

$$\langle n'', m'' | i\hbar\omega_c y \nabla_x | n, m \rangle = i\hbar\omega_c \langle m'' | y | m \rangle \langle n'' | \frac{\partial}{\partial x} | n \rangle, \quad (\text{A.7})$$

where

$$\langle m'' | y | m \rangle = \langle m'' | \frac{a_w}{2} (a + a^\dagger) | m \rangle = a_w \left[\sqrt{\frac{m}{2}} \delta_{m'',m-1} + \sqrt{\frac{m+1}{2}} \delta_{m'',m+1} \right], \quad (\text{A.8})$$

with $a(a^\dagger)$ being the lowering(raising) operator of Harmonic oscillator, respectively, and

$$\langle n'' | \frac{\partial}{\partial x} | n \rangle = I_{n'',n} = \begin{cases} \frac{4nn''(-1)^{\frac{n''+n-1}{2}}}{L_x(n''^2-n^2)} & \text{if } n'' + n = 3, 5, 7, \dots \\ 0 & \text{if } n'' + n = 2, 4, 6, \dots \end{cases} \quad (\text{A.9})$$

Substituting Eq. (A.8) and Eq. (A.9) into Eq. (A.7) we obtain

$$\langle n'', m'' | i\hbar\omega_c y \nabla_x | n, m \rangle = i\hbar\omega_c a_w I_{n'',n} \left[\sqrt{\frac{m}{2}} \delta_{m'',m-1} + \sqrt{\frac{m+1}{2}} \delta_{m'',m+1} \right], \quad (\text{A.10})$$

Then adding Eq. (A.5), Eq. (A.6), and Eq. (A.10) together to get the matrix element of the first part of the Hamiltonian in the following form

$$\begin{aligned} \langle n'', m'' | h_{\text{ES}} | n, m \rangle &= \left[\frac{n^2 \pi^2}{2} \left(\frac{a_w^2}{L_x} \right)^2 + \left(m + \frac{1}{2} \right) \right] (\hbar\Omega_w) \delta_{n'',n} \delta_{m'',m} \\ &+ i\hbar\omega_c a_w I_{n'',n} \left[\sqrt{\frac{m}{2}} \delta_{m'',m-1} + \sqrt{\frac{m+1}{2}} \delta_{m'',m+1} \right]. \end{aligned} \quad (\text{A.11})$$

A.1.2. Matrix elements of a Gaussian potential

The second part of Eq. (A.2) describes the matrix elements of the potential describing the geometry of the system. A Gaussian potential has been chosen to describe parts of the central system

$$V_G(x, y) = -V_0 e^{(-\beta_x^2(x-x_0)^2 - \beta_y^2(y-y_0)^2)}, \quad (\text{A.12})$$

where V_0 is the strength of the potential, β_x and β_y define the range of the potential, and (x_i, y_i) is the center of the potential. The matrix elements of the Gaussian potential are

$$\langle n'', m'' | V_G(x, y) | n, m \rangle = -V_0 V_{n'',n} V_{m'',m}, \quad (\text{A.13})$$

herein, the x -component of the matrix elements is governed by

$$V_{n'',n} = \langle n'' | e^{-\beta_x^2(x-x_0)^2} | n \rangle,$$

and the y -component is

$$V_{m'',m} = \langle m'' | e^{-\beta_y^2(y-y_0)^2} | m \rangle.$$

The derivation of both x - and y -component is shown in the following.

x -component ($V_{n'',n}$)

There are four possibilities of integration in the x -component regarding to the quantum numbers n'' and n : (a) n'' and n are odd, (b) n'' is odd and n is even, (c) n'' is even and n is odd, and (d) n'' and n are even. Using Eq. (2.5), the integration in the case of (a) and (d) is not zero but for the other two cases is zero. We now calculate the non-vanishing terms, if n'' and n are odd integer then

$$V_{n'',n} = \langle n'' | e^{-\beta_x^2(x-x_0)^2} | n \rangle = \frac{2}{L_x} \int_{-\frac{L_x}{2}}^{+\frac{L_x}{2}} dx \cos\left(\frac{n''\pi x}{L_x}\right) e^{-\beta_x^2(x-x_0)^2} \cos\left(\frac{n\pi x}{L_x}\right), \quad (\text{A.14})$$

and in the case of even integer of n'' and n the integration is

$$V_{n'',n} = \langle n'' | e^{-\beta_x^2(x-x_0)^2} | n \rangle = \frac{2}{L_x} \int_{-\frac{L_x}{2}}^{+\frac{L_x}{2}} dx \sin\left(\frac{n''\pi x}{L_x}\right) e^{-\beta_x^2(x-x_0)^2} \sin\left(\frac{n\pi x}{L_x}\right). \quad (\text{A.15})$$

The substitution of $u_x = \frac{x}{L_x}$ gives

$$V_{n'',n} = 2 \int_{-\frac{1}{2}}^{+\frac{1}{2}} du_x \cos(n''\pi u_x) e^{-[\beta_x L_x(u_x - u_{x0})]^2} \cos(n\pi u_x), \quad (\text{A.16})$$

and

$$V_{n'',n} = 2 \int_{-\frac{1}{2}}^{+\frac{1}{2}} du_x \sin(n''\pi u_x) e^{-[\beta_x L_x(u_x - u_{x0})]^2} \sin(n\pi u_x). \quad (\text{A.17})$$

A. Matrix elements of the single-electron Hamiltonian

y -component ($V_{m'';m}$)

The matrix elements of the y -component are

$$V_{m'';m} = \langle m'' | e^{-\beta_y^2(y-y_0)^2} | m \rangle = \int dy \psi_{m''}^*(y) e^{-\beta_y^2(y-y_0)^2} \psi_m(y), \quad (\text{A.18})$$

using the basis wave functions in Eq. (2.6), the integral is then given by

$$V_{m'';m} = \frac{1}{a_w [2^{(m''+m)} m''! m! \pi]^{\frac{1}{2}}} \times \int dy e^{[-\beta_y^2 a_w^2 ((y/a_w) - (y_0/a_w))^2 - (y/a_w)^2]} H_{m''}(y/a_w) H_m(y/a_w). \quad (\text{A.19})$$

To simplifying further the matrix elements, one can use $u_y = y/a_w$ and $\tilde{\beta}_y = \beta_y^2 a_w^2$

$$V_{m'';m} = \frac{1}{[2^{(m''+m)} m''! m! \pi]^{\frac{1}{2}}} \int du e^{-[\tilde{\beta}_y(u_y - u_{y_0})^2 + u_y^2]} H_{m''}(u_y) H_m(u_y). \quad (\text{A.20})$$

In order to be able to perform the integration, we need to modify

$$\begin{aligned} \tilde{\beta}_y(u_y - u_{y_0})^2 + u_y^2 &= \tilde{\beta}_y u_y^2 - 2\tilde{\beta}_y u_y u_{y_0} + \tilde{\beta}_y u_{y_0}^2 + u_y^2 \\ &= \tilde{\beta}_y u_y^2 - 2\tilde{\beta}_y u_y u_{y_0} + \tilde{\beta}_y u_{y_0}^2 + u_y^2 - \frac{\tilde{\beta}_y u_{y_0}^2}{1 + \tilde{\beta}_y} + \frac{\tilde{\beta}_y u_{y_0}^2}{1 + \tilde{\beta}_y} \\ &= - \left[(1 + \tilde{\beta}_y)^{\frac{1}{2}} u_y - \frac{\tilde{\beta}_y u_{y_0}}{(1 + \tilde{\beta}_y)^{\frac{1}{2}}} \right] - \frac{\tilde{\beta}_y u_{y_0}^2}{1 + \tilde{\beta}_y}. \end{aligned} \quad (\text{A.21})$$

Using Eq. (A.21) and assuming $z = (1 + \tilde{\beta}_y)^{\frac{1}{2}} u_y$, then Eq. (A.20) is transformed to

$$V_{m'';m} = \frac{1}{[2^{(m''+m)} m''! m! \pi]^{\frac{1}{2}}} \frac{e^{-[\tilde{\beta}_y u_{y_0}^2 / (1 + \tilde{\beta}_y)]}}{(1 + \tilde{\beta}_y)^{\frac{1}{2}}} \times \int dz e^{-[z - \tilde{\beta}_y u_{y_0} / (1 + \tilde{\beta}_y)^{\frac{1}{2}}]^2} H_{m''} \left(\frac{z}{(1 + \tilde{\beta}_y)^{\frac{1}{2}}} \right) H_m \left(\frac{z}{(1 + \tilde{\beta}_y)^{\frac{1}{2}}} \right). \quad (\text{A.22})$$

An identity of integral Hermite polynomials is

$$\begin{aligned} \int dz e^{-(z-z_0)^2} H_{m''}(\alpha z) H_m(\alpha z) &= \pi^{\frac{1}{2}} \sum_{k=0}^{\min(m'', m)} 2^k k! \binom{m''}{k} \binom{m}{k} \\ &\times (1 - \alpha^2)^{(\frac{m''+m}{2} - k)} H_{m''+m-2k} \left(\frac{\alpha z_0}{(1 - \alpha^2)^{\frac{1}{2}}} \right). \end{aligned} \quad (\text{A.23})$$

Comparing Eq. (A.22) to Eq. (A.23), we explicitly obtain $\alpha = 1/(1 + \tilde{\beta}_0)^{\frac{1}{2}}$. Then Eq. (A.22) can be written as

$$V_{m'';m} = \frac{1}{[2^{(m''+m)} m''!m!]^{\frac{1}{2}}} \frac{e^{-[\tilde{\beta}_y u_{y0}^2/(1+\tilde{\beta}_y)]}^{\min(m'',m)}}{(1 + \tilde{\beta}_y)^{\frac{1}{2}}} \sum_{k=0}^{\min(m'',m)} 2^k k! \binom{m''}{k} \binom{m}{k} \\ \times \left(\frac{\tilde{\beta}_y}{(1 + \tilde{\beta}_y)} \right)^{(\frac{m''+m}{2}-k)} H_{m''+m-2k} \left(\frac{\tilde{\beta}_y^{\frac{1}{2}} u_{y0}}{(1 + \tilde{\beta}_y)^{\frac{1}{2}}} \right). \quad (\text{A.24})$$

Finally replacing the values $u_y = y/a_w$, $u_{y0} = y_0/a_w$ and $\tilde{\beta}_y = \beta_y^2 a_w^2$ to get the matrix elements of the y -component

$$V_{m'';m} = \frac{1}{[2^{(m''+m)} m''!m!]^{\frac{1}{2}}} \frac{e^{-[(\beta_y^2 y_0^2)/(1+\beta_y^2 a_w^2)]}^{\min(m'',m)}}{(1 + \beta_y^2 a_w^2)^{\frac{1}{2}}} \sum_{k=0}^{\min(m'',m)} 2^k k! \binom{m''}{k} \binom{m}{k} \\ \times \left(\frac{\beta_y^2 a_w^2}{(1 + \beta_y^2 a_w^2)} \right)^{(\frac{m''+m}{2}-k)} H_{m''+m-2k} \left(\frac{\beta_y y_0}{(1 + \beta_y^2 a_w^2)^{\frac{1}{2}}} \right). \quad (\text{A.25})$$

A.1.3. Matrix elements of V_{pg} and h_Z terms

The third term of Eq. (A.2) describes the matrix elements of the plunger-gate voltage which is governed by

$$\langle n'', m'' | eV_{\text{pg}} | n, m \rangle = eV_{\text{pg}} \int dx \psi_{n''}^*(x) \psi_n(x) \times \int dy \psi_{m''}^*(y) \psi_m(y) \\ = eV_{\text{pg}} \delta_{n''n} \delta_{m''m} = eV_{\text{pg}} \delta_{n'',n} \delta_{m'',m}. \quad (\text{A.26})$$

And the fourth term of Eq. (A.2) indicates the Zeeman energy which is a constant value for a fixed magnetic field added to the matrix elements of the canonical momentum operator

$$\langle n'', m'' | h_Z | n, m \rangle = \langle n'', m'' | (\pm \frac{1}{2} g^* \mu_B B) | n, m \rangle, \quad (\text{A.27})$$

where $\mu_B = \frac{e\hbar}{m_0}$ with $m_0 = m_e/m^*$. Using $m^* = 0.067$, $g^* = -0.44$, and $\omega_c = eB/m_e$ we get

$$\langle n'', m'' | h_Z | n, m \rangle = \pm 00737 \hbar \omega_c \delta_{n'',n} \delta_{m'',m}. \quad (\text{A.28})$$

A. Matrix elements of the single-electron Hamiltonian

The total matrix elements of the Eq. (A.2) can be expressed as the following

$$\begin{aligned} \langle n'', m'' | H_{\text{SE}} | n, m \rangle = & \left[\frac{n^2 \pi^2}{2} \left(\frac{a_w^2}{L_x} \right)^2 + \left(m + \frac{1}{2} \right) \right] (\hbar \Omega_w) \delta_{n'', n} \delta_{m'', m} \\ & + i \hbar \omega_c a_w I_{n'', n} \left[\sqrt{\frac{m}{2}} \delta_{m'', m-1} + \sqrt{\frac{m+1}{2}} \delta_{m'', m+1} \right] \\ & - V_0 V_{n'', n} V_{m'', m} + e V_{\text{pg}} \delta_{n'', n} \delta_{m'', m} \\ & \pm 00737 \hbar \omega_c \delta_{n'', n} \delta_{m'', m}. \end{aligned} \quad (\text{A.29})$$

A.2. Matrix elements of the lead Hamiltonian in the SE basis

In this appendix, the matrix elements shown in Eq. (2.17) are calculated. We use the Hamiltonian of the lead presented in Eq. (2.9) to get

$$\langle m'', q'' | \hat{H}_{\text{SE}}^l | m, q \rangle = \langle m'', q'' | \left(\frac{-\hbar^2}{2m^*} \nabla_x^2 + \left[\frac{-\hbar^2}{2m^*} \nabla_y^2 + \frac{1}{2} m^* (\Omega_w^l)^2 y^2 \right] + i \hbar \omega_c y \nabla_x \right) | m, q \rangle. \quad (\text{A.30})$$

Using the basis eigenfunctions in Eq. (2.13) and Eq. (2.14), the matrix elements of the lead Hamiltonian are divided into three parts. The first part is the matrix elements of the Hard-well confined potential

$$\langle m'', q'' | \left(\frac{-\hbar^2}{2m^*} \nabla_x^2 \right) | m, q \rangle = \frac{\hbar \Omega_w^l}{2} (a_l q)^2 \delta_{m'', m} \delta(q'' - q), \quad (\text{A.31})$$

and the second part is the matrix elements for the Harmonic oscillator Hamiltonian

$$\langle m'', q'' | \left(\frac{-\hbar^2}{2m^*} \nabla_y^2 + \frac{1}{2} m^* \Omega_w^2 y^2 \right) | m, q \rangle = \hbar \Omega_w \left(m + \frac{1}{2} \right) \delta_{m'', m} \delta(q'' - q). \quad (\text{A.32})$$

Putting these two parts together results in

$$\langle m'', q'' | \left(\frac{-\hbar^2}{2m^*} \nabla_x^2 + \left[\frac{-\hbar^2}{2m^*} \nabla_y^2 + \frac{1}{2} m^* \Omega_w^2 y^2 \right] \right) | m, q \rangle = \varepsilon_m^l(q) \delta_{m'', m} \delta(q'' - q) \quad (\text{A.33})$$

where $\varepsilon_m^l(q)$ are the eigenvalues presented in Eq. (2.15).

The third part is a Hamiltonian mixing the motion of the x - and the y -directions, the matrix elements consists of two terms

$$\langle m'', q'' | i \hbar \omega_c y \nabla_x | m, q \rangle = i \hbar \omega_c \langle q'' | \frac{\partial}{\partial x} | q \rangle \langle m'' | y | m \rangle, \quad (\text{A.34})$$

where the x -component is

$$\begin{aligned}\langle q'' | \frac{\partial}{\partial x} | q \rangle &= \frac{2}{\pi} \int_{-\infty}^{-\frac{L_x}{2}} dx \sin \left(q'' \left(x + \frac{L_x}{2} \right) \right) \frac{\partial}{\partial x} \sin \left(q \left(x + \frac{L_x}{2} \right) \right) \\ &= \frac{2iq}{\pi} \int_{-\infty}^{-\frac{L_x}{2}} dx \sin \left(q'' \left(x + \frac{L_x}{2} \right) \right) \cos \left(q \left(x + \frac{L_x}{2} \right) \right).\end{aligned}\quad (\text{A.35})$$

We assume $u = (x + \frac{L_x}{2})$, so $x = (u - \frac{L_x}{2})$ and $dx = du$

$$\langle q'' | \frac{\partial}{\partial x} | q \rangle = \frac{2iq}{\pi} \int_{-\infty}^0 du \sin(q''u) \cos(qu) \quad (\text{A.36})$$

The identity $\sin(q''u) \cos(qu) = \frac{1}{2} [\sin(u(q'' + q)) + \sin(u(q'' - q))]$ [106] modifies Eq. (A.36) to

$$\begin{aligned}\langle q'' | \frac{\partial}{\partial x} | q \rangle &= \frac{iq}{\pi} \int_{-\infty}^0 du \sin(u(q'' + q)) + \sin(u(q'' - q)) \\ &= \frac{q}{2\pi} \int_0^{\infty} du [\exp(-iu(q'' + q)) - \exp(iu(q'' + q)) \\ &\quad + \exp(-iu(q'' - q)) - \exp(iu(q'' - q))]\end{aligned}\quad (\text{A.37})$$

We use the formula $\zeta(q) = -i \int_0^{\infty} du \exp(iqu) = \frac{\mathfrak{B}}{u} - i\pi\delta(u)$ [107] to obtain

$$\begin{aligned}\langle q'' | \frac{\partial}{\partial x} | q \rangle &= \frac{iq}{2\pi} [\zeta(-q'' - q) - \zeta(q'' + q) + \zeta(q - q'') - \zeta(q'' - q)] \\ &= \frac{iq}{\pi} \left[-\frac{\mathfrak{B}}{q'' + q} + \frac{\mathfrak{B}}{q - q''} \right] \\ &= -\frac{2iq''q}{\pi} \frac{\mathfrak{B}}{q'^2 - q^2} \\ &:= I_{q''q}.\end{aligned}\quad (\text{A.38})$$

And the y -component of Eq. (A.34) is

$$\langle m'' | y | m \rangle = a_l \left[\sqrt{\frac{m}{2}} \delta_{m'', m-1} + \sqrt{\frac{m+1}{2}} \delta_{m'', m+1} \right]. \quad (\text{A.39})$$

The matrix elements of both the x - and the y -components of Eq. (A.34) give

$$\langle m'', q'' | i\hbar\omega_c y \nabla_x | m, q \rangle = i\hbar\omega_c a_l I_{q''q} \left[\sqrt{\frac{m}{2}} \delta_{m'', m-1} + \sqrt{\frac{m+1}{2}} \delta_{m'', m+1} \right]. \quad (\text{A.40})$$

Substituting Eq. (A.33) and Eq. (A.40) into Eq. (A.30) we obtain

$$\begin{aligned}\langle m'', q'' | \hat{H}_{\text{SE}}^l | m, q \rangle &= \varepsilon_m^l(q) \delta_{m'', m} \delta(q'' - q) \\ &\quad + i\hbar\omega_c a_l I_{q''q} \left[\sqrt{\frac{m}{2}} \delta_{m'', m-1} + \sqrt{\frac{m+1}{2}} \delta_{m'', m+1} \right].\end{aligned}\quad (\text{A.41})$$

A. Matrix elements of the single-electron Hamiltonian

Putting the matrix elements shown in Eq. (A.41) into Eq. (2.17) we get the following structure

$$\begin{aligned}
E_{\text{SE}}^l(m', q') C_{m', m''}(q', q'') &= \sum_m \int dq \varepsilon_m^l(q) C_{m', m}(q', q) \delta_{m'', m} \delta(q'' - q) \\
&\quad + i\hbar\omega_c a_l \sum_m \left[\sqrt{\frac{m}{2}} \delta_{m'', m-1} + \sqrt{\frac{m+1}{2}} \delta_{m'', m+1} \right] \\
&\quad \times \int dq I_{q'' q} C_{m', m}(q', q), \tag{A.42}
\end{aligned}$$

where the integral is

$$\begin{aligned}
\int dq I_{q'' q} C_{m', m}(q', q) &= -\frac{2iq''}{\pi} \int_0^\infty dq \frac{\Im q}{q'^2 - q^2} C_{m', m}(q', q) \\
&= \frac{iq''}{\pi} \int_{-\infty}^\infty dq \frac{\Im |q|}{q^2 - q'^2} C_{m', m}(q', |q|) \\
&= \frac{iq''}{2\pi} \int_{-\infty}^\infty dq \Im |q| C_{m', m}(q', |q|) \frac{1}{q''} \left[\frac{1}{q - q''} - \frac{1}{q + q''} \right] \\
&= \frac{i}{2\pi} i\pi \left[|q''| C_{m', m}(q', |q''|) - |q''| C_{m', m}(q', |q''|) \right] = 0. \tag{A.43}
\end{aligned}$$

As the result, the second term of Eq. (A.42) vanishes

$$E_{\text{SE}}^l(m', q') C_{m', m''}(q', q'') = \sum_m \int dq \varepsilon_m^l(q) C_{m', m}(q', q) \delta_{m'', m} \delta(q'' - q) \tag{A.44}$$

Performing the summation we get

$$E_{\text{SE}}^l(m', q') C_{m', m''}(q', q'') = \varepsilon_{m''}^l(q'') C_{m', m''}(q', q''). \tag{A.45}$$

If we considered $C_{m', m''}(q', q'') = \delta_{m', m''} \delta(q' - q'')$ then we obtain

$$E_{\text{SE}}^l(m', q') = \varepsilon_{m'}^l(q'). \tag{A.46}$$

The Eq. (A.46) shows that the third term of the Hamiltonian presented in Eq. (2.9) does not influence the eigenvalues.

B. Many-Body Hamiltonian

Further derivation of the MB Hamiltonian of the system coupled to a photon cavity is demonstrated in this appendix.

B.1. Electron-photon coupling function

We first show the constant of the coupling function shown in Eq. (2.52). If we substitute the vector potential into the paramagnetic Hamiltonian shown in Eq. (2.50), then the constant of the Hamiltonian becomes

$$\frac{g_{ph}}{m^* \times \Omega_w a_w}$$

but $a_w^2 = \frac{\hbar}{m^* \Omega_w}$, so one can write $\frac{1}{m^* \Omega_w a_w} = \frac{a_w}{\hbar}$. The constant is thus given by

$$\frac{g_{ph}}{m^* \times \Omega_w a_w} = \frac{g_{ph} a_w}{\hbar}.$$

Then the coupling function describing the interaction between the electrons and the photons presented in Eq. (2.52) can be written as

$$g_{i,j} = \frac{a_w}{\hbar} g_{ph} \int dr \Psi_i^*(r) (\hat{\mathbf{e}} \cdot \boldsymbol{\pi}) \Psi_j(r) = \frac{a_w}{\hbar} g_{ph} \times \langle \Psi_i | \hat{\mathbf{e}} \cdot \boldsymbol{\pi} | \Psi_j \rangle. \quad (\text{B.1})$$

We assume $\hat{\mathbf{e}} = \hat{\mathbf{e}}_x + \hat{\mathbf{e}}_y$ and $\hat{\pi} = \hat{\pi}_x + \hat{\pi}_y$, where $\hat{\pi}_x = p_x + eA_x = -i\hbar\partial_x - eBy$ and $\hat{\pi}_y = p_y + eA_y = -i\hbar\partial_y$ to get

$$g_{i,j} = \frac{a_w}{\hbar} g_{ph} \times \langle \Psi_i | (e_x(-i\hbar\partial_x - eBy) + e_y(-i\hbar\partial_y)) | \Psi_j \rangle. \quad (\text{B.2})$$

Further modifying Eq. (B.2)

$$g_{i,j} = g_{ph} \times \left[e_x(-ia_w) \times \langle \Psi_i | \partial_x | \Psi_j \rangle - e_x\left(\frac{eBa_w}{\hbar}\right) \times \langle \Psi_i | y | \Psi_j \rangle - ie_y \times \langle \Psi_i | a_w \partial_y | \Psi_j \rangle \right] \quad (\text{B.3})$$

The constant of the second term eBa_w/\hbar needs to be scaled. The effective magnetic length is $a_w = \hbar/(m\Omega_w a_w)$, and $eB/m = \omega_c$, then one can write the constant of the

B. Many-Body Hamiltonian

second term of Eq. (B.3) as $eBa_w/\hbar = \omega_c/\Omega_w a_w$. We further rearrange Eq. (B.3), and multiplying the first term by $\frac{L_x}{L_x}$

$$g_{i,j} = g_{\text{ph}} \times \left[-ie_x \left(\frac{a_w}{L_x} \right) \times \langle \Psi_i | L_x \partial_x | \Psi_j \rangle - ie_y \times \langle \Psi_i | a_w \partial_y | \Psi_j \rangle - e_x \left(\frac{\omega_c}{\Omega_w} \right) \times \langle \Psi_i | \frac{y}{a_w} | \Psi_j \rangle \right]. \quad (\text{B.4})$$

For sake of consistency, we use Dirac notation for the single-electron eigenstate basis $|n, m\rangle$ to calculate the matrix elements in Eq. (B.4)

$$g_{i,j} = g_{\text{ph}} \times \left[-ie_x \left(\frac{a_w}{L_x} \right) \times \langle n' | L_x \partial_x | n \rangle \delta_{m',m} - ie_y \times \langle m' | a_w \partial_y | m \rangle \delta_{n',n} - e_x \left(\frac{\omega_c}{\Omega_w} \right) \times \langle m' | \frac{y}{a_w} | m \rangle \delta_{n',n} \right]. \quad (\text{B.5})$$

The matrix elements of the first and the last terms are calculated in A.1.1, we do not repeat it here. And the matrix elements of the second term are

$$\begin{aligned} \langle m' | a_w \partial_y | m \rangle &= \langle m' | \left(\sqrt{\frac{m}{2}} |m-1\rangle - \sqrt{\frac{m+1}{2}} |m+1\rangle \right) \\ &= \sqrt{\frac{m}{2}} \delta_{m',m-1} - \sqrt{\frac{m+1}{2}} \delta_{m',m+1}. \end{aligned} \quad (\text{B.6})$$

Adding the matrix elements of all three terms of Eq. (B.5) together

$$\begin{aligned} g_{i,j} &= g_{\text{ph}} \times \left[-ie_x \left(\frac{a_w}{L_x} \right) \times \delta_{m',m} - ie_y \times \left(-\sqrt{\frac{m+1}{2}} \delta_{m',m+1} + \sqrt{\frac{m}{2}} \delta_{m',m-1} \right) \times \delta_{n',n} \right. \\ &\quad \left. - e_x \left(\frac{\omega_c}{\Omega_w} \right) \times \left(\sqrt{\frac{m+1}{2}} \delta_{m',m+1} + \sqrt{\frac{m}{2}} \delta_{m',m-1} \right) \times \delta_{n',n} \right]. \end{aligned} \quad (\text{B.7})$$

B.2. \mathbf{A}^2 - term

We show how Eq. (2.54) is obtained from Eq. (2.53). The diamagnetic Hamiltonian shown in Eq. (2.53) is

$$\hat{H}_D = \frac{e^2}{2m^*} \mathbf{A}_{\text{EM}}^2 \sum_{i,j} \langle \Psi_i | \Psi_j \rangle d_i^\dagger d_j, \quad (\text{B.8})$$

using the completeness relation $\sum_j |\Psi_j\rangle \langle \Psi_j| = 1$ and the electron number operator $\hat{N}_e = \sum_i d_i^\dagger d_i$

$$\hat{H}_D = \frac{e^2}{2m^*} \times \mathbf{A}_{\text{EM}}^2 \times \hat{N}_e. \quad (\text{B.9})$$

The vector potential defining in Eq. (2.44) is put into Eq. (B.9) to obtain

$$\hat{H}_D = \frac{e^2}{2m^*} \times \frac{g_{\text{ph}}^2}{e^2 \Omega_w^2 a_w^2} (a + a^\dagger)(a + a^\dagger) \times \hat{N}_e, \quad (\text{B.10})$$

and using $m^* a_w^2 \Omega_w = \hbar$

$$\hat{H}_D = \frac{g_{\text{ph}}^2}{2\hbar \Omega_w} (a + a^\dagger)(a + a^\dagger) \times \hat{N}_e. \quad (\text{B.11})$$

We perform the multiplication of creation and annihilation operators

$$\begin{aligned} \frac{1}{2}(a + a^\dagger)(a + a^\dagger) &= \frac{1}{2}(aa + aa^\dagger + a^\dagger a + a^\dagger a^\dagger) \\ &= \frac{1}{2}(aa^\dagger + a^\dagger a) + \frac{1}{2}(aa + a^\dagger a^\dagger). \end{aligned} \quad (\text{B.12})$$

In addition, the creation and annihilation operators satisfy commutation relation $[a, a^\dagger] = 1 \implies aa^\dagger - a^\dagger a = 1 \implies aa^\dagger = 1 + a^\dagger a$. Then Eq. (B.12) becomes

$$\begin{aligned} \frac{1}{2}(a + a^\dagger)(a + a^\dagger) &= \frac{1}{2}(1 + a^\dagger a + a^\dagger a) + \frac{1}{2}(aa + a^\dagger a^\dagger) \\ &= \frac{1}{2}(2a^\dagger a + 1) + \frac{1}{2}(aa + a^\dagger a^\dagger) \\ &= (a^\dagger a + \frac{1}{2}) + \frac{1}{2}(a^\dagger a^\dagger + aa). \end{aligned} \quad (\text{B.13})$$

Substituting Eq. (B.13) into Eq. (B.11), the final form of the Diamagnetic term of the Hamiltonian is

$$\hat{H}_D = \frac{g_{\text{ph}}^2}{\hbar \Omega_w} \left((a^\dagger a + \frac{1}{2}) + \frac{1}{2}(a^\dagger a^\dagger + aa) \right) \times \hat{N}_e. \quad (\text{B.14})$$

The Eq. (B.14) corresponds to the Eq. (2.54).

C. Charge current density

We calculate the matrix elements of the charge current density demonstrated in Eq. (4.10). The matrix elements are then used to find expectation value of the charge current density in Eq. (4.9). The matrix elements of the charge current density in the SES-basis can be expressed by

$$\begin{aligned} \langle m' | \hat{\mathbf{j}}(\mathbf{r}) | m \rangle = & \sum_{ij} \left(\frac{e\hbar}{2m^*i} \left[\Psi_i^*(\mathbf{r})(\nabla\Psi_j(\mathbf{r})) - (\nabla\Psi_i^*(\mathbf{r}))\Psi_j(\mathbf{r}) \right] \right. \\ & \left. + \frac{e^2}{m^*} \left[\mathbf{A}_{\text{ext}}(\mathbf{r}) + \mathbf{A}_{\text{ph}}(\mathbf{r}) \right] \Psi_i^*(\mathbf{r})\Psi_j(\mathbf{r}) \right) \langle m' | d_i^\dagger d_j | m \rangle. \end{aligned} \quad (\text{C.1})$$

In order to write the matrix elements of the charge current density in MES-basis, we need a unitary transformation ($\mathcal{V}_{\mu'\mu}$) shown in Eq. (2.36) to convert the current density from the SES-basis to the interacting MES-basis

$$\begin{aligned} (\mu' | \hat{\mathbf{j}}(\mathbf{r}) | \mu) = & \sum_{ij} \left(\frac{e\hbar}{2m^*i} \left[\Psi_i^*(\mathbf{r})(\nabla\Psi_j(\mathbf{r})) - (\nabla\Psi_i^*(\mathbf{r}))\Psi_j(\mathbf{r}) \right] \right. \\ & \left. + \frac{e^2}{m^*} \left[\mathbf{A}_{\text{ext}}(\mathbf{r}) + \mathbf{A}_{\text{ph}}(\mathbf{r}) \right] \Psi_i^*(\mathbf{r})\Psi_j(\mathbf{r}) \right) \times \sum_{m'm} \mathcal{V}_{\mu'm'}^\dagger \langle m' | d_i^\dagger d_j | m \rangle \mathcal{V}_{m\mu}. \end{aligned} \quad (\text{C.2})$$

In the closed electron-photon interacting system, the MB-space $\{|\check{\mu}\rangle\}$ is constructed from the tensor product of the electron-electron interacting many-electron (ME) state basis $|\mu\rangle$ and the eigenstates $|M\rangle$ of the photon number operator $a^\dagger a$, namely $|\check{\mu}\rangle = |\mu\rangle \otimes |M\rangle$. Therefore, the matrix elements of the charge current density in the

C. Charge current density

MB-basis are

$$\begin{aligned}
(\check{\mu}'|\hat{\mathbf{j}}(\mathbf{r})|\check{\mu}) &= \sum_{ij} \sum_{M'M} W_{\mu'\check{\mu}}^\dagger \left(\frac{e\hbar}{2m^*i} \left[\Psi_i^*(\mathbf{r})(\nabla\Psi_j(\mathbf{r})) - (\nabla\Psi_i^*(\mathbf{r}))\Psi_j(\mathbf{r}) \right] \langle M'|M \rangle \right. \\
&\quad \left. + \frac{e^2}{m^*} \left[\langle M'|(\mathbf{A}_{\text{ext}}(\mathbf{r}) + \mathbf{A}_{\text{ph}}(\mathbf{r}))|M \rangle \right] \Psi_i^*(\mathbf{r})\Psi_j(\mathbf{r}) \right) \\
&\quad \times \sum_{m'm} \mathcal{V}_{\mu'm'}^\dagger \langle m'|d_i^\dagger d_j|m \rangle \mathcal{V}_{m\mu} W_{\check{\mu}\mu},
\end{aligned} \tag{C.3}$$

where $W_{\check{\mu}\mu}$ is the unitary transformation in the MB-basis demonstrated in Eq. (2.65).

We substitute the magnetic vector potential $\mathbf{A}_{\text{ext}}(\mathbf{r})$ and the photon vector potential shown in Eq. (2.44) into Eq. (C.3) and separate x - and y -component of the charge current density. Then the x -component is written as

$$\begin{aligned}
(\check{\mu}'|\hat{j}_x(\mathbf{r})|\check{\mu}) &= \sum_{ij} \sum_{M'M} W_{\mu'\check{\mu}}^\dagger \left(\frac{e\hbar}{2m^*i} \left[\Psi_i^*(\mathbf{r})(\partial_x\Psi_j(\mathbf{r})) - (\partial_x\Psi_i^*(\mathbf{r}))\Psi_j(\mathbf{r}) \right] \langle M'|M \rangle \right. \\
&\quad \left. + \frac{e^2}{m^*} \left[-By\langle M'|M \rangle + e_x A_{\text{ph}} \langle M'| (a^\dagger + a) |M \rangle \right] \Psi_i^*(\mathbf{r})\Psi_j(\mathbf{r}) \right) \\
&\quad \times \sum_{m'm} V_{\mu'm'}^\dagger \langle m'|d_i^\dagger d_j|m \rangle V_{m\mu} W_{\check{\mu}\mu'},
\end{aligned} \tag{C.4}$$

and the y -component is

$$\begin{aligned}
(\check{\mu}'|\hat{j}_y(\mathbf{r})|\check{\mu}) &= \sum_{ij} \sum_{M'M} W_{\mu'\check{\mu}}^\dagger \left(\frac{e\hbar}{2m^*i} \left[\Psi_i^*(\mathbf{r})(\partial_y\Psi_j(\mathbf{r})) - (\partial_y\Psi_i^*(\mathbf{r}))\Psi_j(\mathbf{r}) \right] \langle M'|M \rangle \right. \\
&\quad \left. + \frac{e^2}{m^*} e_y A_{\text{ph}} \langle M'| (a^\dagger + a) |M \rangle \Psi_i^*(\mathbf{r})\Psi_j(\mathbf{r}) \right) \\
&\quad \times \sum_{m'm} V_{\mu'm'}^\dagger \langle m'|d_i^\dagger d_j|m \rangle V_{m\mu} W_{\check{\mu}\mu'}.
\end{aligned} \tag{C.5}$$

Using the photon creation and annihilation operators properties

$$a^\dagger |n\rangle = \sqrt{n+1} |n+1\rangle,$$

and

$$a |n\rangle = \sqrt{n} |n-1\rangle,$$

where n is the photon number. Then the x -component of the charge current density

is modified to

$$\begin{aligned}
(\check{\mu}'|\hat{j}_x(\mathbf{r})|\check{\mu}) &= \sum_{ij} \sum_{M'M} W_{\mu\check{\mu}'}^\dagger \left(\frac{e\hbar}{2m^*i} \left[\Psi_i^*(\mathbf{r})(\partial_x \Psi_j(\mathbf{r})) - (\partial_x \Psi_i^*(\mathbf{r}))\Psi_j(\mathbf{r}) \right] \delta_{M',M} \right. \\
&\quad \left. + \frac{e^2}{m^*} \left[-By\delta_{M',M} + e_x A_{\text{ph}}(\sqrt{M+1}\delta_{M',M+1} + \sqrt{M}\delta_{M',M-1}) \right] \Psi_i^*(\mathbf{r})\Psi_j(\mathbf{r}) \right) \\
&\quad \times \sum_{m'm} V_{\mu'm'}^\dagger \langle m'|d_i^\dagger d_j|m\rangle V_{m\mu} W_{\check{\mu}\mu'},
\end{aligned} \tag{C.6}$$

and the y -component becomes

$$\begin{aligned}
(\check{\mu}'|\hat{j}_y(\mathbf{r})|\check{\mu}) &= \sum_{ab} \sum_{M'M} W_{\mu\check{\mu}'}^\dagger \left(\frac{e\hbar}{2m^*i} \left[\Psi_i^*(\mathbf{r})(\partial_y \Psi_j(\mathbf{r})) - (\partial_y \Psi_i^*(\mathbf{r}))\Psi_j(\mathbf{r}) \right] \delta_{MN} \right. \\
&\quad \left. + \frac{e^2}{m^*} e_y A_{\text{ph}} [\sqrt{M+1}\delta_{M',M+1} + \sqrt{M}\delta_{M',M-1}] \Psi_i^*(\mathbf{r})\Psi_j(\mathbf{r}) \right) \\
&\quad \times \sum_{m'm} V_{\mu'm'}^\dagger \langle m'|d_i^\dagger d_j|m\rangle V_{m\mu} W_{\check{\mu}\mu'}.
\end{aligned} \tag{C.7}$$

Further rearranging of both components, one can write

$$\begin{aligned}
(\check{\mu}'|\hat{j}_x(\mathbf{r})|\check{\mu}) &= \sum_{ij} \left(\left[\frac{e\hbar}{2m^*i} \left[\Psi_i^*(\mathbf{r})(\partial_x \Psi_j(\mathbf{r})) - (\partial_x \Psi_i^*(\mathbf{r}))\Psi_j(\mathbf{r}) \right] - \frac{eB}{m^*} y \Psi_i^*(\mathbf{r})\Psi_j(\mathbf{r}) \right] \right. \\
&\quad \times \sum_{M'M} \left(W_{\mu\check{\mu}'}^\dagger \delta_{M',M} \sum_{m'm} V_{\mu'm'}^\dagger \langle m'|d_i^\dagger d_j|m\rangle V_{m\mu} W_{\check{\mu}\mu'} \right) \\
&\quad + \sum_{ij} \left(\sum_{M'M} \left[W_{\mu\check{\mu}'}^\dagger \left(\frac{e^2 A_{\text{ph}}}{m^*} \right) e_x (\sqrt{M+1}\delta_{M',M+1} + \sqrt{M}\delta_{M',M-1}) \right. \right. \\
&\quad \left. \left. \times \sum_{m'm} V_{\mu'm'}^\dagger \langle m'|d_i^\dagger d_j|m\rangle V_{m\mu} W_{\check{\mu}\mu'} \right] \Psi_i^*(\mathbf{r})\Psi_j(\mathbf{r}) \right),
\end{aligned} \tag{C.8}$$

C. Charge current density

and

$$\begin{aligned}
(\check{\mu}'|\hat{j}_y(\mathbf{r})|\check{\mu}) &= \sum_{ij} \left(\frac{e\hbar}{2m^*i} \left[\Psi_i^*(\mathbf{r})(\partial_y \Psi_j(\mathbf{r})) - (\partial_y \Psi_i^*(\mathbf{r}))\Psi_j(\mathbf{r}) \right] \right. \\
&\quad \times \sum_{M'M} \left(W_{\mu\check{\mu}'}^\dagger \delta_{M',M} \sum_{m'm} V_{\mu'm'}^\dagger \langle m'|d_i^\dagger d_j|m\rangle V_{m\mu} W_{\check{\mu}\mu'} \right) \Bigg) \\
&\quad + \sum_{ij} \left(\sum_{M'M} \left[W_{\mu\check{\mu}'}^\dagger \left(\frac{e^2 A_{\text{ph}}}{m^*} \right) e_y (\sqrt{M+1} \delta_{M',M+1} + \sqrt{M} \delta_{M',M-1}) \right. \right. \\
&\quad \left. \left. \times \sum_{m'm} V_{\mu'm'}^\dagger \langle m'|d_i^\dagger d_j|m\rangle V_{m\mu} W_{\check{\mu}\mu'} \right] \Psi_i^*(\mathbf{r})\Psi_j(\mathbf{r}) \right). \tag{C.9}
\end{aligned}$$

We should mention that the eigenvalue M is the photon number N_{ph} in both components of the charge current density.

D. Quantum Master equation

In this appendix we show the general properties of the projection operator and few steps of the derivation of non-Markovian master equation in the MB-basis.

D.1. Properties of Projection operator

We write some characteristics of the projection operator \mathcal{P} and the complementary projection operator \mathcal{Q} . We begin with the projection operator which has the following properties

1. $\mathcal{P}^2 = \mathcal{P}$
2. $\mathcal{P}\mathcal{L}_S = \mathcal{L}_S\mathcal{P}$
3. $\mathcal{L}_I\mathcal{P} = 0$
4. $\mathcal{P}\mathcal{L}_I\mathcal{P} = 0$
5. $\mathcal{P}\mathcal{L}\mathcal{P} = \mathcal{L}_S\mathcal{P} + \mathcal{L}_I\mathcal{P} + \mathcal{L}_T\mathcal{P} = \mathcal{L}_S\mathcal{P}$
6. $\mathcal{P}\mathcal{L}_T\mathcal{P} = 0$

and the complementary projection operator properties are

1. $\mathcal{Q}\mathcal{L}\mathcal{Q} = (\mathcal{L}_S + \mathcal{L}_I + \mathcal{Q}\mathcal{L}_T)\mathcal{Q}$
2. $\mathcal{P}\mathcal{L}\mathcal{Q} = \mathcal{P}\mathcal{L}_S\mathcal{Q} + \mathcal{P}\mathcal{L}_I\mathcal{Q} + \mathcal{P}\mathcal{L}_T\mathcal{Q} = \mathcal{P}\mathcal{L}_T\mathcal{Q}$
3. $\mathcal{P}\mathcal{L}_I\mathcal{Q} = 0$
4. $\mathcal{Q}\mathcal{L}\mathcal{P} = \mathcal{Q}\mathcal{L}_S\mathcal{P} + \mathcal{Q}\mathcal{L}_I\mathcal{P} + \mathcal{Q}\mathcal{L}_T\mathcal{P} = \mathcal{L}_T\mathcal{P}$

D. Quantum Master equation

In addition, in the case of weak coupling between the central system and the leads $Q\mathcal{L}_T \ll \mathcal{L}_S$ or \mathcal{L}_l .

D.2. Derivation of Eq. (3.24)

Now, we show further steps of the derivation of the general master equation and demonstrate how the Eq. (3.24) can be obtained from Eq. (3.22). Since the Hamiltonian of the central system commutes with the lead Hamiltonian, the evolution operator can be separable

$$U_0(t - t') = U_S(t - t')U_L(t - t') \quad (\text{D.1})$$

where $U_S(t - t') = \exp(-\frac{i}{\hbar}\hat{H}_S(t - t'))$ and $U_L(t - t') = \exp(-\frac{i}{\hbar}\hat{H}_l(t - t'))$. Using the identity of the creation and annihilation operators of the leads

$$\tilde{c}_{\mathbf{q}}(t) = e^{\frac{i}{\hbar}\hat{H}_l t} c_{\mathbf{q}} e^{(-\frac{i}{\hbar}\hat{H}_l t)} = e^{(-\frac{i}{\hbar}E_{SE}^l(\mathbf{q})t)}, \quad (\text{D.2})$$

and the property

$$\text{Tr}_l(\tilde{c}_{\mathbf{q}}(t)\tilde{c}_{\mathbf{q}'}(t)\rho_l) = 0. \quad (\text{D.3})$$

allow us to write the integral kernel of Eq. (3.22) including the transfer Hamiltonian in the MES basis in the following form

$$\begin{aligned} \int_{t_0}^t dt' \mathcal{K}(t, t') \check{\rho}_S(t') &= -\frac{\chi^l(t)}{\hbar^2} \int_{t_0}^t dt' \chi^l(t') \int d\mathbf{q} d\mathbf{q}' \\ &\times \left[\mathcal{T}^l(\mathbf{q}) \hat{U}_S(t - t') (\mathcal{T}^l(\mathbf{q}'))^\dagger \check{\rho}_S(t') \hat{U}_S^\dagger(t - t') \text{Tr}_l(\tilde{c}_{\mathbf{q}'}^\dagger(t') \tilde{c}_{\mathbf{q}}(t) \rho_l) \right. \\ &+ (\mathcal{T}^l(\mathbf{q}'))^\dagger \hat{U}_S(t - t') \mathcal{T}^l(\mathbf{q}) \check{\rho}_S(t') \hat{U}_S^\dagger(t - t') \text{Tr}_l(\tilde{c}_{\mathbf{q}'}(t') \tilde{c}_{\mathbf{q}}^\dagger(t) \rho_l) \\ &- \hat{U}_S(t - t') (\mathcal{T}^l(\mathbf{q}'))^\dagger \check{\rho}_S(t') \hat{U}_S^\dagger(t - t') \mathcal{T}^l(\mathbf{q}) \text{Tr}_l(\tilde{c}_{\mathbf{q}}(t) \tilde{c}_{\mathbf{q}'}^\dagger(t') \rho_l) \\ &- \hat{U}_S(t - t') \mathcal{T}^l(\mathbf{q}) \check{\rho}_S(t') \hat{U}_S^\dagger(t - t') (\mathcal{T}^l(\mathbf{q}'))^\dagger \text{Tr}_l(\tilde{c}_{\mathbf{q}}^\dagger(t) \tilde{c}_{\mathbf{q}'}(t') \rho_l) \\ &- \mathcal{T}^l(\mathbf{q}) \hat{U}_S(t - t') \check{\rho}_S(t') (\mathcal{T}^l(\mathbf{q}'))^\dagger \hat{U}_S^\dagger(t - t') \text{Tr}_l(\tilde{c}_{\mathbf{q}'}^\dagger(t') \tilde{c}_{\mathbf{q}}(t) \rho_l) \\ &- (\mathcal{T}^l(\mathbf{q}'))^\dagger \hat{U}_S(t - t') \check{\rho}_S(t') \mathcal{T}^l(\mathbf{q}) \hat{U}_S^\dagger(t - t') \text{Tr}_l(\tilde{c}_{\mathbf{q}'}(t') \tilde{c}_{\mathbf{q}}^\dagger(t) \rho_l) \\ &+ \hat{U}_S(t - t') \check{\rho}_S(t') (\mathcal{T}^l(\mathbf{q}'))^\dagger \hat{U}_S^\dagger(t - t') \mathcal{T}^l(\mathbf{q}) \text{Tr}_l(\tilde{c}_{\mathbf{q}}(t) \tilde{c}_{\mathbf{q}'}^\dagger(t') \rho_l) \\ &\left. + \hat{U}_S(t - t') \check{\rho}_S(t') \mathcal{T}^l(\mathbf{q}) \hat{U}_S^\dagger(t - t') (\mathcal{T}^l(\mathbf{q}'))^\dagger \text{Tr}_l(\tilde{c}_{\mathbf{q}}^\dagger(t) \tilde{c}_{\mathbf{q}'}(t') \rho_l) \right]. \quad (\text{D.4}) \end{aligned}$$

We conclude some properties of the trace of the leads

$$\text{Tr}_l(\tilde{c}_{\mathbf{q}}(t) \tilde{c}_{\mathbf{q}'}^\dagger(t) \hat{\rho}_l) = e^{(-i(t-t')E_{SE}^l(\mathbf{q}))} \delta(\mathbf{q} - \mathbf{q}') (1 - f(E_{SE}^l(\mathbf{q}))), \quad (\text{D.5})$$

$$\text{Tr}_l \left(\tilde{c}_{\mathbf{q}'}^\dagger(t) \tilde{c}_{\mathbf{q}}(t) \hat{\rho}_l \right) = e^{(i(t-t')E_{\text{SE}}^l(\mathbf{q}))} \delta(\mathbf{q} - \mathbf{q}') \left(f(E_{\text{SE}}^l(\mathbf{q})) \right), \quad (\text{D.6})$$

and using Eq. (D.5) and Eq. (D.6). Then we take the integral $\int d\mathbf{q}' \delta(\mathbf{q} - \mathbf{q}')$ in order to modifying Eq. (D.4) into

$$\begin{aligned} \int_{t_0}^t dt' \mathcal{K}(t, t') \check{\rho}_S(t') &= -\frac{\chi^l(t)}{\hbar^2} \int_{t_0}^t dt' \chi^l(t') \int d\mathbf{q} \\ &\times \left[\mathcal{T}^l(\mathbf{q}) \hat{U}_S(t-t') (\mathcal{T}^l(\mathbf{q}'))^\dagger \check{\rho}_S(t') \hat{U}_S^\dagger(t-t') [1 - f(E_{\text{SE}}^l(\mathbf{q}))] \right. \\ &\times e^{(-i(t-t')E_{\text{SE}}^l(\mathbf{q}))} \\ &- \mathcal{T}^l(\mathbf{q}) \hat{U}_S(t-t') \check{\rho}_S(t') (\mathcal{T}^l(\mathbf{q}'))^\dagger \hat{U}_S^\dagger(t-t') f(E_{\text{SE}}^l(\mathbf{q})) \\ &\times e^{(-i(t-t')E_{\text{SE}}^l(\mathbf{q}))} \\ &- \hat{U}_S(t-t') (\mathcal{T}^l(\mathbf{q}'))^\dagger \check{\rho}_S(t') \hat{U}_S^\dagger(t-t') \mathcal{T}^l(\mathbf{q}) [1 - f(E_{\text{SE}}^l(\mathbf{q}))] \\ &\times e^{(-i(t-t')E_{\text{SE}}^l(\mathbf{q}))} \\ &+ \hat{U}_S(t-t') \check{\rho}_S(t') (\mathcal{T}^l(\mathbf{q}'))^\dagger \hat{U}_S^\dagger(t-t') \mathcal{T}^l(\mathbf{q}) f(E_{\text{SE}}^l(\mathbf{q})) \\ &\times e^{(-i(t-t')E_{\text{SE}}^l(\mathbf{q}))} \\ &+ \hat{U}_S(t-t') \check{\rho}_S(t') \mathcal{T}^l(\mathbf{q}) \hat{U}_S^\dagger(t-t') (\mathcal{T}^l(\mathbf{q}'))^\dagger [1 - f(E_{\text{SE}}^l(\mathbf{q}))] \\ &\times e^{(i(t-t')E_{\text{SE}}^l(\mathbf{q}))} \\ &- \hat{U}_S(t-t') \mathcal{T}^l(\mathbf{q}) \check{\rho}_S(t') \hat{U}_S^\dagger(t-t') (\mathcal{T}^l(\mathbf{q}'))^\dagger f(E_{\text{SE}}^l(\mathbf{q})) \\ &\times e^{(i(t-t')E_{\text{SE}}^l(\mathbf{q}))} \\ &- (\mathcal{T}^l(\mathbf{q}'))^\dagger \hat{U}_S(t-t') \check{\rho}_S(t') \mathcal{T}^l(\mathbf{q}) \hat{U}_S^\dagger(t-t') [1 - f(E_{\text{SE}}^l(\mathbf{q}))] \\ &\times e^{(i(t-t')E_{\text{SE}}^l(\mathbf{q}))} \\ &+ (\mathcal{T}^l(\mathbf{q}'))^\dagger \hat{U}_S(t-t') \check{\rho}_S(t') \mathcal{T}^l(\mathbf{q}) \hat{U}_S^\dagger(t-t') f(E_{\text{SE}}^l(\mathbf{q})) \\ &\times e^{(i(t-t')E_{\text{SE}}^l(\mathbf{q}))} \left. \right]. \quad (\text{D.7}) \end{aligned}$$

Rearranging Eq. (D.7), we obtain Eq. (3.24).

Bibliography

- [1] J. M. Elzerman, R. Hanson, L.H.W. van Beveren, S. Tarucha, L.M.K. Vandersypen, and L. P. Kouwenhoven. Semiconductor few-electron quantum dots as spin qubits. *Lecture Notes in Physics*, 667:25–95, 2005.
- [2] K. Tomioka, J. Motohisa, S. Hara, K. Hiruma, and T. Fukui. GaAs/AlGaAs core multishell nanowire-based light-emitting diodes on Si. *Nano Lett.*, 10:1639–1644, 2010.
- [3] A. M. See, O. Klochan, A. R. Hamilton, A. P. Micolich, M. Aagesen, and P. E. Lindelof. AlGaAs/GaAs single electron transistor fabricated without modulation doping. *Appl. Phys. Lett.*, 96:112104, 2010.
- [4] R. C. Ashoori. Electrons in artificial atoms. *Nature*, 379:413, 1996.
- [5] M. Larsson. *Electron transport in quantum dots defined in low-dimensional semiconductor structures*. PhD thesis, Physics Department, Lund University, Lund, Sweden 2011.
- [6] Marian Niță, D. C. Marinescu, Andrei Manolescu, and Vidar Gudmundsson. Nonadiabatic generation of a pure spin current in a one-dimensional quantum ring with spin-orbit interaction. *Phys. Rev. B*, 83:155427, Apr 2011.
- [7] Kristinn Torfason, Chi-Shung Tang, and Vidar Gudmundsson. Coherent magnetotransport and time-dependent transport through split-gated quantum constrictions. *Phys. Rev. B*, 80:195322, Nov 2009.
- [8] Vidar Gudmundsson and Chi-Shung Tang. Magnetotransport in a double quantum wire: Modeling using a scattering formalism built on the Lippmann-Schwinger equation. *Phys. Rev. B*, 74:125302, Sep 2006.
- [9] W. G. van der Wiel, S. De Franceschi, J. M. Elzerman, T. Fujisawa, S. Tarucham, and L. P. Kouwenhoven. Electron transport through double quantum dots. *Reviews of modern physics*, 75(1), 1 2003.
- [10] Yun-Sok Shin, Toshiaki Obata, Yasuhiro Tokura, Michel Pioro-Ladrière, Roland Brunner, Toshihiro Kubo, Katsuharu Yoshida, and Seigo Tarucha. Single-Spin Readout in a Double Quantum Dot Including a Micromagnet. *Phys. Rev. Lett.*, 104:046802, Jan 2010.

BIBLIOGRAPHY

- [11] L. W. Molenkamp, H. van Houten, and A. A. M. Staring. Quantum effects in thermal and thermo-electric transport in Semiconductor nanostructures. *Physica Scripta*, 49:441–445, 1993.
- [12] P. Bordone, M. Pascoli, R. Brunetti, A. Bertoni, C. Jacoboni, and A. Abramo. Quantum transport of electrons in open nanostructures with the Wigner-function formalism. *Phys. Rev. B*, 59:3060–3069, Jan 1999.
- [13] S. Datta. *Electronic Transport in Mesoscopic system*. Cambridge University Press, Cambridge, 1995.
- [14] Tomas Orn Rosdahl, Andrei Manolescu, and Vidar Gudmundsson. Spin and impurity effects on flux-periodic oscillations in core-shell nanowires. *Phys. Rev. B*, 90:035421, Jul 2014.
- [15] Valeriu Moldoveanu, Vidar Gudmundsson, and Andrei Manolescu. Transient regime in nonlinear transport through many-level quantum dots. *Phys. Rev. B*, 76:085330, Aug 2007.
- [16] P Lambropoulos, G M Nikolopoulos, T R Nielsen, and S Bay. Fundamental quantum optics in structured reservoirs. *Rep. Prog. Phys.*, 63:455, 2000.
- [17] Massimiliano Esposito and Shaul Mukamel. Fluctuation theorems for quantum master equations. *Phys. Rev. E*, 73:046129, Apr 2006.
- [18] Gavin E. Crooks. Quantum operation time reversal. *Phys. Rev. A*, 77:034101, Mar 2008.
- [19] JunYan Luo, Xin-Qi Li, and YiJing Yan. Calculation of the current noise spectrum in mesoscopic transport: A quantum master equation approach. *Phys. Rev. B*, 76:085325, Aug 2007.
- [20] Sven Welack, Massimiliano Esposito, Upendra Harbola, and Shaul Mukamel. Interference effects in the counting statistics of electron transfers through a double quantum dot. *Phys. Rev. B*, 77:195315, May 2008.
- [21] J. Rammer, A. L. Shelankov, and J. Wabnig. Quantum measurement in charge representation. *Phys. Rev. B*, 70:115327, Sep 2004.
- [22] N G Van Kampen. *Stochastic Processes in Physics and Chemistry*, volume 2nd Ed. North-Holland, Amsterdam, 2001.
- [23] Upendra Harbola, Massimiliano Esposito, and Shaul Mukamel. Quantum master equation for electron transport through quantum dots and single molecules. *Phys. Rev. B*, 74:235309, Dec 2006.
- [24] S. A. Gurvitz and Ya. S. Prager. Microscopic derivation of rate equations for quantum transport. *Phys. Rev. B*, 53:15932–15943, Jun 1996.

- [25] Alessandro Braggio, Jürgen König, and Rosario Fazio. Full Counting Statistics in Strongly Interacting Systems: Non-Markovian Effects. *Phys. Rev. Lett.*, 96:026805, Jan 2006.
- [26] C. Emary, D. Marcos, R. Aguado, and T. Brandes. Frequency-dependent counting statistics in interacting nanoscale conductors. *Phys. Rev. B*, 76:161404, Oct 2007.
- [27] Adam Bednorz and Wolfgang Belzig. Formulation of Time-Resolved Counting Statistics Based on a Positive-Operator-Valued Measure. *Phys. Rev. Lett.*, 101:206803, Nov 2008.
- [28] V. Moldoveanu, A. Manolescu, and V. Gudmundsson. Geometrical effects and signal delay in time-dependent transport at the nanoscale. *New journal of physics*, 11:073019, 2009.
- [29] Valeriu Moldoveanu, Andrei Manolescu, Chi-Shung Tang, and Vidar Gudmundsson. Coulomb interaction and transient charging of excited states in open nanosystems. *Phys. Rev. B*, 81:155442, Apr 2010.
- [30] Eduardo Vaz and Jordan Kyriakidis. Transient dynamics of confined charges in quantum dots in the sequential tunneling regime. *Phys. Rev. B*, 81:085315, Feb 2010.
- [31] V Gudmundsson, C Gainar, C.-S. Tang, V Moldoveanu, and A Manolecu. Time-dependent transport via the generalized master equation through a finite quantum wire with an embedded subsystem. *New J. Phys.*, 11:113007, 2009.
- [32] G. Juska, V. Dimastrodonato, L. O. Mereni, T. H. Chung, A. Gocalinska, E. Pelucchi, B. Van Hattem, M. Ediger, and P. Corfdir. Complex optical signatures from quantum dot nanostructures and behavior in inverted pyramidal recesses. *Phys. Rev. B*, 89:205430, May 2014.
- [33] G. Wailfred, van der Wiel, T. Fujisawa, S. Tarucha, and L. P. Kouwenhoven. A double quantum dot as an artificial two-level system. *Jpn. J. Appl. Phys.*, 40:2100–2104, 2001.
- [34] Morten Holm Pedersen and Markus Büttiker. Scattering theory of photon-assisted electron transport. *Phys. Rev. B*, 58:12993–13006, Nov 1998.
- [35] A. Ramamoorthy, R. Akis, and Jonathan P. Bird. Influence of Realistic Potential Profile of Coupled Electron Waveguide on Electron Switching Characteristics. *IEEE Transaction on nanotechnology*, 5(6):712, 2006.
- [36] Y Nakamura, Yu A Pashkin, and J S Tsai. Coherent control of macroscopic quantum states in a single-Cooper-pair box. *Nature*, 398:786, 1999.

BIBLIOGRAPHY

- [37] J Villavicencio, I Moldonado, R Sanchez, E Cota, and G Platero. Tunnel spectroscopy in ac-driven quantum dot nanoresonators. *Appl. Phys. Lett.*, 92:192102, 2008.
- [38] M P van Kouwen, M H M van Weert, M E Reimer, N Akopian, U Perinetti, R E Algra, E P A M Bakkers, L P Kouwenhoven, and V Zwiller. Single quantum dot nanowire photodetectors. *Appl. Phys. Lett.*, 97:113108, 2010.
- [39] L. P. Kouwenhoven, S. Jauhar, K. McCormick, D. Dixon, P. L. McEuen, Yu. V. Nazarov, N. C. van der Vaart, and C. T. Foxon. Photon-assisted tunneling through a quantum dot. *Phys. Rev. B*, 50:2019–2022, Jul 1994.
- [40] T. H. Stoof and Yu. V. Nazarov. Time-dependent resonant tunneling via two discrete states. *Phys. Rev. B*, 53:1050–1053, Jan 1996.
- [41] Luis E. F. Foa Torres. Mono-parametric quantum charge pumping: Interplay between spatial interference and photon-assisted tunneling. *Phys. Rev. B*, 72:245339, Dec 2005.
- [42] K Ishibashi and Y Aoyagi. Interaction of electromagnetic wave with quantum dots. *Physica B*, 314:437–443, 2002.
- [43] Linda E. Reichl and Michael G. Snyder. Coulomb entangler and entanglement-testing network for waveguide qubits. *Phys. Rev. A*, 72:032330, Sep 2005.
- [44] N R Abdullah, C S Tang, A Manolescu, and V Gudmundsson. Electron transport through a quantum dot assisted by cavity photons. *Journal of Physics:Condensed Matter*, 25:465302, 2013.
- [45] C. A. Stafford and N. S. Wingreen. Resonant photon-assisted tunneling through a double quantum dot: An electron pump from spatial rabi oscillations. *Phys. Rev. Lett.*, 76(11):1916, 1996.
- [46] T. H. Stoof and Yu. V. Nazarov. Time-dependent resonant tunneling via two discrete states. *Phys. Rev. B*, 53(3):1050–1053, Jan 1996.
- [47] M Bagheri Tagani and H Rahimpour Soleimani. Photon-assisted thermoelectric effects in a two-level molecules. *Physica B: Condensed Matter*, 413:86:91, 2013.
- [48] Canran Xu and Maxim G. Vavilov. Quantum photovoltaic effect in double quantum dots. *Phys. Rev. B*, 87:035429, Jan 2013.
- [49] G. Muñoz Matutano, M. Royo, J. I. Climente, J. Canet-Ferrer, D. Fuster, P. Alonso-González, I. Fernández-Martínez, J. Martínez-Pastor, Y. González, L. González, F. Briones, and B. Alén. Charge control in laterally coupled double quantum dots. *Phys. Rev. B*, 84:041308, Jul 2011.

- [50] P Kaczmarkiewicz, P Machnikowski, and T Kuhn. Double qunatum dot in a quantum dash:Optical properties. *Journal of Applied Physics*, 114:183108, 2013.
- [51] Fabrício M. Souza, Thiago L. Carrara, and E. Vernek. Enhanced photon-assisted spin transport in a quantum dot attached to ferromagnetic leads. *Phys. Rev. B*, 84:115322, Sep 2011.
- [52] C. Niu and D. L. Lin. Electron population inversion in photon-assisted tunneling through a quantum wire. *Phys. Rev. B*, 56:R12752–R12755, Nov 1997.
- [53] Qing Hu. Photon-assisted quantum transport in quantum point contacts. *Appl. Phys. Lett.*, 62:837, 1993.
- [54] C. S. Tang and C. S. Chu. Coherent quantum transport in the presence of a finit-range transversely polarized time-dependent field. *Physica B*, 292:127–135, 2000.
- [55] J Wätzel, A S Moskalenko, and J Berakdar. Photon-induced spin filtering in a double quantum dot. *Appl. Phys. Lett.*, 99:192101, 2011.
- [56] R. Shang, H.-O. Li, G. Gao, M. Xiao, T. Tu, H. Jiang, G.-C. Guo, and G.-P. Guo. Photon-assisted-tunneling in a coupled double qunatum dot under high microwaves excitation powers. *Appl. Phys. Lett.*, 103:162109, 2013.
- [57] A. Imamoglu and Y. Yamamoto. Turnstile device for heralded single photons: Coulomb blockade of electron and hole tunneling in quantum confined $p - i - n$ heterojunctions. *Phys. Rev. Lett.*, 72:210–213, Jan 1994.
- [58] D. Loss and D. P. DiVincenzo. Quantum computation with qunatum dots. *Physical Review A*, 57(1):120, 1998.
- [59] D. P. DiVincenzo. Double quantum dot as a quantum bit. *Science*, 309, 2173 2005.
- [60] L. I. Chuang and M. A. Nielsen. *Quantum Computation and Quantum Information*. Cambridge University Press, 2010.
- [61] K. Shibata, A. Umeno, K. M. Cha, and K. Hirakawa. Photon-Assisted Tunneling through Self-Assembled InAs Quantum Dots in the Terahertz Frequency Range. *Phys. Rev. Lett.*, 109:077401, Aug 2012.
- [62] A Joshi, S S Hassan, and M Xiao. Photon-assisted tunneling current in a double quantum dot excitonic system. *Appl. Phys. A*, 102:537–544, 2011.
- [63] R. Ionicioiu, G. Amaratunga, and F. Udrea. Quantum Computation with Ballistic Electrons. *Int. J. of Mod. Phys. B*, 15:125, 2001.

BIBLIOGRAPHY

- [64] M. J. Gilbert, R. Akis, and D. K. Ferry. Magnetically and electrically tunable semiconductor quantum waveguide inverter. *Appl. Phys. Lett.*, 81:4284, 2002.
- [65] I. van Weperen, B. D. Armstrong, E. A. Laird, J. Medford, C. M. Marcus, M. P. Hanson, and A. C. Gossard. Charge-State Conditional Operation of a Spin Qubit. *Phys. Rev. Lett.*, 107:030506, Jul 2011.
- [66] P. Zhang, Ze-Liang Xiang, and Franco Nori. Spin-orbit qubit on a multiferroic insulator in a superconducting resonator. *Phys. Rev. B*, 89:115417, Mar 2014.
- [67] John M. Martinis, S. Nam, J. Aumentado, and C. Urbina. Rabi Oscillations in a Large Josephson-Junction Qubit. *Phys. Rev. Lett.*, 89:117901, Aug 2002.
- [68] Michael G. Snyder and Linda E. Reichl. Ballistic electron waveguide adder. *Phys. Rev. A*, 70:052330, Nov 2004.
- [69] A. Marchi, A. Bertoni, S. Reggiani, and M. Rudan. Investigation on Single-Electron Dynamics in Coupled GaAs-AlGaAs Quantum Wires. *IEEE Transaction on nanotechnology*, 3(1):129, 2003.
- [70] A. Bertoni, P. Bordone, R. Brunetti, C. Jacoboni, and S. Reggiani. Quantum Logic Gates based on Coherent Electron Transport in Quantum Wires. *Phys. Rev. Lett.*, 84:5912–5915, Jun 2000.
- [71] P. Pingue, V. Piazza, F. Beltram, I. Farrer, D. R. Ritchie, and M. Pepper. Coulomb blockade directional coupler. *Appl. Phys. Lett.*, 86:052102, 2005.
- [72] J. Harris, R. Akis, and D. K. Ferry. Magnetically switched quantum waveguide qubit. *Appl. Phys. Lett.*, 79:2214, 2001.
- [73] D. K. Ferry, R. Akis, and J. Harris. Quantum wave processing. *Superlattices and Microstructures*, 30(2), 2001.
- [74] P. Bordone, A. Bertoni, M. Rosini, and C. Jacoboni. Coherent transport in coupled quantum wires assisted by surface acoustic waves. *Semicond.Sci.Technol.*, 19:412–414, 2004.
- [75] E. Schrödinger. An Undulatory Theory of the Mechanics of Atoms and Molecules. *Phys. Rev.*, 28:1049–1070, Dec 1926.
- [76] P. Harrison. *Quantum Wells, Wires and Dots*. 3rd Edition, A John Wiley and Sons,Ltd, Publication, USA, 2009.
- [77] V. Gudmundsson and Rolf R. Gerhardts. The Hofstadter energy spectrum for an interacting 2DEG. *Surface Science*, 361/362:505–508, 1996.
- [78] C. Rossler, T. Feill, P. Mensch, T. Ihn, K. Ensslin, D. Schun, and Wegscheider W. Gating of high-mobility two-dimensional electron gases in GaAs/AlGaAs heterostructure. *New journal of physics*, 12:043007, 2010.

- [79] S. R. Hemley, N. Ostrowsky, and D. Ostrowsky. *Quantum Mechanics - Volume one*. Hermann and Wiley & Sons. Inc, France, Paris, France 1977.
- [80] S. R. Hemley, N. Ostrowsky, and D. Ostrowsky. *Quantum Mechanics - Volume two*. Hermann and Wiley & Sons. Inc, France, Paris, France 1977.
- [81] A. L Fetter and J. D. Walecka. *Quantum Theory of many-particle Systems*. McGraw-Hill, United States of America, 1971.
- [82] H. Bruus and K. Flensberg. *Introduction to Many-body quantum theory in condensed matter physics*. Oxford University Press, 2005.
- [83] Olafur Jonasson, Chi-Shung Tang, Hsi-Sheng Goan, Andrei Manolescu, and Vidar Gudmundsson. Nonperturbative approach to circuit quantum electrodynamics. *Phys. Rev. E*, 86:046701, Oct 2012.
- [84] O. Jonasson. Nonperturbative approach to circuit quantum electrodynamics, School of Engineering and Natural Science, University of Iceland, Reykjavik, 2012.
- [85] L. A. Thorsten. *The influences of cavity photons on the transient transport of correlated electrons through a quantum ring with magnetic field and spin-orbit interaction*. PhD thesis, School of Engineering and Natural Science, University of Iceland, Reykjavik, 2014.
- [86] Daniela Pfannkuche, Vidar Gudmundsson, and Peter A. Maksym. Comparison of a Hartree, a Hartree-Fock, and an exact treatment of quantum-dot helium. *Phys. Rev. B*, 47:2244–2250, Jan 1993.
- [87] Vidar Gudmundsson and Gunnar Pálsson. Screening of an impurity in a two-dimensional electron gas within the Hartree and the Hartree-Fock approximation in the quantum Hall regime. *Phys. Rev. B*, 49:13712–13720, May 1994.
- [88] A. H. Thorolfsson, A. Manolescu, D.C. Marinescu, and V. Gudmundsson. Coulomb interaction effects on the spin polarization and currents in quantum wires with spin-orbit interaction. *Nanoscale Systems:Mathematical Modeling, Theory and Applications*, 01:23–37, 2012.
- [89] J. C. Slater. A Simplification of the Hartree-Fock Method. *Phys. Rev.*, 81:385–390, Feb 1951.
- [90] Per-Olov Löwdin. Quantum Theory of Many-Particle Systems. III. Extension of the Hartree-Fock Scheme to Include Degenerate Systems and Correlation Effects. *Phys. Rev.*, 97:1509–1520, Mar 1955.
- [91] F. Cavaliere and U. D. Giovannini. General Hartree-Fock method and symmetry breaking in quantum dots. *Physica E*, 42:606–609, 2010.

BIBLIOGRAPHY

- [92] Shiwei Zhang and D. M. Ceperley. Hartree-Fock Ground State of the Three-Dimensional Electron Gas. *Phys. Rev. Lett.*, 100:236404, Jun 2008.
- [93] C. Yannouleas and Landman U. Symmetry breaking and quantum correlations in finit systems: studies of quantum dots and ultracold Bose gases and related nuclear and chemical methods. *Reports on progress in physics*, 70:2067–2148, 2007.
- [94] Valeriu Moldoveanu, Andrei Manolescu, and Vidar Gudmundsson. Dynamic correlations induced by Coulomb interactions in coupled quantum dots. *Phys. Rev. B*, 82:085311, Aug 2010.
- [95] Sajeev Chacko, Dhani Nafday, D. G. Kanhere, and T. Saha-Dasgupta. Exact diagonalization study for nanographene: Modulation of charge and spin, magnetic phase diagram, and thermodynamics. *Phys. Rev. B*, 90:155433, Oct 2014.
- [96] D. K. Cheng. *Field and wave electromagnetics*. Addison-Wesley series in electrical engineering. Addison-Wesley, 1989.
- [97] H.-P. Breuer and F Petruccione. *The Theory of Open Quantum Systems*. Oxford University Press, Oxford, 2002.
- [98] H. Louisell William. *Quantum Statistical Properties of Radiation*. Wiley Classics Library, 1990.
- [99] S. Nakajima. On quantum theory of transport phenomena steady diffusion. *Prog. of Theor. Phys.*, 20:948, 1958.
- [100] Robert Zwanzig. Ensemble Method in the Theory of Irreversibility. *The Journal of Chemical Physics*, 33(5):1338–1341, 1960.
- [101] B. Knezevic and B. Novakovic. Time-dependent transport in open system based on quantum master equation. *J. Comput Electron*, 12:363–374, 2013.
- [102] F Haake. Quantum Statistics in Optics and Solid-state Physics. *Quantum Statistics in Optics and Solid-state Physics, edited by G. Hohler and E.A. Niekisch, Springer Tracts in Modern Physics Vol.*, 66, Springer, Berlin, Heidelberg, New York, 1973, p. 98.
- [103] N R Abdullah, C S Tang, A Manolescu, and V Gudmundsson. Delocalization of electrons by cavity photons in transport through a quantum dot molecule. *Physica E*, 64:254–262, 2014.
- [104] Tobias Zibold, Peter Vogl, and Andrea Bertoni. Theory of semiconductor quantum-wire-based single- and two-qubit gates. *Phys. Rev. B*, 76:195301, Nov 2007.

- [105] J. Gong, F-H. Yang, and S-L. Feng. coherent tunneling in coupled quantum wells under a uniform magnetic field. *Chin. Phys. Lett.*, 24(8):2383, 2007.
- [106] M. Abramowitz and Stegun I. A. *Handbook of Mathematical Functions*. National Bureau of Standards Applied Mathematics Series, U.S., 1964.
- [107] W. Heitler. *The quantum theory of radiation*. Oxford University Press, 1984.

Included publications

Article I

Electron transport through a quantum dot assisted by cavity photons.

N. R. Abdullah, C-S Tang, A. Manolescu, and V. Gudmundsson
Journal of Physics: Condensed Matter **25**, 465302 (2013).

Electron transport through a quantum dot assisted by cavity photons

Nzar Rauf Abdullah¹, Chi-Shung Tang², Andrei Manolescu³ and Vidar Gudmundsson¹

¹ Science Institute, University of Iceland, Dunhaga 3, IS-107 Reykjavik, Iceland

² Department of Mechanical Engineering, National United University, 1, Lienda, Miaoli 36003, Taiwan

³ School of Science and Engineering, Reykjavik University, Menntavegur 1, IS-101 Reykjavik, Iceland

E-mail: cstang@nuu.edu.tw and vidar@raunvis.hi.is

Received 28 August 2013, in final form 20 September 2013

Published 17 October 2013

Online at stacks.iop.org/JPhysCM/25/465302

Abstract

We investigate transient transport of electrons through a single quantum dot controlled by a plunger gate. The dot is embedded in a finite wire with length L_x assumed to lie along the x -direction with a parabolic confinement in the y -direction. The quantum wire, originally with hard-wall confinement at its ends, $\pm L_x/2$, is weakly coupled at $t = 0$ to left and right leads acting as external electron reservoirs. The central system, the dot and the finite wire, is strongly coupled to a single cavity photon mode. A non-Markovian density-matrix formalism is employed to take into account the full electron–photon interaction in the transient regime. In the absence of a photon cavity, a resonant current peak can be found by tuning the plunger-gate voltage to lift a many-body state of the system into the source–drain bias window. In the presence of an x -polarized photon field, additional side peaks can be found due to photon-assisted transport. By appropriately tuning the plunger-gate voltage, the electrons in the left lead are allowed to undergo coherent inelastic scattering to a two-photon state above the bias window if initially one photon was present in the cavity. However, this photon-assisted feature is suppressed in the case of a y -polarized photon field due to the anisotropy of our system caused by its geometry.

(Some figures may appear in colour only in the online journal)

1. Introduction

Electronic transport through quantum dot (QD) related systems has received tremendous attention in recent years due to its potential application in various fields, such as the implementation of quantum computing [1], nanoelectromechanical systems [2], photodetectors [3], and biological sensors [4]. The QD-embedded structure can be fabricated in a two-dimensional electron gas, controlled by a plunger-gate voltage, and connected to the leads by applying an external source–drain bias voltage.

Electronic transport under the influence of time-varying external fields is one of the interesting areas. Transport phenomena in the presence of photons have been intensively studied in many mesoscopic systems [5–14]. Among the various quantum confined geometries to characterize the photon-assisted features are, for example, a quantum ring

with an embedded dot for exploring mono-parametric quantum charge pumping [7], a single QD for investigating single-electron (SE) tunneling [8], a quantum wire for studying electron population inversion [9], and a quantum point contact involving photon-induced intersubband transitions [10, 11]. Recently, the electrical properties of double QD systems influenced by electromagnetic irradiation have been studied [12, 13], indicating a spin-filtering effect [12], and two types of photon-assisted tunneling related to the ground state and excited state resonances [13]. The classical and quantum response was investigated experimentally in terms of the sharpness of the transition rate, which depends on the thermal broadening of the Fermi level in the electrodes and the broadening of the confined levels [14].

In the above-mentioned examples the photon-assisted transport was induced by a classical electromagnetic field. It is also interesting to investigate electronic transport through

a QD system influenced by a quantized photon field. A single-photon source is an essential building block for the manipulation of the quantum information coded by a quantum state [15]. This issue has been considered by calculating the resonant current carried by negatively charged excitons through a double QD system confined in a cavity [16], where resonant tunneling between two QDs is assisted by a single photon. Recently several experimental groups have successfully coupled a single quantum dot with one cavity mode [17–20]. However, modeling of transient electronic transport through a QD in a photon cavity is still in its infancy.

To study time-dependent transport phenomena in mesoscopic systems, a number of approaches have been employed. In closed systems, the Jarzynski equation was derived by defining the free-energy difference of the system between the initial and final equilibrium state in terms of a stochastic Liouville equation [21] or microscopic reversibility [22]. In open quantum systems where the system is connected to electron reservoirs, the Jarzynski equation can be derived using a master equation approach to investigate fluctuation theorems [23] and dissipative quantum dynamics [24]. In order to investigate interaction effects on the transport behavior, several approaches have been proposed based on the quantum master equation (QME) applied to a quantum measurement of a two-state system [25], calculation of current noise spectrum [26], and the counting statistics of electron transfers through a double QD [27]. The QME describes the evolution of the reduced density (RD) operator caused by the Hamiltonian of the closed system in the presence of electron or photon reservoirs. Thus, the QME usually consists of two parts: one describing the unitary evolution of the closed system and the other being a dissipative part describing the influence of the reservoirs [28].

In an open current-carrying system weakly coupled to leads, master equations within the Markovian and wide-band approximations have been commonly derived and used [29–31]. The coupling to electron or photon reservoirs can be considered to be Markovian and the rotating wave approximation is often used for the electron–photon coupling [29]. The QME may reduce to a ‘birth and death master equation’ for populations [30], or modified rate equations [31]. The energy dependence of the electron tunneling rate or the memory effect in the system are usually neglected.

The non-Markovian density-matrix formalism with energy-dependent coupling elements should be considered to study the full counting statistics for electronic transport through interacting electron systems [32–34]. It was noticed that the Markovian limit neglects coherent oscillations in the transient regime, and the rate at which the steady state is reached does not agree with the non-Markovian model [35]. The Markov approximation shows significantly longer times to reach a steady state when the tunneling anisotropy is high, thus confirming its applicability only in the long-time limit. To investigate the transient transport, a non-Markovian density-matrix formalism involving energy-dependent coupling elements should be explicitly considered [36].

The aim of this work is to investigate how the x - and y -polarized single-photon modes influence the ballistic

transient electronic transport through a QD embedded in a finite quantum wire in a uniform perpendicular magnetic field based on the non-Markovian dynamics. We explicitly build a transfer Hamiltonian that describes the contact between the central quantum system and semi-infinite leads with a switching-on coupling in a certain energy range. By controlling the plunger gate, we shall demonstrate robust photon-assisted electronic transport features when the physical parameters of the single-photon mode are appropriately tuned to cooperate with the electron–photon coupling and the energy levels of the Coulomb interacting electron system.

The paper is organized as follows. In section 2, we model a QD with interacting electrons embedded in a quantum wire coupled to a single-photon mode in a uniform magnetic field, in which the full electron–photon coupling is considered. The transient dynamics is calculated using a generalized QME based on a non-Markovian formalism. Section 3 demonstrates the numerical results and transient transport properties of the plunger-gate controlled electron system coupled to the single-photon mode with either x - or y -polarization. Concluding remarks will be presented in section 4.

2. Model and theory

In this section, we describe how the embedded QD, realized in a two-dimensional electron gas in gallium arsenide (GaAs), can be described by the potential V_{QD} in a finite quantum wire and its connection to the leads in a uniform perpendicular magnetic field. The plunger-gate controlled central electronic system is strongly coupled to a single-photon mode that can be described by a many-body (MB) system Hamiltonian H_S , in which the electron–electron interaction and the electron–photon coupling to the x - and y -polarized photon fields are explicitly taken into account, as depicted in figure 1(a). A generalized QME is numerically solved to investigate the dynamical transient transport of electrons through the single QD system.

2.1. QD-embedded wire in magnetic field

The electron system under investigation is a two-dimensional finite quantum wire that is hard-wall confined at $x = \pm L_x/2$ in the x -direction, and parabolically confined in the y -direction. The system is exposed to an external perpendicular magnetic field $\mathbf{B} = B\hat{z}$, defining a magnetic length $l = (\hbar/eB)^{1/2} = 25.67[B(\text{T})]^{-1/2}$ nm, and the effective confinement frequency $\Omega_w^2 = \omega_c^2 + \Omega_0^2$, being expressed in the cyclotron frequency $\omega_c = eB/m^*c$ as well as in the bare confinement energy $\hbar\Omega_0$ characterizing the transverse electron confinement. The system is scaled by the effective magnetic length $a_w = (\hbar/m^*\Omega_w)^{1/2}$. Figure 1(b) shows the embedded QD subsystem scaled by a_w , where the QD potential is considered of a symmetric Gaussian shape

$$V_{\text{QD}}(x, y) = V_0 \exp[-\beta_0^2(x^2 + y^2)] \quad (1)$$

with strength $V_0 = -3.3$ meV and $\beta_0 = 3.0 \times 10^{-2} \text{ nm}^{-1}$ such that the radius of the QD is $R_{\text{QD}} \approx 33.3$ nm.

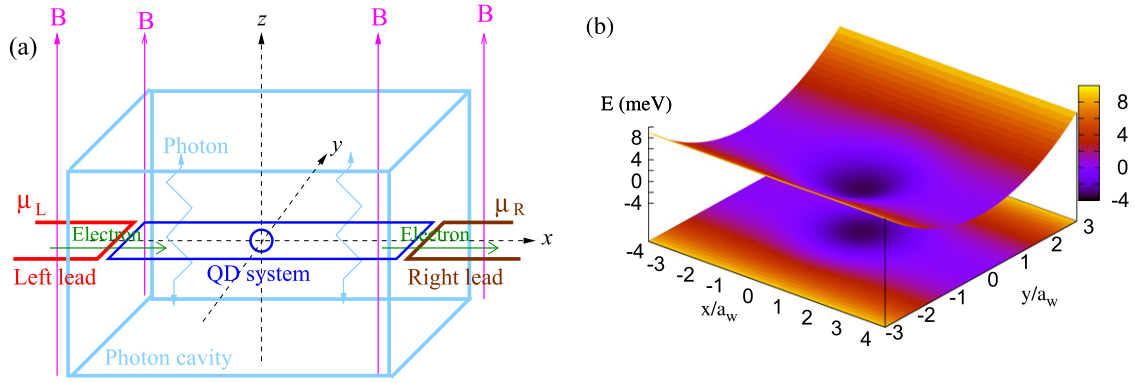


Figure 1. (a) Schematic of a QD embedded in a quantum wire coupled to a photon cavity, connected to the left lead (red) with chemical potential μ_L , and the right lead (brown) with chemical potential μ_R in an external magnetic field B . (b) Schematic diagram depicting the potential representing the QD embedded in a quantum wire with parameters $B = 0.1$ T, $a_w = 23.8$ nm, and $\hbar\Omega_0 = 2.0$ meV.

2.2. Many-body model

In this section, we describe how to build up the time-dependent Hamiltonian $H(t)$ of an open system that couples the QD-embedded MB system to the leads. The Coulomb and photon interacting electrons of the QD system are described by a MB system Hamiltonian H_S . In the closed electron–photon interacting system, the MB-space $\{|\tilde{\nu}\rangle\}$ is constructed from the tensor product of the electron–electron interacting many-electron (ME) state basis $|\nu\rangle$ and the eigenstates $|N\rangle$ of the photon number operator $a^\dagger a$, namely $|\tilde{\nu}\rangle = |\nu\rangle \otimes |N\rangle$ [37]. The Coulomb interacting ME states of the isolated system are constructed from the SE states [38]. The time-dependent Hamiltonian describing the MB system coupled to the leads

$$H(t) = H_S + \sum_{l=L,R} [H_l + H_{Tl}(t)] \quad (2)$$

consists of a disconnected MB system Hamiltonian H_S , and the ME Hamiltonian of the leads H_l where the electron–electron interaction is neglected. In addition, L and R refer to the left and the right lead, respectively. Moreover, $H_{Tl}(t)$ is a time-dependent transfer Hamiltonian that describes the coupling between the QD system and the leads.

The isolated QD system including the electron–electron and the photon–electron interactions is governed by the MB system Hamiltonian

$$H_S = \sum_{i,j} \langle \psi_i | \left\{ \frac{\pi^2}{2m^*} + V_{\text{QD}} + eV_{\text{pg}} \right\} | \psi_j \rangle d_i^\dagger d_j + H_{e-e} + H_{\text{ph}} + H_Z \quad (3)$$

where $|\psi\rangle$ is a SE state, d_i^\dagger (d_j) are the electron creation (annihilation) operators in the central system, and $H_{\text{ph}} = \hbar\omega_{\text{ph}} a^\dagger a$ is the photon Hamiltonian. In addition, $\pi = \pi_e + \frac{e}{c} \mathbf{A}_{\text{ph}}$, where $\pi_e = p + \frac{e}{c} \mathbf{A}_{\text{ext}}$ is composed of the momentum operator p of the electronic system and the vector potential $\mathbf{A}_{\text{ext}} = (0, -By, 0)$ represented in the Landau gauge. H_Z is the Zeeman energy $\pm \frac{1}{2} g^* \mu_B B$, where μ_B is the Bohr magneton and g^* the effective Lande g -factor for the material.

In the Coulomb gauge, the photon vector potential can be represented as

$$\mathbf{A}_{\text{ph}} = A_{\text{ph}}(a + a^\dagger)\hat{\mathbf{e}}, \quad (4)$$

if the wavelength of the cavity mode is much larger than the size of the central system. Herein, A_{ph} is the amplitude of the photon field. The electron–photon coupling strength is thus defined by $g_{\text{ph}} = eA_{\text{ph}}\Omega_w a_w / c$. In addition, $\hat{\mathbf{e}} = (e_x, 0)$ indicates the electric field is polarized parallel to the transport direction in a TE_{011} mode, and $\hat{\mathbf{e}} = (0, e_y)$ denotes the electric field is polarized perpendicular to the transport direction in a TE_{101} mode. Moreover, we introduce the plunger-gate voltage V_{pg} to control the alignment of quantized energy levels in the QD system relative to the electrochemical potentials in the leads. In the second term of equation (3), $\hbar\omega_{\text{ph}}$ is the quantized photon energy, and a^\dagger (a) are the operators of photon creation (annihilation), respectively. The last term H_{e-e} describes the electron–electron interaction.

In a second quantized form, the isolated MB system Hamiltonian H_S can be separated as

$$H_S = H_e + H_{\text{ph}} + H_{e-\text{ph}} + H_Z. \quad (5)$$

The first part of H_S is the Coulomb interacting electron Hamiltonian

$$H_e = \sum_i (E_i + eV_{\text{pg}}) d_i^\dagger d_i + \frac{1}{2} \sum_{ijrs} \langle V_{\text{Coul}} \rangle d_i^\dagger d_j^\dagger d_s d_r, \quad (6)$$

where E_i is the energy of a SE state, V_{pg} is the electrostatic potential of the plunger gate, and

$$\begin{aligned} \langle V_{\text{Coul}} \rangle &= \langle ij | V_{\text{Coul}} | rs \rangle \\ &= \int d\mathbf{r} d\mathbf{r}' \psi_i^S(\mathbf{r})^* \psi_j^S(\mathbf{r}')^* \\ &\quad \times V(\mathbf{r} - \mathbf{r}') \psi_r^S(\mathbf{r}') \psi_s^S(\mathbf{r}) \end{aligned} \quad (7)$$

are the Coulomb matrix elements in the SE state basis, with $\psi^S(\mathbf{r})$ being the SE state wavefunctions and $V(\mathbf{r} - \mathbf{r}')$ the Coulomb interaction potential [38]. The second part in equation (5) is the photon Hamiltonian $H_{\text{ph}} = \hbar\omega_{\text{ph}} \hat{N}_{\text{ph}}$, with $\hat{N}_{\text{ph}} = a^\dagger a$ being the photon number operator. The third part

in equation (5) is the electron–photon coupling Hamiltonian

$$H_{\text{e-ph}} = g_{\text{ph}} \sum_{ij} d_i^\dagger d_j g_{ij} \{a + a^\dagger\} + \frac{g_{\text{ph}}^2}{\hbar \Omega_w} \sum_i d_i^\dagger d_i \left[\hat{N}_{\text{ph}} + \frac{1}{2} (a^\dagger a^\dagger + aa + 1) \right] \quad (8)$$

with the dimensionless electron–photon coupling factor g_{ij} [39]. An exact diagonalization method is used to solve the Coulomb interacting ME Hamiltonian for the central system [40]. In order to couple the central system to the leads connecting to the left (right) reservoir with chemical potential μ_L (μ_R), it is important to consider all MB states in the system and SE states in the leads within an extended energy interval $[\mu_R - \Delta_R, \mu_L + \Delta_L]$ in order to include all the relevant MB states involved in the dynamical transient transport.

The second term in equation (2) is the noninteracting ME Hamiltonian in the lead l given by

$$H_l = \int d\mathbf{q} \epsilon_l(\mathbf{q}) c_{\mathbf{q}l}^\dagger c_{\mathbf{q}l} \quad (9)$$

where we combine the momentum of a state q and its subband index n_{yl} in lead l into a single dummy index $\mathbf{q} = (n_{yl}, q)$; we thus use $\int d\mathbf{q} \equiv \sum_{n_y} \int dq$ to symbolically express the summation and integration for simplicity. In addition, $c_{\mathbf{q}l}^\dagger$ and $c_{\mathbf{q}l}$ are, respectively, the electron creation and annihilation operators of the electron in the lead l .

The system–lead coupling Hamiltonian is expressed as

$$H_{\text{TL}}(t) = \chi_l(t) \sum_i \int d\mathbf{q} \left[c_{\mathbf{q}l}^\dagger T_{\mathbf{q}il} d_i + d_i^\dagger (T_{\mathbf{q}il})^* c_{\mathbf{q}l} \right] \quad (10)$$

where $\chi_l(t) = 1 - 2[\exp[\alpha_l(t - t_0)] + 1]^{-1}$ is a time-dependent switching function with a switching parameter α_l , and

$$T_{\mathbf{q}il} = \int d\mathbf{r} d\mathbf{r}' \psi_{\mathbf{q}l}(\mathbf{r}')^* g_{\mathbf{q}il}(\mathbf{r}, \mathbf{r}') \psi_i^S(\mathbf{r}) \quad (11)$$

indicates the state-dependent coupling coefficients describing the electron transfer between a SE state $|i\rangle$ in the central system and the extended state $|\mathbf{q}\rangle$ in the leads, where $\psi_{\mathbf{q}l}(\mathbf{r})$ is the SE wavefunction in the lead l and $g_{\mathbf{q}il}(\mathbf{r}, \mathbf{r}')$ denotes the coupling function [36].

2.3. General formalism of the master equation

The time evolution of electrons in the QD-leads system satisfies the Liouville–von Neumann (LvN) equation [41, 42]

$$i\hbar \dot{W}(t) = [H(t), W(t)] \quad (12)$$

in the MB-space, where the density operator of the total system is $W(t)$, with the initial condition $W(t < t_0) = \rho_L \rho_R \rho_S$. Electrons in the lead l in steady state before coupling to the central QD system are described by the grand canonical density operator [43]

$$\rho_l = \frac{e^{-\beta(H_l - \mu_l N_l)}}{\text{Tr}_l \{e^{-\beta(H_l - \mu_l N_l)}\}} \quad (13)$$

where μ_l denotes the chemical potential of lead l , $\beta = 1/k_B T_l$ is the inverse thermal energy, and N_l indicates the total number of electrons in lead l . The LvN (equation (12)) can be projected on the central system by taking the trace over the Hilbert space of the leads to obtain the RD operator $\rho(t) = \text{Tr}_L \text{Tr}_R W(t)$, where $\rho(t_0) = \rho_S$ [44, 45].

We diagonalize the electron–photon coupled MB system Hamiltonian H_S within a truncated Fock space built from 22 SE states $\{|\mu\rangle\}$ [39, 46], then the system is connected to the leads at time $t = t_0$ thus containing a variable number of electrons. We include all sectors of the MB Fock space, where the ME states with zero to four electrons are dynamically coupled to the photon cavity with zero to 16 photons. The diagonalization gives us a new interacting MB state basis $\{|\check{\nu}\rangle\}$, in which $|\check{\nu}\rangle = \sum_\alpha \mathcal{W}_{\mu\alpha} |\check{\alpha}\rangle$, with $\mathcal{W}_{\mu\alpha}$ being a unitary transformation matrix with size $N_{\text{MB}} \times N_{\text{MB}}$. SE states are labeled with Latin indices and many-particle states have a Greek index. The spin information is implicit in the index. The spin degree of freedom is essential to describe correctly the structure of the few-body Fermi system. This allows us to obtain the RD operator in the interacting MB state basis $\check{\rho}(t) = \mathcal{W}^\dagger \rho(t) \mathcal{W}$.

Using the notation

$$\Omega_{\mathbf{q}l}(t) = U_S^\dagger(t) \int_{t_0}^t ds \chi_l(s) \Pi_{\mathbf{q}l}(s) \times \exp \left[-\frac{i}{\hbar} (t - s) \epsilon_l(\mathbf{q}) \right] U_S(t), \quad (14)$$

where

$$\Pi_{\mathbf{q}l}(s) = U_S(s) [(\check{T}_l)^\dagger \check{\rho}(s) [1 - f_l(\epsilon(\mathbf{q}))] - \check{\rho}(s) (\check{T}_l)^\dagger f_l(\epsilon(\mathbf{q}))] U_S^\dagger(s),$$

with $U_S(t) = \exp[iH_S(t - t_0)/\hbar]$ being the time evolution operator of the closed central system and $f_l(\epsilon(\mathbf{q})) = \{\exp[\epsilon(\mathbf{q}) - \mu_l] + 1\}^{-1}$ being the Fermi function in lead l at $t = t_0$, the time evolution of the RD operator can then be expressed as

$$\frac{d\check{\rho}(t)}{dt} = -\frac{i}{\hbar} [H_S, \check{\rho}(t)] - \frac{1}{\hbar^2} \sum_{l=L,R} \chi_l(t) \times \int d\mathbf{q} [(\check{T}_l(\mathbf{q}), \Omega_{\mathbf{q}l}(t)] + \text{h.c.}). \quad (15)$$

The first term governs the time evolution of the disconnected central interacting MB system. The second term describes the energy dissipation of interacting electrons through charging and discharging effects in the central system by the leads. In the second term, $\check{T}_l(\mathbf{q})$ is the interacting MB coupling matrix

$$\check{T}_l(\mathbf{q}) = \sum_{\mu,\nu} \check{T}_{\mu\nu l}(\mathbf{q}) |\check{\nu}\rangle \langle \check{\mu}|, \quad (16)$$

in which both the Coulomb interaction and the electron–photon coupling have been included. Here $\check{T}_{\mu\nu l}(\mathbf{q}) = \sum_i T_{i\mathbf{q}l} \langle \check{\mu} | d_i^\dagger | \check{\nu} \rangle$ indicates the coupling of MB states $|\check{\nu}\rangle$ in the central system caused by the coupling to the SE states in the leads described by the coupling matrix $T_{i\mathbf{q}l}$.

2.4. Charge and current

We now focus on the physical observables that we calculate for the QD system. The mean photon number in each MB state $|\check{\nu}\rangle$ can be written as

$$N_{\text{ph}} = \langle \check{\nu} | \hat{N}_{\text{ph}} | \check{\nu} \rangle, \quad (17)$$

where \hat{N}_{ph} is the photon number operator. The average of the electron number operator can be found by taking the trace of the MB states $\{|\check{\nu}\rangle\}$ in the Fock space, namely $\langle \hat{N}_e(t) \rangle = \text{Tr}\{W(t)\hat{N}_e\}$.

The mean value of the interacting ME charge distribution in the QD system is thus defined by

$$\mathcal{Q}(\mathbf{r}, t) = e \sum_{ij} \psi_i^*(\mathbf{r}) \psi_j(\mathbf{r}) \sum_{\mu, \nu} (\check{\mu} | d_i^\dagger d_j | \check{\nu}) \check{\rho}_{\nu\mu}(t) \quad (18)$$

where $e > 0$ stands for the magnitude of the electron charge, and $\check{\rho}_{\nu\mu}(t) = \langle \check{\nu} | \check{\rho}(t) | \check{\mu} \rangle$ is the time-dependent RD matrix in the MB-space.

In order to analyze the transient transport dynamics, we define the net charging current

$$I_Q(t) = I_L(t) + I_R(t) \quad (19)$$

where $I_L(t)$ indicates the partial charging current from the left lead into the system, and $I_R(t)$ represents the partial charging current from the right lead into the system. Here, the left and right partial currents $I_l(t)$ can be explicitly expressed in the following form

$$I_l(t) = -\frac{e}{\hbar^2} \chi_l(t) \times \sum_{\mu} \int d\mathbf{q} (\check{\mu} | [\check{T}_l(\mathbf{q}), \Omega_{\mathbf{q}l}(t)] + \text{h.c.} | \check{\mu}). \quad (20)$$

3. Results and discussion

In this section, we consider a QD embedded in a finite quantum wire system, made of a high-mobility GaAs/AlGaAs heterostructure with an electron effective mass $m^* = 0.067m_e$ and relative dielectric constant $\epsilon_r = 12.4$, with length $L_x = 300$ nm and bare transverse electron confinement energy $\hbar\Omega_0 = 2.0$ meV. A uniform perpendicular magnetic field $B = 0.1$ T is applied and, hence, the effective magnetic length is $a_w = 23.8$ nm and the characteristic Coulomb energy is $E_C = e^2/(2\epsilon_r a_w) \approx 2.44$ meV. The effective Lande g -factor $g^* = 0.44$.

We select $\beta_0 = 3.0 \times 10^{-2} \text{ nm}^{-1}$ such that the radius of the embedded QD is $R_{\text{QD}} = 1.4a_w$. The QD system is transiently coupled to the leads in the x -direction that is described by the switching parameter $\alpha^l = 0.3 \text{ ps}^{-1}$ and the nonlocal system-lead coupling strength $\Gamma_l = 1.58 \text{ meV nm}^2$ [38]. A source-drain bias V_{bias} is applied, giving rise to the chemical potential difference $\Delta\mu = eV_{\text{bias}} = 0.1 \text{ meV}$.

To take into account all the relevant MB states, an energy window $\Delta_E = 5.5 \text{ meV}$ is considered to include all active states in the central system contributing to the

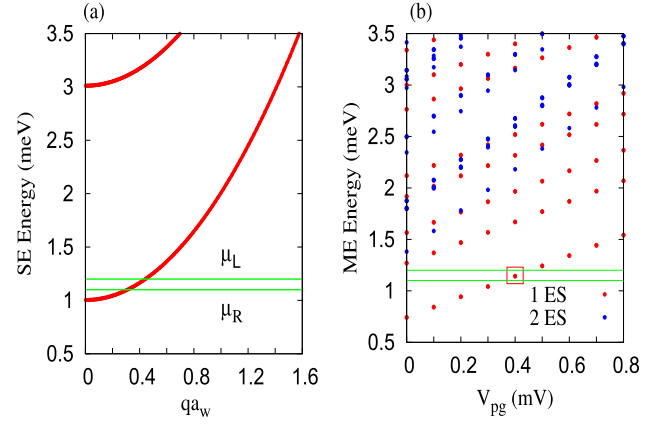


Figure 2. Energy spectra in the case of no photon cavity with a magnetic field $B = 0.1$ T. (a) The SE energy spectrum in the leads (red) is plotted as a function of wavenumber q , where the chemical potentials are $\mu_L = 1.2$ meV and $\mu_R = 1.1$ meV (green). (b) The ME energy spectrum in the central system as a function of plunger-gate voltage V_{pg} including SE states (1ES, red dots) and two-electron states (2ES, blue dots). The SE state in the bias window is almost doubly degenerate due to the small Zeeman energy.

transport. The temperature of the system is assumed to be $T = 0.01$ K, such that the typical MB energy level spacing is greater than the thermal energy, namely $\Delta E_{\text{MB}} > k_B T$, the thermal smearing effect is thus sufficiently suppressed. In the following, we shall select the energy $\hbar\omega_{\text{ph}}$ of the photon mode to be smaller than the characteristic Coulomb energy, namely $E_C > \hbar\omega_{\text{ph}}$. In the following, we shall demonstrate the plunger-gate controlled transient transport properties both in the case without a photon cavity and in the case including a photon cavity with either an x - or y -polarized photon field.

The energy of the photons, $\hbar\omega_{\text{ph}}$ will in both polarization cases be held at 0.3 meV. For the length of the central system, $L_x = 300$ nm, the photon energy will be comparable to the spacing of energy levels connected to motion of the electrons in the x -direction. We can thus expect the x -polarized photons to be able to promote resonances with translation in the x -direction—the transport direction. The confinement energy in the y -direction, $\hbar\Omega_0 = 2.0$ meV, on the other hand, is large enough to ensure almost all photon-induced motion in the y -direction to be out-of-resonance phenomena. This simple picture is slightly modified by the embedded quantum dot. The anisotropy of the central system can be expected to show up in the photon-activated processes investigated, due to the interplay of the photon energy and the characteristic energy scales for x - and y -motion.

3.1. Without a photon cavity

First, we consider the QD embedded in a quantum wire without a photon cavity in a uniform magnetic field $B = 0.1$ T that is coupled to the leads acting as SE reservoirs controlled by a source-drain bias. In figure 2(a), we show the SE energy spectrum in the leads (red) as a function of wavenumber q scaled by the effective magnetic length a_w^{-1} . The first subband, $n_y = 0$, contributes to the propagating

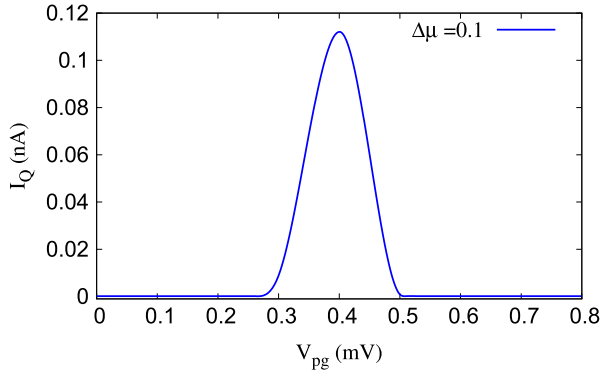


Figure 3. The net charging current I_Q is plotted as a function of plunger-gate voltage V_{pg} at time $t = 220$ ps in the case of no photon cavity. Other parameters are $B = 0.1$ T and $\Delta\mu = 0.1$ meV.

modes, while higher subbands contribute to the evanescent modes. In addition, the chemical potential (green) is $\mu_L = 1.2$ meV in the left lead and $\mu_R = 1.1$ meV in the right lead, implying the chemical potential difference $\Delta\mu = 0.1$ meV. Figure 2(b) shows the ME energy spectrum of the QD system, in which the electron–electron interaction is included while no electron–photon coupling has been introduced. Both the energies of SE states $N_e = 1$ (1ES, red dots) and two-electron states $N_e = 2$ (2ES, blue dots) vary linearly proportional to the applied plunger-gate voltage V_{pg} , but with different slopes. The two-electron states are located at relatively higher energies due to the Coulomb repulsion effect in the QD-embedded system.

The SE state energy is tunable as a function of plunger-gate voltage V_{pg} following $E_{SE}(V_{pg}) = E_{SE}(0) + eV_{pg}$. We rank the SE and ME states by energy. In the absence of a plunger-gate voltage, the lowest active SE states in the central system are $|4\rangle$ and $|5\rangle$, with energies $E_4(0) = 0.741$ meV and $E_5(0) = 0.744$ meV, respectively. These two SE states may enter the chemical potential window $[\mu_L, \mu_R] = [1.1, 1.2]$ meV by tuning the plunger-gate voltage to be $V_{pg} \approx [0.35, 0.45]$ mV. Consequently, the SE states occupying the first subband in the left lead are allowed to tunnel into the central ME system, resonantly tunneling from the left to the right lead, manifesting a main-peak feature in charging current $I_Q = 0.112$ nA at $V_{pg} = 0.4$ mV, as shown in figure 3.

In the following sections, we shall place the QD system in a photon cavity with a single-photon mode. We shall analyze the transient transport properties for the cases with linear polarizations in either the x - or y -direction.

3.2. x -polarized photon mode

Here, we demonstrate how the QD embedded in a quantum wire can be controlled by the plunger gate and how it is influenced by the photon field, where the electric field of the TE₀₁₁ mode is polarized in the x -direction. The initial condition of the system under investigation is an empty central system (no electron) that is coupled to a single-photon mode with one photon present, connected to the leads with a source–drain bias. The MB energy spectrum

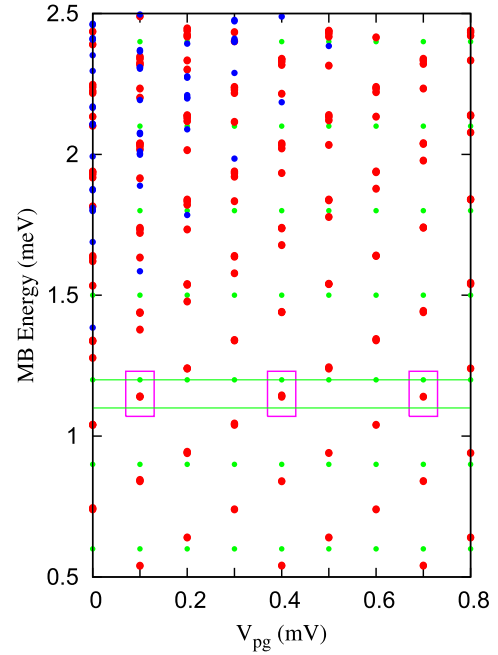


Figure 4. MB energy spectrum versus the plunger-gate voltage V_{pg} in the case of an x -polarized photon field, where zero-electron states ($N_e = 0$, green dots), single-electron states ($N_e = 1$, red dots), and two-electron states ($N_e = 2$, blue dots) are included. Other parameters are $B = 0.1$ T, $\Delta\mu = 0.1$ meV, and $\hbar\omega_{ph} = 0.3$ meV.

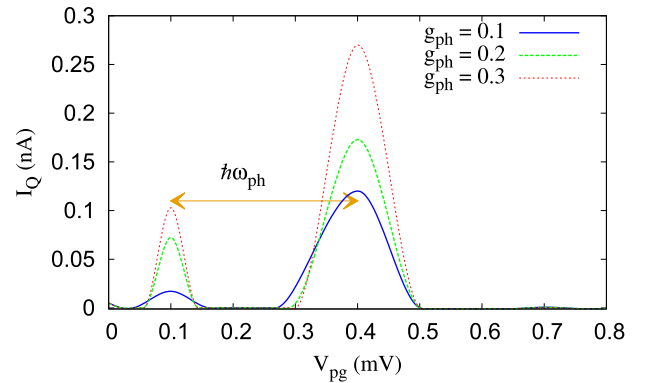


Figure 5. The net charging current I_Q versus the plunger-gate voltage V_{pg} in the case of an x -polarized photon field at time $t = 220$ ps with different electron–photon coupling strengths: $g_{ph} = 0.1$ meV (blue solid), $g_{ph} = 0.2$ meV (green dashed), and $g_{ph} = 0.3$ meV (red dotted). Other parameters are $\hbar\omega_{ph} = 0.3$ meV, $\Delta\mu = 0.1$ meV, and $B = 0.1$ T.

of the electron–photon interacting MB system is illustrated in figure 4. As shown in the previous section, active states enter the bias window around $V_{pg}^0 = 0.4$ mV in the case with no photon cavity. It is interesting to note that additional active states can be included around $eV_{pg} = eV_{pg}^0 \pm \hbar\omega_{ph}$, as is clearly seen in figure 4, implying that the x -polarized photon field induced active propagating states can be found around $V_{pg} = 0.1$ and 0.7 mV when the photon energy is $\hbar\omega_{ph} = 0.3$ meV. The additional photon-induced propagating states play an important role in enhancing the electron tunneling from the leads to the QD system.

Figure 5 shows the net charging current I_Q as a function of the plunger-gate voltage V_{pg} in the presence

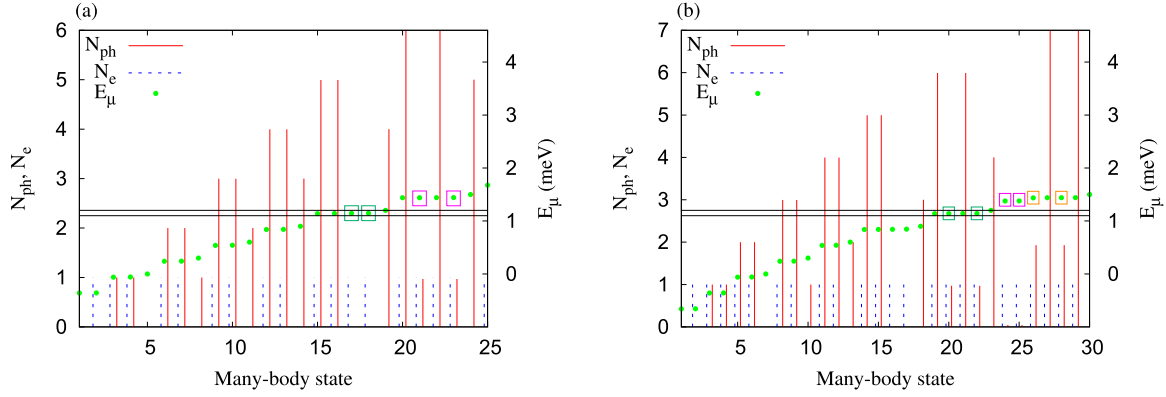


Figure 6. The MB energy spectrum E_μ (dotted green), the mean electron number in the MB state $|\check{\mu}\rangle$ (blue dashed line), and the mean photon number N_{ph} (red line) in the case of an x -polarized field: (a) $V_{pg} = 0.4$ meV and (b) $V_{pg} = 0.7$ meV. Other parameters are $B = 0.1$ T, $\Delta\mu = 0.1$ meV, $g_{ph} = 0.1$ meV, $\hbar\omega_{ph} = 0.3$ meV.

of the x -polarized photon field at time $t = 220$ ps. We fix the photon energy at $\hbar\omega_{ph} = 0.3$ meV and change the electron–photon coupling strength g_{ph} . A main peak around $V_{pg}^0 = 0.4$ mV is found, a robust left side peak around $eV_{pg} = eV_{pg}^0 - \hbar\omega_{ph}$ is clearly shown, and a right side peak around $eV_{pg} = eV_{pg}^0 + \hbar\omega_{ph}$ can be barely recognized. The left side peak exhibits photon-assisted transport feature from the SE MB states $|\check{20}\rangle$ and $|\check{22}\rangle$ in the bias window by absorbing a photon energy $\hbar\omega_{ph}$ to the SE MB states $|\check{26}\rangle$ and $|\check{28}\rangle$ above the bias window. However, the opposite photon-assisted transport feature caused by a photon emission (the right side peak) is significantly suppressed.

The main charge current peaks for $V_{pg} = 0.4$ mV are $I_Q^M = 0.120, 0.173$, and 0.270 nA corresponding to $g_{ph} = 0.1$ meV (blue solid), $g_{ph} = 0.2$ meV (green dashed), and $g_{ph} = 0.3$ meV (red dotted), as shown in figure 5. Our results demonstrate that the current carried by the electrons with energy within the bias window can be strongly enhanced by increasing the electron–photon coupling strength. At $V_{pg} = 0.1$ mV, the left side peaks in the charging current are $I_Q^S = 0.017, 0.072$, and 0.103 nA, corresponding to $g_{ph} = 0.1, 0.2$, and 0.3 meV. This implies that the electrons may absorb the energy of a single photon and, hence, the charging current manifests photon-assisted transport.

To identify the active MB states contributing to the transient transport, we show the characteristics of the MB states at $V_{pg} = 0.4$ and 0.1 meV in figures 6(a) and (b), corresponding, respectively, to the main peak and the left side peak in I_Q shown in figure 5. More precisely, there are five MB states contributing to the main peak in I_Q at $V_{pg} = 0.4$ meV. The five active MB states are: $|\check{17}\rangle$ and $|\check{18}\rangle$, with energies $E_{17} = 1.143$ meV and $E_{18} = 1.145$ meV in the bias window ($N_e = 1, N_{ph} = 0.04$), $|\check{21}\rangle, |\check{23}\rangle$, with energies $E_{21} = 1.439$ meV and $E_{23} = 1.441$ meV above the bias window ($N_e = 1, N_{ph} = 0.96$) shown in figure 6(a), and $|\check{53}\rangle$ with energy 2.488 meV (not shown). It is interesting to notice that $E_{17} + \hbar\omega_{ph} \cong E_{21}$ and $E_{18} + \hbar\omega_{ph} \cong E_{23}$, implying a photon-assisted transport through the higher MB states.

When an electron enters the QD system it interacts with the photon in the cavity. Its energy is thus not in

resonance with the electron states in the bias window, but with the electron states, photon replicas, which are with a photon energy $\hbar\omega_{ph}$ above the states in the bias window. The photon-activated states above the bias window contain approximately one more photon than the states in the bias window and, hence, the main peak in I_Q is mainly due to a single-photon absorption mechanism. In addition to the main-peak feature at the plunger-gate voltage V_{pg}^M , two side peaks can be recognized at $eV_{pg}^S = eV_{pg}^M \pm \hbar\omega_{ph}$, induced by photon-assisted transport, where the system satisfies $e\Delta V_{pg}^{MS} = e|V_{pg}^M - V_{pg}^S| \cong \hbar\omega_{ph}$. It has been pointed out that this plunger-gate controlled photon-assisted transport is repeatable with a period related to the Coulomb charging energy [47].

Figure 6(b) shows how the left side peak in the net charging current I_Q shown previously in figure 5 is contributed by the MB states. First, the left current $I_L = 0.001$ nA and the right current $I_R = -0.001$ nA contributed by the $|\check{20}\rangle$ and $|\check{22}\rangle$ MB states (green squared dot) containing $N_e = 1$ and $N_{ph} = 0.96$ within the bias window are almost negligible, implying the left side peak in I_Q is not induced by the resonant tunneling effect. Second, the $|\check{24}\rangle$ and $|\check{25}\rangle$ MB states (pink squared dot) contain $N_e = 1$ and $N_{ph} = 0.04$, with energies $E_{24} = 1.376$ meV and $E_{25} = 1.379$ meV above the bias window. These two states contribute, respectively, to the charging current $I_{24} = 0.0$ nA ($I_{L,24} = 0.003$ nA, $I_{R,24} = -0.003$ nA) and $I_{25} = 0.001$ nA ($I_{L,25} = 0.007$ nA, $I_{R,25} = -0.006$ nA) and, hence, generate a charging current $I_Q^c = 0.001$ nA. Third, the $|\check{26}\rangle$ and $|\check{28}\rangle$ MB states (orange squared dot) contain $N_e = 1$ and $N_{ph} = 1.96$, with energies $E_{26} = 1.435$ meV and $E_{28} = 1.438$ meV above the bias window. These two states contribute, respectively, to the charging current $I_{26} = 0.01$ nA ($I_{L,26} = 0.010$ nA, $I_{R,26} = 0.0$ nA) and $I_{28} = 0.004$ nA ($I_{L,28} = 0.005$ nA, $I_{R,28} = -0.001$ nA) and, hence, generate a photon-assisted tunneling current $I_Q^{ph} = 0.014$ nA. The main contribution of the left side peak in the charging current is then $I_Q \approx I_Q^c + I_Q^{ph} = 0.015$ nA, which coincides with the result shown in figure 5.

The schematic diagram in figure 7 is shown to illustrate the dynamical photon-assisted transport processes involved in

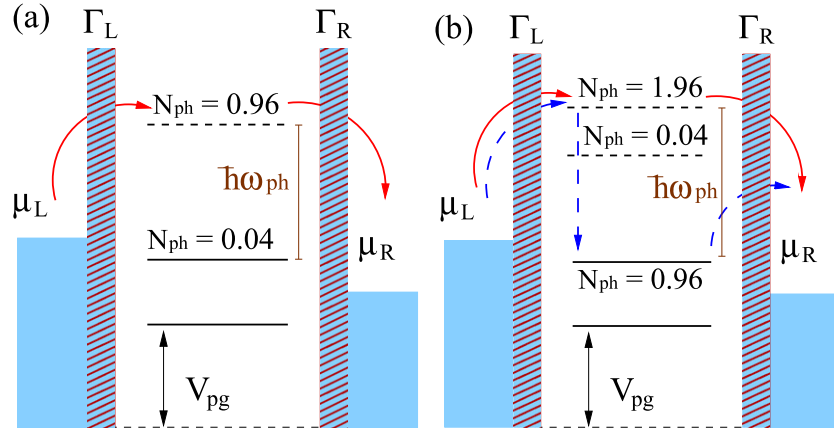


Figure 7. Schematic representation of photon-activated resonance energy levels and electron transition by changing the plunger-gate voltage V_{pg} at the main peak (a) and the left side peak (b) in figure 5. The QD system is embedded in a photocavity with a photon energy $\hbar\omega_{ph}$ and photon content N_{ph} in each many-body state. The chemical potential difference is $\Delta\mu = \mu_L - \mu_R$, and $\Gamma_{L,R}$ is the coupling strength between the QD system and the leads.

the formation of the main peak and the left side peak in the net charging current I_Q shown in figure 5. It is illustrated in figure 7(a) that the transport mechanism forming the main peak in I_Q is mainly due to the photon-assisted tunneling to the MB states above the bias window containing approximately a single photon. Figure 7(b) represents the two main transport mechanisms forming the left side peak in I_Q . The electrons in the left lead may absorb two photons to the MB states containing approximately two photons above the bias window. After that, the electrons may either perform resonant tunneling to the right lead (red solid arrow) or undergo multiple inelastic scattering by absorbing and emitting a photon energy $\hbar\omega_{ph}$ in the QD system (blue dashed arrow). This is the key result of this paper.

To get better insight into the dynamical electronic transport, the spatial distribution of the ME charge at $t = 220$ ps is shown in figure 8. Similar to the QD system in the absence of the photon cavity, the ME charge distribution at the main peak in I_Q forms resonant peaks at the edges of the QD, as shown figure 8(a), that are related to an antisymmetric state in the QD. The partial occupation contributed by the photon-activated resonant MB states $|21\rangle$ and $|23\rangle$ are $0.432e$ and $0.454e$, respectively. Comparing to the case with no photon cavity, the slight enhancement in the ME charge indicates that the tunneling of electrons into the QD system becomes faster in the presence of the photon cavity and, hence, the charging current is enhanced. It is shown in figure 8(b) that the ME charge in the case of the side peak in I_Q manifests an extended SE state, which is formed outside the QD. The partial occupations contributed by the photon-activated resonant MB states $|24\rangle$ and $|25\rangle$ are $0.018e$ and $0.025e$, respectively. By increasing the photon energy $\hbar\omega_{ph}$, the left side peak in I_Q can be enhanced and is shifted to lower energy (not shown). The slight asymmetry seen in the charge distribution in figure 8(b) is caused by the x -polarized electric field of the photons.

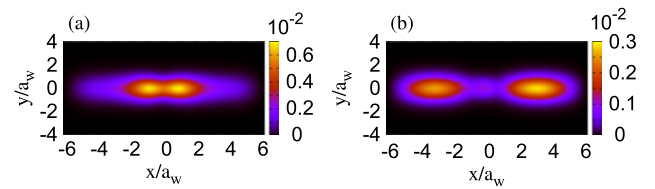


Figure 8. The spatial distribution of the many-electron charge density of the QD system with an x -polarized photon field at time 220 ps corresponding to the main peak (a) and the left side peak (b) for the case of $g_{ph} = 0.1$ meV shown in figure 5 (blue solid line). Other parameters are $\hbar\omega_{ph} = 0.3$ meV, $B = 0.1$ T, $a_w = 23.8$ nm, $L_x = 300$ nm, and $\hbar\Omega_0 = 2.0$ meV.

3.3. y -polarized photon mode

We consider here the TE_{101} y -polarized photon mode, where the electric field of the photons is perpendicular to the transport direction through the QD system. The QD system is assumed initially to contain no electron $N_e = 0$, but one photon in the cavity $N_{ph} = 1$. Since our system is considered to be anisotropic, elongated in the x -direction, we shall demonstrate that the photon-assisted transport effect is much weaker in the case of a y -polarized photon mode in comparison with that of x -polarization discussed in section 3.2.

In figure 9, we present the MB energy spectrum as a function of plunger-gate voltage V_{pg} for a QD system influenced by a y -polarized field with photon energy $\hbar\omega_{ph} = 0.3$ meV. Besides the propagating state at $V_{pg} = 0.4$ mV within the bias window (green lines), there are two additional electronic propagating states appearing at $V_{pg} = 0.1$ and 0.7 mV, caused by the presence of the photon field, as marked by the square dots shown in the figure.

Figure 10 shows the net charging current in the case of a y -polarized photon field, in which there is initially one photon $N_{ph} = 1$ with energy $\hbar\omega_{ph} = 0.3$ meV fixed while the electron-photon coupling strength is changed. It is seen that the main-peak currents at $V_{pg} = 0.4$ mV are:

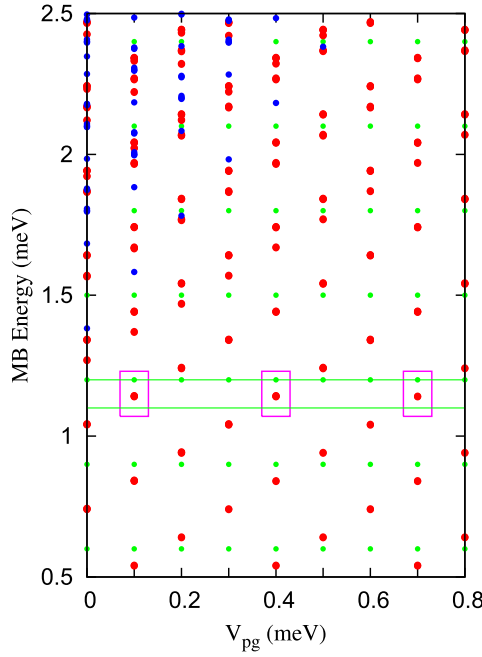


Figure 9. MB energy spectrum versus the plunger-gate voltage V_{pg} in the case of a y -polarized photon field: zero-electron states $N_e = 0$ (green dots), single-electron states $N_e = 1$ (red dots), and two-electron states $N_e = 2$ (blue dots). Other parameters are $B = 0.1$ T, $\Delta\mu = 0.1$ meV, $\hbar\Omega_0 = 2.0$ meV, $\hbar\omega_{ph} = 0.3$ meV, and $g_{ph} = 0.1$.

$I_Q^M = 0.115$ nA for $g_{ph} = 0.1$ meV (blue solid), $I_Q^M = 0.127$ nA for $g_{ph} = 0.2$ meV (green dashed), and $I_Q^M = 0.159$ nA for $g_{ph} = 0.3$ meV (red dotted). Moreover, a weak left side-peak current at $V_{pg} = 0.1$ mV can be recognized: $I_Q^S = 1.0$ pA for $g_{ph} = 0.1$ meV, $I_Q^S = 1.7$ pA for $g_{ph} = 0.2$ meV, and $I_Q^S = 3.2$ pA for $g_{ph} = 0.3$ meV. We notice that both the side- and main-peak currents are enhanced when the electron–photon coupling strength is increased. In order to get a better understanding of the current enhancement, we repeat the analysis of the photon-activated MB energy states contributing to the electronic transport.

In figure 11(a), we show the MB states at $V_{pg} = 0.4$ mV and $g_{ph} = 0.1$. The active MB states are $|\check{16}\rangle$ and $|\check{18}\rangle$, with energies 1.141 and 1.144 meV in the bias window ($N_{ph} = 0$), $|\check{21}\rangle$ and $|\check{23}\rangle$, with energies 1.441 and 1.444 meV above the bias window ($N_{ph} = 1$), and $|\check{53}\rangle$ with energy 2.483 meV ($N_{ph} = 1$). It should be noticed that $E_{16} + \hbar\omega_{ph} \cong E_{21}$ and $E_{18} + \hbar\omega_{ph} \cong E_{23}$, indicating that these two MB states above the bias window are photon-activated states. Furthermore, the higher active MB state with energy approximately the same as the characteristic Coulomb energy, that is $E_{53} \approx E_C$, indicates a correlation induced active two-electron state.

The net charging current at $V_{pg} = 0.4$ mV exhibiting the main current peak in figure 10 at $t = 220$ ps is mainly contributed by the MB states $|\check{21}\rangle$ ($I_{L,21} = 0.127$ nA, $I_{R,21} = 0.125$ nA) and $|\check{23}\rangle$ ($I_{L,23} = -0.032$ nA, $I_{R,23} = -0.018$ nA). This indicates that the electrons in the left lead can absorb one photon to the state $|\check{21}\rangle$, then emit one photon, performing resonant tunneling to the right lead and contributing to the

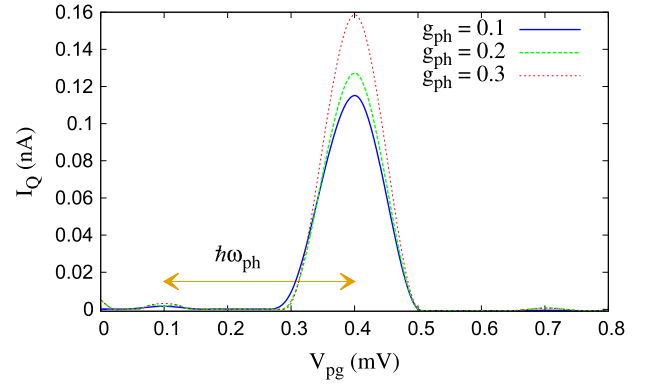


Figure 10. Net charging current versus the plunger-gate voltage V_{pg} at time $t = 220$ ps in the case of a y -polarized photon field. The electron–photon coupling is varied as: $g_{ph} = 0.1$ meV (blue solid), $g_{ph} = 0.2$ meV (green dashed), and $g_{ph} = 0.3$ meV (red dotted). Other parameters are $\hbar\omega_{ph} = 0.3$ meV, $\Delta\mu = 0.1$ meV, and $B = 0.1$ T.

charging current $I_{21} = 0.252$ nA. Moreover, an opposite transport mechanism can occur for the electrons in the right lead through the state $|\check{23}\rangle$, thus contributing to the charging current $I_{23} = -0.05$ nA. The scattering processes through these two states result in a photon-assisted tunneling current $I_Q^{ph} = 0.202$ nA. A small current through $|\check{53}\rangle$ is found due to the charging effect, namely $I_L = 0.002$ nA and $I_R = -0.087$ nA, hence contributing to the charging current $I_Q^c = -0.085$ nA due to the charging effect. The contribution to the main peak in the charging current is therefore $I_Q \approx I_Q^{ph} + I_Q^c = 0.117$ nA. This analysis is consistent with the result shown in figure 10.

In figure 11(b), we show the MB states at $V_{pg} = 0.1$ mV and $g_{ph} = 0.1$. The active MB states are: $|\check{20}\rangle$ and $|\check{22}\rangle$, with energies $E_{20} = 1.141$ meV and $E_{22} = 1.144$ meV in the bias window ($N_{ph} = 1$); $|\check{24}\rangle$ and $|\check{25}\rangle$, with energies 1.368 and 1.371 meV above the bias window ($N_{ph} = 0$); and $|\check{27}\rangle$ and $|\check{29}\rangle$, with energies $E_{27} = 1.441$ meV and $E_{29} = 1.444$ meV ($N_{ph} = 2$). We notice that $E_{20} + \hbar\omega_{ph} \cong E_{27}$ and $E_{22} + \hbar\omega_{ph} \cong E_{29}$. This implies that the two MB states $|\check{27}\rangle$ and $|\check{29}\rangle$ above the bias window are photon-activated states.

In figure 10, the net charging current at $V_{pg} = 0.1$ mV manifests a small side-peak current $I_Q^S = 1.0$ pA at $t = 220$ ps. This left side-peak structure in I_Q is mainly contributed by the MB states $|\check{20}\rangle$ ($I_L = 1.1$ pA, $I_R = -0.9$ pA) and $|\check{22}\rangle$ ($I_L = 1.2$ pA, $I_R = -0.9$ pA) in the bias window. These two states contribute to the resonant tunneling current, $I_Q^r = 0.5$ pA, which is related to the charge accumulation effect. In addition, the states $|\check{27}\rangle$ ($I_{27} = 4 \times 10^{-3}$ pA) and $|\check{29}\rangle$ ($I_{29} = 2 \times 10^{-3}$ pA) contribute to a very weak charging current $I_Q^{ph} = 6 \times 10^{-3}$ pA due to photon-assisted tunneling. The contribution to the side-peak current is therefore $I_Q^S \approx I_Q^r + I_Q^{ph} = 0.51$ pA. The suppression of the side-peak current in the case of y -polarization is due to the anisotropy of our system. The dipole momentum in the y -direction is much smaller than in the x -direction, and so is the electron–photon interaction strength.

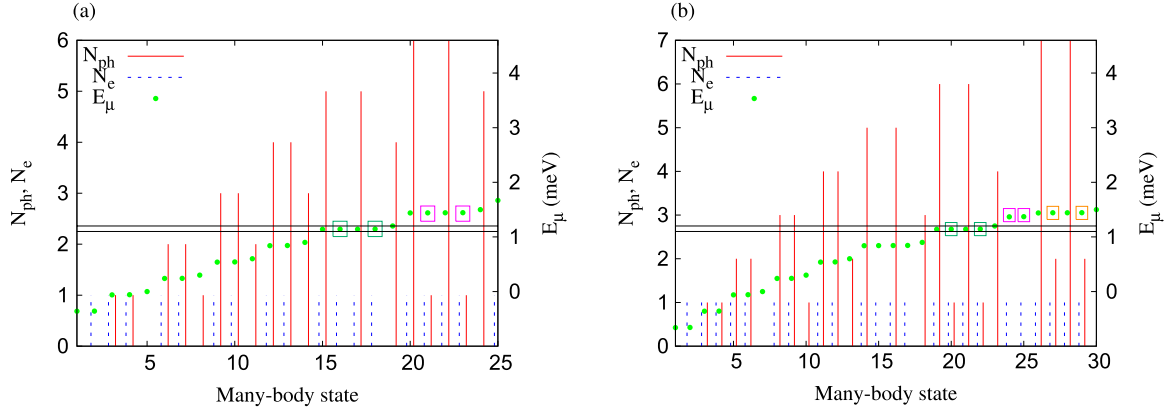


Figure 11. The many-body energy spectrum E_μ (dotted green), the mean electron number in the many-body state $\langle \bar{\mu} \rangle$ (blue dashed line), the mean photon number N_{ph} (red line) of the main peak $V_{pg} = 0.4$ meV (a), and the left side peak $V_{pg} = 0.1$ meV (b). The magnetic field is $B = 0.1$ T, $\Delta\mu = 0.1$ meV, $g_{ph} = 0.1$ meV, $\hbar\omega_{ph} = 0.3$ meV. In the case of a y-polarized photon field.

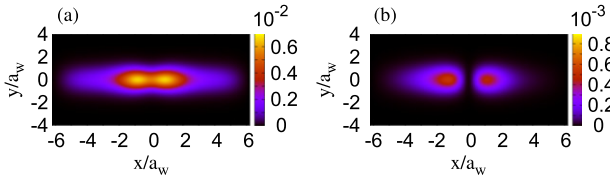


Figure 12. The spatial distribution of the ME charge density in the case of a y-polarized photon field at time 220 ps: (a) $V_{pg} = 0.4$ mV and (b) $V_{pg} = 0.1$ mV corresponding, respectively, to the main peak and the left side peak in figure 10 (blue line, $g_{ph} = 0.1$ meV). Other parameters are $\hbar\omega_{ph} = 0.3$ meV, $B = 0.1$ T, $a_w = 23.8$ nm, $L_x = 300$ nm, and $\hbar\Omega_0 = 2.0$ meV.

The ME charge distribution in the presence of the y-polarized photon mode is shown in figure 12. It is seen that the main-peak current in figure 10 forms an elongated broad bound state in the central system due to the electron–photon interaction, as shown in figure 12(a). Moreover, the side-peak current in figure 10 forms a photon-assisted resonant state at the edges of the QD embedded in the quantum wire, as is shown in figure 12(b). We notice that the charge distribution maxima around $x \approx \pm a_w$ of the main peak in I_Q at $V_{pg} = 0.4$ mV with $g_{ph} = 0.1$ meV are almost the same in the cases without and with the photon mode. As a consequence, the main-peak current $I_Q^M \simeq 0.1$ nA for these cases. Furthermore, the charging current maxima are located around $x \approx \pm 3a_w$ in the case of x-polarization and around $x \approx \pm 2a_w$ in the case of y-polarization. The charge distribution maxima in the case of x-polarization are closer to the edges of the central system, implying a higher left side-peak current at $V_{pg} = 0.1$ mV.

4. Concluding remarks

We have performed numerical calculations to investigate the transient current and charge distribution of electrons through a QD embedded in a finite wire coupled to a single-photon mode with x- or y-polarization. A non-Markovian theory is utilized, where we solve a generalized QME that includes the electron–electron Coulomb interaction and electron–photon coupling. Initially, we examined the case without a photon

cavity. In the short-time regime, the charging current exhibits a significant charge accumulation effect. In the long-time regime, the charging current is suppressed due to the Coulomb blocking effect. Furthermore, we have analyzed the photon-assisted current and the characteristics of photon-activated MB states with various parameters coupled to a single-photon mode in the photon cavity. The photon-assisted current peaks are enhanced by increased electron–photon coupling strength.

In the case of a QD system coupled to an x-polarized photon mode, the main current peak is enhanced by the electron–photon coupling. The electrons may absorb a single photon, manifesting a photon-assisted secondary peak which also incorporates correlation effects. In the case of a QD coupled to a y-polarized photon mode, the main current peak is contributed to by two photon-activated single-electron states and a correlation induced two-electron state. The secondary peak current in the case of y-polarization is suppressed due to the anisotropy of our system.

The cavity photon assisted or enhanced transport here was attainable by selecting a narrow bias window in order to facilitate the resonant placement and isolation of a spin-pair of states with a single-electron component by the plunger gate in the bias window. The bias window was kept in the lowest part of the MB energy spectrum and the low photon energy guarantees in most cases that only states close to this very discrete part of the spectrum are relevant to the transport. This is in contrast to our experience with a large bias window, where the coupling to the cavity photons most often reduces the charging of the central system [39, 46, 48].

Our proposed plunger-gate controlled transient current in a single-photon mode influenced QD system should be observable due to recent rapid progress of measurement technology [49]. The realization of a single-photon influenced QD device and the generation of plunger-gate controlled transient transport may be useful in quantum computation applications.

Acknowledgments

This work was financially supported by the Icelandic Research and Instruments Funds, the Research Fund of

the University of Iceland, The Nordic High Performance Computing facility in Iceland, and the National Science Council in Taiwan through Contract No. NSC100-2112-M-239-001-MY3.

References

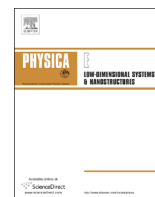
- [1] Nakamura Y, Pashkin Yu A and Tsai J S 1999 Coherent control of macroscopic quantum states in a single-Cooper-pair box *Nature* **398** 786
- [2] Villavicencio J, Moldonado I, Sanchez R, Cota E and Platero G 2008 Single quantum dot nanowire photodetectors *Appl. Phys. Lett.* **92** 192102
- [3] van Kouwen M P, van Weert M H M, Reimer M E, Akopian N, Perinetti U, Algra R E, Bakkers E P A M, Kouwenhoven L P and Zwiller V 2010 Tunnel spectroscopy in ac-driven quantum dot nanoresonators *Appl. Phys. Lett.* **97** 113108
- [4] Jin S, Hu Y, Gu Z, Liu L and Wu H-C 2011 Application of quantum dots in biological imaging *J. Nanomater.* **2011** 834139
- [5] Pedersen M H and Büttiker M 1998 Scattering theory of photon-assisted electron transport *Phys. Rev. B* **58** 12993–3006
- [6] Stoof T H and Nazarov Yu V 1996 Time-dependent resonant tunneling via two discrete states *Phys. Rev. B* **53** 1050–3
- [7] Torres L E F F 2005 Mono-parametric quantum charge pumping: interplay between spatial interference and photon-assisted tunneling *Phys. Rev. B* **72** 245339
- [8] Kouwenhoven L P, Jauhar S, McCormick K, Dixon D, McEuen P L, Nazarov Yu V, van der Vaart N C and Foxon C T 1994 Photon-assisted tunneling through a quantum dot *Phys. Rev. B* **50** 2019–22
- [9] Niu C and Lin D L 1997 Electron population inversion in photon-assisted tunneling through a quantum wire *Phys. Rev. B* **56** R12752
- [10] Hu Q 1993 Photon-assisted quantum transport in quantum point contacts *Appl. Phys. Lett.* **62** 837
- [11] Tang C S and Chu C S 2000 Coherent quantum transport in the presence of a finite-range transversely polarized time-dependent field *Physica B* **292** 127–35
- [12] Wätzel J, Moskalenko A S and Berakdar J 2011 Photon-induced spin filtering in a double quantum dot *Appl. Phys. Lett.* **99** 192101
- [13] Shibata K, Umeno A, Cha K M and Hirakawa K 2012 Photon-assisted tunneling through self-assembled InAs quantum dots in the terahertz frequency range *Phys. Rev. Lett.* **109** 077401
- [14] Ishibashi K and Aoyagi Y 2002 Interaction of electromagnetic wave with quantum dots *Physica B* **314** 437–43
- [15] Imamoglu A and Yamamoto Y 1994 Turnstile device for heralded single photons: Coulomb blockade of electron and hole tunneling in quantum confined p–i–n heterojunctions *Phys. Rev. Lett.* **72** 210–3
- [16] Joshi A, Hassan S S and Xiao M 2011 Photon-assisted tunneling current in a double quantum dot excitonic system *Appl. Phys. A* **102** 537–44
- [17] Reinhard A, Volz T, Winger M, Badolato A, Hennessy K J, Hu E L and Imamoglu A 2012 Strongly correlated photons on a chip *Nature Photon.* **6** 93–6
- [18] Hennessy K J, Badolato A, Winger M, Gerace D, Atatüre M, Gulde S, Fält S, Hu E L and Imamoglu A 2012 Quantum nature of a strongly coupled single quantum dot-cavity system *Nature* **444** 896–9
- [19] Delbecq M R, Schmitt V, Parmentier F D, Roch N, Viennot J J, Fève G, Huard B, Mora C, Cottet A and Kontos T 2011 Coupling a quantum dot, fermionic leads, and a microwave cavity on a chip *Phys. Rev. Lett.* **107** 256804
- [20] Toida H, Nakajima T and Komiyama S 2013 Vacuum Rabi splitting in a semiconductor circuit QED system *Phys. Rev. Lett.* **110** 066802
- [21] Mukamel S 2003 Quantum extension of the Jarzynski relation: analogy with stochastic dephasing *Phys. Rev. Lett.* **90** 170604
- [22] Monnai T 2005 Unified treatment of the quantum fluctuation theorem and the Jarzynski equality in terms of microscopic reversibility *Phys. Rev. E* **72** 027102
- [23] Esposito M and Mukamel S 2006 Fluctuation theorems for quantum master equations *Phys. Rev. E* **73** 046129
- [24] Crooks G E 2008 Quantum operation time reversal *Phys. Rev. A* **77** 034101
- [25] Rammer J, Shelankov A L and Wabnig J 2004 Quantum measurement in charge representation *Phys. Rev. B* **70** 115327
- [26] Luo J, Li X-Q and Yan Y 2007 Calculation of the current noise spectrum in mesoscopic transport: a quantum master equation approach *Phys. Rev. B* **76** 085325
- [27] Welack S, Esposito M, Harbola U and Mukamel S 2008 Interference effects in the counting statistics of electron transfers through a double quantum dot *Phys. Rev. B* **77** 195315
- [28] Lambropoulos P, Nikolopoulos G M, Nielsen T R and Bay S 2000 Fundamental quantum optics in structured reservoirs *Rep. Prog. Phys.* **63** 455
- [29] Van Kampen N G 2001 *Stochastic Processes in Physics and Chemistry* 2nd edn (Amsterdam: North-Holland)
- [30] Harbola U, Esposito M and Mukamel S 2006 Quantum master equation for electron transport through quantum dots and single molecules *Phys. Rev. B* **74** 235309
- [31] Gurvitz S A and Prager Ya S 1996 Microscopic derivation of rate equations for quantum transport *Phys. Rev. B* **53** 15932–43
- [32] Braggio A, König J and Fazio R 2006 Full counting statistics in strongly interacting systems: non-Markovian effects *Phys. Rev. Lett.* **96** 026805
- [33] Emary C, Marcos D, Aguado R and Brandes T 2007 Frequency-dependent counting statistics in interacting nanoscale conductors *Phys. Rev. B* **76** 161404
- [34] Bednorz A and Belzig W 2008 Formulation of time-resolved counting statistics based on a positive-operator-valued measure *Phys. Rev. Lett.* **101** 206803
- [35] Vaz E and Kyriakidis J 2010 Transient dynamics of confined charges in quantum dots in the sequential tunneling regime *Phys. Rev. B* **81** 085315
- [36] Gudmundsson V, Gainar C, Tang C-S, Moldoveanu V and Manolea A 2009 Time-dependent transport via the generalized master equation through a finite quantum wire with an embedded subsystem *New J. Phys.* **11** 113007
- [37] Jonasson O, Tang C-S, Goan H-S, Manolescu A and Gudmundsson V 2012 Nonperturbative approach to circuit quantum electrodynamics *Phys. Rev. E* **86** 046701
- [38] Abdullah N R, Tang C-S and Gudmundsson V 2010 Time-dependent magnetotransport in an interacting double quantum wire with window coupling *Phys. Rev. B* **82** 195325
- [39] Gudmundsson V, Jonasson O, Tang C-S, Goan H-S and Manolescu A 2012 Time-dependent transport of electrons through a photon cavity *Phys. Rev. B* **85** 075306
- [40] Yannouleas C and Landman U 2007 Symmetry breaking and quantum correlations in finite systems: studies of quantum dots and ultracold Bose gases and related nuclear and chemical methods *Rep. Prog. Phys.* **70** 2067
- [41] Breuer H-P and Petruccione F 2002 *The Theory of Open Quantum Systems* (Oxford: Oxford University Press)

- [42] Esposito M, Harbola U and Mukamel S 2007 Entropy fluctuation theorems in driven open systems: application to electron counting statistics *Phys. Rev. E* **76** 031132
- [43] Jin J S, Zheng X and Yan Y 2008 Exact dynamics of dissipative electronic systems and quantum transport: hierarchical equations of motion approach *J. Chem. Phys.* **128** 234703
- [44] Haake F 1971 Density operator and multitime correlation functions for open systems *Phys. Rev. A* **3** 1723–34
- [45] Haake F 1973 *Quantum Statistics in Optics and Solid-state Physics (Springer Tracts in Modern Physics)* vol 66, ed G Hohler and E A Niekisch (Berlin: Springer) p 98
- [46] Gudmundsson V, Jonasson O, Arnold Th, Tang C-S, Goan H-S and Manolescu A 2013 Stepwise introduction of model complexity in a general master equation approach to time-dependent transport *Fortschr. Phys.* **61** 305
- [47] Kouwenhoven L P, Jauhar S, Orenstein J, McEuen P L, Nagamune Y, Motohisa J and Sakaki H 1994 Observation of photon-assisted tunneling through a quantum dot *Phys. Rev. Lett.* **73** 3443–6
- [48] Arnold T, Tang C-S, Manolescu A and Gudmundsson V 2013 Magnetic-field-influenced nonequilibrium transport through a quantum ring with correlated electrons in a photon cavity *Phys. Rev. B* **87** 035314
- [49] Fève G, Mahé A, Berroir J-M, Kontos T, PlacMais B, Glatli D C, Cavanna A, Etienne B and Jin Y 2007 Stepwise introduction of model complexity in a general master equation approach to time-dependent transport *Science* **316** 1169

Article II

Delocalization of electrons by cavity photons in transport through a quantum dot molecule.

N. R. Abdullah, C-S Tang, A. Manolescu, and V. Gudmundsson
Physica E: Low-dimensional Systems and Nanostructures **64**, 254 (2014).



Delocalization of electrons by cavity photons in transport through a quantum dot molecule



Nzar Rauf Abdullah ^{a,*}, Chi-Shung Tang ^b, Andrei Manolescu ^c, Vidar Gudmundsson ^a

^a Science Institute, University of Iceland, Dunhaga 3, IS-107 Reykjavik, Iceland

^b Department of Mechanical Engineering, National United University, 1, Lienda, Miaoli 36003, Taiwan

^c School of Science and Engineering, Reykjavik University, Menntavegur 1, IS-101 Reykjavik, Iceland

ARTICLE INFO

Article history:

Received 27 May 2014

Accepted 29 July 2014

Available online 7 August 2014

Keywords:

Cavity quantum electrodynamics

Electronic transport

Quantum dot

Electro-optical effect

ABSTRACT

We present results on cavity-photon-assisted electron transport through two lateral quantum dots embedded in a finite quantum wire. The double quantum dot system is weakly connected to two leads and strongly coupled to a single quantized photon cavity mode with initially two linearly polarized photons in the cavity. Including the full electron–photon interaction, the transient current controlled by a plunger-gate in the central system is studied by using quantum master equation. Without a photon cavity, two resonant current peaks are observed in the range selected for the plunger gate voltage: The ground state peak, and the peak corresponding to the first-excited state. The current in the ground state is higher than in the first-excited state due to their different symmetry. In a photon cavity with the photon field polarized along or perpendicular to the transport direction, two extra side peaks are found, namely, photon-replica of the ground state and photon-replica of the first-excited state. The side-peaks are caused by photon-assisted electron transport, with multiphoton absorption processes for up to three photons during an electron tunneling process. The inter-dot tunneling in the ground state can be controlled by the photon cavity in the case of the photon field polarized along the transport direction. The electron charge is delocalized from the dots by the photon cavity. Furthermore, the current in the photon-induced side-peaks can be strongly enhanced by increasing the electron–photon coupling strength for the case of photons polarized along the transport direction.

© 2014 Elsevier B.V. All rights reserved.

An opto-electronic device provides a different platform of electron transport, namely photon-assisted transport (PAT) [1]. In the PAT, the energy levels of an electronic system have to match to photon frequency of a radiation source to control the electron motion. Therefore, the photon emission and the photon absorption processes play an essential role to enhance electron transport [2]. For that purpose, an electrostatic potential produced by a plunger-gate is applied to the electronic system to shift its energy levels in and out of resonance. The plunger-gate is widely used to control charge current [3], thermal current [4], photo-current [5] and spin-dependent current [6] for various quantized systems coupled to photon radiation.

The PAT controlled by plunger-gate has been investigated to study electrical [7] and optical [8,9] properties of a double-quantum dot (DQD) system, in which the PAT can be used as a spectroscopic tool in two different regimes defined by a zero [10], and non-zero [11] bias voltage. At zero-bias voltage, the DQD

works as a proper electron pumping device in which the photon absorption process leads to electron tunneling producing a dc current. In the non-zero bias voltage, both the photon absorption and the photon emission processes generate a dc current. Recently, both regimes have been realized experimentally in a DQD system at low temperature [12,13].

The most important application of a DQD system in the quantum regime is intended for information storage in a quantum state [14], quantum-bits for quantum computing [15,16], and quantum information processing in two-state system [17]. Recent experimental work has focused on using the two lowest energy states contributing to tunneling processes in a DQD working as a two state system: The ground state resonance, and a photon-induced excited state resonance. They observed multiphoton absorption processes up to the four-order contributing to the electron transport [13].

Based on the above-mentioned considerations, we analyze PAT in serial double quantum dots embedded in a quantum wire. The DQD system is connected to two leads and coupled to a photon cavity with linearly polarized photons in the *x*- and *y*-directions, where the transport along the quantum wire is in the *x*-direction. As will be seen in our results the essential difference from the

* Corresponding author.

E-mail addresses: nra1@hi.is (N.R. Abdullah), cstang@nuu.edu.tw (C.-S. Tang), vidar@hi.is (V. Gudmundsson).

more traditional modeling of photo assisted transport is the presence of a photon cavity with few photons and the fact that we will monitor the resonant transport in the transient regime approaching a steady state regime for single-electron tunneling processes.

A quantum master equation (QME) formalism is utilized to investigate transient transport of electrons controlled by the plunger-gate in the system without and with a single-photon mode [3]. Generally, there are two types of QME when characterized according to memory effects, energy-dependent coupling, and the system-leads coupling strength: The Markovian and the non-Markovian QME. In the case of the Markovian approximation, the system-leads coupling is assumed weak and independent of energy, memory effect are ignored and most commonly a steady state is sought [18–21]. In the non-Markovian approach, the system is energetically coupled to the leads including memory effect in the system [22–24]. Since we are interested in studying transient transport of electrons in a regime with possible resonances, the non-Markovian model is used in our system [25].

In addition, we assume the DQD system to be connected to the leads through a non-zero or small bias window, where the two lowest energy states of the QDQ system can be isolated in the bias window: The ground state and the first-excited state. Our model of the DQD system can be seen as a qubit. In which the states $|0\rangle$ and $|1\rangle$ can be represented in terms of the ground state and the first-excited state. We will show how the single-photon mode affects the electron transport through both states when located in the bias window and demonstrate the role of photon activated states in the transient current. The double serial quantum dot is essential here: The two lowest single-electron states of the dot molecule have very different symmetry. The ground state has a symmetric wavefunction, but the excited state has an antisymmetric one. The conduction through the ground state is thus higher than through the excited one. The “inter-dot tunneling” can be influenced by a photon mode polarized in the transport direction, thus strongly modifying the conduction through the photon replicas of the states in a photon cavity. The nontrivial details of this picture will be analyzed in this paper reminding us that the effects rely on the geometry of the system and states beyond the ground state and the first excited one.

The rest of the paper is organized as follows. In Section 1 we introduce the model to describe the electron transport through a DQD embedded in a quantum wire connected to two leads and a photon cavity. Section 2 contains two subsections, the system without and with the photon cavity. In the absence of the photon cavity, the transient current through the system controlled by the plunger-gate is demonstrated in the presence of the electron–electron interactions in the DQD system. In the photon cavity, the photon-assisted electron transport in the system is presented for a system initially with no electron, but with two linearly polarized photons in the single-photon mode. Finally, conclusions are provided in Section 3.

1. Model and computational methods

The aim of this study is to model a photon-assisted electron transport in a DQD system connected to two identical electron reservoirs (lead) and coupled to a single photon mode in a cavity. Our first step is to look at the central system, in which electrons are confined in two dimensions. We assume a finite quantum wire with hard-wall ends at $x = \pm L_x/2$ with length $L_x = 165$ nm. It is parabolically confined in the y -direction (perpendicular to the transport direction) with transverse confinement energy $\hbar\Omega_0 = 2.0$ meV. The embedded quantum dots are modeled by

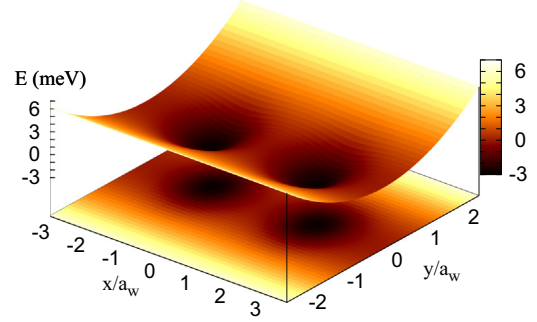


Fig. 1. Schematic diagram depicts the potential representing the DQD embedded in a quantum wire with parameters $B = 0.1$ T, $a_w = 23.8$ nm, and $\hbar\Omega_0 = 2.0$ meV.

two identical Gaussian potentials in the quantum wire defined as

$$V_{\text{DQD}}(x, y) = \sum_{i=1}^2 V_i \exp[-\beta_i^2 ((x-x_i)^2 + y^2)], \quad (1)$$

with quantum-dot strength $V_{1,2} = -2.8$ meV, $x_1 = 35$ nm, $x_2 = -35$ nm, and $\beta_{1,2} = 5.0 \times 10^{-2} \text{ nm}^{-1}$ such that the radius of each quantum-dot is $R_{\text{QD}} \approx 20$ nm. A sketch of the DQD system under investigation is shown in Fig. 1. We should mention that the distance between the dots is $L_{\text{DQD}} = 35 \text{ nm} \approx 1.47a_w$, and each dot is $25 \text{ nm} = 1.05a_w$ away from the nearest lead, where a_w is the effective magnetic length.

The DQD system is in a rectangular photon cavity with a single photon mode. The photons in the single photon mode are linearly polarized in the x - or y -directions, meaning that the photon polarization in the cavity is assumed to be parallel or perpendicular to the transport direction with respect to the electric field

$$\mathbf{A}_{\text{ph}} = A_{\text{ph}}(a + a^\dagger)\hat{\mathbf{e}}, \quad (2)$$

where A_{ph} is the amplitude of the photon vector potential, $a^\dagger(a)$ are the creation (annihilation) operators for a photon, respectively, and $\hat{\mathbf{e}}$ determines the polarization with

$$\hat{\mathbf{e}} = \begin{cases} (e_x, 0), & \text{TE}_{011} \\ (0, e_y), & \text{TE}_{101}, \end{cases}$$

where TE_{011} (TE_{101}) indicates the parallel (perpendicular) polarized photon in the transport direction, respectively.

In the following sections, we shall couple the DQD system to both the photon cavity and the leads.

1.1. DQD system coupled to cavity

We consider the closed DQD system to be strongly coupled to a photon cavity. The many-body (MB) Hamiltonian

$$H_S = H_{\text{DQD}} + H_{\text{Cavity}} + H_{\text{Int}} \quad (3)$$

consists of the Hamiltonian for the closed DQD system with the electron–electron interaction H_{DQD} , the free photon cavity Hamiltonian H_{Cavity} , and the Hamiltonian for the electron–photon interaction H_{Int} .

The DQD system (and the external leads) is placed in an external uniform perpendicular magnetic field $B\hat{z}$ in the z -direction defining an effective lateral confinement length $a_w = (\hbar/m^* \sqrt{(\omega_c^2 + \Omega_0^2)})^{1/2}$, where the effective electron mass is $m^* = 0.067m_e$ for GaAs material and $\omega_c = eB/m^*c$ is the cyclotron frequency. The Hamiltonian for the DQD system in a magnetic field including the electron–electron interaction can be written as

$$H_{\text{DQD}} = \sum_{ij} \langle \psi_i | \left\{ \frac{\pi_e^2}{2m^*} + V_{\text{DQD}} + eV_{\text{pg}} \right\} | \psi_j \rangle \delta_{ij} d_i^\dagger d_j + H_{\text{Coul}} + H_Z, \quad (4)$$

where $|\psi_i\rangle$ stands for a single-electron (SE) states, V_{pg} is the plunger gate potential that shifts the energy levels of the DQD system with respect to the chemical potentials of the leads, d_i^\dagger (d_i) is an operator that creates (annihilates) an electron in the DQD system, respectively. Moreover, the canonical momentum is $\pi_e = \mathbf{p} + (e/c)\mathbf{A}_{ext}$ with the kinetic momentum operator \mathbf{p} , and the vector potential in the Landau gauge $\mathbf{A}_{ext} = (0, -By, 0)$. The electron–electron interaction in the central system is given by

$$H_{Coul} = \frac{1}{2} \sum_{ijrs} V_{ijrs} d_i^\dagger d_j^\dagger d_s d_r, \quad (5)$$

with the Coulomb matrix elements V_{ijrs} [26]. The characteristic Coulomb energy is $E_C = e^2/(2\epsilon_r a_w) \approx 2.44$ meV at $B = 0.1$ T with $a_w = 23.8$ nm and $\epsilon_r = 12.4$, the dielectric constant of GaAs. The characteristic Coulomb energy is greater than the thermal energy of the leads. An exact numerical diagonalization method is used here for solving the Coulomb interacting many-electron (ME) Hamiltonian in a truncated Fock space to obtain the ME energy spectrum of the DQD system [27]. The Zeeman Hamiltonian shown in the third part of Eq. (4) describes the interaction between the external magnetic field and the magnetic moment of an electron

$$H_Z = \pm \frac{g^* \mu_B B}{2}, \quad (6)$$

where \pm stands for z-spin components, $\mu_B = e\hbar/2m_e c$ is the Bohr magneton, and the effective Lande g-factor is $g^* = -0.44$ for GaAs.

In order to investigate photon-assisted electron transport in the DQD system, the electronic system is coupled to a photon cavity. The Hamiltonian of the free photon cavity is given by

$$H_{Cavity} = \hbar\omega_{ph} \hat{N}_{ph}, \quad (7)$$

where $\hbar\omega_{ph}$ is the energy of the single mode in the cavity, and $\hat{N}_{ph} = a^\dagger a$ is the photon number operator. The interaction of the single quantized electromagnetic mode with the electronic system is described by the Hamiltonian including both the diamagnetic and the paramagnetic interaction of photons and electrons

$$H_{Int} = g_{ph} \sum_{ij} d_i^\dagger d_j g_{ij} \{a + a^\dagger\} + \frac{g_{ph}^2}{\hbar\Omega_w} \sum_i d_i^\dagger d_i \left[\hat{N}_{ph} + \frac{1}{2}(a^\dagger a^\dagger + aa + 1) \right] \quad (8)$$

herein, $g_{ph} = eA_{ph}\Omega_w a_w/c$ is the electron–photon coupling strength, and g_{ij} are dimensionless electron–photon coupling matrix elements [28].

Finally, the MB system Hamiltonian H_S is diagonalized in a MB Fock-space $\{|\tilde{\alpha}\rangle\}$ to obtain the MB energy spectrum of the DQD system coupled to the photon cavity [29]. The diagonalization builds a new interacting MB state basis $\{|\tilde{\nu}\rangle\}$, in which $|\tilde{\nu}\rangle = \sum_\alpha \mathcal{W}_{\mu\alpha} |\tilde{\alpha}\rangle$ with $\mathcal{W}_{\mu\alpha}$ being a unitary transformation matrix. The unitary transformation is used to convert the QME and the physical observables from non-interacting MB basis to the interacting MB basis.

1.2. DQD system connected to leads

The DQD system is connected to two semi-infinite leads with the same width. The chemical potential of the lead l is μ_l , with $l \in \{L, R\}$ being the left L and the right R lead. The Fermi function in the isolated lead l before coupling to the central system is $f_l(\epsilon_l(\mathbf{q})) = [\exp[\epsilon_l(\mathbf{q}) - \mu_l] + 1]^{-1}$, where ϵ_l is the SE subband energy of the lead l (\mathbf{q} is the momentum dummy index [3].) found from the non-interacting ME Hamiltonian of lead l

$$H_l = \int d\mathbf{q} \epsilon_l(\mathbf{q}) c_{ql}^\dagger c_{ql}, \quad (9)$$

with c_{ql}^\dagger (c_{ql}) the electron creation(annihilation) operator in lead l , respectively [30].

In order to instigate electron transport between the subsystems, the DQD system is coupled to the leads with energy dependent coupling coefficients reflecting the geometry of the system

$$T_{qil} = \int d\mathbf{r} d\mathbf{r}' \psi_{ql}(\mathbf{r}')^* g_{qil}(\mathbf{r}, \mathbf{r}') \psi_i^S(\mathbf{r}). \quad (10)$$

An electron may be transferred from a state $|\mathbf{q}\rangle$ with the wavefunction $\psi_{ql}(\mathbf{r}')$ in the leads to a SE state $|i\rangle$ with the SE wavefunction $\psi_i^S(\mathbf{r})$ in the DQD system and vice versa, where the coupling function is $g_{qil}(\mathbf{r}, \mathbf{r}')$ [25]. The coupling coefficients are utilized to construct a time-dependent coupling Hamiltonian in the second quantization language

$$H_{TI}(t) = \chi_l(t) \sum_i \int d\mathbf{q} [c_{ql}^\dagger T_{qil} d_i + d_i^\dagger (T_{qil})^* c_{ql}], \quad (11)$$

with a time-dependent switching function $\chi_l(t) = 1 - 2\{\exp[\alpha_l(t - t_0)] + 1\}^{-1}$ with $\alpha_l = 0.3$ ps $^{-1}$ being a switching parameter.

After the DQD system is coupled to the leads at $t=0$, we calculate the time evolution of the electrons and photons using the density operator and its equation of motion, the Liouville-von Neumann (Lv-N) equation $i\hbar\dot{W}(t) = [H(t), W(t)]$ for the whole system. As this cannot be accomplished we resort to using a projection formalism taking a trace over the Hilbert space of the leads introducing the reduced density operator

$$\rho(t) = \text{Tr}_L \text{Tr}_R W(t) \quad (12)$$

with $\rho(t_0) = \rho_S$ [31] and the condition that $W(t < t_0) = \rho_L \rho_R \rho_S$ is the density operator of the total system before the coupling with ρ_S being the density operator of the isolated DQD system [32]. The density operator of the leads before the coupling is $\rho_l = \exp[-\beta(H_l - \mu_l N_l)] / \text{Tr}_l \{\exp[-\beta(H_l - \mu_l N_l)]\}$, where $\beta = 1/k_B T_l$ is the inverse thermal energy, and N_l is the number operator for electrons in the lead l [30].

The time-dependent mean charge in the central system and the current in the leads are calculated from the reduced density operator as has been detailed in earlier publications [3,29].

We choose to explore the charging currents at time $t=220$ ps. At this time point the transport through the single-electron states lying low in the energy spectrum has almost reached a steady state in case of no photon cavity. This will not necessarily be the case for the photon replicas of the states when the system is placed in a cavity with strong coupling to the electrons, but we still observe charging resonances into these states. We are thus studying resonant transport through the central system in the transient to the steady state regime. The charge is strictly conserved in the total system, central system and leads, but not in the central system in the transient regime. The central system is an open system, weakly coupled to the leads.

2. Numerical results

In this section, we discuss the transport properties through the DQD system controlled by plunger-gate voltage in both cases without a photon cavity and with x- or y-polarized photons in a cavity.

In order to obtain the PAT, the system has to satisfy the following conditions: the MB energy level spacing has to be greater than the thermal energy $\Delta E_{MB} > k_B T$, and the MB energy level spacing has to be smaller or equal to the photon energy $\Delta E_{MB} \leq \hbar\omega_{ph}$ [33]. Initially the temperature of the central system is assumed to be $T=0$ K, and the leads are at $T=0.01$ K initially. Other physical parameters of the system are presented in Table 1.

In addition, we assume the external magnetic field to be $B=0.1$ T with the effective lateral confinement length $a_w=23.8$ nm and initially no electron is in the DQD system.

2.1. The DQD system without a photon cavity

In this section, the properties of the electron transport through the DQD system are presented in the absence of the photon cavity in order to establish a comparison for later results for transport through the system inside a cavity.

Fig. 2(a) shows the energy spectrum of the leads versus wave number qa_w . The horizontal black lines are chemical potentials of the left lead μ_L and the right lead μ_R . The chemical potentials are considered to be $\mu_L=1.4$ meV and $\mu_R=1.3$ meV, implying a small bias voltage $\Delta\mu=0.1$ meV. Therefore, the first subband in the parabolic energy spectrum becomes the most active subband contributing to the electron transport process in the energy range [1.3,1.4] meV.

In Fig. 2(b), the ME energy spectrum of the DQD-system as a function of applied plunger-gate voltage V_{pg} is shown. The energies of two-electron states $N_e=2$ (2ES, blue dots) are higher than the SE states $N_e=1$ (1ES, red dots) due to the electron–electron interaction. In the absence of the photon cavity, two resonant SE states are situated in the bias window for the range of plunger gate voltage selected here, namely, the ground state resonance and first-excited state resonance (blue squared dots).

The almost degenerate two spin states of the single-electron ground state are $|2\rangle$ and $|3\rangle$ with energies $E_2=1.343$ meV and $E_3=1.346$ meV. These two states get into resonance with the first-subband of the leads at $V_{pg}^G=1.2$ mV, where the superscript G refers to the ground state. By tuning the plunger-gate voltage, the two spin states of the first-excited state $|4\rangle$ and $|5\rangle$ with energies $E_4=1.358$ meV and $E_5=1.361$ meV contribute to the electron

transport at $V_{pg}^{FE}=0.8$ mV, where the superscript FE stands for the first-excited state.

Fig. 3 displays the left current I_L (red solid) and the right current I_R (dashed blue) through the DQD system. We notice two resonance peaks in the currents: The ground state peak at $V_{pg}^G=1.2$ mV and the first-excited state peak at $V_{pg}^{FE}=0.8$ mV. The reason for the two current peaks is resonance of the SE states in the DQD system with the first subband energy of the leads. An electron in the first-subband of the left lead may tunnel to the state $|2\rangle$ or $|3\rangle$ of the DQD system and subsequently tunnel out to the right lead. Consequently the ground state peak is observed at $V_{pg}^G=1.2$ mV. In addition, the first-excited state peak reflects a resonance with the states $|4\rangle$ and $|5\rangle$ at plunger-gate potential $V_{pg}^{FE}=0.8$ mV.

Fig. 4 shows the charge density distribution in the DQD system at time $t=220$ ps (after the initial transient, close to a steady state) in the ground state peak (a), and the first-excited state peak (b).

In the case of the ground state peak at $V_{pg}^G=1.2$ mV, the electron state accumulates in the dots with a strong inter-dot tunneling. Therefore, the left and right currents increase in the system. But in the case of first-excited state peak at $V_{pg}^{FE}=0.8$ mV, the electron state is strongly localized in the dots without much tunneling between the dots. Thus the tunneling between the dots is sufficiently suppressed and the current drops as shown in Fig. 3.

2.2. x -photon polarization (TE_{011} mode)

In this section we analyze the electron transport through the DQD system in the presence of an x -polarized single-photon mode with initially two photons in the cavity. The photons in the cavity can excite electrons in the DQD system and enhance the electric current, similar to the “classical” PAT case [11]. The condition for PAT involving N_{ph} photon(s) is $|E_i - E_f| = N_{ph}\hbar\omega_{ph}$ [34], where $E_i(E_f)$

Table 1
Characteristic energy scales of the system.

Quantity	Typical parameter
Thermal energy in leads ($k_B T$)	$\approx 8.6 \times 10^{-4}$ meV
Characteristic Coulomb energy (E_C)	≈ 2.44 meV
Photon energy ($\hbar\omega_{ph}$)	$= 0.25$ meV

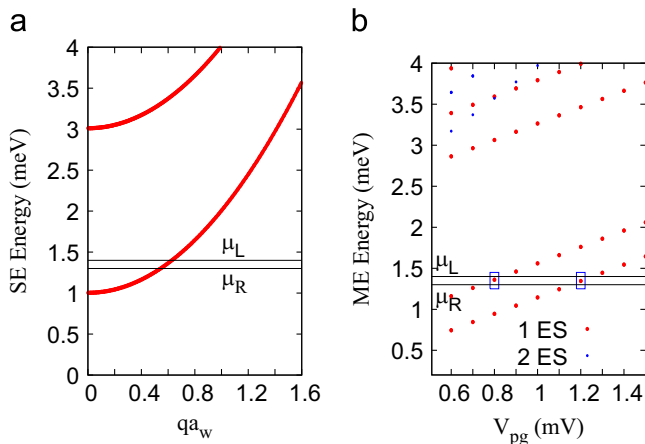


Fig. 2. Energy spectra in the case of no photon cavity with magnetic field $B=0.1$ T. (a) SE energy spectrum in the leads (red) is plotted as a function of scaled wave number qa_w , where the chemical potentials are $\mu_L=1.4$ meV and $\mu_R=1.3$ meV (black). (b) ME energy spectrum in the central system as a function of plunger gate voltage V_{pg} including SE states (1ES, red dots) and two electron states (2ES, blue dots). The SE state in the bias window is almost doubly degenerate due to the small Zeeman energy. (For interpretation of the references to color in this figure caption, the reader is referred to the web version of this paper.)

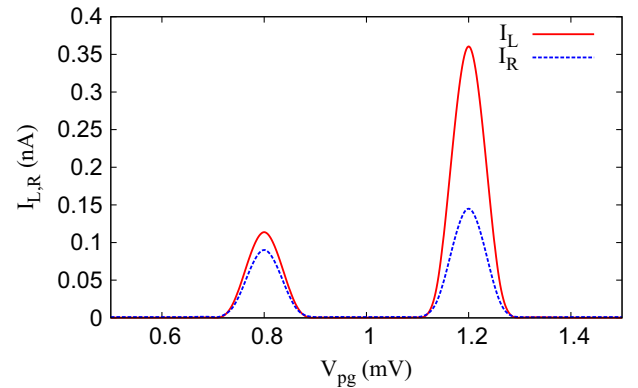


Fig. 3. The left current I_L (red solid) and right current I_R (blue dashed) are plotted as a function of plunger gate voltage V_{pg} at time $t=220$ ps in the case of no photon cavity. Other parameters are $B=0.1$ T and $\Delta\mu=0.1$ meV. (For interpretation of the references to color in this figure caption, the reader is referred to the web version of this paper.)

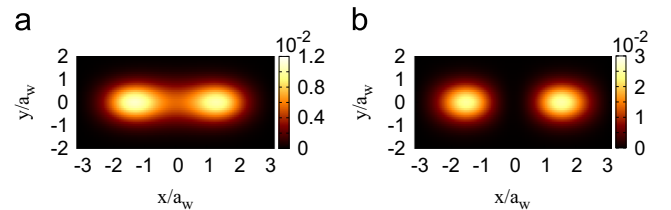


Fig. 4. The charge density distribution at $t=220$ ps in the ground state peak (a) and first-excited state peak (b) shown in Fig. 3 in the case with no photon cavity. Other parameters are $B=0.1$ T, $a_w=23.8$ nm, $L_x=165$ nm $=6.93a_w$, and $\Delta\mu=0.1$ meV.

is the highest possible initial (lowest possible final) MB energy level of the DQD system, respectively [33]. We vary the applied plunger-gate to match $|E_i - E_f|$ to the photon energy, thus the PAT is an active process in the system.

Fig. 5 shows the MB energy spectrum of the DQD system including the photons with zero-electron states $N_e=0$ (OES, green dots) and SE states $N_e=1$ (1ES, red dots).

In addition to the former states at $V_{pg}^G = 1.2$ mV and $V_{pg}^{FE} = 0.8$ mV, two extra active MB-states are observed in the presence of the photon cavity at $eV_{pg}^{G;FE} = eV_{pg}^{G;FE} - \hbar\omega_{ph}$ in the bias window (pink squared dots), where the photon energy is $\hbar\omega_{ph} = 0.25$ meV, and $G_r(FE_r)$ stands for the photon-replica of the ground state(first-excited state), respectively. We notice that all states in the bias window are SE states containing only one-electron $N_e = 1$.

Fig. 6 displays the left current I_L (a) and the right current I_R (b) as a function of the plunger-gate voltage V_{pg} in the presence of the x -polarized photon field at time $t=220$ ps for different electron-photon coupling strength $g_{ph} = 0.1$ meV (blue solid), 0.2 meV (green dashed), and 0.3 meV (red dotted). The positive value of the left current indicates electrons tunneling from the left lead to the DQD system, while the negative value of the right current denotes electrons tunneling from the right lead to the DQD system and vice versa.

In the absence of the photon cavity, two main-peaks are found at $V_{pg}^{FEM} = 0.8$ mV and $V_{pg}^{GM} = 1.2$ mV as shown in Fig. 3. In the presence of the photon cavity, two extra side-peaks at $eV_{pg}^{GS;FES} = eV_{pg}^{GM;FEM} - \hbar\omega_{ph}$ are observed in addition to the original main-peaks at $V_{pg}^{GM;FEM}$. The superscripts GM(FEM) refers to the ground states(first-excited state) main-peak, respectively, and GS (FES) stands for photon-induced ground state(first-excited state) side-peak, respectively.

The side-peaks indicate the PAT, where the system satisfies $e|V_{pg}^{GM;FEM} - V_{pg}^{GS;FES}| \cong \hbar\omega_{ph}$ [33]. The two new side-peaks at $V_{pg}^{GS} = 0.95$ mV and $V_{pg}^{FES} = 0.55$ mV shown in Fig. 6 are caused by photon-replica of the ground state and photon-replica of the first-excited state, respectively. We find that the separation of the photon replica side-peaks from the original main-peaks corresponds to the photon energy.

It should be noted that the current in the photon-induced side-peaks is strongly enhanced by increasing the electron-photon

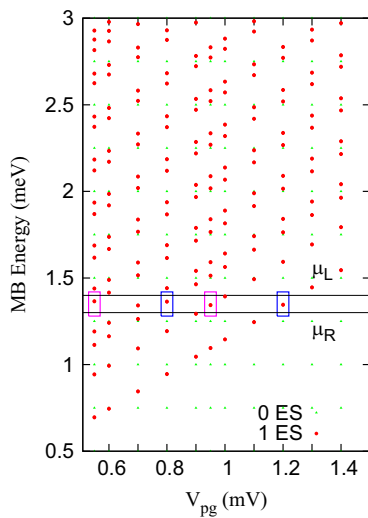


Fig. 5. MB Energy spectrum versus the plunger gate voltage V_{pg} in the case of x -polarized photon field, where OES indicates zero electron states ($N_e=0$, green dots), and 1ES stands for single electron states ($N_e=1$, red dots). Other parameters are $B=0.1$ T, $\Delta\mu=0.1$ meV, and $\hbar\omega_{ph}=0.25$ meV. (For interpretation of the references to color in this figure caption, the reader is referred to the web version of this paper.)

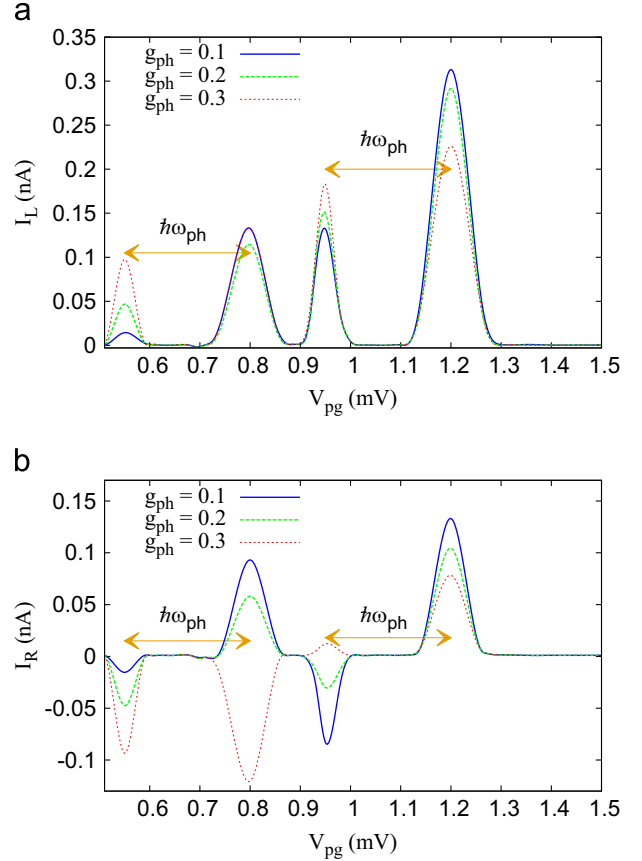


Fig. 6. The left current I_L (a), and the right current I_R (b) versus the plunger gate voltage V_{pg} in the case of x -polarized photon field at time $t=220$ ps with different electron-photon coupling strength: $g_{ph} = 0.1$ meV (blue solid), 0.2 meV (green dashed), and 0.3 meV (red dotted). Other parameters are $\hbar\omega_{ph}=0.25$ meV, $\Delta\mu=0.1$ meV, and $B=0.1$ T. (For interpretation of the references to color in this figure caption, the reader is referred to the web version of this paper.)

coupling strength. Thus the photon-induced side-peaks exhibits a PAT process with different photon absorption mechanisms from the main-peaks.

In order to show the dynamics of the PAT process involved in the formation of the photon-induced side-peaks in the left and right current shown in Fig. 6, we schematically present the photon absorption process in Fig. 7.

Fig. 7(a) demonstrates the tunneling processes forming the FES at $V_{pg}^{FES} = 0.55$ mV. The electron from the left or the right lead absorbs two photons and is transferred to the MB states containing two photons $N_{ph}=2$ (red solid arrows) situated above the bias window with photon energy $\hbar\omega_{ph}$. The electron tunneling process in the states containing one photon $N_{ph}=1$ (blue dashed arrows) and three photons $N_{ph}=3$ (green dashed arrows) is very weak. Fig. 7(b) shows the dynamical mechanism that makes the GS at $V_{pg}^{GS} = 0.95$ mV. In addition to the electron tunneling in the state containing two photons $N_{ph}=2$ (red solid arrows), the tunneling process in one photon state $N_{ph}=1$ (blue solid arrows) and three photons $N_{ph}=3$ states (green solid arrows) becomes active. The tunneling mechanism here is a multiphoton absorption process with up to three photons with a strong inter-dot tunneling. In which the electron is scattered between one, two, and three photon(s) states by absorbing and emitting photon energy $N_{ph} \times \hbar\omega_{ph}$. The two photons state here has a shorter lifetime than the two photons' states in the FES, because whenever an electron from the left lead tunnels into the two photon states in the DQD system it subsequently directly tunnels out to the right lead.

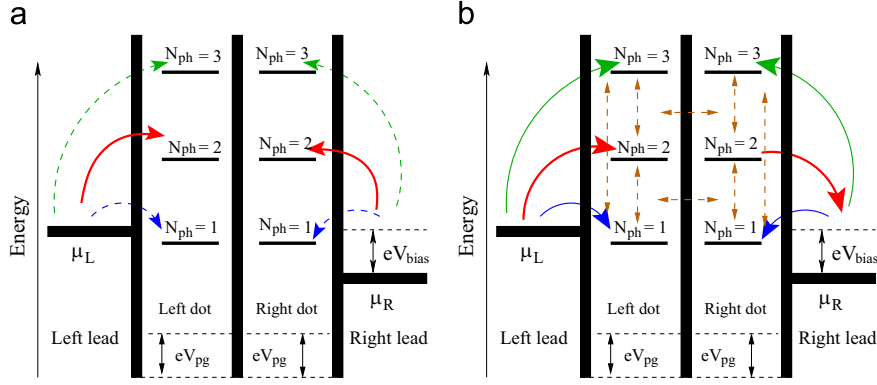


Fig. 7. Schematic representation of photon-activated resonance energy levels and electron transition by changing the plunger gate voltage V_{pg} in the photon-induced first-excited state side-peak at $V_{pg}^{FES} = 0.55$ mV (a), and the photon-induced ground state side-peak at $V_{pg}^{GS} = 0.95$ mV (b) of Fig. 6. The DQD-system is embedded in a photo cavity with the photon energy $\hbar\omega_{ph}$ and photon content N_{ph} in each many-body state. The chemical potential difference is $eV_{bias} = \Delta\mu = \mu_L - \mu_R$. (For interpretation of the references to color in this figure caption, the reader is referred to the web version of this paper.)

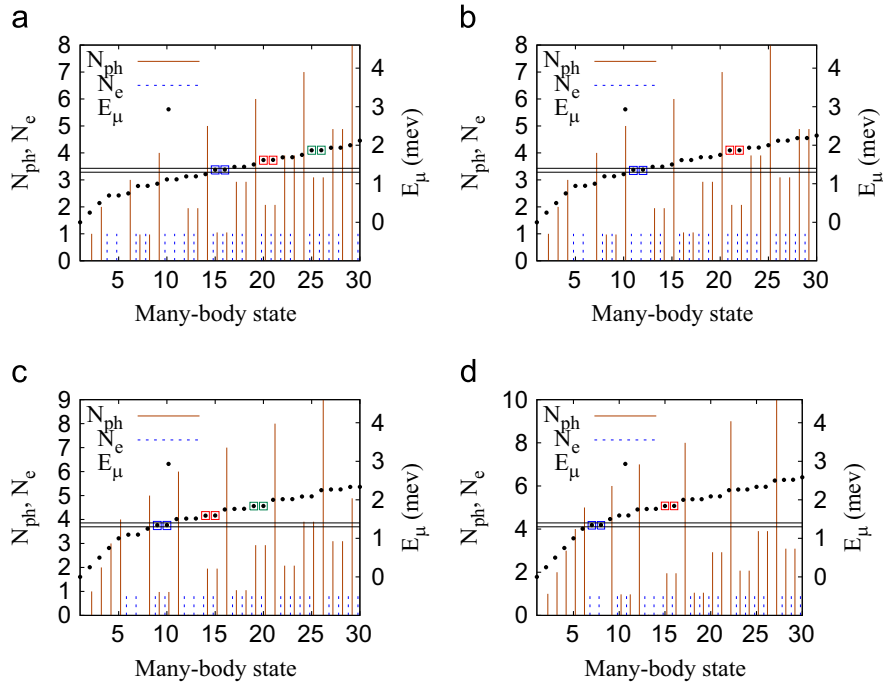


Fig. 8. The MB energy spectrum E_μ (dotted black), the mean electron number in the MB state (\bar{n}) (blue dashed line), the mean photon number N_{ph} (red line) in the case of x-polarized field with plunger-gate voltage at (a) photon-induced first-excited side-peak $V_{pg}^{FES} = 0.55$ mV, (b) first-excited main-peak $V_{pg}^{FEM} = 0.8$ mV, (c) photon-induced ground-state side-peak $V_{pg}^{GS} = 0.95$ mV, and (d) ground-state main-peak $V_{pg}^{GM} = 1.2$ mV of Fig. 6 for the case of $g_{ph} = 0.1$ meV (blue solid line). The chemical potentials are $\mu_L = 1.4$ meV and $\mu_R = 1.3$ meV (black line), thus $\Delta\mu = 0.1$ meV. Other parameters are $B = 0.1$ T, and $\hbar\omega_{ph} = 0.25$ meV. The color of the square is referred to in the text. (For interpretation of the references to color in this figure caption, the reader is referred to the web version of this paper.)

To further illustrate the characteristics of the most active MB states in the tunneling process forming the two main current peaks and the two side current peaks in Fig. 6, we present Fig. 8 which shows the characteristics of the MB states at plunger-gate voltage $V_{pg}^{FES} = 0.55$ mV (a), $V_{pg}^{FEM} = 0.8$ mV (b), $V_{pg}^{GS} = 0.95$ mV (c), and $V_{pg}^{GM} = 1.2$ mV (d) in the case of $g_{ph} = 0.1$ meV.

Fig. 8(a) indicates how the FES is contributed to by the MB states at $V_{pg}^{FES} = 0.55$ mV. Since there are two photons initially in the cavity, we shall seek the MB-states that contain one, two, and three photon(s), to observe multiple inelastic electron scattering in the states of DQD system at the side-peaks [2]. Here, we focus on six MB states, two inactive MB states $|15\rangle$ and $|16\rangle$ in the bias window (blue squared dot) with $N_{ph} = 1.052$ in each state and the energies $E_{15} = 1.364$ meV and $E_{16} = 1.366$ meV. There are four MB states above the bias window: Two photon-activated states $|20\rangle$ and $|21\rangle$ (red squared dot) with $N_{ph} = 2.073$ in each state and

energies $E_{20} = 1.616$ meV and $E_{21} = 1.618$ meV, and two more MB states $|25\rangle$ and $|26\rangle$ (green squared dot) with $N_{ph} = 3.094$ in each state and energies $E_{25} = 1.867$ meV and $E_{26} = 1.870$ meV. We clearly see that the energy difference between the inactive states and the photon-activated states is appropriately equal to the $(N_{ph,ac} - N_{ph,in}) \times \hbar\omega_{ph}$, where $N_{ph,ac}$ and $N_{ph,in}$ are the photon number in the photon-activated states and the inactive states, respectively. We observe that the electrons can undergo the following possible tunneling process: An electron from either lead may absorb two photons from the cavity being transferred to two photons' states $|20\rangle$ and $|21\rangle$ with absorption energy $E_{20} - E_{15} = (N_{ph,20} - N_{ph,15}) \times \hbar\omega_{ph} \simeq 0.252$ meV or $E_{21} - E_{16} = (N_{ph,21} - N_{ph,16}) \times \hbar\omega_{ph} \simeq 0.252$ meV which is approximately equal to the energy required to transfer an electron from the leads to two photons' states as schematically shown in Fig. 7(a). Therefore, the two photon absorption mechanism dominates here

without making electron inelastic scattering to the one and three photon states. The electron tunneling process from the leads to the DQD system suggests that the electrons are collected in either individual dot.

Fig. 8(b) shows the MB states of the first-excited state main-peak at $V_{pg}^{FEM} = 0.8$ mV. There are two inactive states $|11\rangle$ and $|12\rangle$ (blue squared dot) with energies $E_{11} = 1.362$ meV and $E_{12} = 1.364$ meV in the bias window ($N_e = 1$, $N_{ph} = 0.029$) and two photon-activated states $|21\rangle$, and $|22\rangle$ (red squared dot) with energies $E_{21} = 1.866$ meV and $E_{22} = 1.868$ meV above the bias window ($N_e = 1$, $N_{ph} = 2.073$). The photon-activated states that contain two photons are responsible for the electron transport with energy values $E_{21} - E_{11} \cong (N_{ph,21} - N_{ph,11}) \times \hbar\omega_{ph} \cong 0.504$ meV or $E_{22} - E_{12} \cong (N_{ph,22} - N_{ph,12}) \times \hbar\omega_{ph} \cong 0.504$ meV.

Fig. 8(c) demonstrates the MB states that participate in the electron transport in the GS at $V_{pg}^{GS} = 0.95$ mV. The electron transport mechanism here is different from the one for the FES. The contributions to the GS is by the following significant MB states: Two active MB states $|9\rangle$ and $|10\rangle$ (blue squared dot) containing $N_{ph} = 0.976$ with energies $E_9 = 1.342$ meV and $E_{10} = 1.344$ meV are located in the bias window, two photon-activated states $|14\rangle$ and $|15\rangle$ (red squared dot) have $N_{ph} = 1.95$ above the bias window with energies $E_{14} = 1.5901$ meV and $E_{15} = 1.5902$ meV, and two more photon-activated states $|19\rangle$ and $|20\rangle$ (green squared dot) contain $N_{ph} = 2.93$ with energies $E_{19} = 1.838$ meV and $E_{20} = 1.840$ meV. Significantly, these six MB states participate in the electron transport with the following important photon absorption processes with inter-dot tunneling as schematically shown previously in Fig. 7(b): (1) Electron from either lead absorbs one photon tunneling to the one photon states $|9\rangle$ and $|10\rangle$. (2) An electron from the left lead absorbs two photons and is transferred to two photons' states $|14\rangle$ and $|15\rangle$ with absorption energy $E_{14} - E_9 = (N_{ph,14} - N_{ph,9}) \times \hbar\omega_{ph} \cong 0.248$ meV or $E_{15} - E_{10} = (N_{ph,15} - N_{ph,10}) \times \hbar\omega_{ph} \cong 0.247$ meV which is approximately equal to the energy required to transfer electron from one photon state to two photons' states, then the electron tunnels to the right lead emitting photons. (3) Absorbing three photons, an electron from either the left lead or the right lead transfers to three photons states $|19\rangle$ and $|20\rangle$ with energy $E_{19} - E_9 = (N_{ph,19} - N_{ph,9}) \times \hbar\omega_{ph} \cong 0.496$ meV or $E_{20} - E_{10} = (N_{ph,20} - N_{ph,10}) \times \hbar\omega_{ph} \cong 0.496$ meV that is approximately the energy amount needed to transfer an electron to a three photons' state. The tunneling processes from the leads to the DQD system and all activated six-MB states suggest that the electrons perform multiple scattering absorption and emission processes between the states in each individual dot with inter-dot tunneling. These possible tunneling processes indicate to us that the existence of the FES is caused by multiphoton absorption processes with up to three photons. In addition, we should mention that the tunneling process from the left lead to two photon states in the DQD system and the tunnel out to the right lead decreases the dwell time of electron in the central system, while the dwell time of electron in the FES was longer due to charge accumulation in the DQD system.

Fig. 8(d) demonstrates the MB states of the ground state main-peak at $V_{pg}^{GM} = 1.2$ mV. Four MB states are also important here, two inactive states $|7\rangle$ and $|8\rangle$ (blue squared dot) with energies $E_7 = 1.344$ meV and $E_8 = 1.346$ meV in the bias window ($N_e = 1$, $N_{ph} = 0.029$) and two photon-activated states $|15\rangle$ and $|16\rangle$ (red squared dot) with energies $E_{15} = 1.840$ meV and $E_{16} = 1.842$ meV above the bias window ($N_e = 1$, $N_{ph} = 1.951$). The energy difference between photon-activated states above the bias window and the inactive states in the bias window satisfies the same rule of the FEM, such that $E_{15} - E_7 \cong (N_{ph,15} - N_{ph,7}) \times \hbar\omega_{ph} \cong 0.496$ meV and $E_{16} - E_8 \cong (N_{ph,16} - N_{ph,8}) \times \hbar\omega_{ph} \cong 0.496$ meV.

These results suggest that each photon-activated state above the bias window has two more photons than the inactive states in the bias window at both the main peaks. When an electron from

the left lead tunnels to the DQD system it absorbs (or forms a quasi-particle with) two photons from the cavity and is transferred to the photon-activated states above the bias window, then it tunnels to the right lead. Therefore, both main-peaks are caused by two photons absorption processes in the transport.

Observing all these photon activated processes it is important to have in mind that the fact that we retained the dia- and the paramagnetic parts of the electron–photon interaction (Eq. (8)) thus allowing for a broader range of transitions possibilities than only the paramagnetic term describes.

Fig. 9 indicates the charge density distribution in the DQD system with x -polarized photon field at plunger-gate $V_{pg}^{FES} = 0.55$ mV (a), $V_{pg}^{FEM} = 0.8$ mV (b), $V_{pg}^{GS} = 0.95$ mV (c), and $V_{pg}^{GM} = 1.2$ mV (d) of Fig. 6 at time $t = 220$ ps and $g_{ph} = 0.1$ meV.

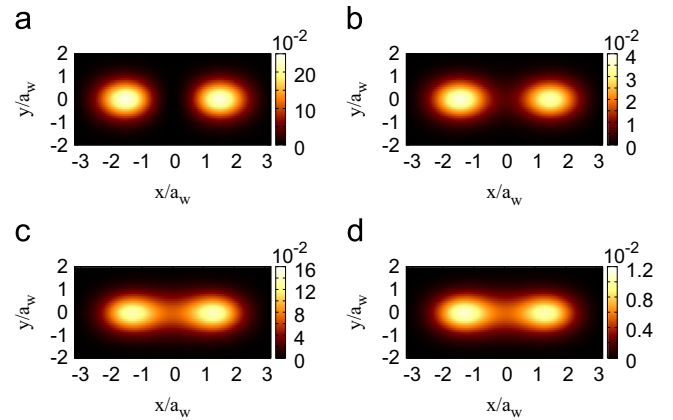


Fig. 9. The charge density distribution of the DQD system with x -polarized photon field at time 220 ps corresponding to (a) photon-induced first-excited side-peak $V_{pg}^{FES} = 0.55$ mV, (b) first-excited main-peak $V_{pg}^{FEM} = 0.8$ mV, (c) photon-induced ground-state side-peak $V_{pg}^{GS} = 0.95$ mV, and (d) ground-state main-peak $V_{pg}^{GM} = 1.2$ mV of Fig. 6. for the case of $g_{ph} = 0.1$ meV (blue solid line). Other parameters are $\hbar\omega_{ph} = 0.25$ meV, $B = 0.1$ T, $a_w = 23.8$ nm, $L_x = 300$ nm, and $\hbar\omega_0 = 2.0$ meV. (For interpretation of the references to color in this figure caption, the reader is referred to the web version of this paper.)

In the FES at $V_{pg}^{FES} = 0.55$ mV, the electron charge density forms two peaks which are strongly localized in the dots without inter-dot tunneling shown in Fig. 9(a), thus the electron dwell time is increased and the electrons stay longer time in the DQD system.

In the case of $V_{pg}^{FEM} = 0.8$ mV, the electrons are accumulated in the dots with a weak inter-dot tunneling. Comparing to the case with no photon cavity Fig. 4(a), a slight inter-dot tunneling is observed indicating charge polarization between the dots. As a result, the electron charge density is slightly enhanced in the x -polarized photon field, but more importantly it is also slightly delocalized resulting in a higher conductance through the serial dot molecule.

In the GS at $V_{pg}^{GS} = 0.95$ mV, the electron charge density is enhanced and exhibits charge accumulation in the dots with a very strong inter-dot tunneling shown in Fig. 9(c) which decreases the electron dwell time in the DQD-system. This is the reason why the current in the GS is relatively higher than the current in FES.

In the case of $V_{pg}^{GM} = 1.2$ mV, the electron–photon interactions do not have a big effect on the charge density distribution, the charge distribution of the dots is already overlapping.

2.3. y -photon polarization (TE_{101} mode)

In this section, we assume the photon-cavity is linearly polarized in the y -direction with photon energy $\hbar\omega_{ph} = 0.25$ meV and initially two photons in the single photon mode. The MB energy spectrum of the DQD-system in the y -polarization is very similar

to that in the x -polarization photon mode as shown in Fig. 5. Two extra MB states are observed with the spin states of the ground state and first-excited state in the bias window, the extra MB states indicate the photon-replica states in the presence of the photon cavity.

Fig. 10 shows the left current (a) and the right current (b) at time $t=220$ ps for different electron–photon coupling strength $g_{ph}=0.1$ meV, (blue solid), 0.2 meV (green dashed), and 0.3 meV (red dotted). Similar to the x -polarized photon field, two extra photon-induced side-peaks at $V_{pg}^{FES}=0.55$ mV and $V_{pg}^{GS}=0.95$ mV are observed with the main-peaks at $V_{pg}^{FEM}=0.8$ mV and $V_{pg}^{GM}=1.2$ mV. A very weak current enhancement in the photon-induced side-peaks is predicted by increasing the electron–photon coupling strength, while the current enhancement in the photon-induced side-peaks is very strong in the x -polarized photon field shown in Fig. 6. The weaker effects for the y -polarization are expected since the photon energy is farther from resonance for states describing motion in that direction, i.e. the confinement energy in the y -direction is much higher.

The characteristics of the MB states in the bias window and above the bias window in the y -polarized photon field are very similar to that in the x -direction shown in Fig. 8. The main-peaks and the photon-induced side-peaks in the y -polarized photon are contributed to by almost the same absorption processes of the x -polarized photon.

Fig. 11 demonstrates the charge density distribution in the DQD system in the case of y -polarized photon field at plunger-gate voltage $V_{pg}^{FES}=0.55$ mV FES (a), $V_{pg}^{FEM}=0.8$ mV FEM (b),

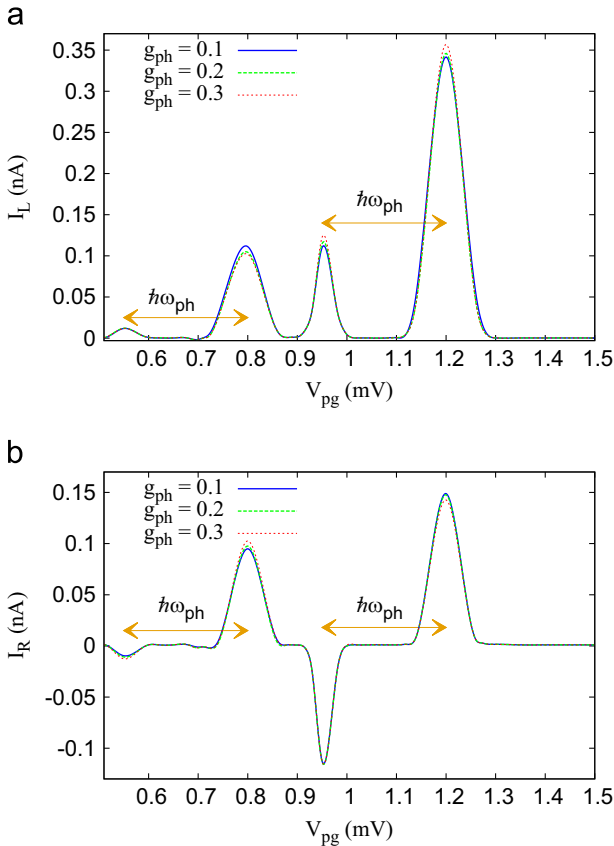


Fig. 10. The left current (a) and the right current (b) versus the plunger gate voltage V_{pg} at time ($t=220$ ps) in the case of y -polarized photon field. The electron–photon coupling is changed to be $g_{ph}=0.1$ meV (blue solid), 0.2 meV (green dashed), and 0.3 meV (red dotted). Other parameters are $\hbar\omega_{ph}=0.25$ meV, $\Delta\mu=0.1$ meV, and $B=0.1$ T. (For interpretation of the references to color in this figure caption, the reader is referred to the web version of this paper.)

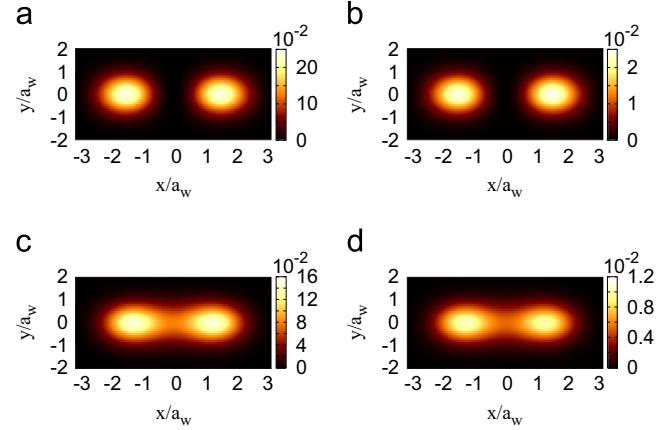


Fig. 11. The charge density distribution of the DQD system with y -polarized photon field at time 220 ps corresponding to (a) photon-induced first-excited side-peak $V_{pg}^{FES}=0.55$ mV, (b) first-excited main-peak $V_{pg}^{FEM}=0.8$ mV, (c) photon-induced ground-state side-peak $V_{pg}^{GS}=0.95$ mV, and (d) ground-state main-peak $V_{pg}^{GM}=1.2$ mV of Fig. 10 for the case of $g_{ph}=0.1$ meV (blue solid line). Other parameters are $\hbar\omega_{ph}=0.25$ meV, $B=0.1$ T, $a_w=23.8$ nm, $L_x=300$ nm, and $\hbar\Omega_0=2.0$ meV. (For interpretation of the references to color in this figure caption, the reader is referred to the web version of this paper.)

$V_{pg}^{GS}=0.95$ mV GS (c), and $V_{pg}^{GM}=1.2$ mV GM (d) shown in Fig. 10, at time $t=220$ ps and $g_{ph}=0.1$ meV.

In the case of $V_{pg}^{FES}=0.55$ mV (FES), the electrons are strongly localized in the dots with no electron tunneling from the left-dot to the right-dot.

In FEM at $V_{pg}^{FEM}=0.8$ mV, the electron makes a resonance state localized in each dot without inter-dot tunneling, while a weak inter-dot tunneling was observed in the x -polarized photon field at FEM shown in Fig. 9(b). Therefore, the electron dwell time in the DQD system in y -polarized photon is longer than that in the x -polarized photon at FEM.

But at $V_{pg}^{GS}=0.95$ mV (GS), the inter-dot tunneling is very strong and electrons prefer to make inelastic multiple scattering in each dot with inter-dot tunneling.

In GM at $V_{pg}^{GM}=1.2$ mV, the electrons form a state accumulated in the dots with a strong electron tunneling between the dots similar to the charge density distribution in the x -polarization shown in Fig. 9(d). Thus, the current in the GM is higher than that in the FES.

3. Conclusions

We have demonstrated a plunger-gate controlled photon-assisted transient electronic transport through a DQD system that is placed in a photon cavity with initially two linearly polarized photons. The serial double quantum dot molecule is important since the two lowest states of it have very different properties reflecting the fact that the wavefunction of one is symmetric, but antisymmetric of the other.

We analyzed the electron transport through the system without and with a photon cavity by using a non-Markovian QME formalism. In the absence of a photon cavity, two current peaks were found: Ground state peak and a peak due to the first-excited state, originating from resonance energy levels of the DQD system with the first-subband energy of the leads. These two states could be used for a qubit in a quantum computer, in which the ground state resonance exhibits a strong inter-dot electron tunneling while the electrons in the first-excited state resonance form a state localized in each dot.

In the presence of either longitudinally or transversely polarized cavity photon field, two extra side-peaks are found: A peak

due to the photon-replica of the ground state, and a photon replica of the first-excited state. The appearance of side-peaks is due to PAT of electrons in the DQD system. The characteristics of the photon activated MB states have been used to analyze the nature of the PAT. The peak due to the photon-replica of ground state is caused by multiphoton absorption processes with up to three photons. In the peak caused by the photon replica of the first-excited state, the electrons in the leads are transferred to two-photons states in the DQD system accumulation charge in the individual dots without inter-dot tunneling. Furthermore, the current in the photon-induced side-peaks is strongly enhanced by increasing electron–photon coupling strength in the x -polarized of the photon field, while a very slightly enhancement in the photon-induced side-peak current was observed in the y -polarization photon. This discrepancy between the polarizations is explained by the anisotropy of the confinement of the central system.

Change in the photon–electron coupling strength alters the inter-dot tunneling sensitively, altering the conduction through the system. To describe this effect properly it is important to include many higher energy states in the system. Along the similar line of thought our calculations show that in the present system photon processes of more than one photon are important.

The fact that we include both the para- and diamagnetic terms in the electron–photon interaction leads to complex photon–electron processes that all contribute to the PAT resonance peaks observed. This has to be viewed in light of the common practice to use only the paramagnetic part in two-level systems in order to calculate PAT phenomena. In many systems the geometry matters, and the both parts of the interaction can be important for strong enough coupling.

References

- [1] G. Wailfred, v.d. Wiel, T. Fujisawa, S. Tarucham, L.P. Kouwenhoven, *Jpn. J. Appl. Phys.* 40 (2001) 2100.
- [2] W.G. van der Wiel, S. De Franceschi, J.M. Elzerman, T. Fujisawa, S. Tarucham, L.P. Kouwenhoven, *Rev. Modern Phys.* 75 (2003).
- [3] N.R. Abdullah, C.S. Tang, A. Manolescu, V. Gudmundsson, *J. Phys.: Condens. Matter* 25 (2013) 465302.
- [4] M. Bagheri Tagani, H. Rahimpour Soleimani, *Phys. B: Condens. Matter* 413 (2013) 86.
- [5] C. Xu, M.G. Vavilov, *Phys. Rev. B* 87 (2013) 035429. <http://dx.doi.org/10.1103/PhysRevB.87.035429>.
- [6] F.M. Souza, T.L. Carrara, E. Vernek, *Phys. Rev. B* 84 (2011) 115322. <http://dx.doi.org/10.1103/PhysRevB.84.115322>.
- [7] J. Wätzel, A.S. Moskalenko, J. Berakdar, *Appl. Phys. Lett.* 99 (2011) 192101.
- [8] G. Muñoz Matutano, M. Royo, J.I. Climente, J. Canet-Ferrer, D. Fuster, P. Alonso-González, I. Fernández-Martínez, J. Martínez-Pastor, Y. González, L. González, F. Briones, B. Alén, *Phys. Rev. B* 84 (2011) 041308. <http://dx.doi.org/10.1103/PhysRevB.84.041308>.
- [9] P. Kaczmarkiewicz, P. Machnikowski, T. Kuhn, *J. Appl. Phys.* 114 (2013) 183108.
- [10] C.A. Stafford, N.S. Wingreen, *Phys. Rev. Lett.* 76 (1996) 1916.
- [11] T.H. Stoof, Y.V. Nazarov, *Phys. Rev. B* 53 (1996) 1050.
- [12] R. Shang, H.-O. Li, G. Gao, M. Xiao, T. Tu, H. Jiang, G.-C. Guo, G.-P. Guo, *Appl. Phys. Lett.* 103 (2013) 162109.
- [13] K. Shibata, A. Umeno, K.M. Cha, K. Hirakawa, *Phys. Rev. Lett.* 109 (2012) 077401. <http://dx.doi.org/10.1103/PhysRevLett.109.077401>.
- [14] A. Imamoglu, Y. Yamamoto, *Phys. Rev. Lett.* 72 (1994) 210. <http://dx.doi.org/10.1103/PhysRevLett.72.210>.
- [15] D. Loss, D.P. DiVincenzo, *Phys. Rev. A* 57 (1998) 120.
- [16] D.P. DiVincenzo, *Science* 309 (2005).
- [17] L.I. Chuang, M.A. Nielsen, *Quantum Computation and Quantum Information*, Cambridge University Press, New York, US, 2010.
- [18] E. Vaz, J. Kyriakidis, *Phys. Rev. B* 81 (2010) 085315. <http://dx.doi.org/10.1103/PhysRevB.81.085315>.
- [19] S.A. Gurvitz, Y.S. Prager, *Phys. Rev. B* 53 (1996) 15932. <http://dx.doi.org/10.1103/PhysRevB.53.15932>.
- [20] U. Harbola, M. Esposito, S. Mukamel, *Phys. Rev. B* 74 (2006) 235309.
- [21] N.G. Van Kampen, *Stochastic Processes in Physics and Chemistry*, 2nd ed., North-Holland, Amsterdam, 2001.
- [22] A. Bednorz, W. Belzig, *Phys. Rev. Lett.* 101 (2008) 206803. <http://dx.doi.org/10.1103/PhysRevLett.101.206803>.
- [23] A. Braggio, J. König, R. Fazio, *Phys. Rev. Lett.* 96 (2006) 026805. <http://dx.doi.org/10.1103/PhysRevLett.96.026805>.
- [24] C. Emary, D. Marcos, R. Aguado, T. Brandes, *Phys. Rev. B* 76 (2007) 161404. <http://dx.doi.org/10.1103/PhysRevB.76.161404>.
- [25] V. Gudmundsson, C. Gainar, C.-S. Tang, V. Moldoveanu, A. Manolescu, *New J. Phys.* 11 (2009) 113007.
- [26] N.R. Abdullah, C.-S. Tang, V. Gudmundsson, *Phys. Rev. B* 82 (2010) 195325. <http://dx.doi.org/10.1103/PhysRevB.82.195325>.
- [27] C. Yannouleas, U. Landman, *Rep. Prog. Phys.* 70 (2007) 2067.
- [28] V. Gudmundsson, O. Jonasson, C.-S. Tang, H.-S. Goan, A. Manolescu, *Phys. Rev. B* 85 (2012) 075306. <http://dx.doi.org/10.1103/PhysRevB.85.075306>.
- [29] V. Gudmundsson, O. Jonasson, T. Arnold, C.-S. Tang, H.-S. Goan, A. Manolescu, *Fortschr. Phys.* 61 (2013) 305.
- [30] J.S. Jin, X. Zheng, Y. Yan, *J. Chem. Phys. Lett.* 128 (2008) 234703.
- [31] F. Haake, *Phys. Rev. A* 3 (1971) 1723. <http://dx.doi.org/10.1103/PhysRevA.3.1723>.
- [32] H.-P. Breuer, F. Petruccione, *The Theory of Open Quantum Systems*, Oxford University Press, Oxford, 2002.
- [33] L.P. Kouwenhoven, S. Jauhar, J. Orenstein, P.L. McEuen, Y. Nagamune, J. Motohisa, H. Sakaki, *Phys. Rev. Lett.* 73 (1994) 3443. <http://dx.doi.org/10.1103/PhysRevLett.73.3443>.
- [34] G. Platero, R. Aguado, *Phys. Rep.* 395 (2004) 1.

Article III

Cavity-photon-switched coherent transient transport in a double quantum waveguide.

N. R. Abdullah, C-S Tang, A. Manolescu, and V. Gudmundsson
Journal of Applied Physics **116**, 233104 (2014).

Cavity-photon-switched coherent transient transport in a double quantum waveguide

Nzar Rauf Abdullah,^{1,a)} Chi-Shung Tang,² Andrei Manolescu,³ and Vidar Gudmundsson^{1,b)}

¹*Science Institute, University of Iceland, Dunhaga 3, IS-107 Reykjavik, Iceland*

²*Department of Mechanical Engineering, National United University, 1, Lienda, 36003 Miaoli, Taiwan*

³*School of Science and Engineering, Reykjavik University, Menntavegur 1, IS-101 Reykjavik, Iceland*

(Received 21 October 2014; accepted 10 December 2014; published online 19 December 2014)

We study a cavity-photon-switched coherent electron transport in a symmetric double quantum waveguide. The waveguide system is weakly connected to two electron reservoirs, but strongly coupled to a single quantized photon cavity mode. A coupling window is placed between the waveguides to allow electron interference or inter-waveguide transport. The transient electron transport in the system is investigated using a quantum master equation. We present a cavity-photon tunable semiconductor quantum waveguide implementation of an inverter quantum gate, in which the output of the waveguide system may be selected via the selection of an appropriate photon number or “photon frequency” of the cavity. In addition, the importance of the photon polarization in the cavity, that is, either parallel or perpendicular to the direction of electron propagation in the waveguide system is demonstrated. © 2014 AIP Publishing LLC.

[<http://dx.doi.org/10.1063/1.4904907>]

I. INTRODUCTION

In quantum information technology, researchers seek quantum storage devices to develop a quantum computer, in which a qubit is used as an elementary unit for encoding information. In practice, several systems have been suggested to build a qubit. Among many based on semiconductors promising are, for example, double quantum dots¹ and double quantum waveguides (DQW).²

A semiconductor waveguide can be defined as a quantum wire conserving the phase coherence of electrons in the system at low temperature.³ Two parallel quantum waveguides separated by an electrostatic potential barrier and coupled via a coupling region or a window to facilitate an interference between the waveguides, may be one of the candidates to construct a qubit.^{4,5} The characteristics of the transport of electrons through the double waveguide system determines possible quantum logic operations.⁶ A Not-operation is realized if an electron switches from the first waveguide to the second waveguide,⁷ and a square-root-of-Not-operation ($\sqrt{\text{NOT}}$) is formed if the electron wave splits equally between the waveguides.⁸

Several proposals have been suggested to control the electron motion in a waveguide system that provides the qubit operation such as: Magnetic switching, an external magnetic field can be used to transfer an electron wave between two asymmetric waveguides;⁹ Electrostatic potential switching, the coupling window (CW) can be defined by a saddle potential that washes out fluctuation resonance peaks and increases the speed of electron switching processes between the waveguides;¹⁰ A single quantum dot close to the coupling window has been considered to enhance

electron inter-waveguide transport in a Coulomb blockade regime;¹¹ and Electron switching by using acoustic waves.¹²

There are still non-trivial aspects that need to be investigated concerning the control of electron switching in a DQW system for implementing an action of a quantum logic gate. In this work, we show how a cavity-photon can implement a quantum logic gate action in a single semiconductor qubit that is embedded in a photon cavity with a single quantum mode. A qubit system can be constructed from a coupled double semiconductor waveguide. Our DQW system consists of symmetric control- and target-waveguides with a window is placed between them to facilitate inter-waveguide transport. The DQW is weakly connected to two leads with asymmetric coupling, where the left lead is coupled only to the control-waveguide while the right lead is connected to both the control- and the target-waveguide. The DQW system is in a photon cavity, in which the photons can be polarized parallel (x -direction) or perpendicular (y -direction) to the direction of electron propagation with a fixed electron-photon coupling strength. A non-Markovian quantum master equation (QME) is used to explore the electron transport through the DQW system caused by a bias between the external leads.^{13,14}

In the absence of a photon cavity, we observe oscillations in the charge current by varying the length of the CW. The oscillations are caused by inter-waveguide transport due to interference of states between the guides. In the presence of the photon cavity, the current oscillations are affected by the photon polarization, the number of photons, and the photon frequency as these cavity parameters influence the interference between the states in the waveguide system. Therefore, the electron motion can be manipulated to implement a quantum logic gate action by the cavity photon. In the x -polarized photon field, a $\sqrt{\text{NOT}}$ -operation and a NOT-operation quantum logic gates are obtained by tuning the

^{a)}Electronic mail: nra1@hi.is

^{b)}Electronic mail: vidar@raunvis.hi.is

photon number in the cavity. For the y -polarized photon field, electron-switching process can be accomplished if the energy of “absorbed photon(s)” is equal or greater than the confinement energy of electron in that direction in the waveguide system. The many-body (MB) cavity-photon-switching is of importance as yet another mechanism to implement quantum logic gate operations in a semiconductor qubit.

The paper is organized as follows: In Sec. II, we present the model describing the window-coupled double waveguide system based on the QME approach. Section III presents our numerical results and discussion. Concluding remarks are addressed in Sec. IV.

II. MODEL AND THEORETICAL METHOD

We model a two dimensional symmetric double quantum wire in a perpendicular magnetic field. The double waveguide system is placed in a photon cavity, as schematically shown in Fig. 1(a). The waveguide system is connected to two external leads with different chemical potentials μ_l , where l refers to the left (L) or the right (R) lead, respectively. The DQW system consists of a control- and a target-waveguide with the same width providing a symmetric

double waveguide system. A window is placed between the waveguides with length L_{CW} (red arrow) to facilitate inter-waveguide transport. The DQW and the leads are exposed to an external magnetic field B in the z -direction. The total system is designed such that the electrons in the left lead are only injected into the control-waveguide (blue dashed arrow).

Figure 1(b) shows the DQW potential whose dimensions are characterized by the effective magnetic length a_w . The DQW system has a hard-wall confinement in x -direction at $x = \pm L_x/2$, where L_x is the length of the waveguide system and parabolic confinement in the y -direction with, $V_c(y) = \frac{1}{2}m^*\Omega_0^2y^2$, where $\hbar\Omega_0$ is the characteristic energy. The DQW potential is described as

$$V_{DQW}(\mathbf{r}) = V_B \exp(-\beta_0^2 y^2) + V_{CW} \exp(-\beta_x^2 x^2 - \beta_y^2 y^2). \quad (1)$$

The first term of Eq. (1) represents a potential barrier between the quantum waveguide with $V_B = 18.0$ meV and $\beta_0 = 0.03$ nm $^{-1}$. The second term defines the potential of the CW with $V_{CW} = -18.0$ meV and $\beta_y = 0.03$ nm $^{-1}$ implying a barrier width $W_B \simeq 66.5$ nm for the first subband. The CW length can be estimated as $L_{CW} = 2/\beta_x$ and which influences the electron transport between the waveguides. The effective magnetic length, $a_w = \sqrt{\hbar/(m^*\Omega_w)}$, with $\Omega_w^2 = \Omega_0^2 + (eB/m^*)^2$, here essentially the natural length scale of the y -confinement, due to the low magnetic field B , serves as a natural length scale to refer all other lengths to.

A. DQW coupled to cavity

Now, we demonstrate how the DQW system is coupled to the photon cavity. The Hamiltonian of the system can be described by a MB Hamiltonian that describes the DQW and the photon cavity. The MB Hamiltonian consists of the electronic DQW including electron-electron interaction, the photon cavity, and the interaction between the DQW and the photon cavity. The Hamiltonian of the total system can be written as¹⁵

$$\begin{aligned} H_S = & \sum_{n,n'} \langle \psi_n | \left[\frac{\left(\pi_e + \frac{e}{c} \mathbf{A}_{ph} \right)^2}{2m^*} + V_{DQW} \right] | \psi_{n'} \rangle d_n^\dagger d_{n'} \\ & + \frac{1}{2} \sum_{\substack{nn' \\ mm'}} (V_{Coul})_{nn',mm'} d_n^\dagger d_{n'}^\dagger d_m d_{m'} \\ & + \hbar\omega_{ph} a^\dagger a + g_{ph} \sum_{n,n'} d_n^\dagger d_{n'} g_{nn'} \{a + a^\dagger\} \\ & + \frac{g_{ph}^2}{\hbar\Omega_w} \sum_n d_n^\dagger d_n \left[\hat{N}_{ph} + \frac{1}{2} (a^\dagger a^\dagger + aa + 1) \right]. \end{aligned} \quad (2)$$

The first term of Eq. (2) describes the DQW system without the electron-electron interaction, where $|\psi\rangle$ is a single-electron SE state, m^* is the effective mass of an electron, e is the electron charge, and d_n^\dagger and $d_{n'}$ are the electron creation and annihilation operators, respectively. In addition, $\pi_e = p + \frac{e}{c} \mathbf{A}_{ext}$, where p is the momentum operator, \mathbf{A}_{ext} is the vector potential for the static magnetic field which can be

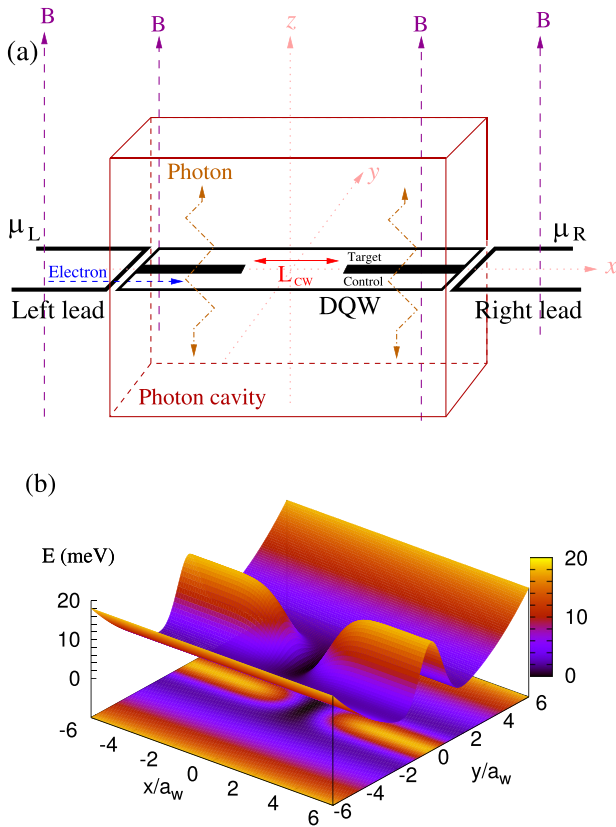


FIG. 1. (a) Schematic of DQW coupled to a photon cavity, connected to the left lead with chemical potential μ_L and the right lead with chemical potential μ_R in an external magnetic field B . A coupling window is placed between the control- and the target-waveguide with a length L_{CW} (red arrow). The electrons from the left lead only enter the control waveguide (blue arrow). (b) The potential defines the double waveguide system with a coupling window between the control- and target-waveguide. All lengths are characterized by the effective magnetic length a_w . The physical parameters are $B = 0.001$ T, $a_w = 33.72$ nm, $L_{CW} = 100$ nm, and $\hbar\Omega_0 = 1.0$ meV.

defined as $\mathbf{A}_{\text{ext}} = (0, -By, 0)$, and \mathbf{A}_{ph} is the photon vector potential that can be introduced as

$$\mathbf{A}_{\text{ph}} = A_{\text{ph}}(a + a^\dagger)\hat{\mathbf{e}}, \quad (3)$$

wherein, A_{ph} is the amplitude of the photon field and $\hat{\mathbf{e}}$ is the unit vector that determines the direction of the photon polarization either parallel (e_x) in a TE₀₁₁ mode or perpendicular (e_y) in a TE₁₀₁ mode to the transport direction. In the second term of Eq. (2), the Coulomb interacting electron Hamiltonian is shown with the Coulomb matrix elements in the SE state basis $(V_{\text{Coul}})_{nn',m'm'}$.¹⁴ The third term of Eq. (2) denotes the free photon field, where $\hbar\omega_{\text{ph}}$ is the quantized photon energy and $a^\dagger(a)$ is the operator of photon creation (annihilation), respectively. In Eq. (2), the para-magnetic (g_{ph} -term) and the dia-magnetic (g_{ph}^2 -term) of the electron-photon interaction are presented, in which $g_{\text{ph}} = eA_{\text{ph}}\Omega_w a_w/c$ is the electron-photon coupling, $g_{nn'}$ are the dimensionless electron-photon coupling tensor elements,¹⁵ and $\hat{N}_{\text{ph}} = a^\dagger a$ is the photon number operator.

In our calculations, we include both the para- and the dia-magnetic interaction terms which lead to more complex photon-electron interaction processes than are present in the resonant two-level Jaynes-Cummings model, where only the paramagnetic term is taken into account.¹⁶ In addition, we use exact diagonalization (configuration interaction) including many levels to treat the electron-electron Coulomb interaction and the electron-photon interaction¹⁷⁻¹⁹ without resorting to the rotating wave approximation.^{20,21}

B. Transport formalism

Our model for the calculation of time dependent properties of transport through an open system requires a coupling to electron reservoirs. Here, we show how the central system is connected to the leads via coupling regions. Later in this section, a time-dependent formalism will be presented to investigate the electron transport in the system.

The total Hamiltonian of the system describing the waveguide system, the leads, and the coupling between the DQW and the leads can be written as¹³

$$H(t) = H_S + \sum_{l=L,R} \int d\mathbf{q} \epsilon^l(\mathbf{q}) c_{\mathbf{q}}^{l\dagger} c_{\mathbf{q}}^l + \sum_{l=L,R} \chi^l(t) \sum_n \int d\mathbf{q} [c_{\mathbf{q}}^{l\dagger} T_{qn}^l d_n + d_n^\dagger (T_{nq}^l)^* c_{\mathbf{q}}^l], \quad (4)$$

where H_S indicates the Hamiltonian of the DQW system coupled to the photon cavity, as shown in Eq. (2). The second term of the Hamiltonian describes the l^{th} lead with \mathbf{q} being the dummy index representing the momentum of the standing electron waves in the semi-infinite leads and their subband number,¹⁴ $\epsilon^l(\mathbf{q})$ being the single-electron energy spectrum in the lead l , and $c_{\mathbf{q}}^{l\dagger}(c_{\mathbf{q}}^l)$ being the electron creation (annihilation) operators, respectively. The last term of the Hamiltonian demonstrates the time-dependent coupling between the DQW and the leads describing a transfer of an electron between a single-electron state of the central system

$|n\rangle$ and a single-electron energy state of the leads $|\mathbf{q}\rangle$ through a coupling tensor¹³

$$T_{qn}^l = \int d\mathbf{r} d\mathbf{r}' \psi_{\mathbf{q}}^l(\mathbf{r}')^* g_{qn}^l(\mathbf{r}, \mathbf{r}') \psi_n^S(\mathbf{r}), \quad (5)$$

with $\psi_n^S(\mathbf{r})$ ($\psi_{\mathbf{q}}^l(\mathbf{r}')$) being a single-electron wave function of the DQW system (leads). In addition, $\chi^l(t)$ is a time-dependent function defining the onset of the coupling, and

$$g_{qn}^l(\mathbf{r}, \mathbf{r}') = g_0^l \exp[-\delta_x^l(x-x')^2 - \delta_y^l(y-y'-\alpha)^2] \times \exp(-\Delta_n^l(\mathbf{q})/\Delta) \quad (6)$$

is a nonlocal coupling, where g_0 is the coupling strength, δ_x^l and δ_y^l are the coupling parameters that control the range of the coupling in the x - and y -direction, respectively, $\Delta_n^l(\mathbf{q}) = |E_n - \epsilon^l(\mathbf{q})|$ and Δ adjust the energy overlap of lead and DQW states and wavefunctions in the contact region,¹³ and α is a skewing parameter that shifts the weight of the coupling from the left lead to the control-waveguide.

We use a non-Markovian QME formalism to calculate the electron transport from the left lead to the right lead through the DQW system.²² The QME approach describing the time-dependent electron transport can be obtained from quantum Liouville-von Neumann equation²³

$$\dot{\rho}(t) = -\frac{i}{\hbar} [H(t), \rho(t)], \quad (7)$$

where $\rho(t)$ is the density operator of the total system. The total density operator before the coupling between the waveguide system and the leads can be written as $\rho(t_0) = \rho_L \rho_R \rho_S(t_0)$, where ρ_L and ρ_R are the density operators of the isolated left and right leads, respectively.²⁴

Our aim in this work is to seek the dynamics of the electron and the inter-waveguide switching processes in the system. To calculate the electron motion in the DQW system under the influence of the leads, we take the trace over the Fock space with respect to the lead variables to build a reduced density operator of the waveguide system $\rho_S(t) = \text{Tr}_L \text{Tr}_R \rho(t)$, which leads to the Nakajima-Zwanzig equation of time-evolution in an open system²⁵

$$\dot{\rho}_S(t) = -i\mathcal{L}_S \rho(t) + \int_{t_0}^t dt' \mathcal{K}(t, t') \rho_S(t'), \quad (8)$$

where $\mathcal{L}_S \cdot = [H_S, \cdot]/\hbar$ is the Liouvillian with respect to the time-independent Hamiltonian H_S of the DQW system and $\mathcal{K}(t, t')$ is the integral kernel representing the dissipative time-dependent coupling to the leads.^{14,25} For the regime of weak coupling by sequential tunneling to the leads treated in our model, we derive the dissipative kernel of Eq. (9) by keeping terms up to second order in the time dependent coupling.^{15,26}

The reduced density operator allows us to calculate the left and the right charge currents into or out of the DQW.²⁴ Therefore, the net charge current can be introduced as

$$I_Q(t) = I_L(t) - I_R(t), \quad (9)$$

where $I_L(t)$ denotes the partial current from the left lead into the control-waveguide and $I_R(t)$ describes to

the partial current into the right lead from both waveguides.²⁴

To explore the properties of the charge switching between the waveguides, the expectation value of the charge current density operator in the central system is calculated. The charge current density can be defined as

$$\mathbf{J}(\mathbf{r}, t) = \text{Tr}(\hat{\rho}_S(t)\hat{\mathbf{J}}(\mathbf{r})), \quad (10)$$

where the charge current density operator is

$$\hat{\mathbf{J}}(\mathbf{r}) = \sum_{nn'} \left(\frac{e\hbar}{2m^*i} [\psi_n^{S*}(\mathbf{r})(\nabla\psi_{n'}^S(\mathbf{r})) - (\nabla\psi_n^{S*}(\mathbf{r}))\psi_{n'}^S(\mathbf{r})] + \frac{e^2}{m^*} [\mathbf{A}_{\text{ext}}(\mathbf{r}) + \mathbf{A}_{\text{ph}}(\mathbf{r})] \psi_n^{S*}(\mathbf{r})\psi_{n'}^S(\mathbf{r}) \right) d_n^\dagger d_{n'}. \quad (11)$$

In light of presently attainable quality factors of photon cavities and our interest in the transient regime with $t \leq 200$ ps, we neglect cavity loss or photon coupling to external reservoirs. In the following, we shall investigate numerically the influence of the cavity photon on the coherent electron transport through the DQW system in the case of x - or y -polarization of the photon field.

III. RESULTS AND DISCUSSION

In this section, we will discuss our numerical results that demonstrate photon-switched coherent electron transport in a double quantum waveguide. To provide coherent electron transport in the system, we consider the double waveguide system to be made of a GaAs semiconductor with length $L_x = 300$ nm. It is known that the phase coherence length L_ϕ of a GaAs semiconductor can be $\sim (30-40) \times 10^3$ nm at low temperature $T \sim 0.1-2.0$ K.²⁷ Thus, the coherence length is much larger than the length of the waveguide system, which is an essential requirement to construct a qubit in quantum information technology.

We have fixed the following physical parameters in the calculations, the temperature of the leads is 0.5 K, the chemical potentials of the leads are considered to be $\mu_L = 4.0$ meV and $\mu_R = 3.0$ meV, the confinement energy of the leads and the DQW system in the y -direction is $\hbar\Omega_l = 1.0$ meV and $\hbar\Omega_0 = 1.0$ meV, respectively, the skewing parameter is $\alpha = 4a_w$, and the electron-photon coupling strength is $g_{\text{ph}} = 0.1$ meV.

A. The system without/with photon cavity

In order to understand the influence of the photons on the transport, we first explore the electron transport characteristics in the system without and with the photon cavity. Initially, the photon energy and the electron-photon coupling strength are assumed to be constant at $\hbar\omega_{\text{ph}} = 0.3$ meV and $g_{\text{ph}} = 0.1$ meV, respectively.

In a previous work,²⁸ we demonstrated the effects of the electron-electron interaction and an external magnetic field on the electron switching process between the waveguides. In this work, we will show how photons in a cavity can be used to switch the electron motion between the waveguides.

Figure 2 shows the net charge current versus the CW length L_{CW} without (w/o) a photon cavity (ph) (blue solid), and with (w) a photon cavity in x -polarized (x -p) (green dashed) and y -polarized (y -p) (red dotted) photon field. The oscillation in the net charge current depends on the transport properties of electrons between the control- and the target-waveguide. The electrons can be subjected to inter-waveguide forward or backward scattering, consequently, a current peak at $L_{\text{CW}} \simeq 40$ and a current dip at $L_{\text{CW}} \simeq 110$ nm are formed. The net charge current decreases in the presence of cavity photon for the x - and y -polarized field where the cavity contains one photon initially.

To explain the current oscillation and the suppression in the net charge current in the presence of photon cavity, we refer to the energy spectrum of the DQW system. Figure 3 shows energy spectra for the DQW system as a function of the CW length L_{CW} for the case of the no photon cavity (a), and for the system in the photon cavity (b). When the CW length L_{CW} is increased, we observe the following effects in the energy spectra: the energy of the states with an electron component decreases monotonically, and generally the degeneration of energy levels reduces. We observe an energy level crossover at $L_{\text{CW}} \simeq 40$ nm, and increased splitting of levels at $\simeq 110$ nm. The weak tunneling through the central barrier between the waveguides leads to almost degenerate symmetric and antisymmetric one-electron states (1ES), but the opening of the coupling window increases the “interaction” between these states leading to a reduced degeneracy.

In Fig. 3(a), the low end of the spectrum with only 1ES (red dots) is shown for the waveguide system without the photon cavity. At $L_{\text{CW}} \simeq 40$ nm (left blue rectangle), higher excited states enter the active bias window resulting in a level crossover with lower excited states.^{29,30} The energy crossover reflects a “resonance” energy levels between the waveguides leading to inter-waveguide transport. The contribution of the

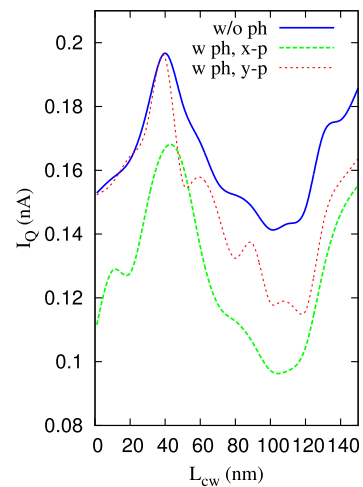


FIG. 2. The net charge current I_Q versus coupling window length L_{CW} without (w/o) a photon (ph) cavity (blue solid), and with a photon (w ph) cavity in the case of x -polarization (green dashed) and y -polarization (red dotted) at time $t = 200$ ps. The photon energy $\hbar\omega_{\text{ph}} = 0.3$ meV, $g_{\text{ph}} = 0.1$ meV, $B = 0.001$ T, and the chemical potentials are $\mu_L = 4.0$ meV and $\mu_R = 3.0$ meV, implying $\Delta\mu = 1.0$ meV.

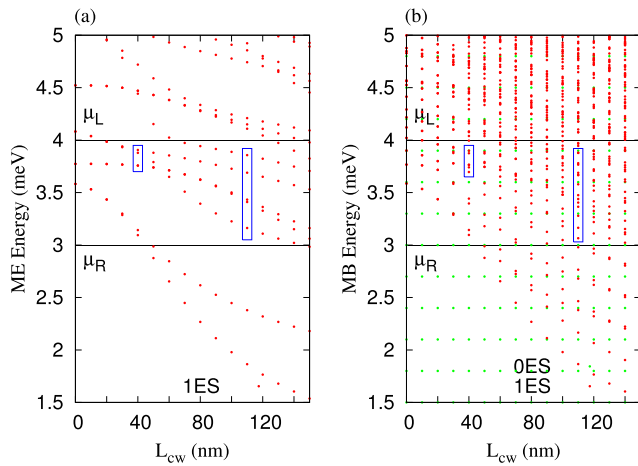


FIG. 3. Energy spectra of the DQW system as a function of CW length L_{CW} without (a) and with (b) photon cavity in the system including zero-electron states (0ES, green dots) and one-electron states (1ES, red dots) at $B = 0.001$ T. The 1ES states in the left blue rectangle are close to the crossover region of states, but the 1ES states in the right blue rectangle are not. The left rectangle contains the most active transport states. The change in the height of the rectangle from left to right indicates the spreading of states from the resonance to the off-resonant condition. The photon energy $\hbar\omega_{ph} = 0.3$ meV with x -polarization, $g_{ph} = 0.1$ meV. The chemical potentials are $\mu_L = 4.0$ meV and $\mu_R = 3.0$ meV (black) implying $\Delta\mu = 1.0$ meV.

higher excited states to the electron transport increases the net charge current forming a current peak, as shown in Fig. 2 (blue line). In the current peak, the charge is transferred from the input to the output of the control-waveguide with a slight inter-waveguide forward scattering (not shown).²⁸ For the regime of increased level splitting at $L_{CW} \simeq 110$ nm (right blue rectangle), the state of the second subband with lowest energy is the highest state in the blue rectangle enters the bias window. Even though the energy splitting indicates an “off-resonance” between the waveguides, the mixing of a state from the second subband with the first subband in the electron transport leads to a stronger coupling between the waveguides. Here, the charge from the control-waveguide partially switches to the target-waveguide due to inter-waveguide backward and forward scattering and is partially transferred to the output of the control-waveguide (not shown).²⁸ The inter-waveguide backward scattering decreases the net charge current forming a current dip, as shown in Fig. 2 (blue line). We should note that the two-electron states (2ES) of the energy spectrum are not active in the presence of the Coulomb interaction because the electron-electron interaction raises the 2ES well above the bias window; consequently, the 2ES are effectively blocked.²⁸

Figure 3(b) presents the MB energy spectrum including zero-electron states (0ES) (green dots) and 1ES (red dots) in the presence of a cavity including one photon initially with the photon energy $\hbar\omega_{ph} = 0.3$ meV and x -polarization. The one-electron states of the energy spectrum decrease monotonically with increasing CW length while the 0ES remain unchanged. We can clearly see that photon replicas for electron state appear with different photon content. The energy difference between two photon replicas is close to multiples of the photon energy in case of weak electron-photon coupling.³¹ The photon replicas of the energy levels at

$L_{CW} \simeq 40$ nm (left blue rectangle) and 110 nm (right blue rectangle) become active in the presence of a photon cavity. To a lesser extent, photon replicas of states originally below the bias region that ends up in the active bias window also contribute. Therefore, more states participate in the electron transport. In addition, the shape of the active states (and the photon replicas) is influenced by the photon field. The photon field stretches or polarizes the wavefunctions.

The photon replicas have a very important and influential role in the electron-switching process in the waveguide system. At $L_{CW} \simeq 40$ nm, the photon replicas of the ground and the first-excited states containing two photons enter the energy crossover region. The replicas containing two photons have a weaker contribution than the replicas containing one photon in the electron transport because the cavity initially contains only one photon. At $L_{CW} \simeq 110$ nm (right blue rectangle), a photon replica of the lowest state of the second subband containing one photon participates in the electron transport. The photon replica is a localized state in the CW region leading to a suppression in the net charge current for both x - (green dashed) and y -polarized (red dotted) photon field at the dip, as shown in Fig. 2. However, the photon replicas of the ground state and the first excited state containing three and four photons are found among the split energy levels. But they do not influence the electron transport in any significant way.

We should mention that the energy spectrum for the y -polarized photon field is very similar to the spectrum shown in Fig. 3(b) with a slightly different photon content in the MB energy states.

Figure 4 shows charge current density for the current peak in the x -polarized (a), and the y -polarized (b) photon field shown in Fig. 2, where the photon energy is $\hbar\omega_{ph} = 0.3$ meV and the electron-photon coupling is $g_{ph} = 0.1$ meV.

In Fig. 4(a), the charge is partially transported through the control-waveguide and partially is subject to inter-waveguide backward scattering, while in the absence of the photon cavity the charge from the input of control-waveguide moves to the output of the control- and target-waveguide. The inter-waveguide backward scattering is partially caused by the charge polarization in the x -direction induced by the photon field, and a weak participation of photon replica states containing two photons in the electron transport. As a result, the net charge current decreases in the dip. In Fig. 4(b), the charge remains completely within the control-waveguide because the photon energy is much smaller than the electron confinement energy in the waveguide system in the y -direction. The confinement and the photon energy are $\hbar\Omega_0 = 1.0$ meV and $\hbar\omega_{ph} = 0.3$ meV, respectively. In this case, the charge from the control-waveguide does not tunnel into the target-waveguide. The dynamic evolution of the charge in the control-waveguide implements a controlled NOT function, which is so called CNOT-operation quantum logic gate leading to enhancement in the net charge current.

B. Variation of the frequency and the initial number of photons

In this section, we demonstrate how the photon frequency influences the electron transport through the DQW

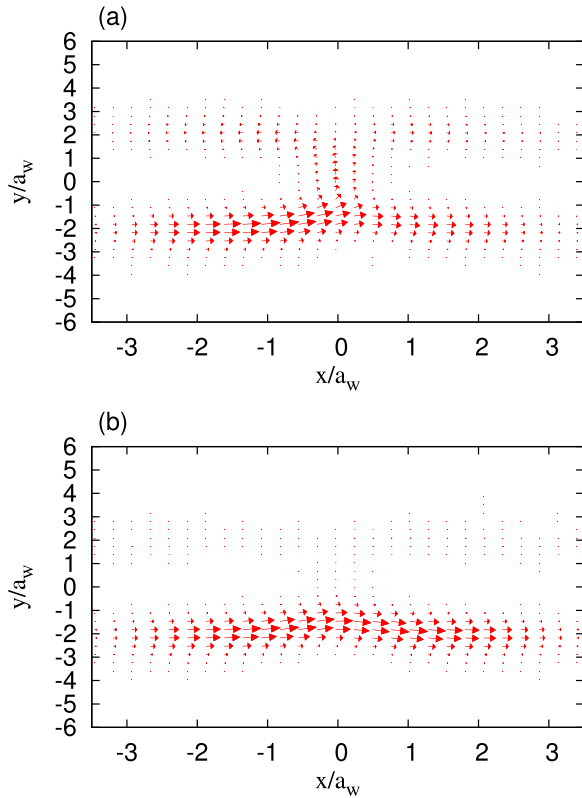


FIG. 4. The charge current density at $t = 200$ ps for x -polarized (a) and the y -polarized (b) photon field in the current peak at $L_{CW} \simeq 40$ nm shown in Fig. 2. The photon energy $\hbar\omega_{ph} = 0.3$ meV, $N_{ph} = 1$, and $g_{ph} = 0.1$ meV. The length of the DQW system is $L_x = 300$ nm, $\hbar\Omega_0 = 1.0$ meV, $B = 0.001$ T, and $a_w = 33.72$ nm.

system in the x - and y -polarized photon cavity. In addition, we show the effects of the number of photons initially in the cavity on electron switching processes between the waveguides. The electron-photon coupling strength is assumed to be constant at $g_{ph} = 0.1$ meV.

Figure 5 displays the net charge current for the x -polarized (a) and y -polarized (b) photon field with initially one

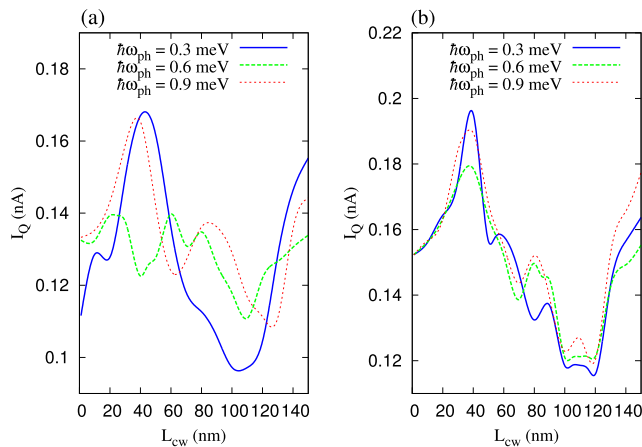


FIG. 5. The net charge current I_Q versus coupling window length L_{CW} at time $t = 200$ ps for the x -polarized (a) and y -polarized (b) photon field with initially one photon in the cavity for different photon energies $\hbar\omega_{ph} = 0.3$ meV (blue solid), 0.6 meV (dashed green), and 0.9 meV (dotted red). The electron-photon coupling $g_{ph} = 0.1$ meV, $B = 0.001$ T, and the chemical potentials are $\mu_L = 4.0$ meV and $\mu_R = 3.0$ meV, implying $\Delta\mu = 1.0$ meV.

photon in the cavity for different photon energies $\hbar\omega_{ph} = 0.3$ meV (blue solid), 0.6 meV (dashed green), and 0.9 meV (dotted red). In Sec. III A, we discussed the electron transport in the system when the photon energy is $\hbar\omega_{ph} = 0.3$ meV for both x - and y -polarized photon field. Now, we explore the results when the photon energy is either $\hbar\omega_{ph} = 0.6$ meV or 0.9 meV.

We begin by analyzing the net charge current in the x -polarized photon field shown in 5(a). In the case of a photon energy $\hbar\omega_{ph} = 0.6$ meV (dashed green), the net charge current is strongly reduced for the crossover energy at $L_{CW} \simeq 40$ nm to a current dip instead of the current peak seen for $\hbar\omega_{ph} = 0.3$ meV, while for the region of split levels at $L_{CW} \simeq 110$ nm the net charge current in the dip is enhanced. If we further increase the photon energy to 0.9 meV (red dotted), a current peak is again seen at $L_{CW} \simeq 40$ nm and a slightly shifted current dip at $L_{CW} \simeq 120$ nm.

To explore the characteristics of the net charge current in the x -polarized photon field, we provide Fig. 6 which shows the MB energy spectrum including 0ES (green dots) and 1ES (red dots) with the photon energy $\hbar\omega_{ph} = 0.6$ meV (a) and 0.9 meV (b). In Fig. 6(a), the MB energy spectrum is shown for the photon energy $\hbar\omega_{ph} = 0.6$ meV. Each MB state has photon replica with a different photon content in the presence of the photon cavity. We notice that the MB ground state is replicated into the CW with one photon and energetically enters the region of levels crossover at $L_{CW} \simeq 40$ nm (left blue rectangle). The effect of this localized photon replicated state here on the electron transport is a suppression of the net charge current leading to a current dip. But at $L_{CW} \simeq 110$ nm (right blue rectangle), the photon replica of the first excited state containing one photon contributes to the electron transport leading to an increasing net charge current at the dip, as shown in Fig. 5 (green dashed).

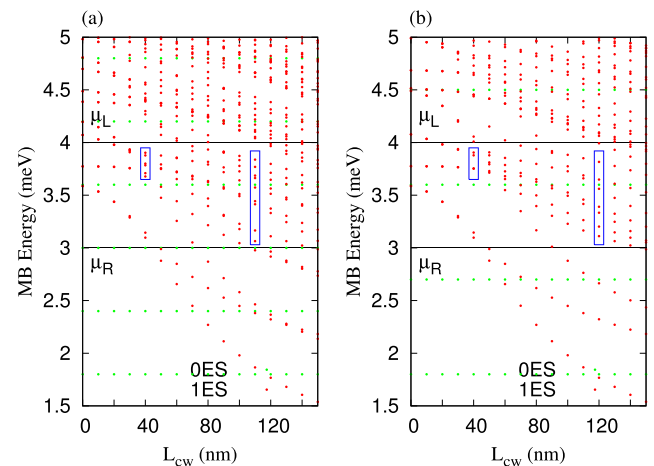


FIG. 6. Energy spectrum of the DQW in a cavity as a function of CW length L_{CW} and photon energy $\hbar\omega_{ph} = 0.6$ meV (a), and photon energy $\hbar\omega_{ph} = 0.9$ meV (b). The spectra include zero-electron states (0ES, green dots) and one-electron states (1ES, red dots) at $B = 0.001$ T. The 1ES in the left blue rectangle are close to be in crossing, but the 1ES states in the right blue rectangle are not. The left rectangle contains the most active transport states. The change in the height of the rectangle from left to right indicates the spreading of states from the resonance to the off-resonant condition. The chemical potentials are $\mu_L = 4.0$ meV and $\mu_R = 3.0$ meV (black) implying $\Delta\mu = 1.0$ meV.

In Fig. 6(b), the MB energy spectrum is displayed for the photon energy $\hbar\omega_{\text{ph}} = 0.9$ meV. The photon replica of neither the ground state nor the first excited states enters the active bias window (left blue rectangle). The result is that the net charge current is almost unaltered. However, at $L_{\text{CW}} \simeq 120$ nm (right blue rectangle), the photon replica of the first excited state is found among the active split energy levels. This photon replica containing one photon enhances the net charge current in the dip.

To clarify further the dynamic motion of the charge and explain the current oscillations, we present Fig. 7 which shows the charge current density at the current peak shown in Fig. 5 in the case of the photon energy $\hbar\omega_{\text{ph}} = 0.6$ meV (a) and $\hbar\omega_{\text{ph}} = 0.9$ meV (b). In Fig. 7(a), the charge current density is seen for the current dip at $L_{\text{CW}} \simeq 40$ nm when the photon energy is $\hbar\omega_{\text{ph}} = 0.6$ meV. The charge is localized in the CW region, which suppresses the net charge current and leads to a current dip. The localized charge can be identified as a contribution of the photon replica of the MB ground state containing one photon.

In Fig. 7(b), the charge current density for the current peak at $L_{\text{CW}} \simeq 40$ nm is presented for photon energy $\hbar\omega_{\text{ph}} = 0.9$ meV. The charge from the input control-waveguide is equally split between the output of the control- and the target-waveguide. The photon replica of neither the ground

state nor the first excited state contributes to the electron transport. But the charge density of the active states occupies both the control- and target waveguide. Therefore, the net charge current remains almost unchanged. The splitting of the charge indicates a $\sqrt{\text{NOT}}$ -operation quantum logic gate action.

We have seen that the charge current density for the current dip at $L_{\text{CW}} \simeq 110$ nm in the case of photon energy $\hbar\omega_{\text{ph}} = 0.6$ meV and 0.9 meV is delocalized (not shown) while a localized charge is observed for $\hbar\omega_{\text{ph}} = 0.3$ meV. The delocalization of charge is due to participation of a photon replica of the first excited MB state. Consequently, the net charge current is enhanced.

We have noticed that the electron-switching process can be achieved by tuning the photon number initially in the cavity. Let us consider two photons initially in the cavity with energy $\hbar\omega_{\text{ph}} = 0.6$ meV and photon-electron coupling strength $g = 0.1$ meV. Figure 8 shows the charge current density at the CW length $L_{\text{CW}} \simeq 40$ nm in the presence two photons in the cavity. Comparing to the charge current density in the case of one photon in the cavity with photon energy $\hbar\omega_{\text{ph}} = 0.6$ meV shown in Fig. 7(a), the charge motion in the DQW system is drastically changed. The electron charge switches totally from the input control- to the output target-waveguide. The dynamic evolution occurring in the DQW system implements a quantum logic gate operation. In this case, a Not-operation is realized by transferring the charge from the control- to the target-waveguide. The electron switching process is due to contribution of a photon replica of the both MB ground state and first-excited state containing two photons to the transport.

Let us now look at the influences of photon frequency in the y -polarized photon field on the electron-switching process. The net charge current I_Q in the presence of y -polarized photon field and initially one photon in the cavity displayed in Fig. 5(b) indicates that the influences of photon frequency on the electron transport is very weak compared to the x -polarized photon field for the same selected photon energies $\hbar\omega_{\text{ph}} = 0.3$ meV (blue solid), 0.6 meV (green dashed), and 0.9 meV (red dotted). This is due to the anisotropy of the geometry of the DQW system. The total charge-switching from the control- to the target-waveguide can not be achieved for

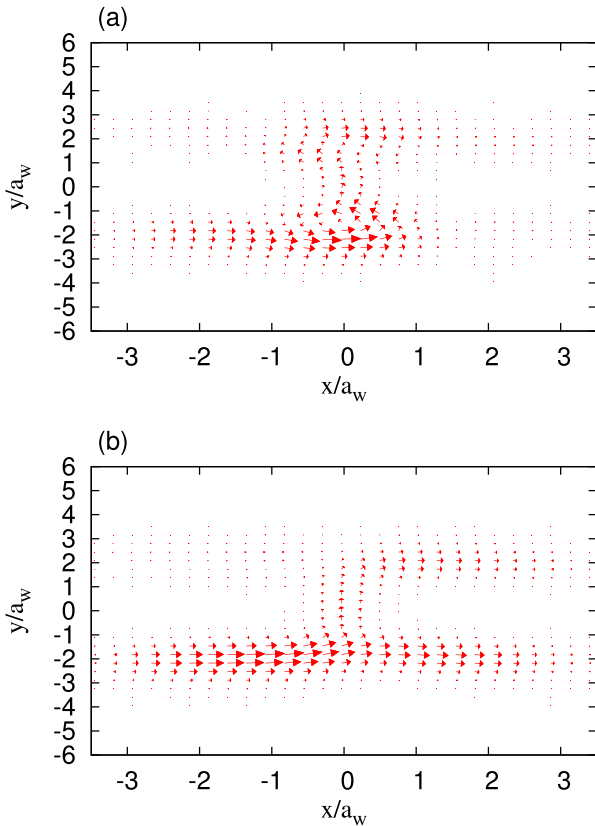


FIG. 7. Charge current density at $t=200$ ps for x -polarized photon field with photon energy $\hbar\omega_{\text{ph}} = 0.6$ meV (a) and 0.9 meV (b) for the current peak at $L_{\text{CW}} \simeq 40$ nm shown in Fig. 5. The initial photon number in the cavity $N_{\text{ph}} = 1$, and the electron-photon coupling $g_{\text{ph}} = 0.1$ meV. The length of the DQW system is $L_x = 300$ nm, $\hbar\Omega_0 = 1.0$ meV, $B = 0.001$ T, and $a_w = 33.72$ nm.

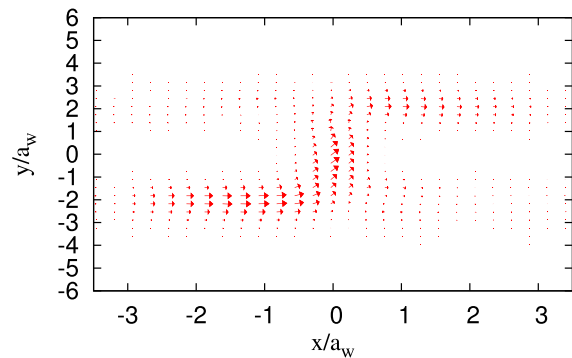


FIG. 8. Charge current density at $t=200$ ps with x -polarized photon field at $L_{\text{CW}} \simeq 40$ nm. The photon energy $\hbar\omega_{\text{ph}} = 0.6$ meV, $g_{\text{ph}} = 0.1$ meV, and initial photon number $N_{\text{ph}} = 2$. The length of the DQW system is $L_x = 300$ nm, $\hbar\Omega_0 = 1.0$ meV, $B = 0.001$ T, and $a_w = 33.72$ nm.

the same selected photon energy as in the case of a x -polarized photon field. For example, Fig. 9 shows the charge current density in the current peak at $L_{\text{CW}} \simeq 40$ nm demonstrated in Fig. 5(b) (red dotted), where the cavity initially contains one photon and the photon energy is $\hbar\omega_{\text{ph}} = 0.9$ meV. Comparing to the charge current density shown in Fig. 4(b) when the photon energy is $\hbar\omega_{\text{ph}} = 0.3$ meV, inter-waveguide transport is enhanced because the photon energy here is $\hbar\omega_{\text{ph}} = 0.9$ meV, which is close to the electron confinement energy in the waveguide system in the y -direction. An electron in the control-waveguide may obtain energy from the photon to partially occupy a state in the second subband of the two parallel waveguides and thus being transferred to the target-waveguide.

In order to facilitate total electron-switching between the waveguides in the y -polarization, we need to increase either the photon energy to be equal to or greater than the confinement energy of the electrons in the waveguide system in the y -direction or the photon number initially present in the cavity. We now consider the photon energy to be $\hbar\omega_{\text{ph}} = 0.6$ meV, which is smaller than the electron confinement energy ($\hbar\Omega_0 = 1.0$ meV) and consider two photons ($N_{\text{ph}} = 2$) initially in the cavity. An electron in the control-waveguide can absorb two photons with total energy $N_{\text{ph}} \times \hbar\omega_{\text{ph}} \simeq 1.2$ meV and then being transferred to the target-waveguide. In this case, the charge from the input control-waveguide totally switches to the target-waveguide, as shown in Fig. 10. As a result a NOT-operation quantum logic gate action is obtained.

Our results for the two different photon polarizations have revealed that a variety of quantum logic gate actions can be observed in the waveguide system with the switching being strongly influenced by the photon energy and the photon number initially in the cavity. In this connection, we have to comment on the fidelity³² of the gates. Ideally, one might want the two states of a quantum bit to be associated with an electron to be found either in the control or the target waveguide, but the situation is more complex due to the geometry of our system. The central hill separating the waveguides makes the low lying single-electron states with respect to energy to come in pairs with nearly degenerate symmetric or antisymmetric wavefunctions with respect to the two

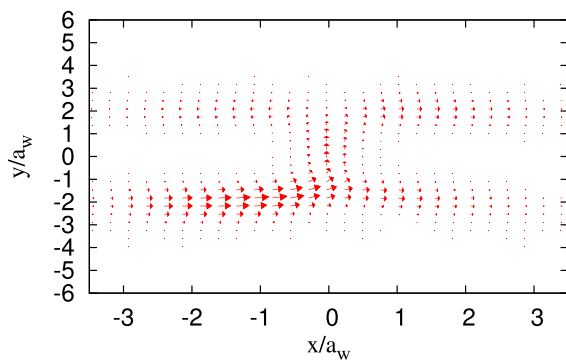


FIG. 9. Charge current density at $t = 200$ ps with y -polarized photon field in the current peak at $L_{\text{CW}} \simeq 40$ nm shown in Fig. 5(b) (red dotted). The photon energy $\hbar\omega_{\text{ph}} = 0.9$ meV, $g_{\text{ph}} = 0.1$ meV, and $N_{\text{ph}} = 1$. The length of the DQW system is $L_x = 300$ nm, $\hbar\Omega_0 = 1.0$ meV, $B = 0.001$ T, and $a_w = 33.72$ nm.

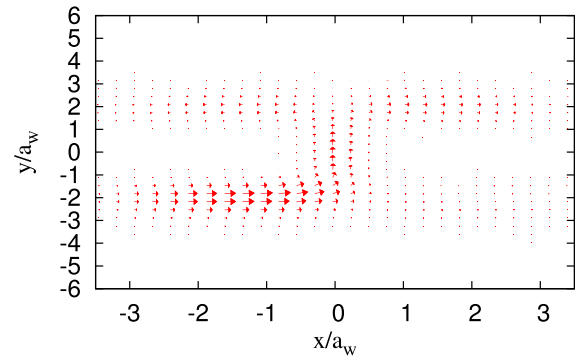


FIG. 10. Charge current density at $t = 200$ ps with y -polarized photon field at $L_{\text{CW}} \simeq 40$ nm. The photon energy $\hbar\omega_{\text{ph}} = 0.6$ meV, $N_{\text{ph}} = 2$, and $g_{\text{ph}} = 0.1$ meV. The length of the DQW system is $L_x = 300$ nm, $\hbar\Omega_0 = 1.0$ meV, $B = 0.001$ T, and $a_w = 33.72$ nm.

waveguides. The injection of electrons into the control waveguide²⁸ breaks this symmetry, i.e., the asymmetric coupling to the left lead breaks it. The coupling window further influences the wavefunctions. Their degeneracy with respect to the symmetry or the antisymmetry along the waveguides is broken by the CW. With all this in mind, we can analyze the situation for the NOT gate shown in Fig. 8. Here, a group of seven one-electron states (with state numbers 31–37, and energy in the range 5.04–5.17 meV) strongly coupled to states in the bias window (with energy around 3.8 meV), by one or two-photon processes, are partially occupied. More importantly, various pairs of them are highly correlated (with off-diagonal terms in the density matrix) resulting in the current mimicking a NOT-gate in Fig. 8. Like seen before, the photon interaction does slow down the charging and at $t = 200$ ps, the system is still not very close to a steady state.¹⁵ This example shows that the complexity of the final state makes the determination of the fidelity of the gate process rather difficult. Clearly, our system will have a difficulty in competing for fidelity with a qubit built from two well isolated states.

IV. CONCLUSIONS AND REMARKS

We have presented the results of a detailed investigation of how to implement a quantum logic gate action in a semiconductor qubit by using a new and different technique, a cavity-photon-switching. In the cavity-photon-switching method, a quantized photon cavity can be used to realize a different quantum logic gate action by varying the photon number, the photon energy, or the photon polarization.

To build a semiconductor qubit, we have considered two parallel symmetric quantum waveguides, the control- and the target-waveguide. A window is placed between them to facilitate interference and inter-waveguide electron transport. The waveguide system is connected to two leads with asymmetric coupling in which the control-waveguide is coupled to the leads from both ends, while the target-waveguide is only coupled to the right lead. The DQW system is embedded in a quantized photon cavity with a photon field polarized either parallel or perpendicular to the direction of electron motion in the system, in which the electron-photon interactions are described by exact numerical

diagonalization. We use a non-Markovian master equation to investigate the transient electron motion in the system.

In the absence of a photon cavity, the electron-switching process depends on the ME states active in the electron transport and their characteristics. By tuning the CW length, the energy spectrum of the DQW system monotonically decreases and new states enter and leave the bias window. Therefore, oscillation in the net charge current occurs, indicating inter-waveguide forward or backward scattering into the target waveguide.

In the presence of the photon cavity, photon replicas for each MB energy state appear. The character of the active photon replicas in the electron transport depend on the photon energy, the photon number, and the photon polarization in the cavity. In the case of an x -polarized photon field, photon replicas contribute to the electron transport processes leading to the following scenarios: First, at high photon energy and one photon initially in the cavity a $\sqrt{\text{NOT}}$ -operation quantum logic gate is found which is due to lifting the photon replica of the ground state out of the active energy states in the electron transport. Second, the charge from the input control-waveguide switches to the output of the target-waveguide in the presence of two photons in the cavity. In this case, an electron in the control-waveguide may interact with two photons and transfer to the target-waveguide. Therefore, a Not-operation quantum logic gate is implemented. For the y -polarized photon field, the electron-switching processes only occur if the photon energy is equal to or greater than the electron confinement energy in the DQW system in the y -direction.

We have demonstrated that the transport properties of a system with nontrivial geometry can be strongly influenced by choosing the type of electron states replicated into the active transport bias window. This control can both be excised with the photon energy and the number of photons in the cavity at the onset of an operation. It should also be stressed that our study of the time-evolution of the switching and charging processes shows that it is not necessary to await the steady state in order to complete an operation.

The optoelectronic device considered here differs from many purely optically operated devices suggested to implement quantum gates, in the sense that it need to be an open system with respect to both electrons and photons in order to operate. This definitely lowers expected values of fidelity and purity needed for quantum operations, as we discuss at the end of Sec. III, but at the same time might open up other possibilities. For example, the behaviour of our system can be continuously switched between different logical functions.

ACKNOWLEDGMENTS

This work was financially supported by the Icelandic Research and Instruments Funds, the Research Fund of the

University of Iceland, the Nordic High Performance Computing facility in Iceland, and the Ministry of Science and Technology, Taiwan through Contract No. MOST 103-2112-M-239-001-MY3.

- ¹I. van Weperen, B. D. Armstrong, E. A. Laird, J. Medford, C. M. Marcus, M. P. Hanson, and A. C. Gossard, *Phys. Rev. Lett.* **107**, 030506 (2011).
- ²M. J. Gilbert, R. Akis, and D. K. Ferry, *Appl. Phys. Lett.* **81**, 4284 (2002).
- ³R. Ionicioiu, G. Amarutunga, and F. Udrea, *Int. J. Mod. Phys. B* **15**, 125 (2001).
- ⁴C. A. Flort, *J. Appl. Phys.* **82**, 6306 (1997).
- ⁵A. Bertoni, P. Bordone, R. Brunetti, C. Jacoboni, and S. Reggiani, *Phys. Rev. Lett.* **84**, 5912 (2000).
- ⁶D. K. Ferry, R. Akis, and J. Harris, *Superlattice Microstruct.* **30**, 81–94 (2001).
- ⁷A. Marchi, A. Bertoni, S. Reggiani, and M. Rudan, *IEEE Trans. Nanotechnol.* **3**, 129 (2003).
- ⁸M. G. Snyder and L. E. Reichl, *Phys. Rev. A* **70**, 052330 (2004).
- ⁹J. Harris, R. Akis, and D. K. Ferry, *Appl. Phys. Lett.* **79**, 2214 (2001).
- ¹⁰A. Ramamoorthy, R. Akis, and J. P. Bird, *IEEE Trans. Nanotechnol.* **5**, 712 (2006).
- ¹¹P. Pingue, V. Piazza, and B. Farrer, *Appl. Phys. Lett.* **86**, 052102 (2005).
- ¹²P. Bordone, A. Bertoni, M. Rosini, and C. Jacoboni, *Semicond. Sci. Technol.* **19**, 412 (2004).
- ¹³V. Gudmundsson, C. Gainar, C.-S. Tang, V. Moldoveanu, and A. Manolescu, *New J. Phys.* **11**, 113007 (2009).
- ¹⁴N. R. Abdullah, C.-S. Tang, and V. Gudmundsson, *Phys. Rev. B* **82**, 195325 (2010).
- ¹⁵V. Gudmundsson, O. Jonasson, C.-S. Tang, H.-S. Goan, and A. Manolescu, *Phys. Rev. B* **85**, 075306 (2012).
- ¹⁶E. T. Jaynes and F. W. Cummings, *Proc. IEEE* **51**, 89 (1963).
- ¹⁷C. Yannouleas and U. Landman, *Rep. Prog. Phys.* **70**, 2067 (2007).
- ¹⁸O. Jonasson, C.-S. Tang, H.-S. Goan, A. Manolescu, and V. Gudmundsson, *New J. Phys.* **14**, 013036 (2012).
- ¹⁹V. Gudmundsson, O. Jonasson, T. Arnold, C.-S. Tang, H.-S. Goan, and A. Manolescu, *Fortschr. Phys.* **61**, 305 (2013).
- ²⁰A. T. Sornborger, A. N. Cleland, and M. R. Geller, *Phys. Rev. A* **70**, 052315 (2004).
- ²¹Y. Wu and X. Yang, *Phys. Rev. Lett.* **98**, 013601 (2007).
- ²²H.-P. Breuer and F. Petruccione, *The Theory of Open Quantum Systems* (Oxford University Press, Oxford, 2002).
- ²³M. Esposito, U. Harbola, and S. Mukamel, *Rev. Mod. Phys.* **81**, 1665 (2009).
- ²⁴N. R. Abdullah, C. S. Tang, A. Manolescu, and V. Gudmundsson, *J. Phys. Condens. Matter* **25**, 465302 (2013).
- ²⁵F. Haake, *Quantum Statistics in Optics and Solid-State Physics*, Springer Tracts in Modern Physics Vol. 66, edited by G. Hohler and E. A. Niekisch (Springer, Berlin, Heidelberg, New York, 1973), p. 98.
- ²⁶V. Moldoveanu, A. Manolescu, and V. Gudmundsson, *New J. Phys.* **11**, 073019 (2009).
- ²⁷S. Datta, *Electronic Transport in Mesoscopic System* (Cambridge University Press, Cambridge, 1995).
- ²⁸N. R. Abdullah, C. S. Tang, A. Manolescu, and V. Gudmundsson, *J. Phys. Condens. Matter* **27**, 015301 (2015).
- ²⁹T. Zibold, P. Vogl, and A. Bertoni, *Phys. Rev. B* **76**, 195301 (2007).
- ³⁰J. Gong, F.-H. Yang, and S.-L. Feng, *Chin. Phys. Lett.* **24**, 2383 (2007).
- ³¹N. R. Abdullah, C. S. Tang, A. Manolescu, and V. Gudmundsson, *Physica E* **64**, 254 (2014).
- ³²J. F. Poyatos, J. I. Cirac, and P. Zoller, *Phys. Rev. Lett.* **78**, 390 (1997).

Article IV

Coherent transient transport of interacting electrons through a quantum waveguide switch.

N. R. Abdullah, C-S Tang, A. Manolescu, and V. Gudmundsson
Journal of Physics: Condensed Matter **27**, 015301 (2015).

Coherent transient transport of interacting electrons through a quantum waveguide switch

Nzar Rauf Abdullah¹, Chi-Shung Tang², Andrei Manolescu³ and Vidar Gudmundsson¹

¹ Science Institute, University of Iceland, Dunhaga 3, IS-107 Reykjavik, Iceland

² Department of Mechanical Engineering, National United University, 1, Lienda, Miaoli 36003, Taiwan

³ Reykjavik University, School of Science and Engineering, Menntavegur 1, IS-101 Reykjavik, Iceland

E-mail: nra1@hi.is and vidar@hi.is

Received 5 August 2014, revised 9 October 2014

Accepted for publication 10 November 2014

Published 26 November 2014



Abstract

We investigate coherent electron-switching transport in a double quantum waveguide system in a perpendicular static or vanishing magnetic field. The finite symmetric double waveguide is connected to two semi-infinite leads from both ends. The double waveguide can be defined as two parallel finite quantum wires or waveguides coupled via a window to facilitate coherent electron inter-wire transport. By tuning the length of the coupling window, we observe oscillations in the net charge current and a maximum electron conductance for the energy levels of the two waveguides in resonance. The importance of the mutual Coulomb interaction between the electrons and the influence of two-electron states is clarified by comparing results with and without the interaction. Even though the Coulomb interaction can lift two-electron states out of the group of active transport states the length of the coupling window can be tuned to locate two very distinct transport modes in the system in the late transient regime before the onset of a steady state. A static external magnetic field and quantum-dots formed by side gates (side quantum dots) can be used to enhance the inter-waveguide transport which can serve to implement a quantum logic device. The fact that the device can be operated in the transient regime can be used to enhance its speed.

Keywords: quantum transport, electron–electron interaction, quantum wire and dot

(Some figures may appear in colour only in the online journal)

1. Introduction

Various schemes associated with quantum computing have been proposed for quantum information storage and transfers, such as superconducting coplanar waveguide resonators and dual waveguide devices [1, 2]. A waveguide can be defined as a quantum wire in which the electron wave propagates in quantized modes without losing phase coherence at low temperature. Various proposals have been suggested to implement a semiconductor qubit [3–5]. Among these, one idea is to use parallel quantum waveguides with a coupling-window placed between them [6]. Tuning the window-coupling allows an electron wave interference between the

waveguides and can switch the electron motion from one waveguide to the other [7].

The interference in the coupling-region specifies the possible types of qubit-operations: The electron wave can be transferred through either waveguide only (pass gate-operation). It can travel through both waveguides, split equally, implementing the so called square-root-of-Not ($\sqrt{\text{NOT}}$) operation [8]. It can switch totally from one waveguide to the other (Not-operation) [9]. Or it might switch from the first waveguide to the second one and then re-enter the first waveguide (CNot-operation) [10]. There are several parameters and phenomena that can modify the efficiency of the kind of qubit-operation that are mentioned above such as an

external magnetic field, the Coulomb interaction, electrostatic gate voltage, and the geometry of the coupling window between the waveguides.

Ferry's group proposed magnetically switching transport in an asymmetric double quantum waveguide, in which an external magnetic field is applied to switch electron motion from one quantum-waveguide to the other [7, 10]. Another suggestion for a switching-qubit is to vary the length of the coupling window (CW) L_{CW} . By varying the length of the CW, a maximum inter-waveguide tunneling can be found that increases the efficiency of the device [7]. Another approach for a switching-qubit is to define a saddle potential in the coupling window instead of a hard-walled well potential. The smoother potential defines a soft barrier between the two waveguides that washes out sharp resonance peaks, but decreases the efficiency of the qubit [11].

In the present work, we consider a double quantum waveguide (DQW) system with a CW between the waveguides in a static perpendicular magnetic field. Both ends of the DQW are connected to semi-infinite leads with an applied source-drain bias. A coherent electron transport is investigated in the system by using a non-Markovian master equation [12–15]. Smooth Gaussian potentials are used to define the barrier between the waveguides and the saddle-like CW potential. In addition, two dots are embedded in the waveguides close to the CW to enhance inter-waveguide transport. We will investigate coherent electron transport in the system by varying the CW length.

Our results lead to the following conclusions: First, we predict a maximum conductance at resonant energy-levels between the two waveguides. At a resonance energy, inter-waveguide forward scattering is enhanced and the charge density splits equally between the waveguides when two-electron states are activated in the transport. In this case, the DQW essentially works as a $\sqrt{\text{NOT}}$ -operation qubit. The Coulomb interaction shifts the two-electron states above the selected bias window and the charge current density does not split equally between the waveguides at the resonance condition. The conductance peak is slightly reduced, but it remains a peak as backward scattering is absent. In the conductance dip that forms when the energy levels of the waveguides are not in resonance backward scattering is sharply increased with or without the Coulomb interaction. The strength of the Coulomb blocking can be varied by the geometry or the material of the system. The transient transport through two capacitively coupled parallel quantum dots has been investigated by Moldoveanu *et al* in a lattice model for a weaker Coulomb interaction than is assumed here [16]. Second, an increased external static magnetic field favors inter-waveguide backward scattering leading to a decrease in the efficiency of the qubit. These results make clear the difference to previous schemes where variable magnetic field was used to control the switching between asymmetric waveguides [6, 11]. Third, the influence of the side quantum dots (QDs) can be to induce more energy-levels into resonance, and consequently increase the coupling between the waveguides and enhance the inter-waveguide transport mechanism. In the presence of side QDs, a Not-operation qubit can be realized. The efficiency

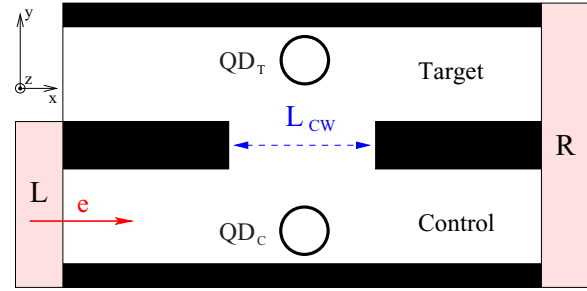


Figure 1. Schematic diagram depicting the double waveguide with a CW of length L_{CW} (blue dashed arrow). A quantum dot QD_C (QD_T) is embedded in the control (target) waveguide. An electron from left side enters the control waveguide (red arrow). Asymmetric contacts are indicated by the light red rectangles marked L and R.

is slightly decreased in the presence of side QDs because inter-waveguide backward scattering is also enhanced. At high magnetic field such that the effective magnetic length is comparable to the radius of the dots, variation of length of the CW does not influence the electron transport characteristics further as the electrons tend to be localized in the side dots. Thus, the net charge current is extremely suppressed.

The paper is organized as follows: in section 2, we present the model describing the window-coupled double waveguide system based on a quantum master equation (QME) approach. Section 3 presents our numerical results and discussion. Concluding remarks are addressed in section 4.

2. Model and theory

In this section, we present a method for calculating the transient ballistic transport in the coupled-window quantum waveguides without and with side QDs. We consider two laterally coupled waveguides connected to two semi-infinite wires from both ends. The lower waveguide (control) and the upper waveguide (target) are coupled through a CW with length L_{CW} as is schematically shown in figure 1. We consider a control-QD (QD_C) and a target-QD (QD_T) embedded, respectively, in the control- and the target-waveguide near the CW. The total system is exposed to an external magnetic field in the z -direction $B\hat{z}$. The system is designed such that the electrons are injected from the left lead to only the control-waveguide (red arrow). Our aim here is to study the charging of, and the output from each of the waveguides by varying the CW length L_{CW} (blue dashed arrow). In addition, the effects of the Coulomb interaction, the external magnetic field, and the side dots on the conductance will be explored.

The DQW is a two dimensional system with hard-wall confinement in the contact area to the external leads at $x = \pm L_x/2$, with L_x the length of the waveguides in the transport direction, but parabolic confinement in the y -direction. The single-electron Hamiltonian of the DQW including side QDs in an external magnetic field is

$$h_S = \frac{(\mathbf{p} + e\mathbf{A}_{\text{ext}})^2}{2m^*} + V_c(x, y) + V_{DW}(\mathbf{r}) + V_{QDs}(\mathbf{r}), \quad (1)$$

where \mathbf{p} indicates the canonical momentum, $\mathbf{A}_{\text{ext}} = (0, -By, 0)$ is vector potential of the external magnetic

field, and m^* is the effective mass of an electron. The confining potential of the DQW is $V_c(x, y) = V_c(x) + V_c(y)$, where $V_c(x)$ stands for a hard-wall confining potential and $V_c(y) = \frac{1}{2}m^*\Omega_0^2 y^2$ refers to a parabolic confining potential with characteristic energy $\hbar\Omega_0$. The Gaussian potential barrier between the two waveguides is presented by $V_{DW}(\mathbf{r})$ and the side QDs are defined by $V_{QDs}(\mathbf{r})$. We diagonalize the Hamiltonian of the central system presented in equation (1) using a basis [15] built with the eigenfunctions of the first two terms of (1) to find the single-electron energy spectrum E_n , where n is the composite quantum number of a single-electron state. The eigenfunctions of (1) are consequentially used to construct a many-electron Fock space for the central system, the DQW, in anticipation of the fact that its electron number will not be constant as it will be opened up to the leads. Below, we demonstrate how the DQW is connected to the leads and how the time evolution of the system is described.

2.1. DQW connected to leads

We connect the DQW to two leads that act as electron reservoirs via a contact region. The central system and the leads have the same confinement energy and the same strength of the perpendicular magnetic field. The total Hamiltonian of system is then

$$H(t) = \sum_n E_n d_n^\dagger d_n + \frac{1}{2} \sum_{nn'mm'} \langle V_{Coul} \rangle d_n^\dagger d_{n'}^\dagger d_m d_{m'} + \sum_{l=L,R} \int d\mathbf{q} \epsilon^l(\mathbf{q}) c_q^{l\dagger} c_q^l + \sum_{l=L,R} \chi^l(t) \sum_n \int d\mathbf{q} \left[c_q^{l\dagger} T_{qn}^l d_n + d_n^\dagger (T_{nq}^l)^* c_q^l \right]. \quad (2)$$

The first term describes the central system, where E_n is the single-electron energy of state $|n\rangle$ of the central system, and d_n^\dagger (d_n) denotes the electron creation (annihilation) operator respectively. The second term is the mutual Coulomb interaction between electrons in the central system. The third term of the Hamiltonian denotes the semi-infinite l th lead, where l refers to the left L or the right R lead with the dummy index \mathbf{q} representing the ‘momentum’ of an electron in the lead and its subband index [15], $\epsilon^l(\mathbf{q})$ is the single-electron energy spectrum in lead l , and the electron creation and annihilation operator in lead l are $c_q^{l\dagger}$ and c_q^l , respectively.

The last term is the time-dependent coupling Hamiltonian that connects the central system, the DQW to the external leads via a coupling tensor T_{qn}^l , and $\chi^l(t)$ dictates the time-dependence of the coupling. The coupling Hamiltonian describes the transfer of an electron between the single-electron state of the central system $|n\rangle$ and the single-electron state of the leads $|\mathbf{q}\rangle$

$$T_{qn}^l = \int d\mathbf{r} d\mathbf{r}' \psi_q^l(\mathbf{r}')^* g_{qn}^l(\mathbf{r}, \mathbf{r}') \psi_n^S(\mathbf{r}). \quad (3)$$

$\psi_n^S(\mathbf{r})$ and $\psi_q^l(\mathbf{r}')$ are the corresponding single-electron wave functions of the DQW system and the leads. $g_{qn}^l(\mathbf{r}, \mathbf{r}')$ is a

nonlocal coupling kernel

$$g_{qn}^l(\mathbf{r}, \mathbf{r}') = g_0^l \exp \left[-\delta_x^l (x - x')^2 - \delta_y^l (y - y' - \alpha)^2 \right] \times \exp \left(-\Delta_n^l(\mathbf{q})/\Delta \right), \quad (4)$$

where g_0 is the coupling strength, δ_x^l and δ_y^l are the coupling range parameters in the x - and y -direction, respectively, Δ controls together with $\Delta_n^l(\mathbf{q}) = |E_n - \epsilon^l(\mathbf{q})|$ the energy affinity between states in the leads and the central system [13], and α is a skewing parameter that shifts the weight of the coupling to the lower waveguide for an appropriate value stated below.

Before coupling the central system to the external leads a many-electron Fock space with sectors for 0-, 1-, 2-, and 3- electron states is constructed for the first term of the total Hamiltonian (2). This noninteracting many-electron (ME) basis is then used to diagonalize the Hamiltonian of the central system, the first two terms in equation (2) obtaining a Coulomb interacting ME basis. This procedure of exact numerical diagonalization of a ME Hamiltonian in a truncated basis is used in order to capture correlation effects that are of crucial importance in small systems with few electrons [17]. The diagonalization and the truncation procedure together with the necessary basis changes is described elsewhere [18, 19].

2.2. QME and Charge current density

In this subsection, we present how the time evolution of the open system is calculated in order to study time-dependent transport properties within the QME approach [20]. The time evolution of our system obeys the quantum Liouville–von Neumann equation

$$\frac{dW(t)}{dt} = -\frac{i}{\hbar} [H(t), W(t)], \quad (5)$$

where $W(t)$ is the density operator of the total system. In order to focus our attention on the open central system we project the dynamical evolution of the whole system on the central system introducing a reduced density operator (RDO), by tracing out all variables of the leads, $\rho(t) = \text{Tr}_L \text{Tr}_R W(t)$, with the initial condition $W(t < t_0) = \rho_L \rho_R \rho_S$, where ρ_L and ρ_R are the density operators of the isolated left and the right leads, respectively. The density operator of the isolated l th lead can be defined as $\rho_l = e^{-\beta(H_l - \mu_l N_l)} / \text{Tr}_l \{e^{-\beta(H_l - \mu_l N_l)}\}$, where $\beta = 1/(k_B T)$ with k_B the Boltzmann constant, and N_l is the number of electrons in the leads. The projection formalism delivers an equation of motion for density operator of the central system, the quantum master equation [21, 22]

$$\frac{d\rho(t)}{dt} = -i\mathcal{L}_S \rho(t) + \int_{t_0}^t dt' \mathcal{K}(t, t') \rho(t'), \quad (6)$$

where $\mathcal{L}_S = [H_S, \cdot]/\hbar$ is the Liouvillian with respect to the time-independent Hamiltonian H_S of the central system and $\mathcal{K}(t, t')$ is an integral kernel describing the dissipative time-dependent coupling to the leads [15, 22]. In our approach the non-Markovian QME is derived keeping terms for the system-lead coupling up to second order in the dissipation term, i.e. the integral kernel. The explicit expressions for the kernel have been published elsewhere [12, 13, 18]. The

QME is appropriate to describe sequential tunneling between the central system and the leads in the weak coupling limit. The structure of the QME as an integro-differential equation with memory effects implies higher order sequential tunneling, but not cotunneling processes.

In order to explore the switching processes between the waveguides, we define the net charge current with respect to the external leads as

$$I_Q(t) = I_L(t) - I_R(t), \quad (7)$$

where $I_L(t)$ refers to the partial current from the left lead into the control-waveguide and $I_R(t)$ indicates the partial current into the right lead from both waveguides [23]. In equation (7) the negative sign in front of I_R is since a positive charge current is defined as the current into the central system, but the currents I_L and I_R are defined positive from left to right.

To monitor the dynamic evolution of the electrons inside the central system, we calculate the expectation value of the local charge current density operator

$$\mathbf{J}(\mathbf{r}, t) = \text{Tr}(\hat{\rho}(t)\hat{\mathbf{J}}(\mathbf{r})), \quad (8)$$

where operator is defined by

$$\begin{aligned} \hat{\mathbf{J}}(\mathbf{r}) = \sum_{nn'} & \left(\frac{e\hbar}{2m^*i} [\psi_n^{S*}(\mathbf{r})(\nabla\psi_{n'}^S(\mathbf{r})) - (\nabla\psi_n^{S*}(\mathbf{r}))\psi_{n'}^S(\mathbf{r})] \right. \\ & \left. + \frac{e^2}{m^*} \mathbf{A}_{\text{ext}}(\mathbf{r})\psi_n^{S*}(\mathbf{r})\psi_{n'}^S(\mathbf{r}) \right) d_n^\dagger d_{n'}. \end{aligned} \quad (9)$$

In the following, we shall demonstrate the influence of the length of the CW, external magnetic field, and the side QDs on the coherent electron transport through the system and the charge current density in the central system in order to investigate inter-waveguide forward and backward scattering processes.

3. Results

In this section, we shall discuss our numerical results of the ballistic transport properties of the double waveguide system made of a GaAs semiconductor with the electron effective mass $m^* = 0.067m_e$. The length of the central system is $L_x = 300$ nm which is assumed to be much smaller than the phase coherent length L_ϕ . At low temperature $T \sim 0.1$ – 2.0 K, the phase coherent length of a semiconductor based (GaAs/Al_{1-x}Ga_xAs) electron waveguide is $\sim (30 - 40) \times 10^3$ nm [24]. The coherence in the electron transport through the double waveguide is an essential requirement for constructing a qubit. For the system placed in a static or vanishing external magnetic field, its length scales can be characterized by the effective magnetic length $a_w = \{\hbar/(m^*\sqrt{(\omega_c^2 + \Omega_0^2)})\}^{1/2}$, where the cyclotron frequency $\omega_c = eB/m^*$, and the transverse confinement energy $\hbar\Omega_0 = 1.0$ meV. Numerically the effective magnetic length can be expressed as

$$\begin{aligned} a_w &= \left(\frac{\hbar}{m^*\Omega_0} \right)^{1/2} \left(\frac{1}{1 + (eB/(m^*\Omega_0))^2} \right)^{1/4} \\ &= \frac{33.74}{\sqrt[4]{1 + 2.982[B(T)]^2}} \text{ nm}. \end{aligned} \quad (10)$$

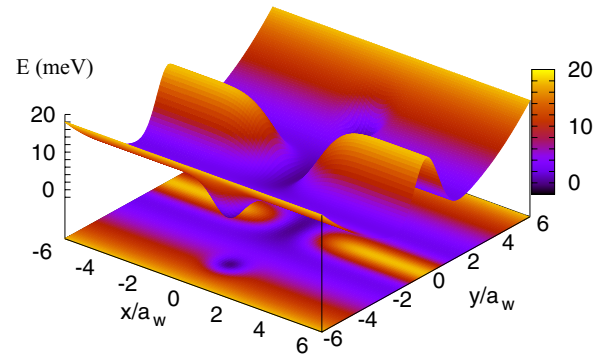


Figure 2. The potential (in meV) defining the DQW central system with the CW and the side QDs. The parameters are $\hbar\Omega_0 = 1.0$ meV, $B = 0.0$ T, $a_w = 33.72$ nm, $L_{\text{CW}} = 100$ nm, and $R_{\text{Dot}} = 25$ nm.

For the case of a vanishing magnetic field we assign to it a finite very small value in order to avoid numerical problems caused by exact degeneration of states with opposite spin.

We assume the central system is connected to the external leads acting as electron reservoirs with chemical potential in the left (right) lead $\mu_L = 4.0$ meV ($\mu_R = 3.0$ meV), implying an applied potential difference or bias window $\Delta\mu = eV_{\text{bias}} = 1.0$ meV. Furthermore, the temperature of the leads is fixed at $T = 0.5$ K. The potential of the double quantum waveguides is shown in figure 2 with the side QDs located near the CW in order to influence the inter-waveguide transport. In the following, we shall explore the influence of the CW and the side QDs on the charging of and the transport through the system.

3.1. DQW without side QDs

We start by considering an ideal window-coupled DQW without side QDs. The injected electrons are assumed to come from the left lead only into the control-waveguide. This asymmetry in the injection is accomplished with the choice of the skewing parameter $\alpha = 4.0a_w$ defined in equation (4) and only used for the left lead. In addition, we assume the two quantum waveguides to be of the same width. They are separated by a Gaussian potential barrier, in which the control- and target-waveguide interact with each other via a CW. The DQW system is described by

$$V_{\text{DQW}}(\mathbf{r}) = V_B(y) + V_{\text{CW}}(x, y), \quad (11)$$

where $V_B(y)$ is the barrier potential between the quantum waveguides defined as

$$V_B(y) = V_0 \exp(-\beta_0^2 y^2), \quad (12)$$

with $V_0 = 18.0$ meV and $\beta_0 = 0.03 \text{ nm}^{-1}$, as well as a CW potential

$$V_{\text{CW}}(x, y) = -V_0 \exp(-\beta_x^2 x^2 - \beta_y^2 y^2), \quad (13)$$

with $V_0 = 18.0$ meV, and $\beta_y = 0.03 \text{ nm}^{-1}$ implying a barrier width $W_B \simeq 66.5$ nm for the first subband which can prevent electron tunneling between the waveguides through the barrier. β_x is a parameter that determines the CW length. Thus, the length of the CW can be defined as $L_{\text{CW}} = 2/\beta_x$.

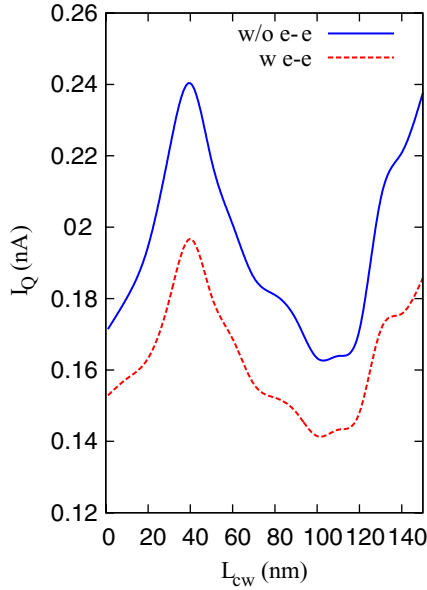


Figure 3. The net charge current I_Q versus CW length L_{CW} without (w/o) (blue solid) and with (w) (red dashed) electron–electron (e–e) interaction for magnetic field $B = 0.0$ T. The chemical potentials are $\mu_L = 4.0$ meV and $\mu_R = 3.0$ meV implying $\Delta\mu = 1.0$ meV.

We begin to analyze the results by presenting figure 3 showing the net charge current I_Q as a function of the CW length L_{CW} at $t = 200$ ps and $B = 0.0$ T for noninteracting electrons (solid blue), and for Coulomb interacting electrons (dashed red). The Coulomb interaction reduces the overall current slightly. The oscillations in the net charge current are indicative of a possible charge transport between the control-waveguide and the target-waveguide. The oscillations give rise to a peak and a dip in the net charge current at $L_{CW} \simeq 40$ and 110 nm, respectively. Similar oscillation features have been found by Zibold *et al* and Gong *et al* in the absence of the Coulomb interaction, and put in relation to energy-dependent inter-waveguide transmission in the quantum regime. They pointed out that the inter-waveguide transmission can be enhanced when the energy levels of the coupled-waveguide system achieve a resonance conditions for a specific CW length [25, 26].

To find resonant energy levels of the two waveguides, we present figure 4 showing the many-electron (ME) energy spectra for the DQW system as a function of the CW length at $B = 0.0$ T including one-electron states (1ES, red dots) and two-electron states (2ES, blue dots). The ME spectrum without the mutual Coulomb interaction is displayed in figure 4(a), but the interacting spectrum in figure 4(b). The only difference between the energy spectra is that the Coulomb interaction has raised most of the 2ES well above the bias window in figure 4(b). The 2ES do not contribute to the electron transport in the presence of the Coulomb interaction because they are far from the chosen bias window, leading to a decrease in the net charge current.

In the case of no coupling window the two waveguides are only weakly coupled through tunneling and the Coulomb interaction [16] leading to nearly degenerate states. When the length of the CW L_{CW} is increased we thus find: First,

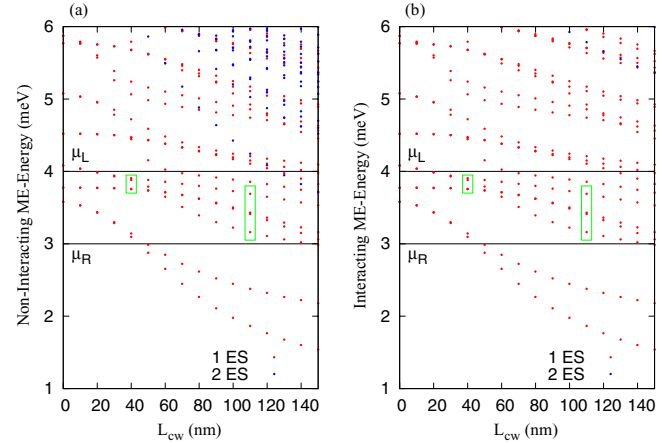


Figure 4. ME energy spectrum in the central system as a function of CW length L_{CW} without (a), and with (b) the electron–electron Coulomb interaction including one-electron states (1ES, red dots) and two-electron states (2ES, blue dots) at $B = 0.0$ T. The one-electron states in the left green rectangle are close to be in resonance, but the one-electron states in the right green rectangle are not. The chemical potentials are $\mu_L = 4.0$ meV and $\mu_R = 3.0$ meV (black) implying $\Delta\mu = 1.0$ meV.

the energy spectrum decreases monotonically [25]. Second, the near degeneration of the energy-levels is lifted. As a result, this leads to a crossover of energy levels (resonance) between the control- and target-waveguide at $L_{CW} \simeq 40$ nm (left green rectangular) which corresponds to the current-peak in figure 3. The resonance between the waveguides enhances the inter-waveguide electron transport and increases the net charge current. The splitting of the energy levels increases at a higher coupling window length such as $L_{CW} \simeq 110$ nm (right green rectangular) indicating weaker resonances and more back-scattering inter-waveguide transport.

To further explain the peak and the dip in the net charge current, we present the charge current density at $B = 0.0$ T and $t = 200$ ps in figure 5 for the noninteracting system (left panels) and the interacting one (right panels) for the peak and the dip net charge current at $L_{CW} \simeq 40$ nm (a)–(b) and 110 nm (c)–(d), respectively, shown in figure 3. The dynamical evolution occurring in the CW exhibits different types of quantum logic gates actions in our system. In the absence of the Coulomb interaction the charge current density shown in figure 5(a) reveals the following electron motion in the waveguides at $L_{CW} \simeq 40$ nm: The charge is injected into the control input, then it exits equally from both control and target output. In the DQW the charge exhibits partial inter-waveguide forward scattering which is similar to the condition of having equal electron transmission ratio in the double waveguides at a resonance [25]. The DQW here can be defined as a beam splitter or a $\sqrt{\text{NOT}}$ -operation quantum logic gate ($\sqrt{\text{NOT}}$ -operation qubit) [8]. Figure 5(c) shows the charge current density in the current-dip at $L_{CW} \simeq 110$ nm. The charge current density switches from the control- to the target-waveguide with a small ratio of inter-waveguide backward scattering. The charge switching property of the system here can be introduced as a Not-operation quantum logic gate [11]. The net charge current is suppressed here due to the presence of

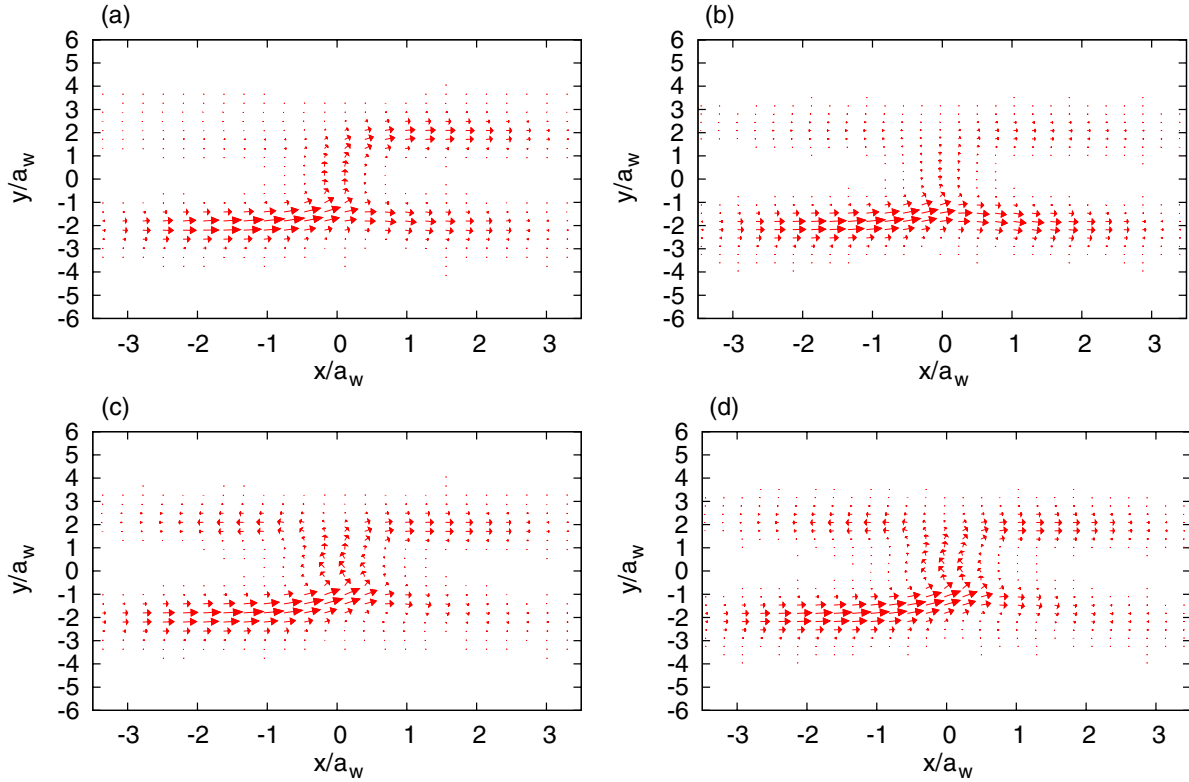


Figure 5. Charge current density in the DQW at $t = 200$ ps without (left panels) with (right panels) electron–electron Coulomb interaction in the peak and the dip net charge current at $L_{CW} \simeq 40$ nm (a, b) and 110 nm (c, d), respectively, shown in figure 3 in the case of $B = 0.0$ T (blue solid). The effective magnetic length is $a_w = 33.72$ nm.

an inter-waveguide backward scattering that forms the current-dip. The cause of the inter-waveguide backward scattering is the geometry of the system, the symmetric waveguides, while in an asymmetric system back scattering can be avoided [6]. In the presence of the Coulomb interaction the charge current density is very similar for the dip near 110 nm (comparing figures 5(c) and (d)), but different for the peak at 40 nm, where very little scattering into the target waveguide is seen (comparing figures 5(a) and (b)). Without the Coulomb interaction 2ES contribute up to 1/3 of the charge current, but the interaction reduces this with Coulomb blocking to a negligible quantity. The forward inter-waveguide scattering in figure 5(a) is facilitated by two-electron processes and states. In the present system the Coulomb interaction blocks these processes to a large extent.

The effects of a static external magnetic field are presented in figure 6(a) which shows the net charge current I_Q as a function of the CW length L_{CW} at $t = 200$ ps in the presence of the Coulomb interaction for different values of the magnetic field $B = 0.0$ T (blue solid), 0.1 T (green dashed), and 0.2 T (red dashed). For comparison we display in figure 6(b) the left and the right currents I_L and I_R at $B = 0.0$ T and the same point in time. The comparison shows that at $t = 200$ ps the system is still in the charging phase, but the overall shape of the currents is similar. The role of the external magnetic field in our system is different from the role it plays in many models where researchers have applied a variable magnetic field to switch between different processes in the waveguides. The external magnetic field has been used to switch an electron

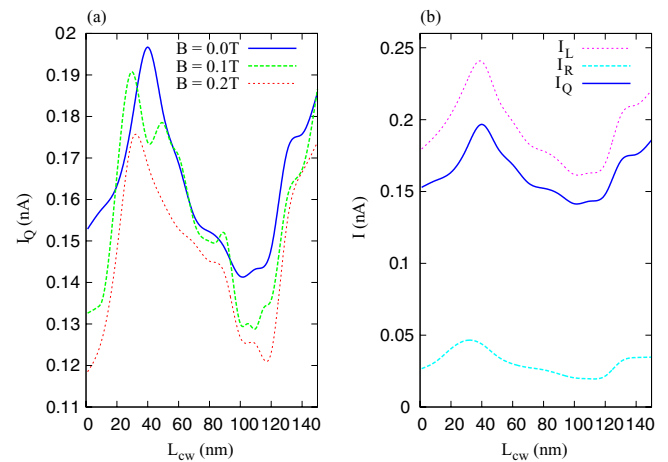


Figure 6. (a) The net charge current I_Q versus CW length L_{CW} in the presence of the Coulomb interaction for different values of the magnetic field $B = 0.0$ T (blue solid), 0.1 T (green dashed), and 0.2 T (red dotted) at time $t = 200$ ps. (b) The current from the left lead I_L (pink dotted), the current into the right lead I_R (blue dashed), and the net charge current I_Q (blue solid) for $B = 0.0$ T versus the CW length. The chemical potentials are $\mu_L = 4.0$ meV and $\mu_R = 3.0$ meV implying $\Delta\mu = 1.0$ meV.

current from one quantum-waveguide to the other one in a window coupled double waveguide [6]. In our model, we observe switching in the *absence* of a magnetic field, i.e. for $B = 0.0$ T. In the presence of stronger magnetic field, the electron motion is affected by the Lorentz force in which the electrons tend to a circular motion in both control- and

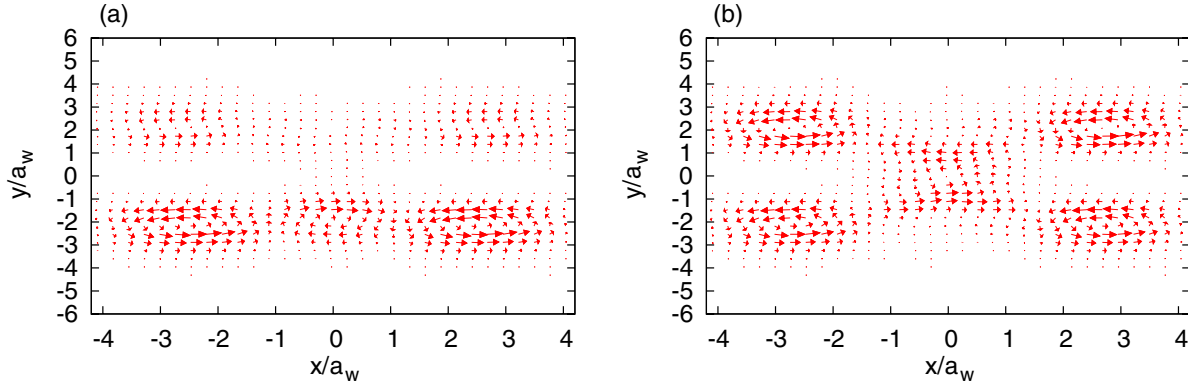


Figure 7. Charge current density in the DQW at $t = 200$ ps in the presence of the Coulomb interaction in the peak at $L_{CW} \simeq 40$ nm (a), and the dip at $L_{CW} \simeq 110$ nm (b) net charge current of figure 6(a) in the case of $B = 0.2$ T (red dotted). The effective magnetic length is $a_w = 32.76$ nm.

target-waveguides increasing the electron dwell-time in the system. The inter-waveguide backward scattering is enhanced while a suppression in the inter-waveguide forward scattering is observed in the presence of strong magnetic field. Therefore, the net charge current decreases as shown in figure 6(a) in the case of $B = 0.1$ T (green dashed) and 0.2 T (red dotted).

To understand the reasons for the suppression of the net charge current in the presence of a higher magnetic field, we show in figure 7 the charge current density at magnetic field $B = 0.2$ T in the peak at $L_{CW} \simeq 40$ nm (a) and the dip at $L_{CW} \simeq 110$ nm (b), of the net charge current shown in figure 6(a) (red dotted). An obvious explanation is: The perpendicular magnetic field reduces the effective barrier height and increases the splitting of the energy levels at the crossover energy or resonance energy (not shown). Therefore the charge current density does not split equally between the waveguides or localize in only control-waveguide, but rather an inter-waveguide backward scattering is observed due to the Lorentz force, consequently the net charge current is suppressed and we observe formation of edge states in each of the waveguides. In this case the double-waveguide system does neither play the role of a $\sqrt{\text{NOT}}$ -operation, nor a Not-operation qubit in the presence of a higher magnetic field.

3.2. DQW with side QDs

In this section, we consider a side dot embedded in each waveguide to enhance the inter-waveguide transport as is shown in figure 2. The dots to the sides of the CW may be expected to increase the dwell time in the coupling region and change the resonance condition between the two waveguides. The window-coupling DQW potential with side QDs is described by

$$V_{DQW}(\mathbf{r}) = V_B(y) + V_{CW}(x, y) + V_{Dot}(x, y), \quad (14)$$

where $V_{Dot}(x, y)$ is the side dot potential that is defined as

$$V_{Dot}(x, y) = -V_D \exp(-\gamma_x^2 x^2 - \gamma_y^2 (y - y_0)^2), \quad (15)$$

with $V_D = 8.0$ meV, $y_0 = 5.6a_w$, and $\gamma_x = \gamma_y = 0.04 \text{ nm}^{-1}$ implying the radius of each side-dot $R_{Dot} \approx 25$ nm.

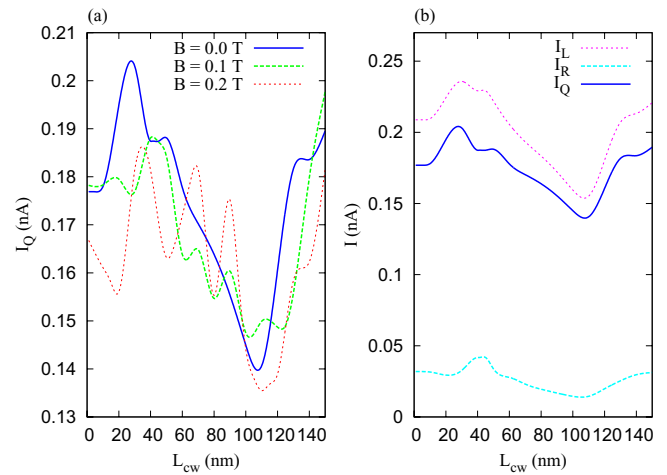


Figure 8. The net charge current I_Q versus the window-coupling length L_{CW} in the presence of the Coulomb interaction for different magnetic field $B = 0.0$ T (blue solid), 0.1 T (green dashed), 0.2 T (red dotted), 0.9 T (pink dotted) at time $t = 200$ ps. (b) The current from the left lead I_L (pink dotted), the current into the right lead I_R (blue dashed), and the net charge current I_Q (blue solid) for $B = 0.0$ T versus the CW length. The chemical potentials are $\mu_L = 4.0$ meV and $\mu_R = 3.0$ meV implying $\Delta\mu = 1.0$ meV.

Figure 8(a) shows the net charge current as a function of the CW length at $t = 200$ ps in the presence of the Coulomb interaction for different values of the magnetic field $B = 0.0$ T (blue solid), 0.1 T (green dashed), and 0.2 T (red dashed). An oscillation in the net charge current is again established in a vanishing magnetic field 0.0 T, while at higher magnetic field values 0.1 and 0.2 T some extra fluctuations in the current are observed. The existence of these fluctuations correlates with the dynamic motion of the charge in the system in which electrons participate in an inter-waveguide backward or forward scattering at different CW length. If the magnetic field is increased to $B = 0.9$ T, such that the effective magnetic length is close to the dot radius $a_w = R_{Dot}$ the net charge current is suppressed to vanishing values (not shown). In that case, varying of the CW length does not affect the electron transport in the system. There are several reasons that lead to the almost vanishing net charge current at high magnetic field such as edge effects, inter-waveguide backward scattering and

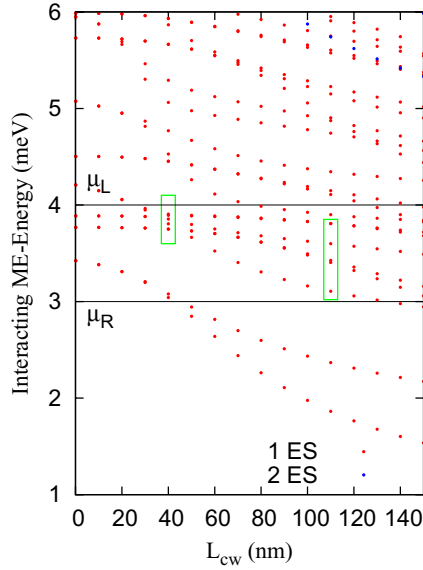


Figure 9. The interacting ME energy spectrum of the central system with side QDs as a function of the CW length L_{CW} including one-electron states (1ES, red dots) and two electron states (2ES, blue dots) at $B = 0.0$ T. The one-electron states in the left green rectangular are close to be in resonance, but the one-electron states in the right green rectangular are not. The chemical potentials are $\mu_L = 4.0$ meV and $\mu_R = 3.0$ meV (black) implying $\Delta\mu = 1.0$ meV.

localized electrons in the dots as the effective magnetic length is close to the dot radius. We present figure 8(b) to compare the left partial current (pink dotted), the right partial current (blue dashed) to the net charge current (blue solid) at $B = 0.0$ T. It can be seen that the partial currents have the same oscillation features and develop a peak and a current dip at the same CW lengths.

In order to understand the characteristics of net charge current, we refer to the energy spectrum and the charge current density. Figure 9 shows the ME-energy versus the window-coupling length at $B = 0.0$ T including one-electron states (1ES, red dots) and two electron states (2ES, blue dots). It should be noted that more energy levels get into resonance at $L_{CW} \simeq 40$ nm (left green rectangular) in the presence of the side-gate dots which indicates a stronger coupling between the control- and the target-waveguide. At larger CW length such as $L_{CW} \simeq 110$ nm (right green rectangular), the energy splitting increases resulting in different electron motion in the system.

The electron motion in the waveguides is completely changed in the presence of the side QDs. Figure 10 displays the charge current density at $B = 0.0$ T and $L_{CW} \simeq 40$ nm (a) and current-dip at $L_{CW} \simeq 110$ nm (b) shown in figure 8(a) (blue solid). In figure 10(a) the charge current density is displayed for $L_{CW} \simeq 40$ nm. The charge in the control-waveguide is switched to the target-waveguide, thus a Not-operation is realized. Comparing to the system without side-gate dots in figure 5(b), the inter-waveguide transport is enhanced due to a stronger coupling between the waveguides at the resonant-energy levels at $L_{CW} \simeq 40$ nm. Therefore, the side QDs play an essential role to convert the qubit operation in the system. In addition, the inter-waveguide backward scattering here reduces the efficiency of the qubit. As we mention previously, the

existence of inter-waveguide backward scattering might be due to symmetric waveguides while the backward-scattering in an asymmetric waveguides can be avoided or reduced [27]. Figure 10(b) shows the charge current density at the current-dip $L_{CW} \simeq 110$ nm. The incoming charge into the control-waveguide encounters the control-QD leading to electron back-scattering in the control-waveguide, thus the net charge current is suppressed forming a current-dip. We can say that the side-dots play a scattering role in the waveguides in such way that the electrons partially get forward- and backward-scattered in and into both waveguides.

By tuning the external magnetic field to a higher value, $B = 0.2$ T, the electrons manifest different dynamical motion in the waveguides. In figure 11 the charge current density is shown in this stronger magnetic field $B = 0.2$ T at the CW length $L_{CW} \simeq 40$ (a) and 110 nm (b). The graphs show circular motion, edge states, in each waveguide. Figure 11(a) shows the current charge density at $L_{CW} \simeq 40$ nm, the electrons in the control-waveguide do not totally switch to the target-waveguide, because of increased energy level splitting at the resonance-energy in the presence of higher magnetic field. In addition, charge is partially localized in the control-QD as the effective magnetic length approaches the radius of the quantum dot $a_w \simeq R_{Dot}$. In figure 11(b), the electrons are mostly localized in the control-QD corresponding to the current-dip at $L_{CW} \simeq 110$ nm. This electron localization is expected because at a larger CW length the splitting of energy levels increases and leads to suppression of the inter-waveguide scattering. Therefore, the electrons move along the control-waveguide and get localized in the control-QD at this higher magnetic field.

4. Concluding remarks

We have presented a model for a double quantum waveguide in an external perpendicular magnetic field. The waveguides are coupled via a window to facilitate inter-waveguide transport. The DQW is weakly connected to two leads with different chemical potentials in which a non-Markovian master equation is utilized to investigate coherent switching in electron transport between the waveguides for the implementation of quantum logic gates.

By tuning the length of the CW, we have demonstrated two important physical characteristics of the waveguide system: resonant energy-levels and oscillations in the net charge current. The resonant energy levels indicate a strong coupling between the DQW and the oscillations reflect that the resonance conditions are governed by the length of the CW.

In the case of an ideal non-Coulomb-interacting window-coupled DQW system without a magnetic field, the charge current density splits equally between the waveguides at resonant energies, therefore, the net charge current reaches its maximum value and the waveguide system works as a $\sqrt{\text{NOT}}$ -operation qubit. The splitting of charge is due to the contribution of 2ES to the electron transport. The inter-waveguide forward scattering leading to the charge splitting at resonant levels is not seen without including two-electrons states in the model. It is strongly reduced by the Coulomb

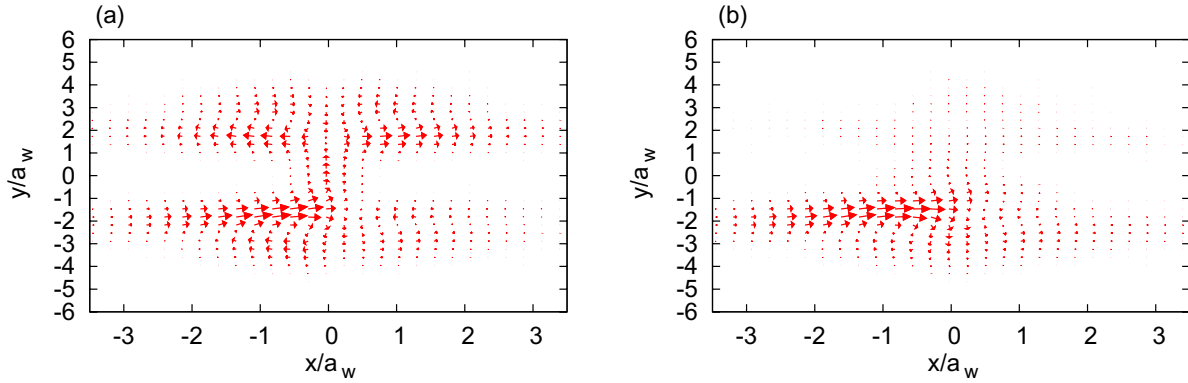


Figure 10. Charge current density in the DQW at $t = 200$ ps in the presence of the Coulomb interaction in the peak $L_{CW} \simeq 40$ nm (a), and the dip $L_{CW} \simeq 110$ nm (b) of the net charge current of figure 8(a) in the case of $B = 0.0$ T. Other parameters are $a_w = 33.72$ nm, and $R_{Dot} \approx 25$ nm.

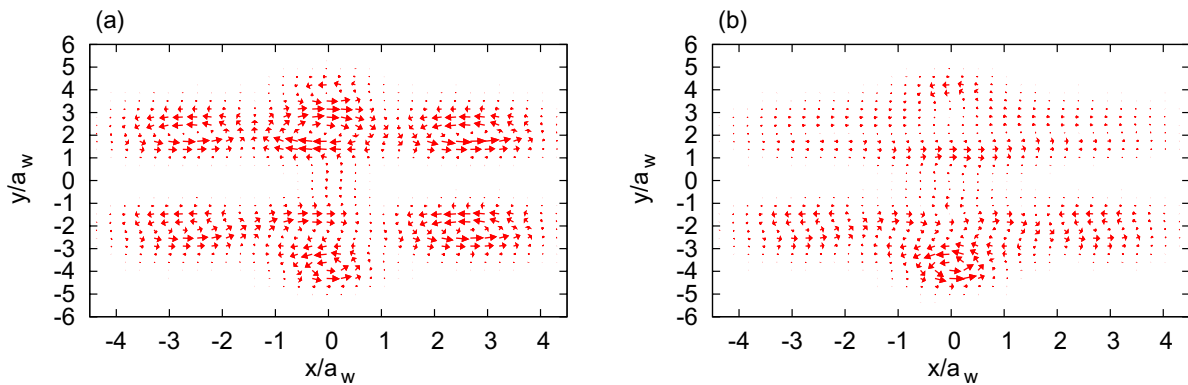


Figure 11. Charge current density in the DQW at $t = 200$ ps in the presence of the Coulomb interaction in the peak $L_{CW} \simeq 40$ nm (a), and the dip $L_{CW} \simeq 110$ nm (b) net charge current of figure 8(a) in the case of $B = 0.2$ T. Other parameters are $a_w = 32.78$ nm, and $R_{Dot} \approx 25$ nm.

interaction that lifts the 2ES out of the group of active states in the transport. This aspect can though be controlled by the exact system size and design as the Coulomb blocking is reduced in a larger system, or by using a higher bias window or different material. Our model only includes sequential tunneling of electrons from the leads to the system, but the addition of higher order tunneling would only increase the importance of the many-electron structure and the Coulomb interaction on the operation of the system. The charge splitting process can not be obtained in the presence of an external magnetic field because inter-waveguide backward scattering is enhanced leading to decrease in the efficiency of the logic gate.

Two parallel waveguides or dots can be coupled in many distinct ways. Moldoveanu *et al* [16] attain it capacitively, while Zibold *et al* [25] fine tune the system by tunneling coupling. Both groups stress the strong dependence of the device on its exact geometry, and the structure and correlations of many-electron states that are active in the transport. Our investigation with a different coupling scheme for the waveguides confirms this sensitive dependence.

In addition, we have embedded a quantum dot in each waveguide to enhance inter-waveguide transport. In the presence of side QDs, more energy-levels of the two waveguides are brought into resonance which can lead to a stronger coupling between them. Effectively, the dots can increase the density of states around the resonant transport

states. The electrons from the control-waveguide switch to the target-waveguide indicating a Not-operation qubit. But on the other hand, the side-dots can also increase the inter-waveguide backward scattering and reduce the qubit efficiency. In a stronger external magnetic field, the electrons get localized in the dots as the effective magnetic length is comparable to the radius of the side dot. In this case, the geometry of the CW does not affect the electron transport anymore. The external magnetic field here is considered static, but one more variable to influence the transport is the shape of the side QDs in the waveguides. We show that the varying of the CW length between the waveguides can specify the type of the qubit logic gate to be implemented by the DQW system.

A comparison between the charge current and the left and right currents in figures 6 and 8 at the time point in time $t = 200$ ps shows that the system has not completely reached a steady state yet, but the sought after function of the DQW is already present in the late transition regime. This is important. The exact steady state takes a long time to reach due to a low rate of charging for 2 and 3 electron states. Valuable time can be gained by operation of a device in the transition regime.

Acknowledgments

This work was financially supported by the Icelandic Research and Instruments Funds, the Research Fund of the University

of Iceland, the Nordic High Performance Computing facility in Iceland, and the National Science Council in Taiwan through Contracts No. NSC100-2112-M-239-001-MY3 and No. MOST103-2112-M-239-001-MY3.

References

- [1] Zhang P, Xiang Z-L and Nori F 2014 Spin-orbit qubit on a multiferroic insulator in a superconducting resonator *Phys. Rev. B* **89** 115417
- [2] Ionicioiu R, Amarutunga G and Udrea F 2001 Quantum computation with ballistic electrons *Int. J. Mod. Phys. B* **15** 125
- [3] Martinis J M, Nam S, Aumentado J and Urbina C 2002 Rabi oscillations in a large Josephson-junction qubit *Phys. Rev. Lett.* **89** 117901
- [4] Bordone P, Bertoni A, Rosini M and Jacoboni C 2004 Coherent transport in coupled quantum wires assisted by surface acoustic waves *Semicond. Sci. Technol.* **19** 412–4
- [5] Reichl L E and Snyder M G 2005 Coulomb entangler and entanglement-testing network for waveguide qubits *Phys. Rev. A* **72** 032330
- [6] Gilbert M J, Akis R and Ferry D K 2002 Magnetically and electrically tunable semiconductor quantum waveguide inverter *Appl. Phys. Lett.* **81** 4284
- [7] Harris J, Akis R and Ferry D K 2001 Magnetically switched quantum waveguide qubit *Appl. Phys. Lett.* **79** 2214
- [8] Snyder M G and Reichl L E 2004 Ballistic electron waveguide adder *Phys. Rev. A* **70** 052330
- [9] Marchi A, Bertoni A, Reggiani S and Rudan M 2003 Investigation on single-electron dynamics in coupled GaAs-AlGaAs quantum wires *IEEE Trans. Nanotechnol.* **3** 129
- [10] Bertoni A, Bordone P, Brunetti R, Jacoboni C and Reggiani S 2000 Quantum logic gates based on coherent electron transport in quantum wires *Phys. Rev. Lett.* **84** 5912–5
- [11] Ramamoorthy A, Akis R and Bird J P 2006 Influence of realistic potential profile of coupled electron waveguide on electron switching characteristics *IEEE Trans. Nanotechnol.* **5** 712
- [12] Moldoveanu V, Manolescu A and Gudmundsson V 2009 Geometrical effects and signal delay in time-dependent transport at the nanoscale *New J. Phys.* **11** 073019
- [13] Gudmundsson V, Gainar C, Tang C-S, Moldoveanu V and Manolecu A 2009 Time-dependent transport via the generalized master equation through a finite quantum wire with an embedded subsystem *New J. Phys.* **11** 113007
- [14] Moldoveanu V, Manolescu A, Tang C-S and Gudmundsson V 2010 Coulomb interaction and transient charging of excited states in open nanosystems *Phys. Rev. B* **81** 155442
- [15] Abdullah N R, Tang C-S and Gudmundsson V 2010 Time-dependent magnetotransport in an interacting double quantum wire with window coupling *Phys. Rev. B* **82** 195325
- [16] Moldoveanu V, Manolescu A and Gudmundsson V 2010 Dynamic correlations induced by Coulomb interactions in coupled quantum dots *Phys. Rev. B* **82** 085311
- [17] Pfannkuche D, Gudmundsson V and Maksym P A 1993 Comparison of a Hartree, a Hartree-Fock, and an exact treatment of quantum dot helium *Phys. Rev. B* **47** 2244
- [18] Gudmundsson V, Tang C-S, Jonasson O, Moldoveanu V and Manolescu A 2010 Correlated time-dependent transport through a two-dimensional quantum structure *Phys. Rev. B* **81** 205319
- [19] Gudmundsson V, Jonasson O, Arnold T, Tang C-S, Goan H-S and Manolescu A 2013 Stepwise introduction of model complexity in a generalized master equation approach to time-dependent transport *Fortschr. Phys.* **61** 305
- [20] Breuer H-P and Petruccione F 2002 *The Theory of Open Quantum Systems* (Oxford: Oxford University Press)
- [21] Haake F 1971 Density operator and multitime correlation functions for open systems *Phys. Rev. A* **3** 1723–34
- [22] Haake F 1973 *Quantum Statistics in Optics and Solid-state Physics (Springer Tracts in Modern Physics)* vol 66, ed G Hohler and E A Niekisch (Berlin: Springer) p 98
- [23] Abdullah N R, Tang C S, Manolescu A and Gudmundsson V 2013 Electron transport through a quantum dot assisted by cavity photons *J. Phys.: Condens. Matter* **25** 465302
- [24] Datta S 1995 *Electronic Transport in Mesoscopic system* (Cambridge: Cambridge University Press)
- [25] Zibold T, Vogl P and Bertoni A 2007 Theory of semiconductor quantum-wire-based single- and two-qubit gates *Phys. Rev. B* **76** 195301
- [26] Gong J, Yang F-H and Feng S-L 2007 coherent tunneling in coupled quantum wells under a uniform magnetic field *Chin. Phys. Lett.* **24** 2383
- [27] Akguc G B, Reichl L E, Shaji A and Snyder M G 2004 Bell states in a resonant quantum waveguide network *Phys. Rev. A* **69** 042303